Designing Microporous Polymers for Separations

by

Kayla R. Storme

B.S. Biochemistry, University of Illinois at Chicago, 2018
A.A.S. Operations Engineering, Joliet Junior College, 2018
A.S., Joliet Junior College, 2015

Submitted to the Department of Chemistry
in partial fulfillment of the requirements for the degree of

DOCTOR OF PHILOSOPHY

at the

MASSACHUSETTS INSTITUTE OF TECHNOLOGY

February 2024

Signature of Author: _____
Department of Chemistry
December 8, 2023

Certified by: _____
Timothy M. Swager
John D. MacArthur Professor of Chemistry
Thesis Supervisor

Certified by: _____
Zachary P. Smith
Robert N. Noyce Career Development Professor of Chemical Engineering
Thesis Supervisor

Accepted by: _____
Adam Willard
Professor of Chemistry
Graduate Officer, Department of Chemistry

This docotoral thesis has been examined by a
Committee of the Department of Chemistry as follows:

Prof. Jeremiah A. Johnson: _____

Professor of Chemistry
Thesis Committee Chair

Prof. Timothy M. Swager: _____

John D. MacArthur Professor of Chemistry
Thesis Supervisor

Prof. Zachary P. Smith: _____

Robert N. Noyce Career Development
Professor of Chemical Engineering
Thesis Supervisor

Designing Microporous Polymers for Separations

by

Kayla R. Storme

Submitted to the Department of Chemistry
on December 8, 2023 in partial fulfillment of the requirements for the degree of

DOCTOR OF PHILOSOPHY

ABSTRACT

In **Chapter 1**, we investigate the influence of side-chain length and dispersity in ring-opening metathesis polymerization (ROMP) polymers with pore-generating side chains. Macromonomers with four discrete monodispersities are separated and polymerized to produce bottlebrush polymers with monodisperse side chains. Each bottlebrush polymer is fabricated into a free-standing film. Pure-gas experiments are performed to explore the impact of dispersity and side chain length on gas separation performance.

In **Chapter 2**, we evaluate the mixed-gas performance of a class of bottlebrush polymers described in Chapter 1. Gas sorption, diffusion, and CO_2-induced plasticization are reported. Competitive sorption effects are studied using 50:50 mixture of CO_2/CH_4. Separation performance at different compositions of CO_2/CH_4 is also explored.

In **Chapter 3**, we incorporate nitrile functionality into the structure of a family of polymers with rigid, porogenic side chains described in Chapters 1 and 2. Statistical and block copolymers are synthesized to demonstrate the role of grafting density on separation performance and CO_2 plasticization resistance. Sorption experiments are performed to determine improvements to selectivity.

In **Chapter 4**, we describe the optimized S_NAr synthesis of a poly(arylene ether) (PAE) that produces high molecular weight polymers. The synthesis of an analogous PAE with C-H functionality instead of C-F is also reported. Porosity and free volume are investigated in both PAEs. Separation performance is characterized and compared to other polymers with similar structural motifs.

Thesis supervisor: Timothy M. Swager
Title: John D. MacArthur Professor of Chemistry

Thesis supervisor: Zachary P. Smith
Title: Robert N. Noyce Career Development Professor of Chemical Engineering

Acknowledgments

I would like to express my deep gratitude to the individuals whose unwavering support and guidance have been instrumental in the completion of this dissertation. Their invaluable contributions have enriched my academic, professional, and personal journey. Their support has made this endeavor a truly collaborative and fulfilling experience.

I am profoundly grateful for the guidance and support provided by my advisors, Professor Tim Swager and Professor Zach Smith, throughout the course of this research. Their expertise, unwavering commitment, and insightful feedback have been the cornerstones of my academic journey. I extend my deepest appreciation to Tim for providing a space for me to learn and find inspiration, your dedication to my professional growth, and encouraging me even when I felt lost and was struggling. I offer my profound gratitude to Zach for your positive and motivating attitude, unwavering patience with me, and your guidance as I considered my next steps after my Ph.D. Your mentorship has been invaluable, shaping not only the outcome of this dissertation but also my growth as a scholar.

To my thesis committee chair, Professor Jeremiah Johnson: thank you for the insightful discussions and suggestions throughout my research. Your feedback has helped motivate me throughout my time at MIT.

To my amazing labmates, both past and present: the members in the Swager and Smith labs have been incredibly supportive, always willing to help, and have aided me in feeling seen, acknowledged, and like I belong throughout my time at MIT. To my research mentors, Dr. You-Chi Mason Wu, Dr. Sharon Lin, and Dr. Francesco M. Benedetti, thank you for your wonderful foundation as I started my Ph.D. and was learning what I got myself into. I was motivated to continue because of your kindness and advice. To Dr. Jessica Beard, you are an invaluable mentor and friend. To Prof. Ben McDonald, for introducing me to NOBCChE and looking out for my best interests early in my Ph.D. To my office and bay mates, Prof. Máté Bezdek, Prof. Alberto Concellón, Dr. Qilin He, Dr. Sohyun Park, Weize Yuan, Dr. Nathan Man Wai Wu, Ashton Davis, Dr. Georgios Toupalas, Dr. Jesús Castro, and Dr. Chi-Hsien Wang for the great conversations and laughs. To Dr. Tiffany Chen for the thoughtful brainstorming discussions and synthetic approaches I could try when everything else seemed to fail. To Dr. Michelle Chen for checking in with me, especially during difficult times, teaching me how to use copper wire to secure water lines, and for the wonderful discussions about science, life, and everything else. To Dr. Michael Ocheje, for always listening to my ideas no matter how wild and giving me a good laugh. To Dr. Benedikt Schreib, for

the laughs, working with me on analyzing NMRs, and always bringing great conversation. To Dr. Harry Bergman for helping me realize the squash player I could become and the positive support to push through. To Taigyu Joo for helping me with my workflow, solve issues with codes, and your motivation. To Haosheng Feng for getting the lab out to more social lunches with each other and sharing your chemistry intuition. To Aristotle Grosz for bringing your love of pigs to the lab and your willingness to problem solve. To Molly Warndorf for pushing through I-Corps with me, being a wonderful collaborator, and interesting games and discussions. To Daniel Martinez for the great discussions over coffee/tea breaks that made sure I got some sunlight. To Pablo Dean and Jing Ying Yeo for helping me understand my sorption data when it made no sense and always checking in when we see each other in lab.

I am sincerely thankful for all my friends who have been a wonderful support for me. I want to give special thanks to Sophia Weng, Angela Lee, Kathleen Wang, Stephanie Smelyansky, Sam Kaser, Brighton Skeel, Abe Herzog-Arbeitman, Andy Dorfeuille, Corshai Williams. It truly takes a community, and you all provided me the opportunity to be build one with you all.

Finally, I offer my profound gratitude to my brother, David Storme, and to my loving partner, Nick Donohue. You have inspired me to follow my dreams and encouraged me multiple times in the last 5 years to continue pursuing my Ph.D. at MIT. To David: I would not be on the east coast without your advice, guidance, and support. To Nick: I cannot thank you enough. From helping me wrangle LaTeX, making sure I was eating, to your excitement and kindness, you have kept me smiling. I look forward to what comes next.

Respective Contributions

Chapter 1
This chapter was a collaborative effort between the author, Francesco M. Benedetti, You-Chi Mason Wu, Sharon Lin, Yuan He, Erica Flear, and Yanchuan Zhao. Francesco M. Benedetti, You-Chi Mason Wu, and Sharon Lin were the leaders of this study and co-wrote the manuscript. Francesco M. Benedetti and Sharon Lin performed the gas separation experiments. You-Chi Mason Wu and Yuan He performed the the design, synthesis, and characterization of the polymers. Yanchuan Zhao contributed to the design and synthesis of the polymers. The author and Erica Flear contributed to the synthesis.

Chapter 2
This chapter was a collaborative effort between the author, Sharon Lin, You-Chi Mason Wu, and Francesco M. Benedetti. Sharon Lin was the leader of this study, performed the gas sorption and gas separation experiments, and wrote the manuscript. The author and You-Chi Mason Wu performed the synthesis and characterization of the polymers. Francesco M. Benedetti assisted Sharon Lin in the gas sorption and gas separation experiments.

Chapter 3
This chapter was a collaborative effort between the author, Sharon Lin, You-Chi Mason Wu, and Sherrie X. Qian. The author performed the design, synthesis, characterization, gas sorption, and gas separation experiments of the copolymers and wrote the manuscript. Sharon Lin performed the gas sorption and gas separation experiments of CN-ROMP. You-Chi Mason Wu performed the design, synthesis, and characterization of CN-ROMP. Sherrie X. Qian assisted the author in the synthesis.

Chapter 4
This chapter was based solely on work by the author.

Contents

Title page **1**

Abstract **5**

Acknowledgments **7**

Respecitve Contributions **9**

1 Side-Chain Length and Dispersity in ROMP Polymers with Pore-Generating Side Chains for Gas Separations **23**

1.1 Abstract . . . 24
1.2 Introduction . . . 24
1.3 Results and discussion . . . 26
1.3.1 Synthesis . . . 26
1.3.2 Gas separation performance . . . 27
1.4 Conclusion . . . 33
1.5 Experimental Section . . . 33
1.5.1 Materials and Methods . . . 33
1.5.2 Synthetic procedures and characterization . . . 34
1.5.3 Membrane fabrication and treatment . . . 39
1.5.4 Pure-gas permeability measurements . . . 39
1.5.5 CO_2-induced plasticization study . . . 46
1.6 Acknowledgments . . . 47

2 Role of side-chain length on gas transport of CO_2/CH_4 mixtures in polymers with side-chain porosity **49**

2.1 Abstract . . . 50
2.2 Introduction . . . 50
2.3 Results and discussion . . . 52
2.3.1 Sorption analysis . . . 52
2.3.2 Mixed-gas permeation analysis . . . 56
2.4 Conclusion . . . 60
2.5 Experimental methods . . . 60
2.5.1 Materials and Methods . . . 60
2.5.2 Polymer synthesis . . . 61
2.5.3 Polymer film preparation . . . 61

2.5.4 High-presure pure-gas sorption measurements . . . 62
2.5.5 Mixed-gas permeation measurements . . . 63
2.5.6 CO_2 Hysteresis . . . 64
2.5.7 Dual-mode Sorption Data . . . 65
2.5.8 Gas Separation Data . . . 67
2.6 Acknowledgments . . . 70

3 Role of grafting density and nitrile functionalization on gas transport in polymers with side chain porosity 73
3.1 Abstract . . . 74
3.2 Introduction . . . 74
3.3 Results and discussion . . . 76
3.3.1 Synthesis . . . 76
3.3.2 Pure-gas sorption analysis . . . 78
3.3.3 Pure-gas permeation analysis . . . 79
3.3.4 CO_2-induced plasticization . . . 80
3.4 Conclusions . . . 81
3.5 Experimental methods . . . 82
3.5.1 Materials . . . 82
3.5.2 Polymer film preparation . . . 82
3.5.3 Chemical Characterization . . . 82
3.5.4 Thermal characterization . . . 83
3.5.5 Physical Characterization . . . 84
3.5.6 Synthesis of monomers . . . 87
3.5.7 Synthesis of polymers . . . 89
3.5.8 Chemical, thermal, and physical characterization . . . 92
3.5.9 Sorption isotherms and dual-mode sorption parameters . . . 96
3.5.10 Pure-gas Permeation Data . . . 98
3.5.11 CO_2 high pressure sweeps . . . 100
3.5.12 NMR spectra of monomers and polymers . . . 101
3.6 Acknowledgments . . . 139

4 Tuning porosity in triptycene-based poly(arylene ether)s 141
4.1 Abstract . . . 142
4.2 Introduction . . . 142
4.3 Results and discussion . . . 144
4.3.1 Thermal Properties of PAEs . . . 144
4.3.2 Free Volume and Packing Structure Analysis . . . 145
4.4 Pure-gas permeation analysis . . . 147
4.5 Conclusions . . . 150
4.6 Experimental methods . . . 150
4.6.1 Materials . . . 150
4.6.2 Preparation of Polymer Films . . . 150
4.6.3 Chemical Characterization . . . 151
4.6.4 Synthesis of polymers . . . 154

4.6.5 NMR spectra of polymers 156
4.6.6 Molecular weight, dispersity, thermal, and physical properties 161
4.6.7 Pure-gas permeation data 161
4.7 Acknowledgments 163

References **165**

List of Figures

Figure 1.1 (a) Comparison of polymer structures between a previous study [20] and this study; (b) reaction conditions to polymerize OMe n-mers; (c) MALDI-TOF MS spectrum of each n-mer in this work. 25

Figure 1.2 BET surface areas of poly(OMe 2-mer) through poly(OMe 5-mer), plus nonuniform OMe-ROMP (average $n = 4.5$). 27

Figure 1.3 Robeson plots of alcohol-treated poly(OMe n-mer)s and OMe-ROMP for (a) CO_2/CH_4, (b) H_2/CH_4, and (c) H_2/N_2 gas pairs. Black and gray lines represent the 2008 and 1991 Robeson upper bounds, respectively [21], [22]. 28

Figure 1.4 (a) O_2 diffusion coefficient for both thermally- and methanol-treated poly(OMe n-mer) samples versus side-chain length (n). Slopes and errors, determined using linear regression and χ^2 analysis, were calculated using the Origin 9.1 fitting tool. (b) O_2/N_2 diffusivity selectivity for $n = 4$ and $n = 5$ uniform poly(OMe n-mer) and nonuniform OMe-ROMP with average $n = 4.5$ 30

Figure 1.5 High-pressure pure-gas CO_2 permeability experiments conducted on (a) poly(OMe 2-mer), (b) poly(OMe 3-mer), (c) poly(OMe 4-mer), and (d) poly(OMe 5-mer). Note that poly(OMe 2-mer) was treated with ethanol while other samples were treated with methanol. 32

Figure 1.6 Example of the method used to obtain NMR integration ratios. . . . 36

Figure 1.7 N_2 adsorption isotherms and pore size distributions (PSDs) calculated using the nonlocal density functional theory (NLDFT) using the standard slit carbon model of (a) poly(OMe 2-mer), (b) poly(OMe 3-mer), (c) poly(OMe 4-mer), (d) poly(OMe 5-mer), and (e) polydispersed OMe-ROMP obtained from Brunauer–Emmett–Teller (BET) analysis. 38

Figure 1.8 Fractional free volume (FFV) as a function of side-chain length (n). Red squares represent calculations using "Method 1" [24]–[26]. Black circles represent calculations using "Method 2" [27].) 40

Figure 1.9 Robeson plots of poly(OMe n-mer)s,OMe-ROMP, and CF_3-ROMP for (a) CO_2/CH_4, (b) H_2/CH_4, and (c) H_2/N_2 gas pairs. Black and gray lines represent the 2008 and 1991 Robeson upper bounds, respectively [21], [22]. Filled shapes represent alcohol-treated samples, and open shapes represent thermally-treated samples. 43

Figure 1.10 Diffusion coefficient for (a) N_2, (b) CH_4, and (c) CO_2 versus side-chain length (n). (d) Diffusivity selectivity for $n = 4$ and $n = 5$ uniform poly(OMe n-mer)and non-uniform OMe-ROMP with average $n = 4.5$ for CO_2/CH_4, N_2/CH_4, and CO_2/N_2 gas pairs. 44
Figure 1.11 Hysteresis induced by conditioning of films at 51 bar of CO_2 for all samples in this study. Results for CF_3-ROMP, OMe-ROMP, and PIM-1 from our previous work[20] are included here for comparison. 46

Figure 2.1 Pure-gas sorption isotherms as a function of fugacity (atm) for (a) poly(OMe 2-mer), (b) poly(OMe 3-mer), (c) poly(OMe 4-mer), and (d) poly(OMe 5-mer). Red points indicate CH_4, while blue points indicate CO_2. Filled points indicate increasing fugacity, while unfilled points indicate decreasing fugacity. Individual points represent experimental data, while curves represent dual-mode model fits. (For interpretation of the references to colour in this figure legend, the reader is referred to the Web version of this article.). 53
Figure 2.2 Sorption at infinite dilution (S_{inf}) for CH_4 (red squares) and CO_2 (blue circles) versus side-chain length for poly(OMe n-mer) samples in this study. Linear fits and R2 values were calculated using the Origin 2019b linear fitting tool, and without regard to the error bars. (For interpretation of the references to colour in this figure legend, the reader is referred to the Web version of this article.) 55
Figure 2.3 Robeson upper bound plots of all poly(OMe n-mer) samples. Unfilled symbols represent pure-gas data collected at ~1.1 atm feed fugacity. Symbols with a dot in the center (20:80 CO_2/CH_4), half-filled symbols (50:50 CO_2/CH_4), and filled symbols (80:20 CO_2/CH_4) represent mixed-gas data collected at ~2.2 atm total feed fugacity. All data were obtained at 35 ∘C. The solid red line represents the 2008 Robeson upper bound [21], the solid black line represents the 1991 Robeson upper bound [22], and the gray dashed line represents the 2018 mixed-gas upper bound [115]. (For interpretation of the references to colour in this figure legend, the reader is referred to the Web version of this article). 57
Figure 2.4 Mixed-gas CO_2 (blue) and CH_4 (red) permeabilities as functions of CO_2 partial fugacity (50:50 CO_2/CH_4 mixture at 35 ∘C) for (a) poly(OMe 3-mer), (b) poly(OMe 4-mer), and (c) poly(OMe 5-mer). Unfilled symbols represent pure-gas data at ~1.1 atm, and filled symbols represent mixed-gas data. (For interpretation of the references to colour in this figure legend, the reader is referred to the Web version of this article). 58
Figure 2.5 Mixed-gas CO_2/CH_4 permselectivity as functions of CO_2 partial fugacity (50:50 CO_2/CH_4 mixture at 35 °C) for (a) poly(OMe 3-mer), (b) poly(OMe 4-mer), and (c) poly(OMe 5-mer). Unfilled symbols represent pure-gas data at ~1.1 atm, and filled symbols represent mixed-gas data. 59

Figure 2.6 Hysteresis induced by conditioning samples at ~39–41 atm CO_2. Note that sorption and desorption data points had slightly offset pressures based on final equilibrium conditions from the pressure decay measurement, so linear interpolation between data points was used for this plot to calculate concentration deviations at equal pressure steps. Error bars were determined using error propagation. 64
Figure 2.7 Dual-mode sorption parameters (a) k_D, (b) $C_H^{'}$, (c) b, (d) $C_H^{'}b$, and (e) $C_H^{'}b/k_D$ for CH_4 (red squares) and CO_2 (blue circles) versus side-chain length for all poly(OMe n-mer) samples considered in this study. Linear fits and R2 values were calculated using the Origin 2019b linear fitting tool, and without regard to the error bars. 66
Figure 2.8 Robeson upper bound plots of all poly(OMe n-mer) samples considered in this study in comparison with commercial membranes and other newly developed materials. Gray diamonds represent commercial membranes, while blue stars represent newly developed materials. The solid red line represents the 2008 Robeson upper bound [21], the solid black line represents the 1991 Robeson upper bound [22], and the gray dashed line represents the 2018 mixed-gas upper bound [115]. . . 68

Figure 3.1 a) Pure-gas CO_2 sorption isotherms with dual-mode model fits and b) ideal CO_2/CH_4 sorption selectivity for CN-ROMP, NNb-24, NN-13, and N-19 copolymers. 78
Figure 3.2 Pure-gas a) permeation of CO_2/CH_4 for NN- and N-based copolymers compared to OMe-ROMP [83] measured at 35°C and 1 atm, b) CO_2/CH_4 sorption selectivity calculated from permselectivity divided by time-lag diffusivity selectivity measurements for each copolymer, and c) CO_2/CH_4 diffusivity selectivity calculated from time-lag for each copolymer. Figures 3.2b and 3.2c also contain selectivity derived from static equilibrium sorption measurements for NN-13 and N-19. These results are reported as DMS results in the figure. 80
Figure 3.3 Normalized CO_2 permeabilities for high pressure sweeps of a) NN- and b) N-based copolymers. 81
Figure 3.4 BET isotherm of N_2 at 77K for CN-ROMP. 92
Figure 3.5 Molecular weight distributions of NNb-24 block copolymer. 92
Figure 3.6 FTIR of NN-based statistical copolymers, NN block copolymer and NN homopolymer. The characteristic nitrile peak ~2260 cm^{-1} is highlighted with a reference band. 94
Figure 3.7 Heating curves of TGA for a) NN- and b) N-based copolymers. 94
Figure 3.8 Last heating cycle of DSC for a) NN- and b) N-based copolymers. . . 94
Figure 3.9 Heating curves from DMA of a) NN-13 and b) N-19 copolymers to confirm T_g. 95
Figure 3.10 WAXS data of a) NN- and b) N-based copolymers. Observed d-spacing values are reported. 95

Figure 3.11 Sorption isotherms at 35°C from CO_2 DMS parameter fitting for CN-ROMP and poly(OMe 5-mer) [133]. Experimental data for CN-ROMP is included. . . . 96
Figure 3.12 CH_4 sorption isotherms at 35°C for CN-ROMP, NNb-24, NN-13, and N-19. . . . 96
Figure 3.13 Pure-gas CO_2 plasticization of a) N-3, b) N-19, c) NN-3, d) NN-13, and e) NNb-24. . . . 100
Figure 3.14 ^{1}H NMR spectrum of 2,3-bis(bromomethyl)naphthalene. . . . 101
Figure 3.15 ^{1}H NMR spectrum of 2,3-bis(cyanomethyl)naphthalene. . . . 102
Figure 3.16 ^{1}H NMR spectrum of CN-ROMP monomer. . . . 104
Figure 3.17 ^{13}C NMR spectrum of CN-ROMP monomer. . . . 105
Figure 3.18 ^{1}H NMR spectrum of CN-macromonomers. . . . 107
Figure 3.19 ^{1}H NMR spectrum of CN-ROMP. . . . 109
Figure 3.20 ^{1}H NMR spectrum of OMe-ROMP. . . . 111
Figure 3.21 HMBC 2D NMR spectrum of OMe-ROMP. . . . 112
Figure 3.22 HSQC 2D NMR spectrum of OMe-ROMP. . . . 113
Figure 3.23 ^{1}H NMR spectrum of NN-13 copolymer. . . . 115
Figure 3.24 HMBC 2D NMR spectrum of NN-13 copolymer. . . . 116
Figure 3.25 HSQC 2D NMR spectrum of NN-13 copolymer. . . . 117
Figure 3.26 COSY 2D NMR spectrum of NN-13 copolymer. . . . 118
Figure 3.27 ^{1}H NMR spectrum of NN-3 copolymer. . . . 120
Figure 3.28 HMBC 2D NMR spectrum of NN-3 copolymer. . . . 121
Figure 3.29 HSQC 2D NMR spectrum of NN-3 copolymer. . . . 122
Figure 3.30 COSY 2D NMR spectrum of NN-3 copolymer. . . . 123
Figure 3.31 ^{1}H NMR spectrum of NNb-24 copolymer. . . . 125
Figure 3.32 HMBC 2D NMR spectrum of NNb-24 copolymer. . . . 126
Figure 3.33 HSQC 2D NMR spectrum of NNb-24 copolymer. . . . 127
Figure 3.34 COSY 2D NMR spectrum of NNb-24 copolymer. . . . 128
Figure 3.35 ^{1}H NMR spectrum of N-19 copolymer. . . . 130
Figure 3.36 HMBC 2D NMR spectrum of N-19 copolymer. . . . 131
Figure 3.37 HSQC 2D NMR spectrum of N-19 copolymer. . . . 132
Figure 3.38 COSY 2D NMR spectrum of N-19 copolymer. . . . 133
Figure 3.39 ^{1}H NMR spectrum of N-3 copolymer. . . . 135
Figure 3.40 HMBC 2D NMR spectrum of N-3 copolymer. . . . 136
Figure 3.41 HSQC 2D NMR spectrum of N-3 copolymer. . . . 137
Figure 3.42 COSY 2D NMR spectrum of N-3 copolymer. . . . 138

Figure 4.1 Heating curves for a) TGA and b) last heating cycle of DSC for PAE-F and PAE-H. . . . 145
Figure 4.2 N_2 adsorption isotherms at 77 K for PAE-F and PAE-H. . . . 146
Figure 4.3 WAXS spectra results for PAE-H and PAE-F. . . . 146
Figure 4.4 Pure-gas permeation of PAE-F compared to 6FDA-OHB, 6FDA-OFB [160], and 6FDA-DATRI [162] for a) N_2/CH_4, b) CO_2/CH_4, c) CO_2/N_2, and d) O_2/N_2. . . . 148
Figure 4.5 Pure-gas CO_2 permeabilities for high pressure sweep of PAE-F. . . . 149

Figure 4.6 ^{1}H NMR of PAE-F. 156
Figure 4.7 ^{13}C NMR of PAE-F. 157
Figure 4.8 ^{19}F NMR of PAE-F. 158
Figure 4.9 ^{1}H NMR of PAE-H. 159
Figure 4.10 ^{13}C NMR of PAE-H. 160

List of Schemes

Scheme 2.1 Chemical structure of poly(OMe n-mer)s considered in this study. . 52

Scheme 3.1 Synthesis of a) CN-ROMP and b) norbornene (N)- and nitrile norbornene (NN)-based copolymers. 76
Scheme 3.2 Synthesis of CN-macromonomers (**4**). 77

Scheme 4.1 Polymerization reaction schemes for a) PAE-F and b) PAE-H. Included are the c) structures of the 6FDA-based polymers referenced for comparisons [120], [160]–[162]. 143

List of Tables

Table 1.1 MALDI-TOF MS data and expected m/z values. 35
Table 1.2 NMR integration ratios of OMe n-mers. 35
Table 1.3 Molecular weights of poly(OMe n-mer)s considered in this study. . . . 36
Table 1.4 BET surface areas of poly(OMe 2-mer) through poly(OMe 5-mer)powders. The discrepancy between the reported BET surface area of OMe-ROMP here (484 $m^2\,g^{-1}$) and the previously reported BET surface area[20] (146 $m^2\,g^{-1}$) is attributed to variation in sample preparation and measurement techniques [46]. 37
Table 1.5 Density, van der Waals volumes (V_W), and fractional free volume (FFV) of poly(OMe n-mer) samples from n = 2–5. "Method 1" refers to group contribution methods developed by Bondi, van Krevelen, and Park and Paul [24]–[26]. "Method 2" refers to an updated group contribution method developed by Wu et al. [27] 40
Table 1.6 Gas separation performance of all poly(OMe n-mer)s in this study. Permeability coefficients(P) are given in barrer ($10^{-10}\ cm^3\ (STP)\ cm\ cm^{-2}\ s^{-1}\ cmHg^{-1}$), diffusion coefficients (D) are given in $10^{-8}\ cm^2\ s^{-1}$, and sorption coefficients(S) are given in $cm^3(STP)\ cm^{-3}\ atm^{-1}$. All data were obtained at 35 °C and ~1 bar upstream pressure. 42
Table 1.7 Diffusivity selectivity for fresh methanol-treated samples of poly(OMe 4-mer), OMe-ROMP(4.5 average side-chain length), and poly(OMe 5-mer). 45

Table 2.1 Sorption at infinite dilution (S_{inf}) for CH_4 and CO_2 of poly(OMe n-mer) samples considered in this study. Units of S_{inf} are in cm^3(STP) cm^{-3}(polymer) atm^{-1}. 65
Table 2.2 Dual-mode sorption model parameters for all poly(OMe n-mer) samples. Units of k_D are in cm^3(STP) cm^{-3}(polymer) atm^{-1}, units of $C_H^{'}$ are in cm^3(STP) cm^{-3}(polymer), and units of b are in atm^{-1}. 65
Table 2.3 CO_2/CH_4 gas transport properties of all poly(OMe n-mer) samples at ~1.1 atm feed fugacity (for pure gases) or ~2.2 atm total feed fugacity (for mixtures). Permeability (P) is given in barrer (10^{-10} cm^3(STP) cm cm−2 s^{-1} $cmHg^{-1}$). All data were obtained at 35 °C. 67
Table 2.4 Reference mixed-gas CO_2/CH_4 permeation data. Total feed pressures for all data presented are ~2 atm (except for Cellulose Acetate, which had a total feed pressure of 3.9 atm). 68

Table 2.5 Variable pressure CO_2/CH_4 mixed-gas separation performance of poly(OMe 3-mer), poly(OMe 4-mer) and poly(OMe 5-mer). Mixture composition was set at 50:50. Permeability (P) is given in barrer (10^{-10} cm^3(STP) cm cm^{-2} s^{-1} $cmHg^{-1}$). All data were obtained at 35 °C. 69

Table 3.1 CH_4 and CO_2 sorption at infinite dilution (S_{inf}) for N-19, NN-13, NNb-24, and CN-ROMP. Data for poly(OMe 5-mer) [133] and PIM-1 [91] is included for comparison. S_{inf} is given in units of cm^3STP cm^{-3}pol atm^{-1}. 79

Table 3.2 Molecular weight information determined by GPC for NN- and N-based copolymers studied. Densities were collected using a geometric method, as outlined in the experimental section. 93

Table 3.3 CO_2 Dual-mode sorption parameters for N-19, NN-13, NNb-24, and CN-ROMP. Data for poly(OMe 5-mer) [133] and PIM-1 [91] is included for comparison. Uncertainties do not account for co-dependencies in coupled parameters, such as b and $C_H^{'}$. 97

Table 3.4 Pure-gas permeabilities, diffusion coefficients and sorption coefficients at 1 atm of NN- and N-based copolymers tested. Permeabilities (P) are given in barrer (10^{-10} cm^3_{STP} cm cm^{-2} s^{-1} $cmHg^{-1}$), diffusion coefficients (D) are given in 10^{-8} cm^2 s^{-1}, and sorption coefficients (S) are given in cm^3_{STP} cm^{-3}_{pol} atm^{-1}. Additional significant figures are provided in certain cases to show data that was used in plotting figures. [a]Calculated from DMS parameters. 98

Table 3.5 Diffusivity selectivity and sorption selectivity at 1 atm and 35°C for each gas tested. Additional significant figures are provided in certain cases to show data that was used in plotting figures. [a]Calculated from DMS parameters. 99

Table 4.1 Molecular weight, thermal properties, and physical characterization (density, FFV, and BET surface area) of PAE-H and PAE-F. Information for 6FDA-OHB, 6FDA-OFB [160], and 6FDA-DATRI [162] is included for reference. 161

Table 4.2 Pure-gas permeability measured at 35 °C and ~1 bar. Permeability is reported in units of barrer. Information for 6FDA-OHB, 6FDA-OFB [160], and 6FDA-DATRI [162] is included for reference. 161

Table 4.3 Diffusion (D) and sorption (S) coefficients for PAE-F and diffusivity selectivity and sorption selectivity for O_2/N_2, N_2/CH_4, CO_2/CH_4, and CO_2/N_2. Values for 6FDA-OHB, 6FDA-OFB [160], and 6FDA-DATRI [162] is included for reference. 162

Chapter 1

Side-Chain Length and Dispersity in ROMP Polymers with Pore-Generating Side Chains for Gas Separations

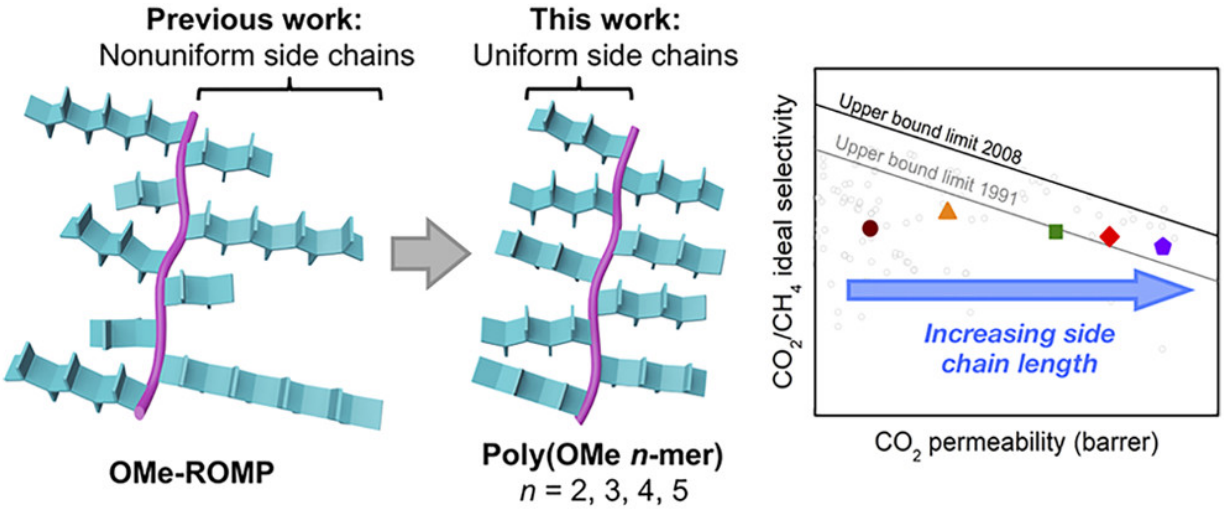

1.1 Abstract

Bottlebrush polymers with flexible backbones and rigid side chains have shown ultrahigh CO_2 permeability and plasticization resistance for membrane-based gas separations. To date, this class of polymers has only been studied with polydisperse side chains. Herein, we report gas transport properties of a methoxy (OMe) functionalized polymer synthesized via ring-opening metathesis polymerization (ROMP) with uniform side-chain lengths ranging from n = 2 to 5 repeat units to elucidate the role of both side-chain length and dispersity on gas transport properties and plasticization resistance. As side-chain length increased, both Brunauer–Emmett–Teller (BET) surface area and gas permeability increased with minimal losses in gas selectivity. Increased plasticization resistance was also observed with increasing side-chain length, which can be attributed to increased interchain rigidity from longer side chains. Controlling the side-chain length provides an effective strategy to rationally control and optimize the performance of ROMP polymers for CO_2-based gas separations.

1.2 Introduction

The use of membranes for gas separations is a promising alternative to traditional industrial separations due to their energy efficiency, low capital investment, and operational simplicity (i.e., no moving parts or phase changes) [1], [2]. In order to be suitable for scale-up and operation, such membranes must be solution-processable as well as highly permeable and selective [3]. Recently, polymers of intrinsic microporosity (PIMs) have emerged to define the state of the art in pure-gas performance due to their rigid and contorted backbones that lead to inefficient packing and concomitant pore generation, which results in very high gas permeabilities [4]–[8]. Since the discovery of PIMs, a range of design strategies (e.g., the incorporation of rigid groups such as iptycenes, Tröger's base and analogous motifs, fused norbornyl benzocyclobutene repeat units (CANALs), and polybenzoxazoles through thermally rearranged (TR) polymers) have been used to generate pores for improved separation performance [9]–[18].

We recently introduced an alternative method to generate free volume using a "bottlebrush"-type polymer with a flexible poly(norbornene) backbone decorated with rigid, free-volume-generating side chains [19], [20]. A variety of functionalities can be incorporated into the rigid macromonomers prior to their polymerization, allowing for the effects of these functionalities on polymer packing and gas transport properties to be studied. To that end, we investigated gas transport properties of two porous polymers generated via ring-opening metathesis polymerization (ROMP) with two different chemical substituents (CF_3-ROMP and OMe-ROMP) and found that CF_3-ROMP possessed ultrahigh CO_2 permeability (>21000 barrer) and exceptional plasticization resistance (CO_2 plasticization pressure > 51 bar) [20]. Although OMe-ROMP also displayed similar exceptional plasticization resistance, the CO_2 permeability was lower (~2900 barrer) [20]. These outstanding permeabilities, coupled with moderate selectivities of the major gas pairs considered, positioned CF_3-ROMP and OMe-ROMP across the separation performance upper bounds developed by Robeson for polymer materials [20]–[22]. The overall moderate selectivity of ROMP polymers compared to other PIMs

with similar permeability was found to be related to limited diffusivity selectivity [20]. This finding is potentially related to the nonuniformity in side-chain length and the stereochemistry of the rigid side chains. Thus, we hypothesized that creating side chains of uniform length could potentially improve diffusivity selectivity, and consequently the permselectivity, in ROMP polymers.

In this study, we report gas transport properties of OMe-ROMP with uniform side chains ranging from n = 2 to 5 repeat units (Figure 1.1), which we designate as poly(OMe n-mer)s. We found that increasing side-chain length (i.e., the value of n) led to increased pure-gas permeability and diffusion coefficients for all gases considered, with minimal loss in selectivity. Although we hypothesized that forming side chains of uniform length could improve selectivity, the dispersity of side-chain length in samples did not influence gas transport properties. For example, permeabilities, diffusivities, and selectivities of OMe-ROMP with polydisperse side chains (average n = 4.5) fell between those of poly(OMe 4-mer) and poly(OMe 5-mer). When measuring high-pressure pure-gas CO_2 permeation, increasing side-chain length correlated with increased plasticization pressures, suggesting that side-chain length presents a tunable parameter for enhancing plasticization resistance.

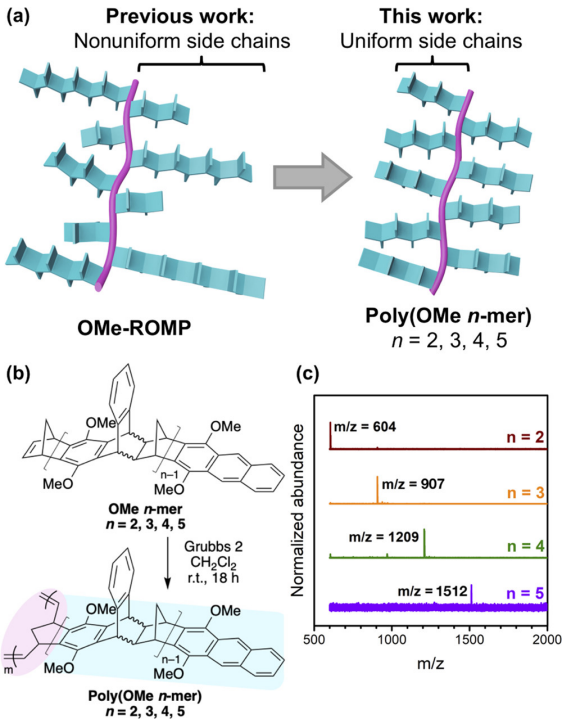

Figure 1.1: (a) Comparison of polymer structures between a previous study [20] and this study; (b) reaction conditions to polymerize OMe n-mers; (c) MALDI-TOF MS spectrum of each n-mer in this work.

1.3 Results and discussion

1.3.1 Synthesis

Figure 1.1a compares the architecture of the samples considered in our previous study [20] to those considered here. Poly(OMe n-mer)s were synthesized from their respective telechelic oligomers of uniform lengths (Figure 1.1b; see the Experimental Section for detailed procedure). These pure, but stereoirregular, OMe n-mers were obtained using silica gel column chromatography to separate the OMe-oligomer mixture obtained from Diels–Alder oligomerization. We successfully separated OMe n-mers of n = 1–5, whereas higher n-mers began to coelute (n = 1 corresponds to the unreacted monomer and was not further studied). We were unable to separate the fluorophilic CF_3 oligomers on silica gel, so they were not considered in this study. After isolation of the OMe n-mers, their identity and purity were confirmed by nuclear magnetic resonance (NMR) spectroscopy and matrix-assisted laser desorption/ionization–time-of-flight mass spectrometry (MALDI–TOF MS). The MALDI–TOF spectra, shown in Figure 1.1c, demonstrate expected m/z values with minimal impurities (see Table 1.1 for a comparison of expected and observed m/z values). In addition to MALDI, quantitative 1H NMR integration ratios were also consistent for each OMe n-mer, confirming the assigned oligomer lengths (see Figure 1.6 and Table 1.2 for integration method and observed ratios). ROMP of the purified OMe n-mers using Grubbs second-generation catalyst provided the corresponding poly(OMe n-mer)s (Figure 1.1b). Monomer-to-initiator ratios ([M]/[I], based on molar concentrations) between 100 and 150 produced polymers of high molecular weights ($M_n \geq$ 75 kDa; see Table 1.3) that were suitable for producing free-standing films via solution casting.

Brunauer–Emmett–Teller (BET) surface areas of poly(OMe 2-mer)–poly(OMe 5-mer) were obtained from N_2 adsorption isotherms (Figure 1.7) at 77 K and are shown in Figure 1.2 and Table 1.4. The BET surface areas show an increasing trend with increasing n, demonstrating the porogenic nature of the side chains. The BET surface area of OMe-ROMP falls between those of poly(OMe 4-mer) and poly(OMe 5-mer), which is consistent with an average n of 4.5 in OMe-ROMP as determined by NMR integration. The same N_2 adsorption data were used to determine the pore size distribution (PSD) of poly(OMe n-mer)s by means of nonlocal density functional theory (NLDFT) using the standard slit carbon model (Figure 1.7) [23]. Interestingly, the model indicates that, with increasing n, average pore size decreases (e.g., with max at 20 Å for poly(OMe 2-mer) to 7.6 Å for poly(OMe 5-mer)). Additionally, the pore size distribution becomes narrower, and micropores are more abundant (i.e., incremental pore volume increases with increasing n).

In addition, the fractional free volume (FFV) of thermally treated films was determined using group contribution methods first developed by Bondi [24] van Krevelen and Te Nijenhuis [25], and Park and Paul [26] and updated by Wu et al. [27]. Results are shown in Table 1.5 and Figure 1.8. Although there is a clear increase of FFV from n = 2 to 4, which suggests that the increasing rigidity from longer side chains leads to more frustrated chain packing, the FFV values for poly(OMe 4-mer) and poly(OMe 5-mer) are equivalent, regardless of the calculation method. Taken together, FFV and BET characterization support the

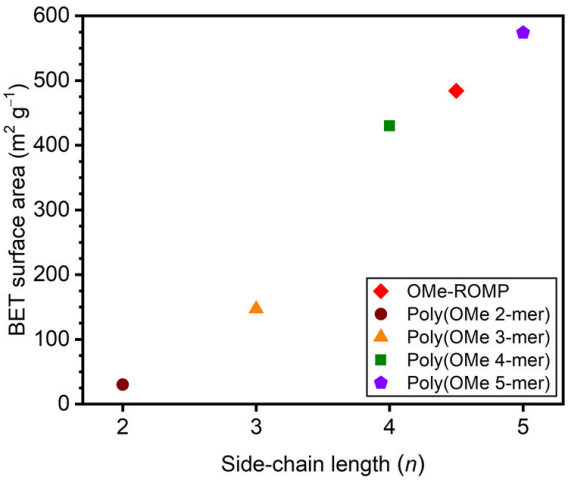

Figure 1.2: BET surface areas of poly(OMe 2-mer) through poly(OMe 5-mer), plus nonuniform OMe-ROMP (average $n = 4.5$).

interpretation that free volume and free volume distribution generally increase and narrow, respectively, with increasing side-chain length, but indirect probes such as gas permeation, which will be presented next, are required to clarify this physical picture [28].

1.3.2 Gas separation performance

Pure-gas separation performance of all poly(OMe n-mer)s at ~1 bar upstream pressure and 35 °C are shown in Figure 1.3 and Table 1.6 for several gas pairs. Self-standing films were made by dissolving polymers in chloroform (3 wt %) and then cast into 50 mm flat-bottom glass dishes lined with Norton™fluorinated ethylene propylene liners. After 4–5 days of evaporation at room temperature in a fume hood, free-standing films were generated. Before testing, films were soaked in methanol for 48 h, dried under ambient conditions for 24 h, and then degassed under full vacuum at 35 °C for 8 h. Since poly(OMe 2-mer) films were unable to withstand methanol treatment, ethanol treatment was used instead. Similar to methanol treatment, ethanol treatment has been shown to reset the thermal history of glassy polymers [29]–[33].

Data for OMe-ROMP from our previous study is included in Figure 1.3 for comparison [20]. Similar to poly(OMe 2-mer), OMe-ROMP was treated with ethanol. For all samples tested, gas permeability increased as follows: $P(N_2) < P(CH_4) < P(O_2) < P(He) < P(H_2) < P(CO_2)$. As CO_2 is more permeable than H_2, this makes OMe-ROMP and poly(OMe n-mer)s reverse-selective membranes for this gas pair, indicating a strong sorption component to permeability [34]. As n increases, permeabilities for all gases increase, which correlates with increasing BET surface areas. Conversely, there is a weak negative correlation between selectivity and increasing side-chain length. Taken together, these findings indicate that side-chain length is a critical parameter for controlling permeability in the OMe-ROMP series, but there is only a limited effect on selectivity. In contrast with other PIMs, the bottlebrush design enables control of transport though side-chain synthesis. In addition, the upper bound

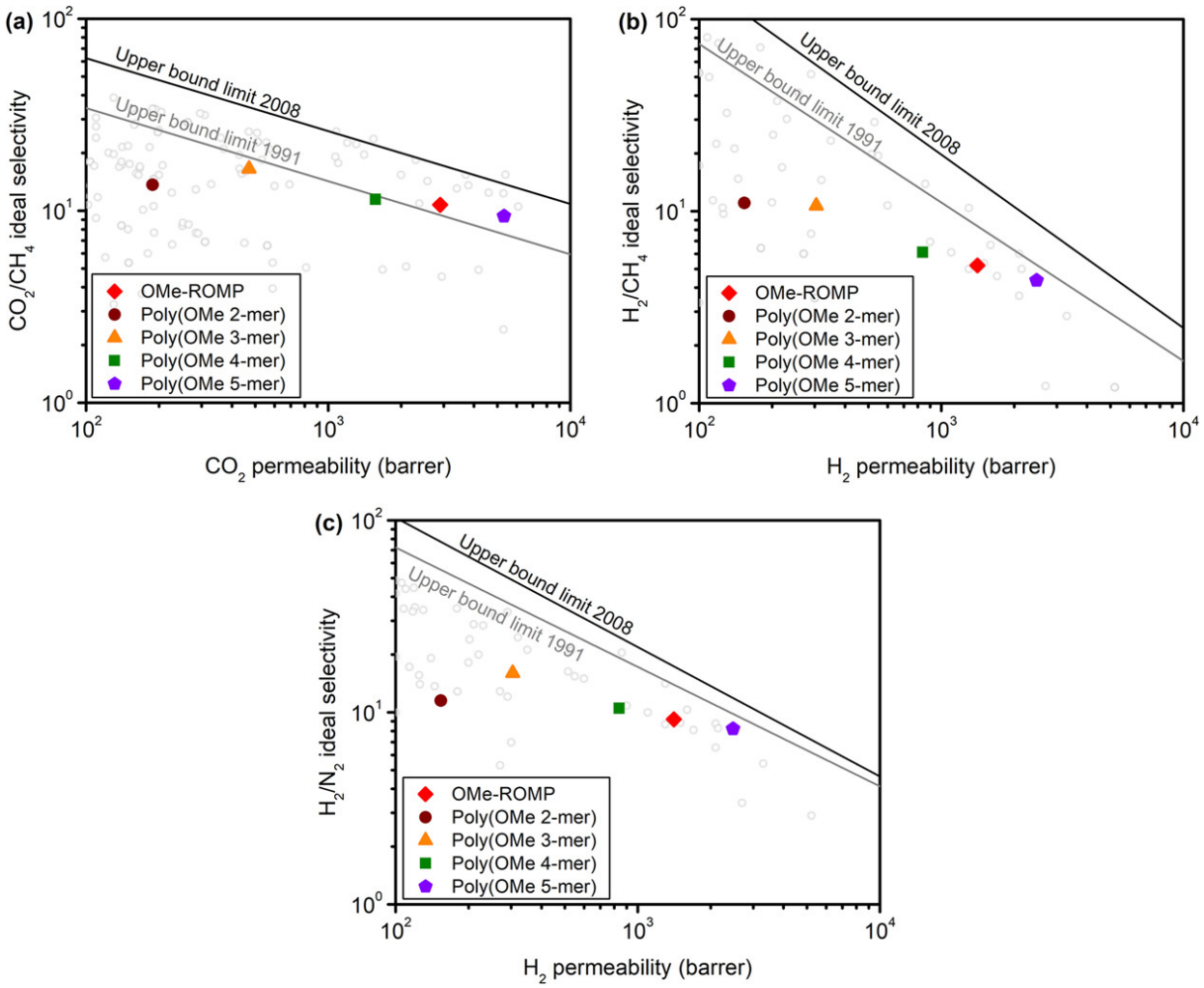

Figure 1.3: Robeson plots of alcohol-treated poly(OMe n-mer)s and OMe-ROMP for (a) CO_2/CH_4, (b) H_2/CH_4, and (c) H_2/N_2 gas pairs. Black and gray lines represent the 2008 and 1991 Robeson upper bounds, respectively [21], [22].

performance of OMe-ROMP is in between that of poly(OMe 4-mer) and poly(OMe 5-mer), which is consistent with the average n of 4.5 for OMe-ROMP. Gas separation performance for thermally treated poly(OMe n-mer) samples, as well as data at different aging times, are shown in Figure 1.9 and Table 1.6.

In order to evaluate our original hypothesis that forming side chains of uniform length leads to increased diffusivity selectivity, we decoupled permeability, P, into diffusion, D, and sorption, S, coefficients using the sorption–diffusion model (P = DS) [35]. Diffusion coefficients were determined using the time-lag method ($D = l^2/6\theta$), where l is the film thickness and θ is the time lag [36]. Since the time lags of He and H2 were outside of the resolution of our permeation system (1–2 s), D and S are not reported for these gases. Tabulated diffusion and sorption coefficients for all samples in this study can be found in Table 1.6.

The effect of n on diffusion coefficients for O_2 is shown in Figure 1.4a for both thermally treated and methanol-treated samples. Analogous plots for N_2, CH_4, and CO_2 are shown in Figure 1.10a–c. For the four gases considered, as n increases, diffusivity increases in an exponential manner. As FFV generally increased with increasing n (Figure 1.8 and Table 1.5), this finding is in agreement with free volume theory, which states that the logarithm of diffusion (logD) is a linear function of 1/FFV [37]–[40]. For each gas, diffusion is lower in thermally treated samples compared to samples treated with methanol. This finding relates to methanol dilation of the membrane that leads to increased free volume [30], [41]–[45]. The slopes of the semilog plots for thermally treated samples for each gas remain largely invariant, indicating that the change in diffusivity with respect to n is similar across all gases considered (Figures 1.4a abd 1.10). However, for methanol-treated samples, the slopes of the semilog diffusivity plots increase ((0.38 $\pm$ 0.03) O_2 $<$ (0.42 $\pm$ 0.03) CO_2 $<$ (0.47 $\pm$ 0.07) N_2 $<$ (0.53 $\pm$ 0.06) CH_4) in accordance with the effective diameter of the gas ((3.44 Å) O_2 $<$ (3.63 Å) CO_2 (3.66 Å) N_2 $<$ (3.81 Å) CH_4). This result indicates that methanol-treated samples have a higher average FFV and a free volume distribution that more easily accommodates larger molecules with increasing side-chain length [42], [44]. Table 1.7 reports diffusivity selectivity of OMe-ROMPs for a number of gas pairs, showing that diffusivity selectivity decreases with n and that uniformity of side chains has no effect on this trend. This data can be visualized in Figure 1.4b for O_2/N_2 and Figure 1.10d for other gas pairs.

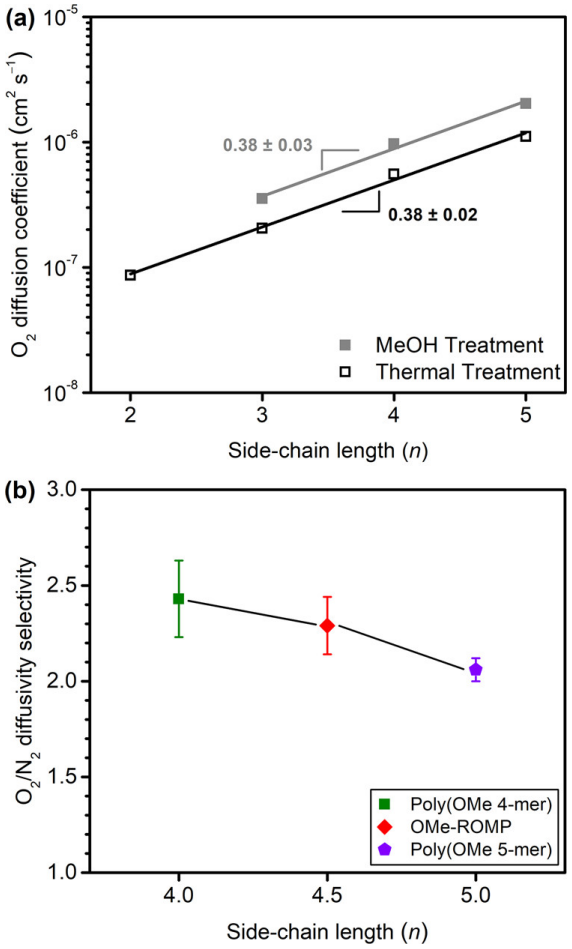

Figure 1.4: (a) O_2 diffusion coefficient for both thermally- and methanol-treated poly(OMe n-mer) samples versus side-chain length (n). Slopes and errors, determined using linear regression and χ^2 analysis, were calculated using the Origin 9.1 fitting tool. (b) O_2/N_2 diffusivity selectivity for $n = 4$ and $n = 5$ uniform poly(OMe n-mer) and nonuniform OMe-ROMP with average $n = 4.5$

Given the plasticization resistance of ROMPs [20], methanol-treated poly(OMe n-mer)s were subjected to CO_2 pressures as high as 51 bar at 35 °C (Figure 1.5). The hysteresis induced by conditioning samples at 51 bar of CO_2 is also shown in Figures 1.5 and 1.11. Data for OMe-ROMP from our previous publication is included for comparison. Although poly(OMe 4-mer) and poly(OMe 5-mer) show excellent plasticization resistance similar to OMe-ROMP (CO_2 plasticization pressure >51 bar), poly(OMe 3-mer) exhibits a plasticization pressure of ~10 bar. For the poly(OMe 2-mer) film, the plasticization test was conducted on a thermally treated sample due to the mechanical fragility of the ethanol-treated sample, resulting in a plasticization pressure of ~15 bar. With increasing n, a decrease in hysteresis behavior was observed. For example, permeability at ~30 bar was ~18% higher upon depressurization for poly(OMe 5-mer), whereas OMe-ROMP exhibited a difference of 26% and poly(OMe 2-mer) of 67% under the same conditions (Figure 1.11. We previously hypothesized that large interchain cohesive energy present in ROMPs contributed to plasticization resistance [20]. Our results in this study indicate that higher n leads to stronger interchain cohesive energy and greater interchain rigidity. Detailed mixed-gas studies to deepen an understanding on the plasticization resistance of ROMPs will be the subject of a future publication.

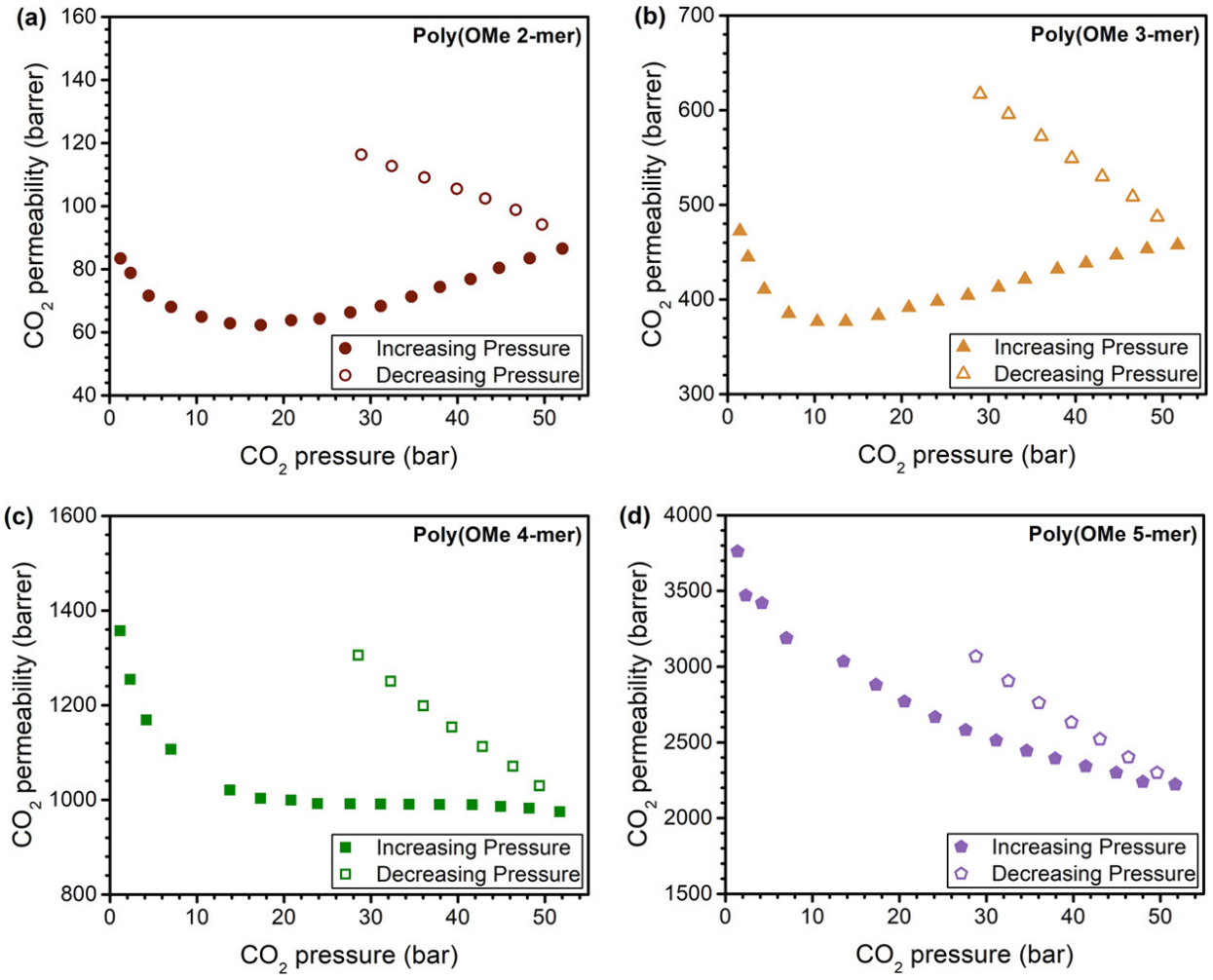

Figure 1.5: High-pressure pure-gas CO_2 permeability experiments conducted on (a) poly(OMe 2-mer), (b) poly(OMe 3-mer), (c) poly(OMe 4-mer), and (d) poly(OMe 5-mer). Note that poly(OMe 2-mer) was treated with ethanol while other samples were treated with methanol.

1.4 Conclusion

In conclusion, we have polymerized discrete OMe oligomers to make bottlebrush polymers with uniform side-chain lengths of n = 2–5 to study the effects of n on gas transport. BET and permeability measurements indicated that both surface area and gas permeability increase as n increases. Although diffusivity increased exponentially as n increased, there was not an appreciable effect on selectivity. Moreover, we found that uniform side-chain lengths did not lead to improved diffusivity selectivity as was originally hypothesized. CO_2 plasticization pressures increased with increasing n, suggesting that the exceptional stability of ROMPs is attributed to the inclusion of long, rigid side chains. Longer side chains than what have been studied here could further improve property sets such as permeability and plasticization resistance.

1.5 Experimental Section

1.5.1 Materials and Methods

Materials

Dicyclopentadiene(Alfa Aesar), sodium hydride(Sigma–Aldrich), methyl iodide(Alfa Aesar), and Grubbs 2^{nd}-generation catalyst(Sigma–Aldrich)were purchased from commercial sources and used as received. Anhydrous dimethylformamide (DMF) was purchased fromSigma–Aldrich in SureSeal bottles and dried over 4Å molecular sieves prior to use. Anhydrous dichloromethane (CH_2Cl_2) was obtained from an INERT PureSolv MD5 solvent purification system and stored under Ar over 4 Å molecular sieves. All other solvents were purchased at ACS grade or higher and used as received. 1,4-Anthraquinone was purified with a silica plug (using dichloromethane as the eluent) prior to use.

Silica gel chromatography

Silica gel chromatography was performed on a Biotage Isolera flash chromatography system with Biotage SNAP Ultra columns containing HP-Sphere 25 μm silica.

Nuclear magnetic resonance (NMR) spectroscopy

^{1}H and ^{13}C NMR spectra were obtainedusing Bruker Avance spectrometers at 400 or 600 MHz (100 or 150 MHz) for ^{1}H(^{13}C), in deuterated solvents as specified, and referenced to the residual solvent signal. Spectra for quantitative integration were recorded using 16 scans and 5s relaxation time.

Size exclusion chromatography (SEC)

SEC was performed in HPLC-grade tetrahydrofuran using an Agilent 1260 Infinity system with a guard column (Agilent PLgel; 5μm; 50 x 7.5 mm) and three analytical columns (Agilent PLgel; 5μm; 300 x 7.5 mm; 10^5, 10^4, and 10^3 Å pore sizes). The instrument was calibrated with polystyrene standards between 1.7 and 3150 kg mol^{-1}. All runs were performed at 1.0 mL min^{-1} flow rate and 35 °C. Molecular weight values were calculated using ChemStation GPC Data Analysis Software (Rev. B.01.01) based on the refractive index signal.

Matrix-assisted laser desorption/ionization (MALDI)–time of flight (TOF) mass spectrometry (MS)

MALDI–TOF MS was performed on a Bruker Autoflex Speed machine using reflector mode and positive ionization. The compound trans-2-[3-(4-tert-butylphenyl)-2-methyl-2-propenylidene]malononitrile(DCTB) was used as the matrix.

Brunauer–Emmett–Teller (BET) surface area

BET surface areas of polymerpowders were measured using N_2 sorption at 77 K using a Micromeritics ASAP 2020 analyzer. Powder samples were degassed under high vacuum at 120 °C for at least 4 hours prior to analysis.

1.5.2 Synthetic procedures and characterization

The synthetic procedures for the OMe monomer, oligomerization, and polymerization were previously reported [19], [20] and used without modification other than the separation step. Representative procedures are presented below.

OMe oligomer

OMe monomer was added to an oven-dried Schlenk flask, which was evacuated and backfilled with Ar threetimes. The monomer was heated at 220 °C for 18 h.

Separation of oligomers

The oligomer mixture was separated by silica gel chromatography using a Biotage Isolera flash chromatography system. Generally, a solvent gradient of 5% to 40% EtOAc/hexanes was successful in providing sufficient separation. Retention factor (R_f)decreases with increasing n. The isolated oligomers were dissolved in a small amount of CH_2Cl_2 and precipitated

Table 1.1: MALDI-TOF MS data and expected m/z values.

	Expected m/z	Observed m/z
OMe 2-mer	604.261	604.267
OMe 3-mer	906.392	907.415
OMe 4-mer	1208.523	1208.521
OMe 5-mer	1511.657	1511.625

Table 1.2: NMR integration ratios of OMe n-mers.

	Expected ratio	Experimental ratio
OMe 2-mer	1	1.03
OMe 3-mer	2	2.05
OMe 4-mer	3	3.27
OMe 5-mer	4	4.20

in MeOH prior to polymerization in order to remove impurities, presumably from the evaporated solvent used for chromatography. OMe n-mers were dried in the vacuum oven at 60 °C for at least 3 h.

MALDI–TOS MS was used to confirm the identity and purity of the separated OMe n-mers.The observed m/z values match the expected values, as shown in Table 1.1.

In addition to MALDI (see Figure 1.1c), ^{1}H NMR integration ratios were used to verify the separated OMe n-mers. Figure 1.6 demonstrates the method used for NMR integration, and Table 1.2 shows the expected and experimentally obtained ratios.

Polymerization

OMe 4-mer (168 mg, 0.14 mmol, 1 equiv.) was added to an oven-dried Schlenk flask, which was evacuated and backfilled with Ar three times, and then dissolved in CH_2Cl_2 (1 mL). In a separate oven-dried vial, Grubbs 2nd-generation catalyst (1.18 mg, 0.0014 mmol, 0.01 equiv.) was dissolved in CH_2Cl_2 (0.4 mL). The catalyst solution was transferred by syringe into the oligomer solution, and the reaction mixture was stirred at room temperature for 18 h. The flask was unsealed and 1 drop of ethyl vinyl ether was added to quench the catalyst. The polymer solution was precipitated in methanol, and the solid was collected by vacuum filtration, washed with methanol, and dried under vacuum.

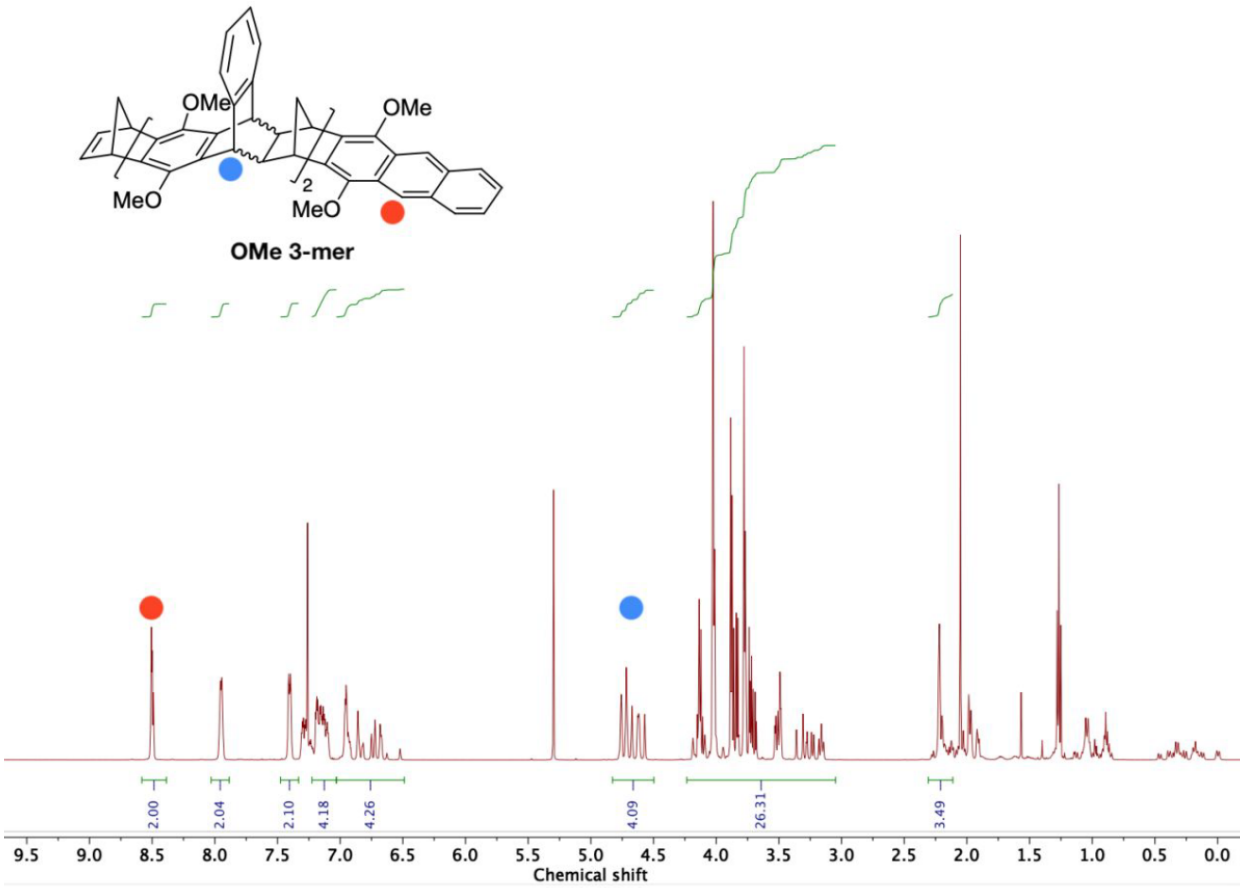

Figure 1.6: Example of the method used to obtain NMR integration ratios.

Table 1.3: Molecular weights of poly(OMe n-mer)s considered in this study.

	[M]/[I]	M_n (kDa)	Đ
Poly(OMe 2-mer)	150	76	1.9
Poly(OMe 3-mer)	150	76	1.9
Poly(OMe 4-mer)	125	116	2.7
Poly(OMe 5-mer)	100	84	2.6

Table 1.4: BET surface areas of poly(OMe 2-mer) through poly(OMe 5-mer)powders. The discrepancy between the reported BET surface area of OMe-ROMP here (484 $m^2 g^{-1}$) and the previously reported BET surface area[20] (146 $m^2 g^{-1}$) is attributed to variation in sample preparation and measurement techniques [46].

	BET Surface Area ($m^2 g^{-1}$)
Poly(OMe 2-mer)	30
Poly(OMe 3-mer)	147
Poly(OMe 4-mer)	430
Poly(OMe 5-mer)	574
OMe-ROMP	484

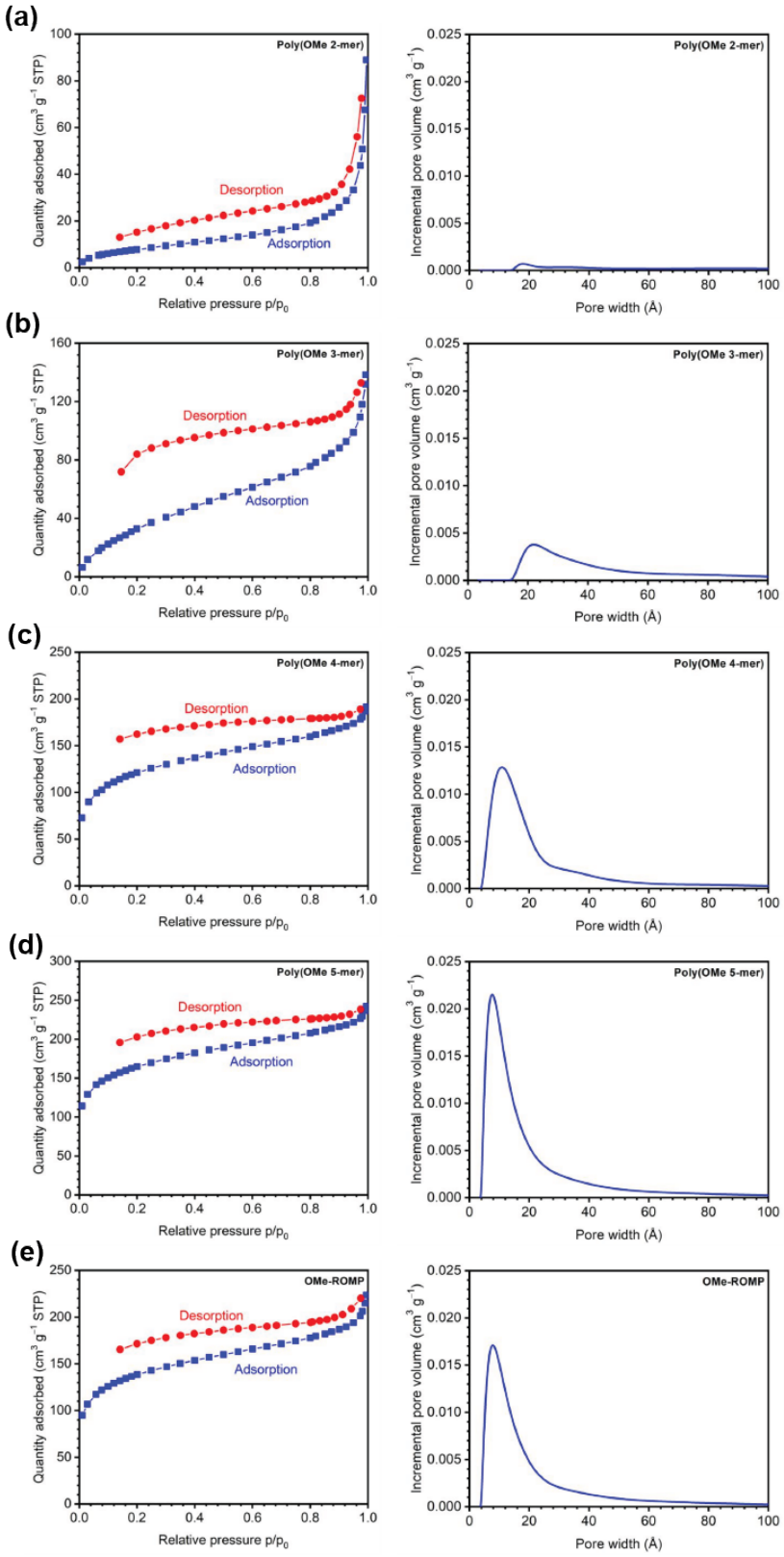

Figure 1.7: N_2 adsorption isotherms and pore size distributions (PSDs) calculated using the nonlocal density functional theory (NLDFT) using the standard slit carbon model of (a) poly(OMe 2-mer), (b) poly(OMe 3-mer), (c) poly(OMe 4-mer), (d) poly(OMe 5-mer), and (e) polydispersed OMe-ROMP obtained from Brunauer–Emmett–Teller (BET) analysis.

1.5.3 Membrane fabrication and treatment

Self-standing films of poly(OMe n-mer)s were made by dissolving polymers in chloroform to create 3 wt% polymer solutions. The solutions were then cast into 50mm diameter flat-bottom glass petri dishes that contained Norton™fluorinated ethylene propylene (FEP) liners (Welch Fluorocarbon). After 4–5 days of slow evaporation at room temperature in a fumehood, stable and defect-free films were formed.

Two different treatments were employed on the self-standing films. Thermally-treated films were dried at 120 °C for 24 h under vacuum to remove residual solvent, then dried at ambient conditions for 24 h and degassed under full vacuum at 35 °C for 8 h.Alcohol-treated films were soaked in either ethanol (poly(OMe 2-mer)) or methanol (poly(OMe 3-mer) through poly(OMe 5-mer)) for 48 h. After alcohol treatment, films were air-dried in a fumehood for 24 h before testing in the permeation system.

Polymer film density for thermally-treated samples was determined using Archimedes' principle using *n*-hexane as the buoyant liquid, since the density of water was expected to be close to the sample density. Measurements were conducted using a density measurement kit from Mettler Toledo (ME-DNY-4). The fractional free volume (FFV) was then calculated for each sample using the following equation:

$$FFV = \frac{V - 1.3V_W}{V} \tag{1.1}$$

where V is the molar volume of the polymer (cm^3 $mol^{\check{}1}$) and V_W is the van der Waals volume of the polymer (cm^3 $mol^{\check{}1}$) determined using group contribution methods. "Method 1" refers to the method first developed by Bondi [24], and updated by Park and Paul [26] in 1997 and van Krevelen [25] in 2009 to account for larger functional groups."Method 2" refers to the methodupdated by Wu et al. that accounts for new, unique structures that contain novel, contorted structural units and pendant groups that have been popularized since the first report of PIM-1 as a gas separation membrane [27], [47].

1.5.4 Pure-gas permeability measurements

Pure-gas permeability measurements of samples were performed on an automated constant-volume, variable-pressure permeation system from Maxwell Robotics. Polymer films were cut, placed on top of a hole in the center of a brass disk, and glued to the brass disk using epoxy glue (Devcon 5 min Epoxy). The glue was left to dry for at least 30 min. Afterwards, the polymer samples were sealed inside a stainless steel permeation cell (Millipore) and immersed in a water bath that was maintained at 35 °C using an immersion circulator (ThermoFisher SC150L). All gases used for testing (He, H_2, CH_4, N_2, O_2, and CO_2) were ultra-high purity from Airgas.

Table 1.5: Density, van der Waals volumes (V_W), and fractional free volume (FFV) of poly(OMe n-mer) samples from n = 2–5. "Method 1" refers to group contribution methods developed by Bondi, van Krevelen, and Park and Paul [24]–[26]. "Method 2" refers to an updated group contribution method developed by Wu et al. [27]

n	Density (g/cm^3)	$V_{W,Method\,1}$ ($cm^3\,mol^{-1}$)	$V_{W,Method\,2}$ ($cm^3\,mol^{-1}$)	FFV Method 1	FFV Method 2
2	1.184±0.005	362.64	325.51	0.077±0.004	0.171±0.004
3	1.134±0.009	529.11	482.15	0.140±0.007	0.216±0.007
4	1.11 ±0.02	695.58	638.79	0.17 ±0.02	0.24 ±0.02
5	1.12 ±0.01	862.05	795.43	0.17 ±0.01	0.23 ±0.01

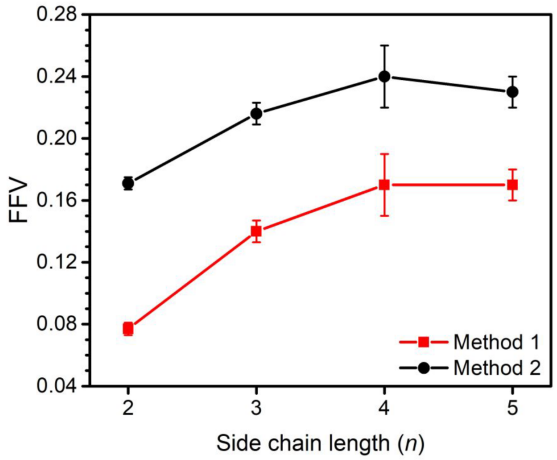

Figure 1.8: Fractional free volume (FFV) as a function of side-chain length (n). Red squares represent calculations using "Method 1" [24]–[26]. Black circles represent calculations using "Method 2" [27].)

The permeabilities of the six aforementioned gases were determined at ~1 bar. Before testing permeation, the testing chamber was dosed with ~2 bar of helium gas to ensure that no residual gas remained in the system. Then, the samples were held under vacuum at 35 °C for 8 h. Before switching to a new permeating gas for testing, samples were again dosed with ~2 bar of helium gas and held under vacuum for at least 1 h. Pure-gas permeability (P) was calculated using the following equation:

$$P = \frac{V_d l}{p_2 ART}\left[\left(\frac{dp}{dt}\right)_{ss} - \left(\frac{dp}{dt}\right)_{leak}\right] \tag{1.2}$$

in which V_d is the volume downstream of the film, l is the film thickness, p_2 is the upstream pressure, A is the area of film exposed to the gas, R is the ideal gas constant, T is the absolute experimental temperature, $\left(\frac{dp}{dt}\right)_{ss}$ is the rate of pressure rise in the permeate at steady state, and $\left(\frac{dp}{dt}\right)_{leak}$ is the leak rate [48]. The ideal gas selectivity ($\alpha_{i,j}$) was taken to be the ratio of the pure-gas permeabilities of the more permeable gas, i, to that of the less permeable gas, j (i.e., $\frac{P_i}{P_j}$). Diffusion coefficients for each gas were determined using the time-lag method, $D = \frac{l^2}{6\theta}$, in which θ is the time lag [36]. Since the diffusion coefficients for smaller gases (i.e., He and H_2) were sometimes outside of the resolution of the acquisition time of the permeation system, which is approximately 1–2 s, diffusion coefficients for these two gases are not reported. Sorption coefficient were back-calculated using the sorption–diffusion model ($S = \frac{P}{D}$) [35]. Error bars for permeability, diffusion coefficients, and sorption coefficients were determined using the error propagation method [49]. Thicknesses of each sample are shown in Table 1.6. Aged samples, which are shown in Table 1.6 with their aging times, are separate samples from "fresh" (i.e., 1 day aged) samples.

Table 1.6: Gas separation performance of all poly(OMe n-mer)s in this study. Permeability coefficients(P) are given in barrer (10^{-10} cm^3 (STP) cm cm^{-2} s^{-1} $cmHg^{-1}$), diffusion coefficients (D) are given in 10^{-8} cm^2 s^{-1}, and sorption coefficients(S) are given in $cm^3(STP)$ cm^{-3} atm^{-1}. All data were obtained at 35 °C and ~1 bar upstream pressure.

Polymer	Treatment		He	H_2	N_2	O_2	CH_4	CO_2
Poly(OMe	120 °C 24 h	P	53 ± 2	80 ± 3	3.6 ± 0.1	12.7 ± 0.4	4.7 ± 0.2	83.4 ± 2.9
2-mer)	vacuum, 1	D	/ ±	/ ±	3.6 ± 0.1	8.7 ± 0.2	0.91± 0.02	4.3 ± 0.1
l = 91 μm	day aged	S	/ ±	/ ±	0.75± 0.03	1.1 ± 0.1	3.8 ± 0.2	14.7 ± 0.6
Poly(OMe	EtOH treat	P	107 ± 3	154 ± 5	13.4 ± 0.4	33 ± 1	13.9 ± 0.4	190 ± 6
2-mer)	48 h, air-dry	D	/ ±	/ ±	13.1 ± 0.2	34.2 ± 1.1	4.5 ± 0.1	13.7 ± 0.2
	24 h, 1 day	S	/ ±	/ ±	0.76± 0.03	0.73± 0.03	2.3 ± 0.1	10.4 ± 0.4
l = 79 μm	aged							
Poly(OMe	120 °C 24 h	P	82 ± 5	135 ± 9	5.4 ± 0.4	26.3 ± 1.7	8.5 ± 0.5	178 ± 11
3-mer)	vacuum, 1 day	D	/ ±	/ ±	6.1 ± 0.1	20.6 ± 0.2	2.0 ± 0.1	9.9 ± 0.1
l = 130 μm	aged	S	/ ±	/ ±	0.7 ± 0.1	1.0 ± 0.1	3.2 ± 0.2	13.5 ± 0.9
Poly(OMe	MeOH treat	P	169 ± 6	304 ± 11	19.0 ± 0.7	65.7 ± 2.3	28.5 ± 1.0	471 ± 17
3-mer)	48 h, air-dry	D	/ ±	/ ±	11.6 ± 0.3	35.4 ± 1.2	3.5 ± 0.1	18.9 ± 4.9
	24 h, 14	S	/ ±	/ ±	1.2 ± 0.1	1.4 ± 0.1	6.1 ± 0.3	18.7 ± 0.8
l = 91 μm	days aged							
Poly(OMe	120 °C 24 h	P	243 ±10	462 ± 19	36.0 ± 1.5	112 ± 5	58.4 ± 2.4	830 ± 34
4-mer)	vacuum, 1 day	D	/ ±	/ ±	22.3 ± 0.9	55.6 ± 3.7	6.7 ± 0.3	33.4 ± 1.6
l = 85 μm	aged	S	/ ±	/ ±	1.2 ± 0.1	1.5 ± 0.1	6.5 ± 0.4	18.6 ± 1.2
Poly(OMe	120 °C 24 h	P	243 ±11	451 ± 21	34.4 ± 1.6	108 ± 5	55.6 ± 2.6	788 ± 36
4-mer)	34 days	D	/ ±	/ ±	19.5 ± 1.1	49.6 ± 3.1	6.1 ± 0.4	29.8 ± 1.8
l = 103 μm	aged	S	/ ±	/ ±	1.2 ± 0.1	1.5 ± 0.1	6.5 ± 0.4	18.6 ± 1.2
Poly(OMe	120 °C 24 h	P	422 ±18	839 ± 35	79.8 ± 3.3	224 ± 9	137 ± 6	1569 ± 66
4-mer)	vacuum, MeOH	D	/ ±	/ ±	45.0 ± 1.9	96.8 ± 8.4	14.9 ± 0.3	55.8 ± 2.8
	treat 48 h,	S	/ ±	/ ±	1.3 ± 0.1	1.7 ± 0.2	6.9 ± 0.3	21.1 ± 1.4
	air-dry 24 h,							
l = 82 μm	1 day aged							
Poly(OMe	120 °C 24 h	P	348 ±23	717 ± 47	62.5 ± 4.1	189 ±12	109 ± 7	1355 ± 89
4-mer)	vacuum, MeOH	D	/ ±	/ ±	35.5 ± 3.5	89.5 ±10.1	12.1 ± 1.1	54.0 ± 5.5
	treat 48 h,	S	/ ±	/ ±	1.3 ± 0.2	1.6 ± 0.2	6.8 ± 0.8	18.8 ± 2.3
	air-dry 24 h,							
l = 94 μm	3 days aged							
Poly(OMe	120 °C 24 h	P	497 ±39	1077 ± 85	107 ± 8	309 ±24	185.1 ±14.6	2247 ±177
5-mer)	vacuum, 10	D	/ ±	/ ±	45.5 ± 6.7	111 ±19	16.2 ± 2.3	67.8 ± 10.4
l = 82 μm	days aged	S	/ ±	/ ±	1.8 ± 0.3	2.1 ± 0.4	8.6 ± 1.4	24.8 ± 4.3
Poly(OMe	120 °C 24 h	P	716 ±27	1656 ± 62	214 ± 8	552 ±21	404 ±15	3762 ±141
5-mer)	vacuum, MeOH	D	/ ±	/ ±	69.2 ± 1.6	146 ± 7	28.6 ± 0.3	81.7 ± 2.2
	treat 48 h,	S	/ ±	/ ±	2.3 ± 0.1	2.8 ± 0.2	10.6 ± 0.4	34.5 ± 1.6
	air-dry 24 h,							
l = 138 μm	1 day aged							
Poly(OMe	120 °C 24 h	P	1076 ±75	2476 ±173	301 ±21	797 ±56	567 ±40	5324 ±372
5-mer)	vacuum, MeOH	D	/ ±	/ ±	102 ± 4	203 ±14	39.9 ± 1.0	129 ± 6
	treat 48 h,	S	/ ±	/ ±	2.3 ± 0.2	3.0 ± 0.3	10.8 ± 0.8	31.5 ± 2.6
	air-dry 24 h,							
l = 134 μm	2 days aged							

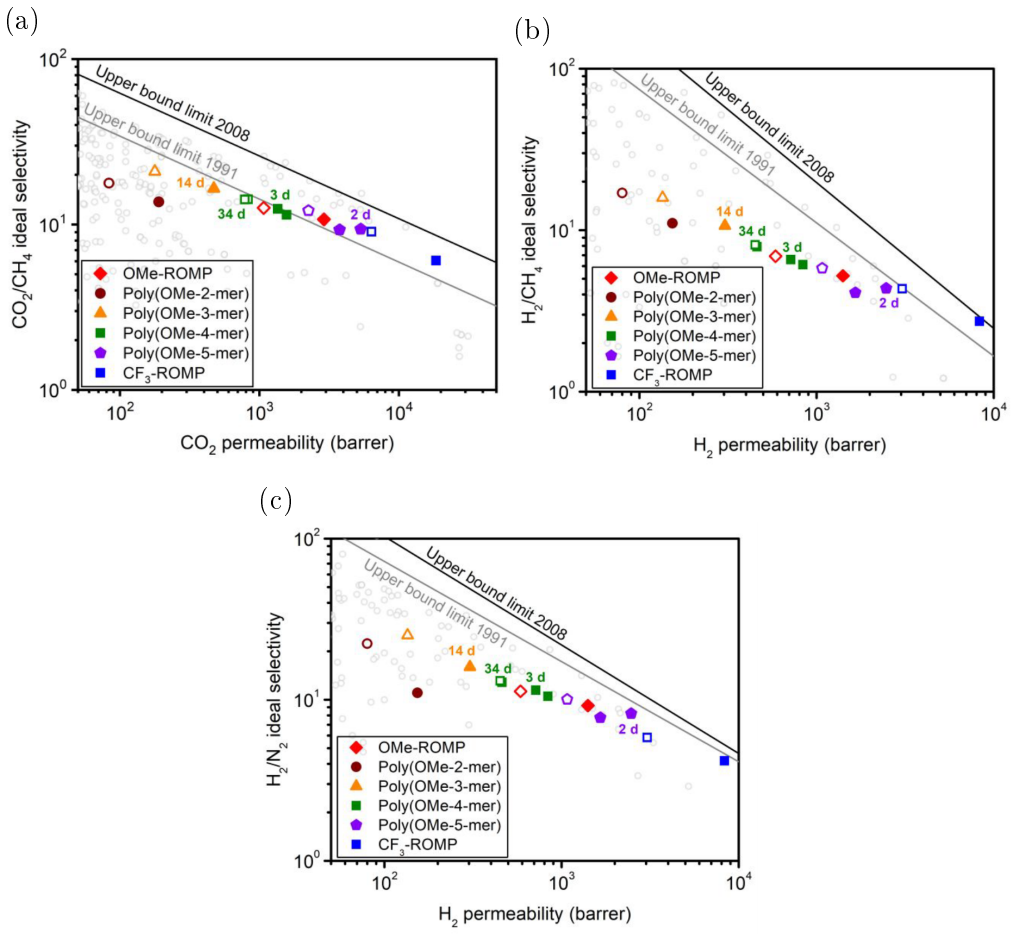

Figure 1.9: Robeson plots of poly(OMe n-mer)s,OMe-ROMP, and CF_3-ROMP for (a) CO_2/CH_4, (b) H_2/CH_4, and (c) H_2/N_2 gas pairs. Black and gray lines represent the 2008 and 1991 Robeson upper bounds, respectively [21], [22]. Filled shapes represent alcohol-treated samples, and open shapes represent thermally-treated samples.

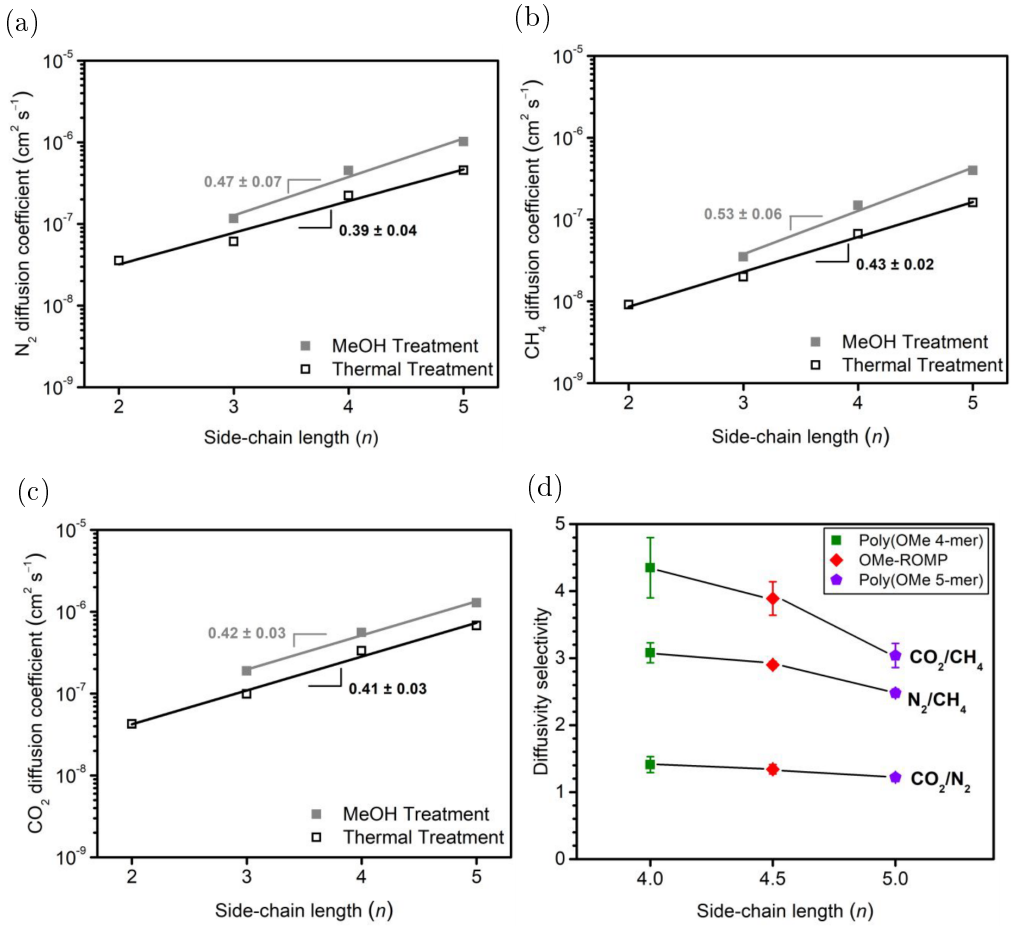

Figure 1.10: Diffusion coefficient for (a) N_2, (b) CH_4, and (c) CO_2 versus side-chain length (n). (d) Diffusivity selectivity for $n = 4$ and $n = 5$ uniform poly(OMe n-mer)and non-uniform OMe-ROMP with average $n = 4.5$ for CO_2/CH_4, N_2/CH_4, and CO_2/N_2 gas pairs.

Table 1.7: Diffusivity selectivity for fresh methanol-treated samples of poly(OMe 4-mer), OMe-ROMP(4.5 average side-chain length), and poly(OMe 5-mer).

	poly(OMe 4-mer)		OMe-ROMP (4.5 average)[20]		poly(OMe 5-mer)	
CO_2/CH_4	4.35±	0.45	3.89±	0.35	3.04±	0.18
CO_2/N_2	1.41±	0.12	1.34±	0.07	1.22±	0.04
O_2/N_2	2.43±	0.20	2.29±	0.15	2.06±	0.06
N_2/CH_4	3.08±	0.15	2.90±	0.05	2.48±	0.06

1.5.5 CO_2-induced plasticization study

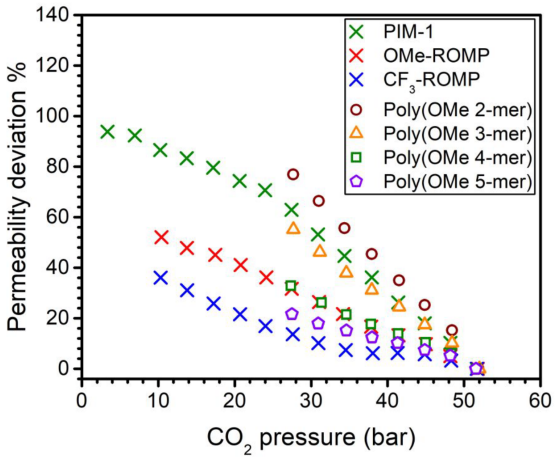

Figure 1.11: Hysteresis induced by conditioning of films at 51 bar of CO_2 for all samples in this study. Results for CF_3-ROMP, OMe-ROMP, and PIM-1 from our previous work[20] are included here for comparison.

1.6 Acknowledgments

This work was supported by the U.S. Department of Energy, Office of Science, Office of Basic Energy Sciences, Separation Science program under Award Number DE-SC0019087 and National Science Foundation DMR-1809740. F.M.B. gratefully acknowledges the funding and support provided by ExxonMobil Research and Engineering Company through the MIT Energy Initiative. F.M.B. and S.L. gratefully acknowledge the funding and support provided by the MIT Deshpande Center for Technological Innovation. The authors would like to thank the members of the Smith Lab at the Massachusetts Institute of Technology for useful discussions.

Chapter 2

Role of side-chain length on gas transport of CO_2/CH_4 mixtures in polymers with side-chain porosity

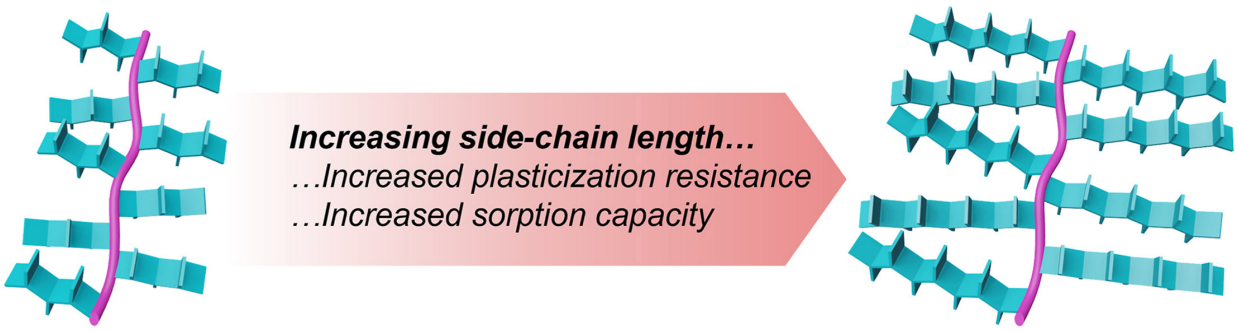

Adapted and reprinted with permission from
Sharon Lin, Kayla R. Storme, You-Chi Mason Wu, Francesco M. Benedetti, Timothy M. Swager, and Zachary P. Smith
"Role of side-chain length on gas transport of CO_2/CH_4 mixtures in polymers with side-chain porosity"
J. Membr. Sci. **2023**, *668*, 121194.
https://doi.org/10.1016/j.memsci.2022.121194

2.1 Abstract

Polymers of intrinsic microporosity (PIMs) are traditionally formed from ladder backbones, but recent synthetic advances have allowed for the formation of non-traditional PIMs using a poly(ladder) motif, whereby rigid PIM-like sidechains are appended onto more flexible backbones. The effect of side-chain length on free volume and gas transport properties was recently evaluated for a methoxy-functionalized poly(ladder) (OMe-ROMP). In this study, we elaborate on the role of side-chain length and its influence on mixed-gas performance and plasticization stability for OMe-ROMP. Pure-gas sorption results are also reported, including hysteresis effects from CO_2 conditioning. Taken together, this study reveals the role of side-chain length on gas sorption, diffusion, and plasticization for CO_2/CH_4 separations. We conclude that the length of a rigid side chain in the poly(ladder) motif is a valuable structural parameter to control sorption, diffusion, and stability towards plasticization for gas separation membrane materials.

2.2 Introduction

Over the past 25 years, natural gas and biogas processing has become one of the most widespread industrial applications for gas separations, with the world consuming over 100 trillion scf (standard cubic feet) of these gases every year [50]–[52]. Compared to other established technologies, membrane-based separations offer an energy-efficient alternative, smaller plant footprints, and modularity [1], [3]. However, membrane-based separations only occupy about 10% of the natural gas processing market, and compositionally-similar emerging markets, such as producing carbon-negative blue hydrogen from biogas feedstocks, have increased the urgency for novel separations technologies [51], [53]–[55]. The limited industrial adoption of membranes for these separations is primarily due to the trade-off that polymer membranes experience between permeability and selectivity. Most commercial membranes for gas separations currently are based on polymers with moderate selectivity but low permeability [1], [11].

Another major issue that precludes adoption of polymer membranes for gas separations is plasticization. When exposed to high pressures of condensable gases (such as CO_2), polymer chains will reorganize more quickly due to increased mobility, which increases gas permeability but reduces selectivity [56]–[58]. This issue is particularly relevant for natural gas and biogas separations, in which separation of CH_4 from CO_2 is the primary separation [51]. Since plasticization involves molecular chain movements, there have been many efforts to mitigate plasticization by increasing polymer chain rigidity either through incorporating interchain interactions such as cross-linking [59]–[62], the formation of charge transfer complexes (CTCs) [63]–[66], and the introduction of hydrogen-bonding functionalities [64], [67]–[73]. Intrachain mobility can also be restricted through the incorporation of rigid groups like triptycene [9], [18], [69], [74]–[76], Tröger's base [10], [11], [77], [78], and ethanoanthracene [79] into the polymer backbone.

One strategy to address current materials limitations, especially those associated with

limited membrane permeability, has been the development of polymers of intrinsic microporosity (PIMs). These polymers have rigid backbones and contorted structures that allow for inefficient packing, enhancing separation performance for a number of gas pairs [4], [5], [80]. Further advances have been made by incorporating bulky groups into PIM-based materials to increase rigidity even further [10], [11], [14], [18], [75], [81]. While the incorporation of interchain interactions has seen some success in mitigating plasticization, enhancements in intrachain rigidity alone has not proven sufficient in suppressing plasticization [82]. Of note, polymers with increased intrachain rigidity, such as PIM-based materials, often have high fractional free volume that leads to increased sorption capacity for condensable gases, which likely exacerbates plasticization effects.

Recently, our group has introduced a different PIM motif using ring-opening metathesis polymerization (ROMP) through incorporation of rigid side chains on a flexible poly(norbornene) backbone [19], [20]. CF_3-ROMP and OMe-ROMP, which were named for their functionality, both showed gas transport properties that were comparable to state-of-the-art PIMs for a number of commonly-tested gas pairs. When both ROMP polymers were tested under high-pressure pure-gas CO_2 permeation up to a feed pressure of 51 bar, neither exhibited a detectable plasticization pressure in this pressure range, as demonstrated by a continuous decrease in pure-gas CO_2 permeability with increasing pressure. A follow-up study investigated the influence of rigid side-chain length on OMe-ROMP on both gas transport properties and pure-gas plasticization pressures [83]. These polymers are referred to as poly(OMe n-mer), in which the side-chain length, n, ranged from 2 to 5. The chemical structure of poly(OMe n-mer)s can be seen in Scheme 2.1. As the side-chain length increased from $n = 2$ units to $n = 5$ units, gas permeability increased with minimal losses in permselectivity. Increasing the side-chain length also led to increased plasticization resistance. While poly(OMe 2-mer) and poly(OMe 3-mer) exhibited plasticization pressures of ~15 and ~10 bar CO_2, respectively, both poly(OMe 4-mer) and poly(OMe 5-mer) did not show any plasticization pressure up to 51 bar CO_2. In addition, after conditioning samples at 51 bar CO_2, hysteresis effects (i.e., the percent change in CO_2 permeability before and after conditioning) were reduced. At a CO_2 feed pressure of ~25 bar, poly(OMe 5-mer) exhibited a CO_2 permeability that was only ~25% higher upon depressurization compared to its initial permeability during pressurization. This difference in permeability was remarkably smaller than those of poly(OMe 4-mer) (~30%), poly(OMe 3-mer) (~55%), and poly(OMe 2-mer) (~80%) under the same testing conditions. This stability to conditioning of monodispersed OMe-ROMP samples with increasing side-chain length was attributed to stronger interchain cohesive energy and greater intrachain rigidity, which correlated with stability observed from plasticization pressure experiments.

However, high-pressure pure-gas tests are not fully sufficient to determine whether a polymer is plasticization resistant. Even in binary CO_2/CH_4 mixtures when no plasticization pressure is detected for CO_2, CO_2 can still act as a plasticizer, resulting in increased diffusion coefficients for CO_2 and more notably in the co-permeating gas, CH_4. Such effects can be detected by tracking changes in permeability of the less strongly sorbing gas and by evaluating if permselectivity decreases more than expected based on dual-mode effects with increasing pressure under mixed-gas conditions [84], [85]. Some studies have shown that CH_4

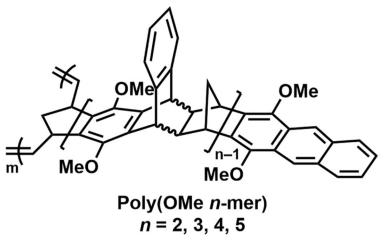

Scheme 2.1: Chemical structure of poly(OMe n-mer)s considered in this study.

permeability increases and the CO_2/CH_4 permselectivity decreases with increasing pressure in CO_2/CH_4 mixed-gas tests, unambiguously indicating plasticization [86]–[88].

In addition to permeation tests, direct sorption measurements are also useful for analyzing the behavior of polymers under aggressive CO_2 feed pressures. Similar to high-pressure CO_2 permeation tests, high-pressure CO_2 sorption tests can involve pressurization, conditioning at a maximum feed pressure, and then depressurization. Hysteresis induced by conditioning at a high feed pressure followed by desorption can provide information on the effect of strongly sorbing gases on polymer chain packing and provide useful connections to plasticization phenomena [89], which will be discussed later.

In this work, we further expand upon the claim that ROMP polymers are plasticization-resistant by evaluating both the pure-gas sorption behavior and mixed-gas CO_2/CH_4 permeation results for monodispersed poly(OMe n-mer) samples with side-chain lengths ranging from n = 2–5. CH_4 and CO_2 pure-gas sorption measurements were performed up to a feed pressure of ~50 atm, and dual-mode sorption parameters were determined for each sample. Binary CO_2/CH_4 mixed-gas experiments at varying feed compositions and pressures were also conducted to determine gas transport behavior under more realistic conditions.

2.3 Results and discussion

2.3.1 Sorption analysis

CH_4 and CO_2 sorption isotherms are presented in Figure 2.1 for all poly(OMe n-mer) samples. Data provided are for individual polymer samples and for single measurements, and error bars were calculated via error propagation. The dual-mode sorption (DMS) model was used to fit sorption isotherms [48]. For all samples considered, sorption was higher for CO_2 than CH_4, following expectations in trends based on critical temperatures and other related metrics [8], [90], [91]. In addition, all samples show good fits to the DMS model. The percent change in CO_2 concentration before and after conditioning at a CO_2 fugacity of ~39–41 atm was also determined for each sample (Figure 2.6, Experimental methods). After conditioning each sample and depressurizing, poly(OMe 2-mer) exhibited the largest hysteresis of all samples (i.e., the largest difference between the concentration of gas in the polymer before and after pressurization), while the remaining three samples (poly(OMe 3-mer), poly(OMe

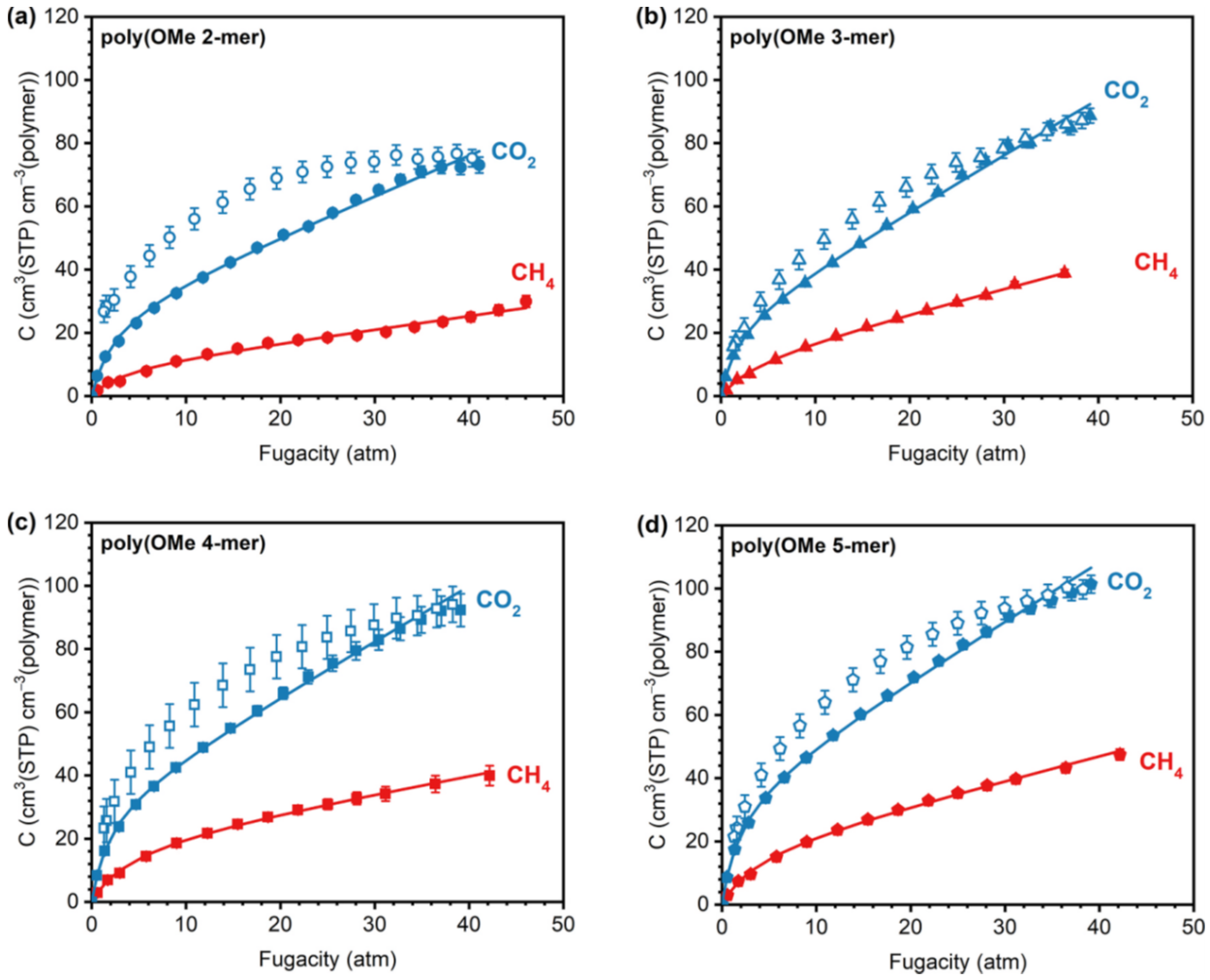

Figure 2.1: Pure-gas sorption isotherms as a function of fugacity (atm) for (a) poly(OMe 2-mer), (b) poly(OMe 3-mer), (c) poly(OMe 4-mer), and (d) poly(OMe 5-mer). Red points indicate CH_4, while blue points indicate CO_2. Filled points indicate increasing fugacity, while unfilled points indicate decreasing fugacity. Individual points represent experimental data, while curves represent dual-mode model fits. (For interpretation of the references to colour in this figure legend, the reader is referred to the Web version of this article.).

4-mer), and poly(OMe 5-mer)) showed similar hysteresis within experimental error.

Hysteresis in glassy polymers can be attributed to one or two primary phenomena. First, hysteresis can indicate structural rearrangements of polymer free volume that occurs due to volume dilation from conditioning. This increase in free volume is often accompanied with decreased activation energies of diffusion for molecular transport, so smaller hysteresis effects can indicate stronger plasticization resistance [65], [92]–[97]. Second, hysteresis can relate to physical and/or chemical interactions between the sorbent and the polymer [98], [99], as well as diffusion limitations via kinetic trapping [100]–[103]. This second effect is common for capillary condensation of subcritical gases in adsorbents [104], [105]. The ROMP polymers considered here can certainly be considered as adsorbents, as indicated by their high BET surface areas, but the gases tested are supercritical. For this reason, desorption would only need to overcome rather weak van der Waals interactions from ultramicropores compared to much stronger enthalpies of vaporization from a condensed phase. Furthermore, for this second feature to be dominant, the material with the lowest BET surface area, poly(OMe 2-mer), would have the smallest hysteresis relative to the longer side-chain samples that have higher BET surface areas. Our results indicate the opposite trend. Poly(OMe 2-mer) experienced the largest CO_2-induced hysteresis, likely due to both conditioning and plasticization, while poly(OMe 3-mer), poly(OMe 4-mer), and poly(OMe 5-mer) exhibited smaller hysteresis behavior. In general, the hysteresis effects decreased as side-chain length increased, which suggests increasing plasticization resistance.

A few salient points can be gleaned from sorption analysis. Perhaps most importantly, the parameter S_{inf}, which describes the sorption at infinite dilution, for both CH_4 and CO_2 increases concomitantly with increasing side-chain length, as shown in Figure 2.2 and Table 2.1 (Experimental methods). This finding is consistent with BET and FFV measurements from our previous study [83] and further corroborates our assertion that increasing side-chain length leads to the generation of additional free volume [106], as noted by the more favorable sorption of the first penetrant. However, given the rather poor correlation between dual-mode parameters (which are used to calculate sorption at infinite dilution) and side-chain length, as will be discussed in the next paragraph, the values of sorption at infinite dilution should only be qualitatively compared among samples in this study.

Dual-mode model fitting was used to provide some additional information on the structural features of the polymers, but this approach revealed weaknesses in applying this model to poly(ladder)s. Dual-mode parameters are shown for poly(OMe n-mer) samples in Table 2.2 and Figure 2.7 (Experimental methods). The parameter k_D describes sorption in the Henry's domain, which represents a hypothetical equilibrium sorption mode in the polymer [107]. In contrast, the parameter $C_H^{'}$ (Figure **??**b, Experimental methods) describes the hypothetical sorption capacity in the Langmuir mode. Both parameters k_D and $C_H^{'}$ showed a weak positive correlation with increasing side-chain length, suggesting that increased sorption may not be solely limited to the non-equilibrium Langmuir mode, a conclusion that was unexpected given the reduced volume of the flexible backbone with increasing side-chain content. However, we note that such conclusions lack strong statistical confidence, espe-

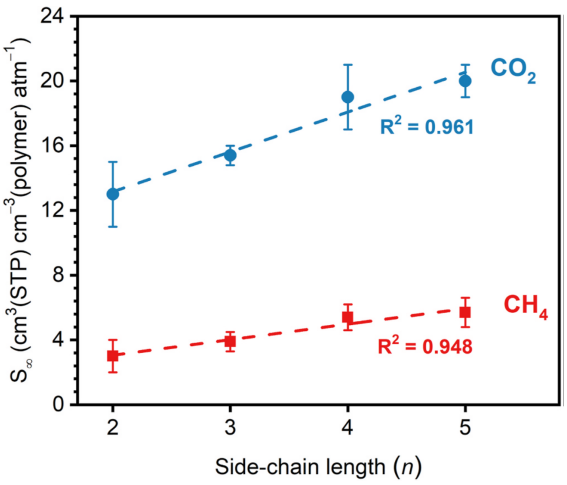

Figure 2.2: Sorption at infinite dilution (S_{inf}) for CH_4 (red squares) and CO_2 (blue circles) versus side-chain length for poly(OMe n-mer) samples in this study. Linear fits and R2 values were calculated using the Origin 2019b linear fitting tool, and without regard to the error bars. (For interpretation of the references to colour in this figure legend, the reader is referred to the Web version of this article.)

cially for the k_D value of CH_4 versus side-chain length, which had an R^2 value of 0.368. The Langmuir affinity constant, b, was relatively invariant with increasing side-chain length, as indicated by weak statistical correlations Figure 2.7c, Experimental methods. For traditional ladder polymers, the parameter b is expected to correlate closely with S_{inf} [91], [108], but we did not observe this trend with the poly(ladder)s. Taken together, these findings suggest that the bottlebrush polymers considered here cannot be easily analyzed using classic dual-mode analysis. Of note, grafting density has a strong influence on entanglement molecular weight [109], and it is known that side chains can be stretched when tightly grafted to a backbone [110], [111], thereby altering free volume. These complicated features, which are interdependent and systematically change with increasing values of n, likely create unique poly(ladder) microstructures for each side-chain length and obscure the use of traditional dual-mode analysis.

To further understand the rather poor correlations between sidechain length and dual-mode parameters, we calculated the overall nonequilibrium contribution to sorption, $C_H^{'}$ (Figure 2.7d, Experimental methods) and the ratio of nonequilibrium sorption to equilibrium sorption at infinite dilution,$C_H^{'}b/k_D$ (Table 2.2 and Figure 2.7e, Experimental methods) [90]. There was a clear trend of increasing nonequilibrium contributions to sorption (i.e., increasing $C_H^{'}b$) with increasing side-chain length, which was consistent with FFV and BET analysis. However, $C_H^{'}b/k_D$ appears to be invariant with increasing values of n, suggesting once again that the dual-mode model does a rather poor job at capturing physical insights for ROMP ladder polymers.

2.3.2 Mixed-gas permeation analysis

Mixed-gas data can differ significantly from pure-gas data, especially in mixtures that contain condensable gases such as CO_2. In some cases, the change in performance from pure-gas calculations to mixed-gas measurements is favorable. Strongly sorbing gases that have high polymer affinity can effectively hinder the transport of less condensable gases, increasing overall permselectivity. For example, Swaidan et al. demonstrated that a thermally-annealed PIM-polyimide (TPDA-APAF) exhibited mixed-gas CO_2/CH_4 permselectivities 10–20% higher than those under pure-gas conditions due to competitive sorption of CO_2 over CH_4 [67]. Du et al. reported increases in CO_2/N_2 permselectivity of TZ-PIM-1 from the pure-to mixed-gas case of over 30% due to favorable sorption of CO_2 [112]. More recently, Mizrahi Rodriguez and Benedetti et al. found that amine-functionalized PIM-1 (PIM-NH2) showed a 140% and 250% increase in mixed-gas CO_2/CH_4 and CO_2/N_2 selectivity, respectively, compared to pure-gas results at the same partial pressure of CO_2 [91].

However, the change in performance from the pure-to mixed-gas scenario can also be unfavorable, a finding which is significantly more common for ladder polymers. The presence of a condensable gas can cause volume dilation and decreased activation energies of diffusion for molecular penetrants, which in turn results in an upturn in the permeability isotherm with increasing pressure. For example, Swaidan et al. reported that in a 50:50 CO_2/CH_4 mixture, the CH_4 permeability of PIM-1 was up to 60% higher than in the pure-gas case [87]. This increase in CH_4 permeability also led to a decrease in CO_2/CH_4 permselectivity, with the CO_2/CH_4 permselectivity of PIM-1 decreasing by about 38% from 4 to 20 bar total pressure [87]. Similar effects have been observed for other microporous polymers and carbon molecular sieve derivatives [81], [82], [88], [113], [114].

In our previous study, the effect of side-chain length of poly(OMe n-mer) on pure-gas CO_2 permeability as a function of pressure was evaluated. It was found that longer side chains exhibited less hysteresis after conditioning at 51 bar CO_2 feed pressure, suggesting that increased rigidity of longer side chains contribute to increased plasticization resistance [83]. Here, this claim is further elucidated using mixed-gas CO_2/CH_4 tests. First, the pure-gas CH_4 and CO_2 permeabilities for all poly(OMe n-mer) samples were tested at ~1.1 atm. Then, samples were tested with a 20:80, 80:20, and 50:50 CO_2/CH_4 mixture at ~2.2 atm. All data are presented in Table 2.3 (Experimental methods). Data provided are for individual polymer samples and for single measurements, and error bars were calculated via error propagation. In addition, the same sample was used for each of the different mixed-gas ratios. As shown in Figure 2.3, at low fugacities, a rise in CO_2/CH_4 permselectivity is observed from the pure-to mixed-gas case for all samples considered, regardless of mixture composition. This finding can likely be attributed to competitive sorption, in which CO_2 preferentially sorbs into the polymer over CH_4, lowering CH_4 sorption and permeability. This phenomenon is also evident in the drop in CH_4 permeability from the pure-to mixed-gas case. Conversely, only slightly lower CO_2 permeabilities in the mixed-gas case were observed compared to the pure-gas case for all samples, which is also expected due to very weak competitive effects from CH_4 sorption excluding some CO_2. The CO_2/CH_4 mixed-gas permeation data of all poly(OMe n-mer) samples in this study in comparison to both commercial membranes and other newly

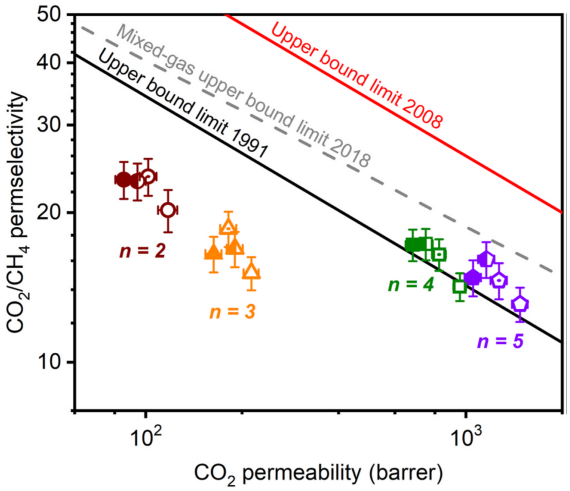

Figure 2.3: Robeson upper bound plots of all poly(OMe n-mer) samples. Unfilled symbols represent pure-gas data collected at ~1.1 atm feed fugacity. Symbols with a dot in the center (20:80 CO_2/CH_4), half-filled symbols (50:50 CO_2/CH_4), and filled symbols (80:20 CO_2/CH_4) represent mixed-gas data collected at ~2.2 atm total feed fugacity. All data were obtained at 35 ∘C. The solid red line represents the 2008 Robeson upper bound [21], the solid black line represents the 1991 Robeson upper bound [22], and the gray dashed line represents the 2018 mixed-gas upper bound [115]. (For interpretation of the references to colour in this figure legend, the reader is referred to the Web version of this article).

developed materials are presented in both Figure 2.8 and Table 2.4 (Experimental methods).

Poly(OMe n-mer) samples from n = 3–5 were then tested with a 50:50 CO_2/CH_4 mixture at 35 ∘C up to a total feed fugacity of ~24 atm. As previously reported, while poly(OMe 3-mer) exhibited a plasticization pressure of ~10 bar, poly(OMe 4-mer) and poly(OMe 5-mer) did not show a plasticization pressure up to a pure-gas CO_2 feed pressure of 51 bar [83]. Mixed-gas CO_2 and CH_4 permeabilities are shown in Figure 2.4, while mixed-gas CO_2/CH_4 permselectivities are shown in Figure 2.5. Gas transport measurements are also summarized in Table 2.5 (Experimental methods). For all three samples, CO_2 permeabilities generally decreased with increasing fugacity up to a CO_2 partial fugacity of 12 atm, which is due to the decreasing sorption coefficient of CO_2 with increasing fugacity [106]. Similarly, CH_4 permeabilities also initially decreased with increasing fugacity for poly(OMe 4-mer) and poly(OMe 5-mer). For poly(OMe 3-mer), CH_4 permeability begins to increase immediately with pressurization. This phenomenon of increasing permeability, which is referred to as "CH_4-creep", is an unambiguous indication of CO_2-induced plasticization [67]. From the lowest to the highest fugacity considered, the increase in CH_4 permeability for poly(OMe 3-mer) was 64% Figure 2.4a. Correspondingly, CO_2/CH_4 permselectivity begins to decrease immediately with pressurization, and the total decrease in permselectivity over the fugacity range tested was ~55% (Figure 2.5a).

For poly(OMe 4-mer), CH_4 permeability does not increase until a CO_2 partial fugacity of ~3.4 atm, suggesting better plasticization resistance than poly(OMe 3-mer). Over the

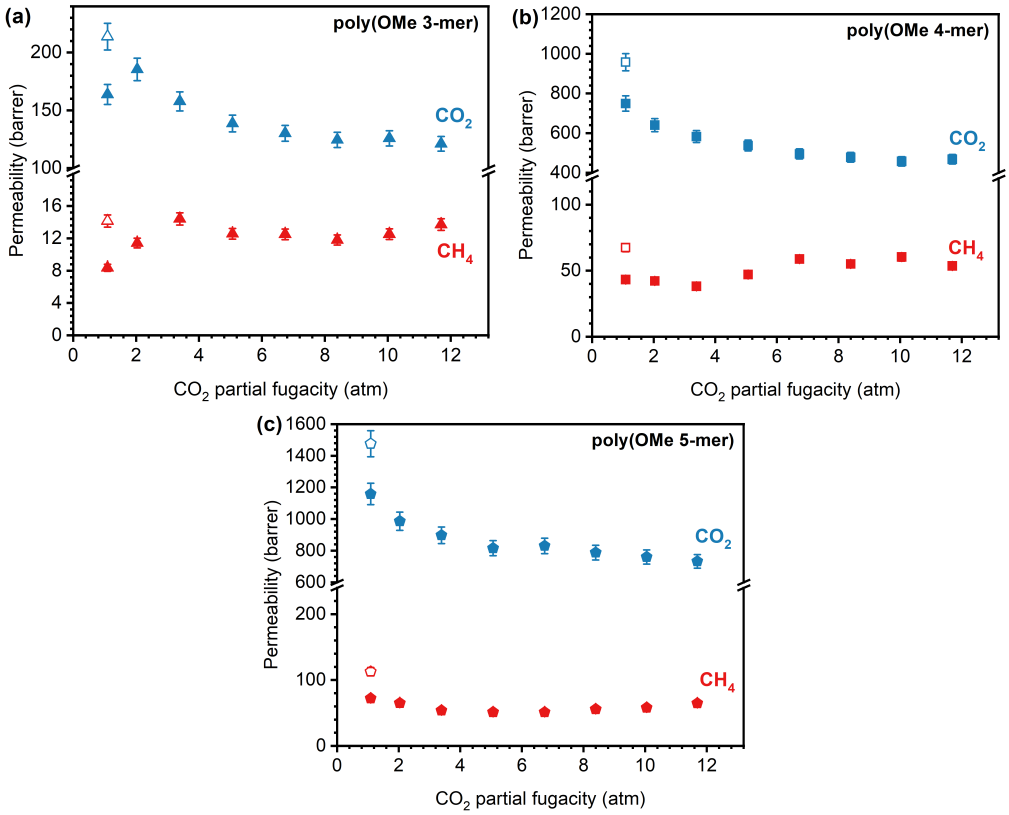

Figure 2.4: Mixed-gas CO_2 (blue) and CH_4 (red) permeabilities as functions of CO_2 partial fugacity (50:50 CO_2/CH_4 mixture at 35 ∘C) for (a) poly(OMe 3-mer), (b) poly(OMe 4-mer), and (c) poly(OMe 5-mer). Unfilled symbols represent pure-gas data at ~1.1 atm, and filled symbols represent mixed-gas data. (For interpretation of the references to colour in this figure legend, the reader is referred to the Web version of this article).

fugacity range tested, CH_4 permeability increased by 25% (Figure 2.4b), and as expected, CO_2/CH_4 permselectivity begins to decrease rapidly after a CO_2 partial fugacity of ~4 atm (Figure 2.5b). The total decrease in permselectivity over the tested fugacity range is ~50%.

For poly(OMe 5-mer), at around a CO_2 partial fugacity of 7 atm, CH_4 permeability began to increase slightly. However, poly(OMe 5-mer) experienced an overall 10% decrease in CH_4 permeability over the fugacity range tested (Figure 2.4c), suggesting that increasing side-chain length is a powerful structural parameter for mitigating plasticization. Nevertheless, this slight CH_4-creep and changes in sorption coefficients resulted in a 30% decrease in CO_2/CH_4 permselectivity (Figure 2.5c). Compared to poly(OMe 3-mer) and poly(OMe 4-mer), poly(OMe 5-mer) exhibited the most plasticization resistance, as both the CH_4 permeability increase and the CO_2/CH_4 permselectivity decrease over the tested fugacity range is much less severe. This result corresponds with the increasing interchain rigidity from increased $\pi - \pi$ stacking and formation of charge transfer complexes (CTCs) from the additional benzene rings on the longer rigid side chains [65], [67], [71], [81], [82].

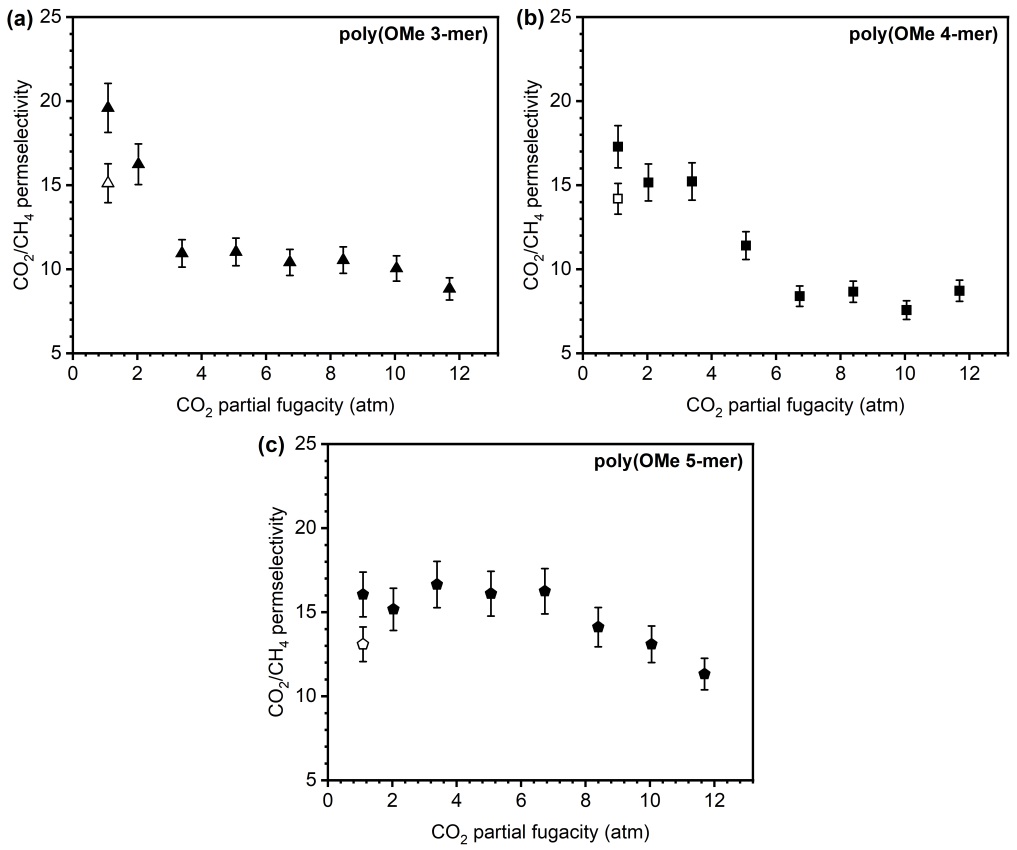

Figure 2.5: Mixed-gas CO_2/CH_4 permselectivity as functions of CO_2 partial fugacity (50:50 CO_2/CH_4 mixture at 35 °C) for (a) poly(OMe 3-mer), (b) poly(OMe 4-mer), and (c) poly(OMe 5-mer). Unfilled symbols represent pure-gas data at ~1.1 atm, and filled symbols represent mixed-gas data.

2.4 Conclusion

Pure-gas CH_4 and CO_2 sorption measurements on poly(OMe n-mer) bottlebrush poly(ladder)s revealed that increasing the side-chain length, n, led to increasing sorption. In addition, with increasing n, hysteresis from sorption experiments generally decreased, suggesting that longer rigid side chains contribute to decreased volume dilation in the presence of CO_2. Fitting isotherms to the dual-mode sorption model revealed that this model was unable to capture expected correlations between the sorption behavior of ROMPs and the physical properties of the polymer. This limitation may apply to other high graft density bottlebrush polymers. Mixed-gas CO_2/CH_4 permeation tests on poly(OMe n-mer) samples were conducted, and it was found that at low fugacities, both CO_2 and CH_4 permeabilities decreased and CO_2/CH_4 permselectivity increased from the pure-to-mixed-gas case for all samples, which is due to competitive sorption effects. High-fugacity mixed-gas tests up to a feed fugacity of ~24 atm were also performed for poly(OMe n-mer) from n = 3–5. For mixture tests, poly(OMe 3-mer) exhibited a 64% increase in CH_4 permeability and a 55% decrease in CO_2/CH_4 permselectivity over the fugacity range tested. Under the same conditions, poly(OMe 4-mer) showed improved plasticization resistance with a 25% increase in CH_4 permeability and a 50% decrease in CO_2/CH_4 permselectivity, but poly(OMe 5-mer) displayed the most plasticization resistance of the three samples with a 10% decrease in CH_4 permeability and a 30% decrease in CO_2/CH_4 permselectivity. This increase in plasticization resistance with increasing side-chain length can be attributed to the increasing interchain rigidity present from the longer side chains. Designing and controlling pore-generating side chains on bottlebrush poly(ladder)s provides a useful tool to manipulate free volume, polymer packing structure, and plasticization resistance under realistic conditions for ROMP polymers for gas separations.

2.5 Experimental methods

2.5.1 Materials and Methods

Materials

Dicyclopentadiene, sodium hydride, and Grubbs 2^{nd}-generation catalyst were purchased from Sigma Aldrich and used as received. Methyl iodine was purchased from TCI Chemicals and used as received. Anhydrous tetrahydrofuran (THF) and anhydrous dichloromethane (DCM) were obtained from an INERT PureSolv MD5 solvent purification system and stored under Ar over 4 Å molecular sieves. All other solvents were purchased at ACS grade or higher and used as received. 1,4-Anthraquinone was purified with a silica plug (using DCM as the eluent) prior to use.

Size exclusion chromatography (SEC)

SEC samples were prepared in HPLC-grade tetrahydrofuran at a concentration of 1.0 mg mL^{-1} and characterized using an Agilent 1260 Infinity system with a guard column (Agilent PLgel; 5 μm; 50 x 7.5 mm) and three analytical columns (Agilent PLgel; 5 μm; 300 x 7.5 mm;

10^5, 10^4, and 10^3 Å pore sizes). The instrument was calibrated with polystyrene standards between 1.7 and 3150 kg mol^{-1}. All runs were performed at 1.0 mL min^{-1} flow rate and 35 °C. Molecular weight values were calculated using ChemStation GPC Data Analysis Software (Rev. B.01.01) based on the refractive index signal.

2.5.2 Polymer synthesis

The polymer synthesis has been previously described [19], [20], [83] and will be summarized as follows with minor modifications. First, the OMe monomer was added to an oven-dried Schlenk flask, which was evacuated and backfilled with Ar three times. The monomer was heated at 140 ∘C (n = 2) or 220 °C (n = 3–5) for 18 h. The oligomer mixture was then separated by silica gel chromatography using a Biotage Isolera flash chromatography system with Biotage Sfär HC columns containing High Capacity 20 μm silica. A solvent gradient of 5%–40% EtOAc/hexanes was successful in providing sufficient separation. The retention factor, R_f , which is defined by the ratio of the distance traveled by a compound to the distance traveled by solvent, decreases with increasing n. Isolated oligomers were dissolved in a small amount of DCM and precipitated in methanol prior to polymerization in order to remove impurities, presumably from the evaporated solvent used for chromatography. OMe n-mers were dried in the vacuum oven at 60 °C for at least 3 h.

For the polymerization, OMe 5-mer (320.2 mg, 0.21 mmol, 1 equiv.) was added to an oven-dried Schlenk flask, which was evacuated and backfilled with Ar three times, and then dissolved in DCM (2 mL). In a separate oven-dried vial, Grubbs 2nd-generation catalyst (1.8 mg, 0.002 mmol, 0.01 equiv.) was dissolved in DCM (1 mL). The catalyst solution was transferred by syringe into the oligomer solution, and the reaction mixture was stirred at room temperature for 18 h. The flask was unsealed and 1 drop of ethyl vinyl ether was added to quench the catalyst. The polymer solution was precipitated in methanol, and the solid was collected by vacuum filtration, washed with methanol, and dried under vacuum. The above procedure was used for the polymerization of poly(OMe 2-mer), poly(OMe 3-mer), and poly(OMe 4-mer).

2.5.3 Polymer film preparation

Similar to our previous work [20], [83], polymers were dissolved in chloroform (2 wt%) and cast onto 50 mm diameter flat-bottom glass petri dishes that contained Norton®fluorinated ethylene propylene (FEP) liners (Welch Fluorocarbon). The dish was then covered with aluminum foil, and another glass dish was placed on top of the foil, allowing slow solvent evaporation and enabling film formation inside a chemical fumehood for 4 days. Afterward, the formed films were dried at 120 °C for 24 h under full vacuum to remove residual solvent. The thicknesses of all film samples were 140 ± 10 μm, as measured by a digital micrometer.

2.5.4 High-presure pure-gas sorption measurements

CH_4 and CO_2 high-pressure sorption isotherms were collected for all poly(OMe n-mer) samples at 35 ∘C using a dual-volume, dual-transducer automated pressure decay system from Maxwell Robotics. Approximately 0.15–0.2 g of polymer film was loaded into the sample cell that was then sealed with a VCR gasket. The system was then degassed for 8 h to remove any residual dissolved gases in the films. The temperature was controlled using a built-in air heating system. For CH_4 and CO_2, isotherms were measured up to 48–51 atm. Additionally for CO_2, depressurization isotherms were subsequently collected back down to 1 atm in order to evaluate the change in sorption after exposure to high pressures of CO_2. Equilibrium hold times for each pressure point were set to 2.5 h for CH_4 and 2 h for CO_2. After measuring the sorption isotherm of CH_4, the system was held under vacuum for 6 h before beginning the sorption isotherm for CO_2. In order to correct for nonidealities, fugacity is reported based on the second virial equation of state [116]. Error bars for individual points were determined using error propagation [117], [118].

To generate sorption isotherms, the amount of moles sorbed into the polymer was determined for each equilibrium fugacity point using a mole balance between the initial and equilibrium conditions [48]. Isotherms were then fit using the dual-mode sorption (DMS) model:

$$C = k_D f + \frac{C_H^{'} b f}{1 + b f} \tag{2.1}$$

where C is the concentration of gas in the polymer (cm^3(STP) cm^{-3}(polymer)), f is the equilibrium fugacity (atm), k_D is Henry's constant (cm^3(STP) cm^{-3}(polymer) atm^{-1}), $C_H^{'}$ is the Langmuir capacity constant (cm^3(STP) cm^{-3}(polymer)), and b is the Langmuir affinity constant (atm^{-1}). The fit was performed via a nonlinear optimization using the χ^2 parameter as the objective function, and uncertainties used for the χ^2 parameter were determined from error propagation [117]. Each gas–polymer pair was optimized independently. Error bars for k_D, $C_H^{'}$, and b were determined by varying each parameter (while all other parameters were fixed) about a quadratic estimation of χ^2 with respect to the varied parameter [119], [120].

The sorption coefficient can be calculated by dividing the concentration by the corresponding fugacity:

$$S = \frac{C}{f} = k_D + \frac{C_H^{'} b}{1 + b f} \tag{2.2}$$

The sorption coefficient at infinite dilution (i.e., the sorption behavior of the first penetrant in the polymer matrix) can be determined by taking the limit of Equation 2.2 as

fugacity approaches zero:

$$\lim_{f \to 0} S = S_{\text{inf}} = k_D + C_H^{'} b \tag{2.3}$$

2.5.5 Mixed-gas permeation measurements

Mixed-gas permeation tests were performed with CO_2/CH_4 mixtures at 35 °C using an automated constant-volume, variable-pressure systems from Maxwell Robotics with an in-line Agilent 7890B gas chromatograph (GC) to measure gas composition in the feed and permeate streams. The temperature was maintained using a built-in air-heating system. To prepare polymer samples for permeation tests, polymer films were attached over a hole on a brass disk using epoxy (Devcon 5 min Epoxy). The epoxy was left to dry for at least 30 min. The active membrane area was 5.8 ± 0.7 cm^2. After loading the sample into a stainless steel permeation cell, the system was degassed overnight to remove residual dissolved gases in the film.

The upstream pressure was set using a proportional–integral–derivative (PID) controller. Feed mixtures were generated at the desired composition with Bronkhorst mass flow controllers that maintained gas flow at high rates (300–800 sccm) in order to avoid concentration polarization. The maximum stage cut used for experiments (ratio of permeate flow to sweep flow) was <0.1%. For all samples, pure-gas permeability tests were conducted first for CH_4 and CO_2 at ~1.1 atm. Then, three CO_2/CH_4 mixture compositions (20:80, 80:20, and 50:50) were tested at a total mixed-gas feed fugacity of ~2.2 atm. Finally, the feed composition was fixed at 50:50 CO_2/CH_4 and the total mixed-gas feed fugacity was increased from 2.2 to ~24 atm. For each mixed-gas step, gas was collected in a downstream volume that had been previously evacuated. All permeation experiments were run for at least 10 time lags of the slower permeating gas (CH_4); after which, the downstream volume was evacuated and re-filled up to a pressure of ~13.5 torr, and this gas was injected into the GC for analysis.

The molar composition of gas in the downstream was calculated using GC calibration curves. Calibration of the GC was performed according to previously reported methods [17], [86] and is summarized as follows. The ratios x_{CO_2}/x_{CH_4} and $_{CO_2}/A_{CH_4}$ were correlated, where A_i is the area of the peak recorded by the GC for gas i determined via integration with Agilent software. A broad range of concentrations (5–95% CO_2) was used, and a linear equation $x_{CO_2}/x_{CH_4} = k'\ A_{CO_2}/A_{CH_4}$ was established (R^2 = ~0.9999) with k' being a calibration constant.

In order to calculate permeability for gas i, the following equation was used:

$$P = \frac{V_d}{RT}\frac{l}{A}\frac{1}{x_i p_2}\left[y_i\left(\frac{dp_1}{dt}\right)_{ss} - \left(\frac{dp_1}{dt}\right)_{leak}\right] \tag{2.4}$$

where V_d is the downstream volume, R is the ideal gas constant, T is the absolute experimental temperature, l is the film thickness, A is the area of film exposed to the gas, p_2 is the upstream pressure, $\left(\frac{dp_1}{dt}\right)_{ss}$ is the rate of pressure rise in the downstream at steady state, and $\left(\frac{dp_1}{dt}\right)_{leak}$ is the rate of pressure rise in the downstream when the system is isolated, and x and y are the mole fractions of gas i in the upstream and downstream, respectively, determined by the GC. Note that for a pure-gas case, both x_i and y_i would equal 1, which leaves Equation 2.4 to be equal to the puregas permeability equation:

$$P = \frac{V_d}{RT}\frac{l}{A}\frac{1}{p_2}\left[\left(\frac{dp_1}{dt}\right)_{ss} - \left(\frac{dp_1}{dt}\right)_{leak}\right] \tag{2.5}$$

2.5.6 CO_2 Hysteresis

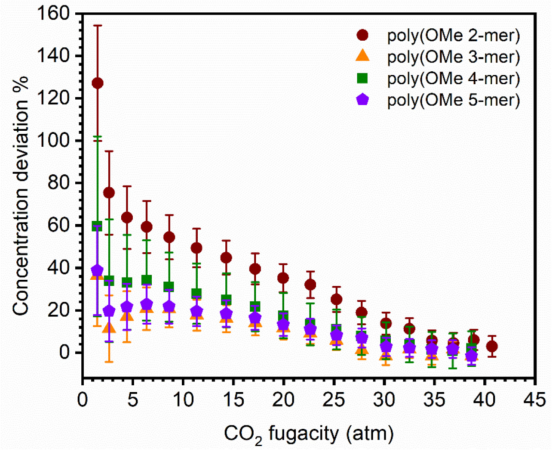

Figure 2.6: Hysteresis induced by conditioning samples at ~39–41 atm CO_2. Note that sorption and desorption data points had slightly offset pressures based on final equilibrium conditions from the pressure decay measurement, so linear interpolation between data points was used for this plot to calculate concentration deviations at equal pressure steps. Error bars were determined using error propagation.

2.5.7 Dual-mode Sorption Data

Table 2.1: Sorption at infinite dilution (S_{inf}) for CH_4 and CO_2 of poly(OMe n-mer) samples considered in this study. Units of S_{inf} are in $\text{cm}^3\text{(STP)}\ \text{cm}^{-3}\text{(polymer)}\ \text{atm}^{-1}$.

	S_{inf,CH_4}	S_{inf,CO_2}
Poly(OMe 2-mer)	3 ±1	13 ±2
Poly(OMe 3-mer)	3.9 ±0.6	15.4 ±0.6
Poly(OMe 4-mer)	5.4 ±0.8	19 ±2
Poly(OMe 5-mer)	5.7 ±0.9	20 ±1

Table 2.2: Dual-mode sorption model parameters for all poly(OMe n-mer) samples. Units of k_D are in $\text{cm}^3\text{(STP)}\ \text{cm}^{-3}\text{(polymer)}\ \text{atm}^{-1}$, units of $C_H^{'}$ are in $\text{cm}^3\text{(STP)}\ \text{cm}^{-3}\text{(polymer)}$, and units of b are in atm^{-1}.

n	Gas	k_D	$C_H^{'}$	b	$C_H^{'}b$	$C_H^{'}b/k_D$
2	CH_4	0.41±0.04	10 ±1	0.3 ±0.1	3 ±1	7 ±3
	CO_2	1.24±0.04	28 ±1	0.41±0.06	12 ±2	9 ±1
3	CH_4	0.76±0.02	12.4 ±0.6	0.25±0.04	3.1 ±0.5	4.1 ±0.6
	CO_2	1.74±0.02	25.3 ±0.4	0.54±0.02	13.7 ±0.6	7.8 ±0.4
4	CH_4	0.54±0.06	20 ±1	0.24±0.04	4.9 ±0.8	9 ±2
	CO_2	1.71±0.08	33 ±1	0.52±0.05	17 ±2	10 ±1
5	CH_4	0.75±0.07	19 ±1	0.26±0.04	4.9 ±0.9	6 ±1
	CO_2	1.83±0.07	37 ±1	0.50±0.07	19 ±1	10.2 ±0.9

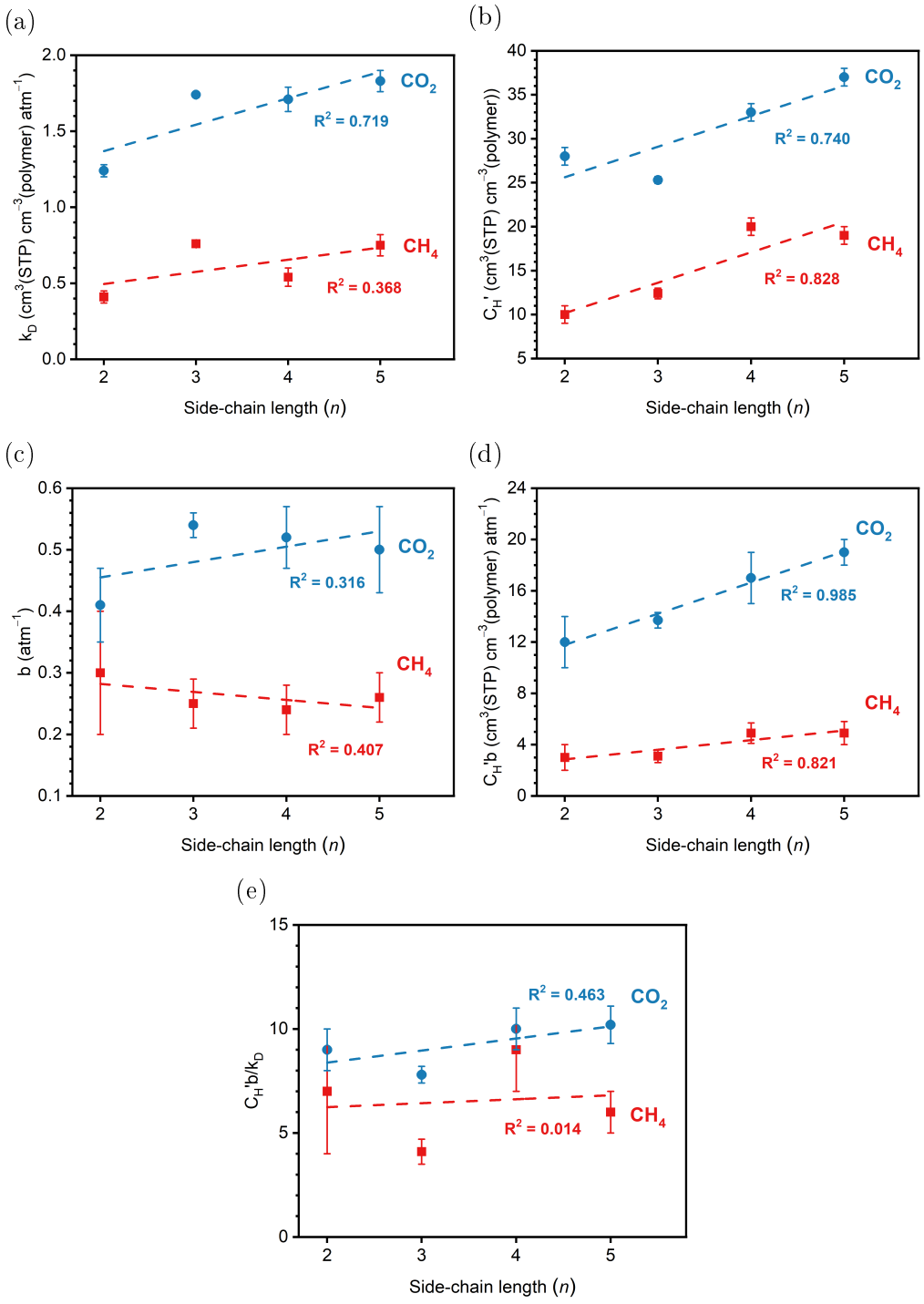

Figure 2.7: Dual-mode sorption parameters (a) k_D, (b) $C_H^{'}$, (c) b, (d) $C_H^{'}b$, and (e) $C_H^{'}b/k_D$ for CH_4 (red squares) and CO_2 (blue circles) versus side-chain length for all poly(OMe n-mer) samples considered in this study. Linear fits and R2 values were calculated using the Origin 2019b linear fitting tool, and without regard to the error bars.

2.5.8 Gas Separation Data

Table 2.3: CO_2/CH_4 gas transport properties of all poly(OMe n-mer) samples at ~1.1 atm feed fugacity (for pure gases) or ~2.2 atm total feed fugacity (for mixtures). Permeability (P) is given in barrer (10^{-10} cm^3(STP) cm cm−2 s^{-1} $cmHg^{-1}$). All data were obtained at 35 °C.

n	Mixture composition (CO_2/CH_4)	P_{CO_2}	P_{CH_4}	α_{CO_2/CH_4}
2	Pure	117 ± 8	5.8 ±0.4	20 ±2
	20:80	102 ± 6	4.3 ±0.3	24 ±2
	50:50	94 ± 6	4.1 ±0.3	23 ±2
	80:20	86 ± 5	3.7 ±0.2	23 ±2
3	Pure	210 ±10	14.1 ±0.8	15 ±1
	20:80	180 ±10	9.8 ±0.6	19 ±2
	50:50	190 ±10	11.2 ±0.7	17 ±1
	80:20	163 ± 9	9.9 ±0.6	17 ±1
4	Pure	960 ±40	67 ±3	14.2 ±0.9
	20:80	830 ±40	42 ±2	16 ±1
	50:50	750 ±40	43 ±2	17 ±1
	80:20	680 ±40	40 ±2	17 ±1
5	Pure	1480 ±80	113 ±6	13 ±1
	20:80	1270 ±70	87 ±5	15 ±1
	50:50	1160 ±60	71 ±4	16 ±1
	80:20	1050 ±70	72 ±4	15 ±1

Table 2.4: Reference mixed-gas CO_2/CH_4 permeation data. Total feed pressures for all data presented are ~2 atm (except for Cellulose Acetate, which had a total feed pressure of 3.9 atm).

Polymer	Temperature (°C)	CO_2/CH_4 Comp.	P_{CO_2} (barrer)	P_{CH_4} (barrer)	α_{CO_2/CH_4}	Reference
PIM-Trip-TB	-	50:50	3914	299	13.1	[114]
CF_3-ROMP	35	50:50	7063	779	9.07	[20]
PIM-MP-TB	25	52:48	766	36	21.3	[77]
PIM-TMN-Trip	25	60:40	11300	489	23.1	[121]
DFTTB	35	50:50	2304	82	28.1	[113]
SPIM-1-6	35	50:50	448	8.6	52.1	[122]
PIM-SBI-Trip	25	35:65	13918	685	20.3	[123]
pim-1	35	50:50	8250	810	10.2	[91]
PIM-NH_2	35	50:50	845	33.5	25.2	[91]
CoPIM-TB-1	25	50:50	6271	654	9.59	[124]
CoPIM-TB-2	25	50:50	5818	536	10.9	[124]
PIM-1/Matrimid(10:9)	25	50:50	212	8.1	26.2	[125]
Polysulfone	35	50:50	5	0.217	23	[126]
Cellulose Acetate	35	50:50	9.08	0.350	25.9	[82]

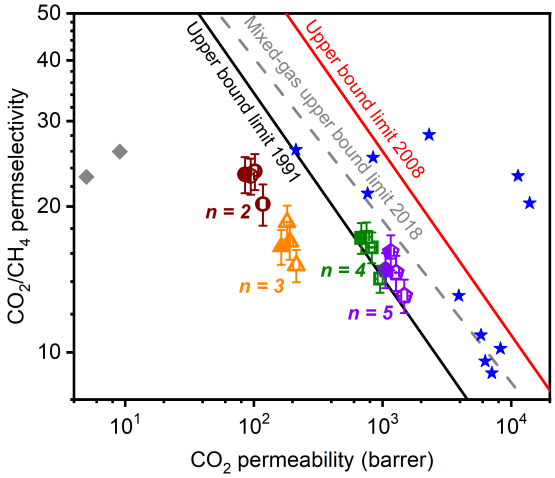

Figure 2.8: Robeson upper bound plots of all poly(OMe n-mer) samples considered in this study in comparison with commercial membranes and other newly developed materials. Gray diamonds represent commercial membranes, while blue stars represent newly developed materials. The solid red line represents the 2008 Robeson upper bound [21], the solid black line represents the 1991 Robeson upper bound [22], and the gray dashed line represents the 2018 mixed-gas upper bound [115].

Table 2.5: Variable pressure CO_2/CH_4 mixed-gas separation performance of poly(OMe 3-mer), poly(OMe 4-mer) and poly(OMe 5-mer). Mixture composition was set at 50:50. Permeability (P) is given in barrer (10^{-10} cm^3(STP) cm cm^{-2} s^{-1} $cmHg^{-1}$). All data were obtained at 35 °C.

n	CO_2 partial pressure (atm)	P_{CO_2}	P_{CH_4}	α_{CO_2/CH_4}
3	1.09	163 ± 9	8.4 ±0.4	20 ±1
	2.04	190 ±10	11.4 ±0.6	16 ±1
	3.40	158 ± 8	14.4 ±0.8	11.0 ±0.8
	5.10	139 ± 7	12.6 ±0.7	11 ±0.8
	6.80	130 ± 7	12.5 ±0.7	10.4 ±0.8
	8.51	124 ± 7	11.8 ±0.6	10.5 ±0.8
	10.21	126 ± 7	12.5 ±0.7	10.1 ±0.7
	11.91	121 ± 6	13.7 ±0.7	8.8 ±0.7
4	1.09	750 ±40	43 ±2	17 ±1
	2.04	640 ±30	42 ±2	15 ±1
	3.40	580 ±30	38 ±2	15 ±1
	5.10	540 ±30	47 ±2	11.4 ±0.8
	6.80	490 ±30	59 ±3	8.4 ±0.6
	8.51	480 ±20	55 ±3	8.7 ±0.6
	10.21	460 ±20	60 ±3	7.6 ±0.6
	11.91	470 ±20	54 ±3	8.8 ±0.6
5	1.09	1160 ±70	72 ±4	16 ±1
	2.04	990 ±60	65 ±4	15 ±1
	3.40	900 ±50	54 ±3	17 ±1
	5.10	830 ±50	51 ±3	16 ±1
	6.80	830 ±50	51 ±3	16 ±1
	8.51	790 ±50	56 ±3	14 ±1
	10.21	760 ±40	58 ±3	13 ±1
	11.91	730 ±40	64 ±4	11.3 ±0.9

2.6 Acknowledgments

This work was supported by the U.S. Department of Energy, Office of Science, Office of Basic Energy Sciences, Separation Science program under Award Number DE-SC0019087. S.L. and F.M.B. gratefully acknowledge the funding and support provided by the MIT Deshpande Center for Technological Innovation. The study on competitive sorption was supported by the Department of Navy, Office of Naval Research under ONR award N00014-21-1-2666. T.M.S. is appreciative of support from the National Science Foundation grant DMR-2207299. K.R.S. was supported by the National Science Foundation Graduate Research Fellowship under Grant No. 1745302. The authors would like to thank Katherine Mizrahi Rodriguez for help with determining experimental procedures and setup, Albert X. Wu for help with optimization of dualmode sorption calculations, and the members of the Smith lab for useful discussions and helpful suggestions.

Chapter 3

Role of grafting density and nitrile functionalization on gas transport in polymers with side chain porosity

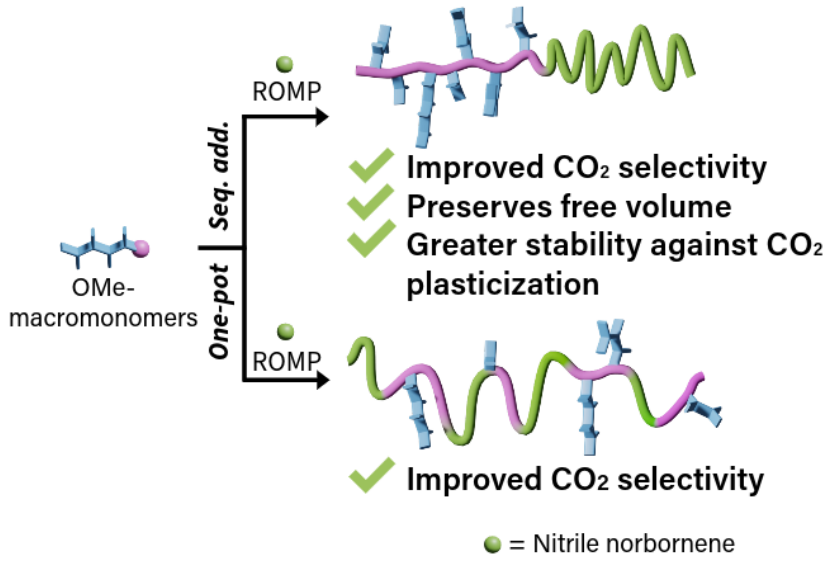

Kayla R. Storme, Sharon Lin, You-Chi Mason Wu, Sherrie X. Qian, Timothy M. Swager, Zachary P. Smith

3.1 Abstract

This study details the enhancement of CO_2 selectivity in ring opening metathesis polymerization (ROMP) polymers that contain nitrile moieties and micro-pore generating ladder side chains. A material, CN-ROMP homopolymer, with nitriles in the ladder side chains was originally targeted and synthesized, however its low molecular weight and backbone rigidity precluded film formation. As a result, an alternative method was pursued wherein copolymers were synthesized using norbornene (N) and nitrile norbornene (NN). Herein, we report an investigation of the structure–property relationships of backbone functionalization and grafting density on the CO_2 transport properties in these ROMP polymers. Nitrile-containing copolymers showed an increase in CO_2/CH_4 sorption selectivity and a concomitant increase in CO_2/CH_4 permselectivity when compared to the unfunctionalized (nitrile free) analogs. The stability in CO_2 rich environments is enhanced as grafting density of the rigid, pore-generating side chains increases and an apparent tunability of CO_2 plasticization pressure was observed as a function of norbornene content. Lower loadings of norbornene resulted in higher plasticization pressure points. Gas permeability in the ROMP copolymers was found to correlate most strongly with the concentration of ladder macromonomers in the polymer chain.

3.2 Introduction

Heat-intensive separation technologies like distillations consume roughly 50% of the energy in the chemical and petrochemical industries in the U.S. and contribute extensively to greenhouse gas (GHG) emissions [127]. Energy-efficient alternatives will be crucial to meet the 80% emissions reduction target for 2050 set by the U.S. Department of Energy [128]. Compared to legacy separation processes, membranes are a promising option that have smaller footprints, do not require solvent regeneration, and do not rely on phase changes or moving parts to perform separations [1], [2], [129]. However, to reduce capital and operating costs membrane materials must be highly permeable and selective for the products of interest [1], [130]. In recent years, researchers have focused efforts to develop high free volume polymers often referred to as polymers of intrinsic microporosity (PIMs). The free volume in these systems is achieved by integrating three dimensional rigid features that are fused into the polymer backbone to create structures that promote stochastic pore formation through inefficient chain packing [9], thereby enhancing gas permeability [8]. Benzotriptycene-based PIMs [131], thermally rearranged (TR) polymers [16], and catalytic arene-norbornene annulation (CANAL) polymers [17] demonstrate remarkable improvements to gas separation performance. Despite exceptional advancements in permeability–selectivity property sets, there are still outstanding questions related to material stability under relevant environments [81], [124], [132]. In 2018, we reported a class of bottlebrush polymers with rigid side chains via ring-opening metathesis polymerization (ROMP) [19] that showed high CO_2 permeability and an impressive resistance to CO_2-induced plasticization. In fact, at 35°C, no CO_2 plasticization pressure was observed up to the maximum testing pressure of 51 bar [20]. In follow-up studies with CO_2/CH_4 mixture testing, we further demonstrated that the stability against CO_2-induced plasticization is modulated by the length of the pore-generating

side chains in these ROMP systems [83], [133]. Unfortunately, the ROMP polymers exhibit only moderate selectivity for CO_2 when compared to other state-of-art PIMs.

Promising approaches to increase CO_2 selectivity in glassy polymers include incorporation of CO_2-philic groups into the polymer structure. To this end, researchers have post-synthetically functionalized the PIM-1 architecture by converting native nitrile groups in the polymer backbone into amidoximes (PIM-AO) [87], thioamides (PIM-TA) [30], carboxylic acids (PIM-COOH) [90], [134], [135], and amines (PIM-NH_2) [136]. Rodriguez et al. evaluated the structure–property relationships between different chemistries and identified CO_2 sorption affinity increases from carboxylic acid < nitrile < amine [91]. Since each functional group discussed previously can be made from a nitrile precursor, similar sorption advancements could be envisioned for the poly(ladder) ROMP family if nitriles could be incorporated into the polymer, which is the aim of this study.

Therefore, we installed nitrile moieties along the rigid side chains using graft-through polymerization methods to afford CN-ROMP (Scheme 3.1a) and we installed nitrile moieties in the backbone through copolymerization (Scheme 3.1b) with commercial nitrile norbornene (NN). CN-ROMP has a BET surface area of 791 $m^2\ g^{-1}$ (Figure 3.4), which is higher than the previously studied OMe- and CF_3-ROMPs [20], and thus a record for the ladder side-chain approach. However, we were unable to obtain flexible, free-standing films for further characterization. Consequently, our gas separation results focus on the copolymerization method to incorporate nitrile moieties. Poly(NN) was identified as an oxygen selective membrane in 1988, but displayed low permeability likely due to strong dipole–dipole interactions from the nitrile moieties and close packing of the polymer chains [137]. Kawakami et al. demonstrated the permeability of poly(NN) could be enhanced by introducing bulky, rigid groups at the methylene alpha to the nitrile bearing carbon of the norbornene monomer [137]. To our knowledge, nitrile norbornene has not been examined in the context of CO_2/CH_4 separations. Considering the high CO_2 permeability and ease of synthesis of OMe-ROMP [20], [83], [133], it was a good candidate for copolymerization with NN to disrupt dense packing of poly(NN) chains. Copolymers with different amounts of NN content were synthesized and simple norbornene (N) analogs were prepared to evaluate the effect of the nitriles. We first demonstrate the NN-based copolymer with 50 wt% loading of NN displays higher CO_2 sorption and CO_2/CH_4 sorption selectivity than the N-based analog. We observed increases in CO_2/CH_4 selectivity in all NN-based copolymers compared to N-based copolymers, supporting the role of the nitrile on CO_2-enhanced transport. Decreasing the loading of NN and N comonomers resulted in increased CO_2 permeability with minimal change in CO_2/CH_4 selectivity. We also found CO_2 plasticization pressures were tunable in N-based copolymers when varying loading of N, whereas the NN-based copolymers did not exhibit this behavior. To evaluate the impact of increasing grafting density on gas transport, we synthesized an NN-based block copolymer using 50 wt% NN loading and observed a reduction of CO_2/CH_4 selectivity relative to the statistical copolymer. This result reflects the similar increases in diffusivity of both CO_2 and CH_4 with the availability of larger pores generated by neighboring rigid side chains.

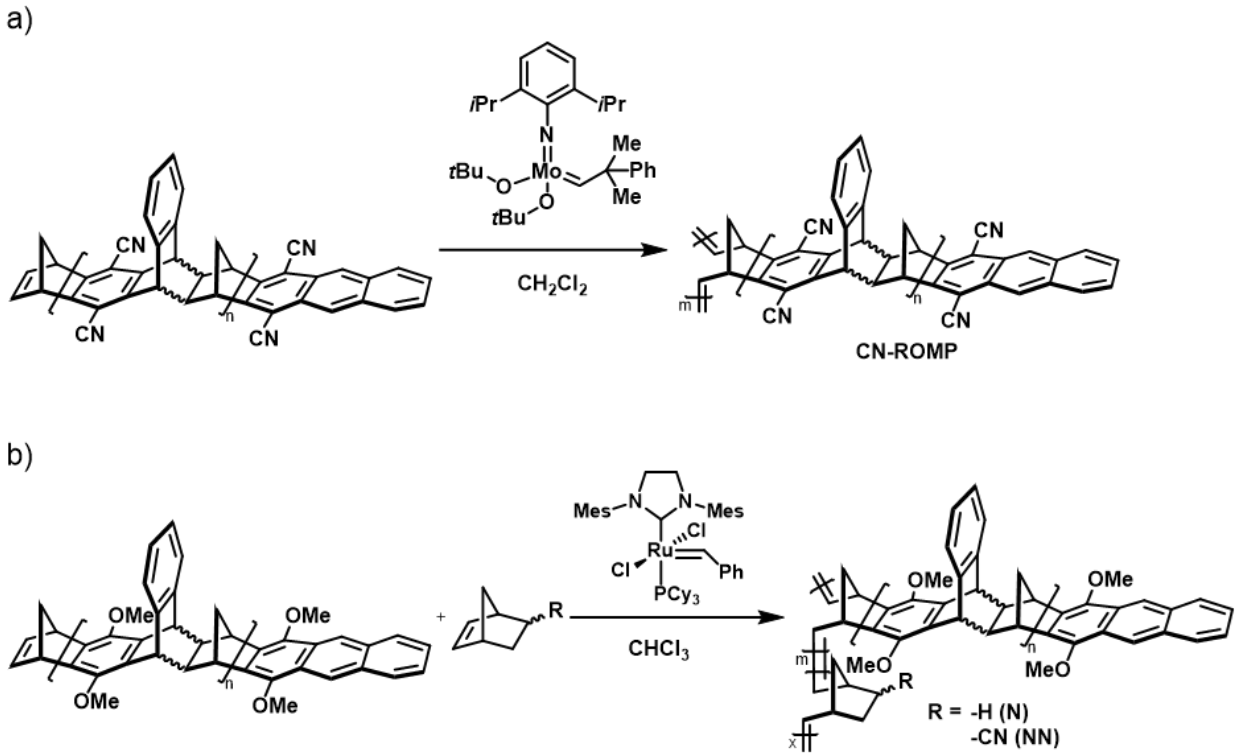

Scheme 3.1: Synthesis of a) CN-ROMP and b) norbornene (N)- and nitrile norbornene (NN)-based copolymers.

3.3 Results and discussion

3.3.1 Synthesis

The synthesis of CN-macromonomers was achieved in four steps (Scheme 3.2). First, 2,3-dimethylnaphthalene was brominated using Wohl-Ziegler conditions to yield 2,3-bis(bromomethyl)naphthalene (**1**). The bromides were then substituted with cyanides to give 2,3-bis(cyano- methyl)naphthalene (**2**). Following the substitution, we performed a condensation reaction with 2,3-bis(cyanomethyl)naphthalene and 2,3-dione-5-norbornene to produce the CN-ROMP monomer (**3**). To synthesize the CN-based macromonomers (**4**), the neat Diels-Alder of the CN-ROMP monomer required a higher temperature (274°C) than the OMe- and CF_3- analogs [19], [20]. The ROMP of the CN-based macromonomers was unsuccessful with Grubbs' and Hoveyda-Grubbs' catalysts likely due to obstruction of the polymerization due to nitrile-ruthenium coordination and/or interaction with the electron accepting π-system [138]. Schrock's catalyst has been used to make CN-containing ROMP polymers previously [139], so we switched to Schrock's catalyst to successfully synthesize CN-ROMP (Scheme 3.1a). The molecular weight of CN-ROMP was lower than our previously reported ROMPs [19], [20] and we were unable to fabricate free-standing films for permeation characterization. In addition to this challenge, repeated polymerization attempts were inconsistent, sometimes yielding lower molecular weight (<35 kDa M_n) or no polymer. Consequently, we

chose to synthesize copolymers using OMe-based oligomers to reduce inconsistencies.

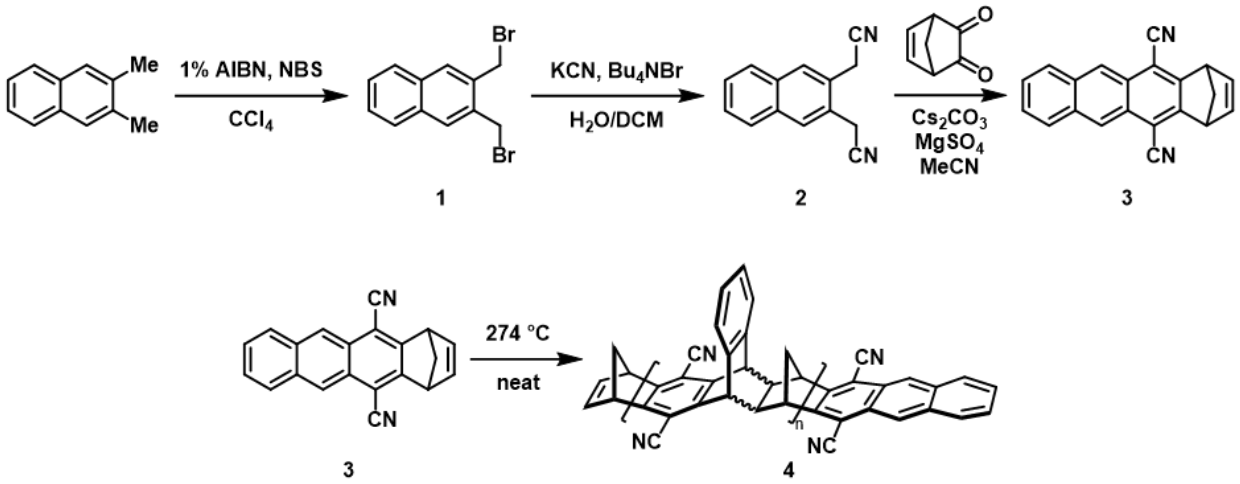

Scheme 3.2: Synthesis of CN-macromonomers (**4**).

We copolymerized the OMe-macromonomers with NN or N using a one-pot synthesis to produce statistical copolymers for this study. A series of copolymers as NN-X or N-X were produced, where X is the molar ratio of NN or N to OMe-macromonomer determined using HMBC, HSQC, and ^{1}H NMR (see the Experimental section for more details). For instance, a copolymer containing 13:1 NN to OMe-macromonomer would be labelled as NN-13. Likewise, a copolymer containing 3:1 N to OMe-macromonomer would be labelled as N-3. Given the significantly higher molecular weight of the OMe-macromonomer, statistical copolymers produced with 50 wt% NN or N loading yielded NN-13 and N-19, respectively. Additionally, we suspect the nitriles are coordinating with the ruthenium-center [138], inducing slower propagation and reducing OMe-macromonomer incorporation efficiencies. Longer OMe-macromonomers present in the reaction may also hinder propagation. Decreasing the loading of NN to 27.5 wt% produced statistical copolymer NN-3 while a 26.3 wt% loading of N gave statistical copolymer N-3. We note that N-3 had the broadest polydispersity (Đ = 5.5) (Table 3.2) compared to all the other copolymers, suggesting intra- and inter-chain side reactions occurred. The NN-based block copolymer, NNb-24, made with 50 wt% NN loading was also prepared for this study. We confirmed successful formation of the block copolymer by analyzing the retention time of polymer aliquots before and after addition of NN (Figure 3.5). The characteristic –C≡N stretch signal near 2260 cm^{-1} was identified in IR spectroscopy (Figure 3.6) for all NN-based copolymers thereby confirming successful incorporation of NN. OMe-ROMP does not show a measurable T_g below its degradation temperature, however poly(N) and poly(NN) homopolymers do have accessible T_gs. Poly(NN) and poly(N) homopolymers have high thermal stability with a $T_{d,5}$ temperature of 401°C and 398°C, respectively (Figure 3.7). The T_gs are observed at 136°C and 45°C for poly(NN) and pol(N), respectively (Figure 3.8), which are close to values reported in literature [137], [140]. All the copolymers show excellent thermal stability with $T_{d,5}$ temperatures between 336°C and 345°C (Figure 3.7). The statistical copolymers NN-13 and N-19 exhibit T_gs at 224°C and 78°C, respectively, as revealed by DSC and DMA analysis (Figures 3.8 and 3.9).

The T_g of block copolymer NNb-24 was found to be 176°C (Figure 3.8).

3.3.2 Pure-gas sorption analysis

The pure-gas CO_2 sorption and CO_2/CH_4 sorption selectivity measured at 35°C of CN-ROMP, block copolymer NNb-24, and statistical copolymers N-19 and NN-13 are presented in Figure 3.1. We observed the highest CO_2 sorption in CN-ROMP and greater CO_2 sorption with increasing nitrile content in the copolymers (Figure 3.1a). Moreover, when compared to OMe-ROMP homopolymers, CN-ROMP had higher overall sorption, demonstrating the benefits of CN incorporation and high BET surface area of this material (Figure 3.4). The relative order of ideal CO_2/CH_4 sorption selectivity (NN-13 > NNb-24 > CN-ROMP > N-19) shown in Figure 3.1b confirms that nitriles boost selectivity for CO_2. Our previous studies identified pore size distributions for poly(OMe 4-mer) and polydisperse OMe-ROMP averaging near 10 Å [83]. When collecting WAXS data of the copolymers, we observed an additional diffuse scattering peak at 10.3 Å for NNb-24 that is not present for NN-13 or poly(NN) homopolymer (Figure 3.10a). Thus, we attributed the larger d-spacing associated with voids to inefficient polymer chain packing from the rigid macromonomer block [141]. We suspect the statistical copolymer architecture enables NN comonomers to occupy free volume generated by the rigid macromonomers, resulting in the absence of larger d-spacing values. When the macromonomers are in a block sequence, this appears to preserve the poly(OMe) homopolymer morphology.

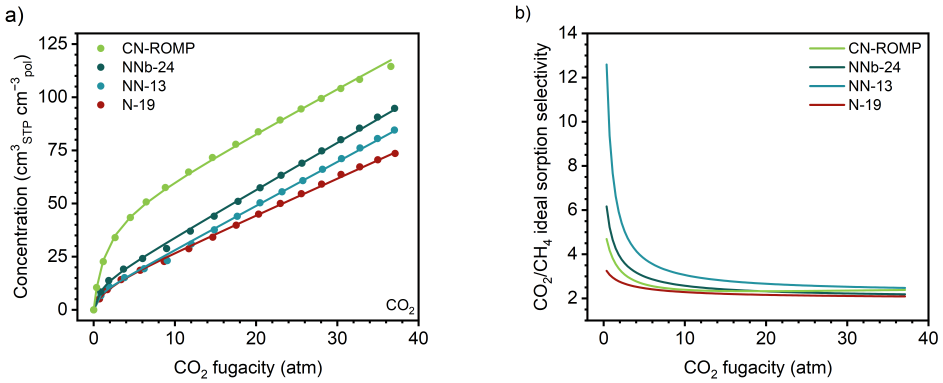

Figure 3.1: a) Pure-gas CO_2 sorption isotherms with dual-mode model fits and b) ideal CO_2/CH_4 sorption selectivity for CN-ROMP, NNb-24, NN-13, and N-19 copolymers.

We calculated dual-mode sorption (DMS) parameters for CN-ROMP, NNb-24, NN-13, and N-19 to investigate the sorption behavior of CO_2 and CH_4 (Table 3.1) and to help with extracting values of sorption at infinite dilution, S_{inf}. The Langmuir affinity constant, b, is an equilibrium constant that describes the likelihood of a specific penetrant to sorb within the Langmuir mode [142]. S_{inf}, is a material property that describes the partitioning of the first penetrant from the gas phase into the polymer matrix [143]. DMS fitting was successful for all polymers tested except for the CH_4 isotherm of NN-13 due to its linearity. Thus, we fitted

Table 3.1: CH_4 and CO_2 sorption at infinite dilution (S_{inf}) for N-19, NN-13, NNb-24, and CN-ROMP. Data for poly(OMe 5-mer) [133] and PIM-1 [91] is included for comparison. S_{inf} is given in units of $cm^3STP\ cm^{-3}pol\ atm^{-1}$.

Gas	N-19	NN-13	NNb-24	CN-ROMP	Poly(OMe 5-mer) [133]	PIM-1 [91]
CH_4	3.17±0.1	0.917±0.009	2.4 ±0.5	6.43±0.07	5.70	9.64
CO_2	11.2 ±0.3	19.1 ±1.7	19.1 ±1.1	35.19±0.04	20.0	48.0

the CH_4 isotherm data for NN-13 to Henry's law as an approximation. We note that CN-ROMP shows higher b and S_{inf} parameters for CO_2 than poly(OMe 5-mer) [133], confirming nitriles enhance affinity for CO_2 relative to methoxy groups. Parameters b and S_{inf} from the CO_2 sorption isotherm are larger for copolymer NNb-24 and NN-13 than N-19, indicating the NN-based copolymers have greater affinity for CO_2 than N-19 (Tables 3.1 and 3.3). Despite greater nitrile content, block copolymer NNb-24 exhibits the same S_{inf} and lower b for CO_2 than statistical copolymer NN-13. The decrease in b appears to be compensated by a larger Langmuir capacity constant, $C_H^{'}$, which could be an artifact of least-squares fitting with these coupled parameters. Furthermore, the physical meaning of $C_H^{'}$ is not well-defined in these phenomenological models, so we decline drawing robust conclusions with this comparison [130], [144]. The NN-13 and NNb-24 copolymers demonstrate an S_{inf} for CO_2 that is 46% lower than CN-ROMP and 60% lower than PIM-1 [91], indicating the position of nitriles relative to pore-generating ladder structures of the polymer may enhance selectivity for CO_2. Compared to PIM-1, S_{inf} is 27% lower in CN-ROMP. When studying sorption in monodisperse OMe-ROMP, we noted improvements in S_{inf} as side chain length increased [133], suggesting monodisperse CN-ROMP with longer sidechains could improve S_{inf}.

3.3.3 Pure-gas permeation analysis

The expected higher CO_2/CH_4 selectivity for the NN-based copolymers is observed in pure-gas permeation tests (Figure 3.2a). We found the NN-3 statistical copolymer exhibits a 1.3-fold and 1.7-fold increase in CO_2/CH_4 selectivity compared to N-3 and OMe-ROMP [83], respectively. Nevertheless, increasing nitrile content from NN-3 to NN-13 provides minimal enhancement to CO_2/CH_4 selectivity and reduces the gas throughput by one order of magnitude. In contrast, the block copolymer NNb-24 displayed a 2-fold increase in permeability compared to the statistical copolymer NN-13 and a 27% decrease in CO_2/CH_4 selectivity. We attribute this decrease in selectivity to a greater diffusivity through excess free volume of the OMe block identified via WAXS (Figure 3.10a) within the rigid macromonomer. To better understand the gas transport behavior, we tabulated diffusivity and sorption coefficients calculated from the time-lag method and compared trends in gas transport between all copolymers tested (Table 3.4). We observed a 2-fold increase in CO_2/CH_4 sorption selectivity for NN-13 relative to N-19 when using coefficients obtained from the time-lag calculations (Figure 3.2b and Table 3.4). We noted a similar increase using data from equilibrium sorption measurements (Table 3.4), and hence, these results cannot be attributed to artifacts from only considering transport diffusivities. Furthermore, the time-lag method is known to have large uncertainties in lab-to-lab studies,[145] so the equilibrium measurements

are helpful for us to report more statistically robust conclusions. Figure 3.2b and Table 3.5 further reveal that NNb-24 displays similar CO_2/CH_4 sorption selectivity to NN-3 despite its higher nitrile content. In Figure 3.2c and Table 3.5, the CO_2/CH_4 diffusivity selectivity in NN-3 and N-3 copolymers is found to be greater than the rest of the copolymers and is close to the CO_2/CH_4 diffusivity selectivity reported for poly (OMe 4-mer). Copolymers with larger amounts of N and NN show similar CO_2/CH_4 diffusivity selectivity, so differences in gas transport between the copolymers arise from changes in CO_2/CH_4 sorption selectivity.

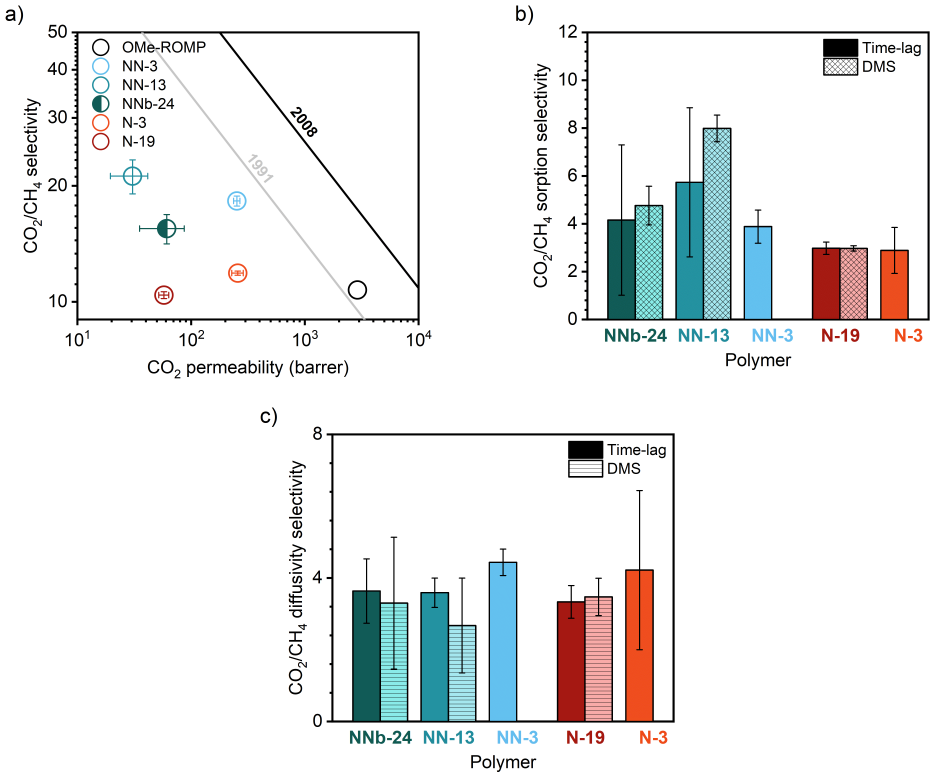

Figure 3.2: Pure-gas a) permeation of CO_2/CH_4 for NN- and N-based copolymers compared to OMe-ROMP [83] measured at 35°C and 1 atm, b) CO_2/CH_4 sorption selectivity calculated from permselectivity divided by time-lag diffusivity selectivity measurements for each copolymer, and c) CO_2/CH_4 diffusivity selectivity calculated from time-lag for each copolymer. Figures 3.2b and 3.2c also contain selectivity derived from static equilibrium sorption measurements for NN-13 and N-19. These results are reported as DMS results in the figure.

3.3.4 CO_2-induced plasticization

We expected that changes in density of the ladder polymer side chains would impact the exceptional plasticization resistance exhibited by OMe-ROMP [20], [83], so we investigated the stability against CO_2 plasticization of each copolymer with pressure-increase experiments (Figure 3.3). The plasticization pressure remained at ~4 bar of CO_2 pressure for all NN-based copolymers tested. However, decreasing nitrile content or using a blocky morphology was

observed to lower the rate of increase in CO_2 permeability, thereby elevating stability against CO_2 plasticization (Figure 3.3a). The N-based copolymers showed higher plasticization pressures (~20 bar) at lower levels of N incorporation (Figure 3.3b). This finding may relate to the lower CO_2 sorption in the N polymers, which would result in reduced T_g suppression and hence a resistance to enhanced corporative chain motion, which is the origin of plasticization [146]. This tunability of the CO_2 plasticization pressure is similar to what was observed with increasing the length of the rigid, pore-generating side chains in OMe-ROMP [83]. Our results suggest a higher density of the rigid ladder oligomer side chain macromonomers promotes greater stability against CO_2 plasticization. Mixed-gas permeation experiments enrich our understanding of the competitive effects arising from the presence of nitriles and will be the focus of future studies of these statistical and block copolymer architectures.

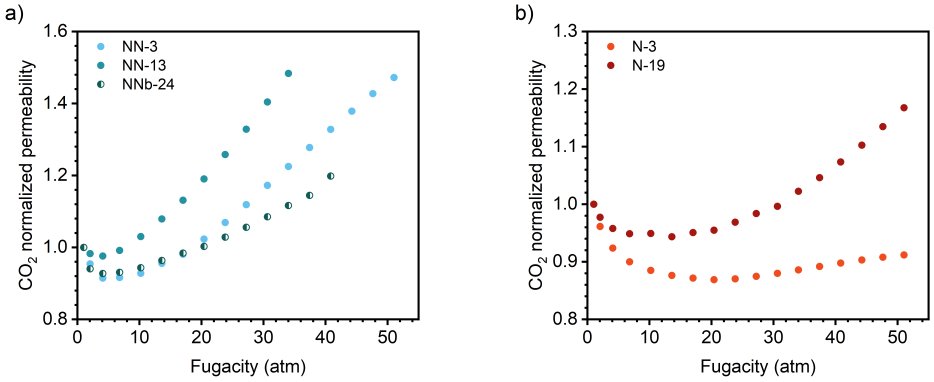

Figure 3.3: Normalized CO_2 permeabilities for high pressure sweeps of a) NN- and b) N-based copolymers.

3.4 Conclusions

Pure-gas sorption of CN-ROMP and transport of five copolymers based on OMe-ROMP were evaluated to investigate the role of free volume promoting ladder side chains and nitrile incorporation on CO_2/CH_4 selectivity and CO_2 plasticization. Equilibrium sorption analysis and permeation experiments confirmed our hypothesis that nitriles enhance CO_2 sorption affinity and CO_2/CH_4 permselectivity. Our findings also revealed that the density and connectivity of the rigid, pore-generating side chains influenced transport properties. Decreasing density of the rigid side chains in NN-13 resulted in a 40% increase in CO_2/CH_4 sorption selectivity compared to the block copolymer NNb-24. Moreover, we also observed a 50% increase in CO_2 and CH_4 diffusivity for NNb-24 compared to NN-13, suggesting a benefit to using a block copolymer approach to enhance diffusivity even with a lower concentration of pore-generating ladder side chains. This finding was supported through WAXS analysis, which demonstrated that blocks of free-volume-generating macromonomers could preserve the high free-volume features found in the poly(ladder) homopolymers. Greater stability against CO_2 plasticization was also attributed to higher density of the rigid macromonomers.

This study introduces a CO_2-philic functional group through copolymerization that improves CO_2 selectivity and highlights the structure–property relationships between the density of pore-generating side chains, backbone functionalization, gas transport, and plasticization stability in an emerging class of PIM materials.

3.5 Experimental methods

3.5.1 Materials

Dicyclopentadiene, sodium hydride (60% in mineral oil), 2-norbornene, and Grubbs 2^{nd}-generation catalyst were purchased from Millipore Sigma. Methyl iodide was purchased from TCI Chemicals, 5-norbornene-2-carbonitrile was purchased from TCI Chemicals and Combi-Blocks, magnesium sulfate and cesium carbonate were purchased from Macron Fine Chemicals, and acetonitrile (MeCN) was purchased from Alfa Aesar in a ChemSeal bottle. Anhydrous tetrahydrofuran (THF) and anhydrous DCM was obtained from an INERT PureSolv MD5 solvent purification system and stored under argon over 4 Å molecular sieves. Chloroform was purchased from Millipore Sigma and sparged with Argon for at least 30 minutes prior to use. 1,4-anthraquinone was purchased from Combi-Blocks and purified with a silica plug using DCM as the eluent prior to use. HPLC-grade THF and HPLC-grade chloroform were purchased from J. T. Baker. All other solvents were purchased at ACS grade or higher and used as received.

3.5.2 Polymer film preparation

Copolymer solutions containing 2 wt% polymer were prepared in chloroform and cast into flat-bottom PTFE petri dishes. After 1–2 days of slow evaporation at room temperature in a fume hood, stable, free-standing, and defect-free films were formed. Each film was soaked in methanol for 24 h then air-dried in a fume hood for 24 h before testing.

3.5.3 Chemical Characterization

The chemical structure was studied using ^{1}H, ^{13}C nuclear magnetic resonance (NMR) spectroscopy in a 400 MHz two-channel Bruker Avance-III HD Nanobay spectrometer or 600 MHz four-channel Bruker Avance Neo spectrometer. HMBC, HSQC, and COSY NMR spectra were also used and collected on a 600 MHz four-channel Bruker Avance Neo spectrometer. Samples were prepared in deuterated chloroform and referenced to the residual solvent signal. Relative ratios of each comonomer were determined using the following method:

We identified peaks near 120 ppm for the NN-based copolymers in HMBC NMR (Figures 3.24, 3.28, and 3.32) that do not appear for OMe-ROMP (Figure 3.21) and designated the protons between 3.32–1.25 ppm to be two to three bonds away from the nitrile moiety. The aliphatic –CH signal at 2.99 ppm identified in the HSQC NMR (Figures 3.25, 3.29,

and 3.33) were assigned to the bridgehead proton next to the nitrile through correlations observed with the backbone –CH protons at 5.75–5.22 ppm in COSY (Figures 3.26, 3.30, and 3.34). Since the peaks between 8.39–8.48 ppm correspond to the protons on the middle ring of the terminal anthracene moiety in the OMe-macromonomers, we integrated the peaks relative to the backbone –CH protons at 5.75–5.22 ppm to find the percentage associated with the OMe-macromonomers. We determined the ratio of NN incorporated by finding the difference and dividing it by the percentage associated with OMe-macromonomers. For the N-based copolymers, we identified the peaks at 2.82 and 2.46 ppm to be the bridgehead protons of cis and trans poly(N) segments by HSQC NMR (Figures 3.37 and 3.41). We followed the same procedure as described for the NN-based copolymers to determine the ratio of N to OMe-macromonomers in ^{1}H NMR (Figures 3.35 and 3.39) to determine the ratio of N to OMe-macromonomers. To identify the –C≡N functional group in NN-based copolymers, infrared spectra were collected using a Thermo Fisher FTIR6700 spectrometer in the attenuated total reflection (ATR) mode for a total of 32 scans between the 500–4000 cm^{-1} range using a resolution of 4 cm^{-1}.

Molecular weight and dispersity of CN-ROMP was obtained using preparative gel permeation chromatography performed on a LabACE LC-5060 recycling preparative HPLC containing refractive index and ultraviolet detectors and equipped with a JAIGEL-2.5HR column from Japan Analytical Industry. All runs were performed in HPLC-grade chloroform at a flow rate of 10 mL min^{-1} at room temperature. Molecular weight and dispersity of the copolymers was obtained using an Agilent 1260 Infinity system with a guard column (Agilent PLgel; 5 μm; 50 x 7.5 mm) and three analytical columns (Agilent PLgel; 5 µm; 300 x 7.5 mm; 10^5, 10^4, and 10^3 Å pore sizes). The instrument was calibrated with polystyrene standards between 1.7 and 3150 kg mol^{-1}. All runs were performed in HPLC-grade tetrahydrofuran at 1.0 mL min^{-1} flow rate and 35°C. Molecular weight values were calculated using ChemStation GPC data analysis software (Rev. B.01.01) based on the refractive index signal.

3.5.4 Thermal characterization

The thermal stability of the copolymers was evaluated under nitrogen atmosphere (Airgas, ultra-high purity grade) using a TGA 550 from TA Instruments. Heating ramp speed was set to 10°C min^{1} between room temperature and 900°C. Differential scanning calorimetry (DSC) measurements were performed on a DSC 250 from TA Instruments using a heating and cooling rate of 10°C min^{-1} from 26–300°C. Glass transition temperatures were determined using the last trace of the cyclic heating cycle. Dynamic mechanical analysis (DMA) measurements were performed on a DMA Q850 from TA Instruments with the oscillation temperature ramp mode at a frequency of 1 Hz, 20 μm amplitude, and heating rate of 3°C min^{-1} between 26–300°C. Film samples of 5.3 mm x 15 mm x 0.05 mm dimensions were prepared for testing.

3.5.5 Physical Characterization

The physical packing structure of the copolymers was evaluated with wide-angle X-ray scattering (WAXS). WAXS measurements were collected on a SAXSLAB instrument equipped with a DECTRIS PILATUS 300K detector and a Rigaku 002 microfocus X-ray source. Each measurement was taken under 0.08 mbar vacuum for 300 s in the 3–70 Å range. Measurements were taken from the forward direction of radiation as a function of scattering angle, 2θ. The scattering profile was normalized to a wavelength independent scale through conversion to momentum transfer, q:

$$q = 4\pi \sin\theta/\lambda \tag{3.1}$$

Where θ is $\frac{1}{2}$ the scattering angle and λ is the wavelength in Ångstroms. The d-spacing, d, is then calculated from the relation shown in Equation 3.2.

$$q = 2\pi/d \tag{3.2}$$

Density of films

A 5 mm hollow steel punch (General Tools MFG. Co. Inc.) was used to produce 3–5 circular films with 5 mm diameter. The film thickness was measured using a micrometer and the volume of each film was calculated as the volume of a cylinder. Each film was weighed using a microbalance. Density was calculated by dividing the weight by the volume of each film.

Pure-gas sorption

Sorption isotherms for CH_4 and CO_2 were measured at 35°C up to 48 bar by an automated pressure decay method using a dual volume and dual transducer sorption system from Maxwell Robotics. Approximately 130–145 mg of polymer film was loaded into the sample cell and sealed with a VCR gasket. Each sample was degassed for at least 15 hours at 35 °C before beginning an experiment. The system was also degassed for 4 hours when switching between CH_4 and CO_2. Equilibrium hold times for each pressure step were set to 1.5 h for CH_4 and 0.8 h for CO_2. We report fugacity based on the second virial equation of state to correct for nonidealities [116].

The amount of moles sorbed into the polymer was determined for each equilibrium fugacity point using a mole balance between the initial and equilibrium conditions [48]. Isotherms were then fitted using the dual-mode sorption (DMS) model:

$$C = k_D f + \frac{C_H^{'} b f}{1 + b f} \tag{3.3}$$

where C is the concentration of gas in the polymer ($\mathrm{cm}^3_{\mathrm{STP}}\ \mathrm{cm}^{-3}_{\mathrm{pol}}$, f is the equilibrium fugacity (atm), k_D is Henry's constant ($\mathrm{cm}^3_{\mathrm{STP}}\ \mathrm{cm}^{-3}_{\mathrm{pol}}\ \mathrm{atm}^{-1}$), $C_H^{'}$ is the Langmuir capacity constant ($^3_{\mathrm{STP}}\ \mathrm{cm}^{-3}_{\mathrm{pol}}$), and b is the Langmuir affinity constant (atm^{-1}). The fit was performed via a nonlinear optimization using the χ^2 parameter as the objective function, and uncertainties used for the χ^2 parameter were determined from error propagation. Each gas–polymer pair was optimized independently. Error for k_D, $C_H^{'}$, and b were determined by varying each parameter (while all other parameters are fixed) about a quadratic estimation of χ^2 with respect to the varied parameter [119], [120].

The sorption coefficient can be calculated by dividing the concentration by the corresponding fugacity:

$$S = \frac{C}{f} = k_D + \frac{C_H^{'} b}{1 + b f} \tag{3.4}$$

The diffusion coefficient was back-calculated for samples evaluated in equilibrium sorption analysis using the solution–diffusion model [35].

$$D = \frac{P}{S} \tag{3.5}$$

The sorption coefficient at infinite dilution, S_{inf}, can be determined by taking the limit of Equation 3.4 as fugacity approaches zero:

$$\lim_{f \to 0} S = S_{\mathrm{inf}} = k_D + C_H^{'} b \tag{3.6}$$

Error for sorption coefficients and diffusion coefficients calculated from equilibrium sorption analysis were determined using error propagation of the relative errors in k_D, $C_H^{'}$, b, and P.

Pure-gas permeation

An automated constant-volume, variable-pressure permeation system from Maxwell Robotics was used to collect pure-gas permeation measurements of samples. Polymer films 50–98 μm were cut and glued to the edges of a hole in the center of a brass disk using epoxy glue (Devcon 5 min Epoxy). Once the glue dried, polymer samples were loaded and sealed into a stainless-steel permeation cell, dosed with ~2 bar of helium gas to remove residual gas in the system, and degassed for 8 h at 35°C before beginning an experiment. The permeabilities of He, H_2, CH_4, N_2, O_2, and CO_2 were determined at ~1 bar. For plasticization studies, sample permeabilities were collected for consecutive increasing CO_2 pressures from 1–51 bar. Before switching to a new gas, samples were dosed with ~2 bar of helium and then degassed for at least 1 h.

Pure-gas permeability (P) was calculated using the following equation:

$$P = \frac{V_d l}{p_2 A R T}\left[\left(\frac{dp}{dt}\right)_{ss} - \left(\frac{dp}{dt}\right)_{leak}\right] \tag{3.7}$$

in which V_d is the volume downstream of the film, l is the film thickness, p_2 is the upstream pressure, A is the area of film exposed to the gas, R is the ideal gas constant, T is the absolute experimental temperature, $\left(\frac{dp}{dt}\right)_{ss}$ is the rate of pressure rise in the permeate at steady state, and $\left(\frac{dp}{dt}\right)_{leak}$ is the leak rate [48]. The ideal gas selectivity ($\alpha_{i,j}$) was taken to be the ratio of the pure-gas permeabilities of the more permeable gas, i, to that of the less permeable gas, j (i.e., $\frac{P_i}{P_j}$). The time lag, θ, was determined and diffusion coefficients were calculated using the time-lag method for each gas [36].

$$D = \frac{l^2}{6\theta} \tag{3.8}$$

For He and H_2, the diffusion coefficients were sometimes outside of the acquisition time resolution of the permeation system (approximately 1–2 s), so the diffusion coefficients for these two gases are not reported. Sorption coefficients derived from the time lag were calculated using the sorption–diffusion model [35].

$$S = \frac{P}{D} \tag{3.9}$$

Error was calculated as the standard deviation of triplicate measurements.

3.5.6 Synthesis of monomers

Synthesis of 2,3-bis(bromomethyl)naphthalene (1)

1

2,3-dimethylnaphthalene (500 mg, 3.2 mmol, 2 equiv.), N-bromosuccinimide (NBS, 1.139 g, 6.4 mmol, 2 equiv.), and azobisisobutyronitrile (AIBN, 5 mg, 0.032 mmol, 0.01 equiv.) was charged into a round bottom flask. The flask was degassed and backfilled with argon three times before injecting 10 mL of sparged carbon tetrachloride. The reaction was heated to 80°C under nitrogen overnight. The reaction was then cooled to room temperature and solids were filtered off using a Celite plug rinsed with a small amount of 1:1 toluene/hexanes. The solvent was evaporated and the resultant solid was recrystallized from ~25 mL of 5% toluene/hexanes to give compound **1** as light beige crystals (603 mg, 60% yield). ^{1}H NMR (400 MHz, $CDCl_3$) δ 7.87 (s, 2H), 7.81 (dd, J = 6.2, 3.3 Hz, 2H), 7.52 (dt, J = 6.2, 3.4 Hz, 2H), 4.89 (s, 4H).

Synthesis of 2,3-bis(cyanomethyl)naphthalene (2)

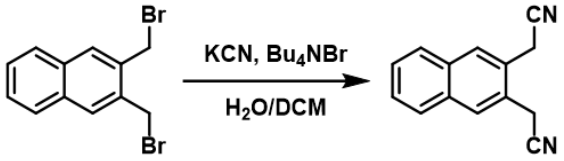

1 2

Compound **1** (7.107 g, 22.6 mmol, 1 equiv.) was dissolved in 110 mL of DCM. Tetrabutylammonium bromide (Bu_4NBr, 1.45 g, 4.52 mmol, 0.2 equiv.) was added followed by 110 mL of water. Potassium cyanide (KCN, 8.85 g, 136 mmol, 6 equiv.) in 110 mL of water was added to the reaction mixture and stirred at room temperature for 4 h. The solution was diluted with DCM and washed three times with saturated sodium bicarbonate, once with water, and once with brine. The organic phases were collected and dried over sodium sulfate. Solvent was removed *invacuo* to give compound **2** (4.690 g, quantitative yield). ^{1}H NMR (400 MHz, $CDCl_3$) δ 7.96 (s, 2H), 7.87 (dd, J = 6.2, 3.3 Hz, 2H), 7.58 (dd, J = 6.3, 3.2 Hz, 2H), 3.93 (d, J = 0.7 Hz, 4H).

Synthesis of CN-ROMP monomer (3)

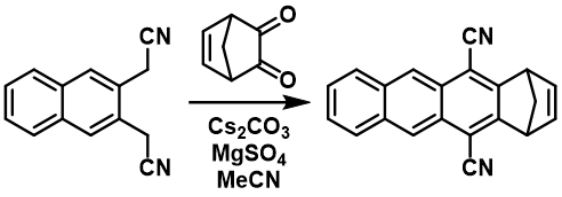

2 3

2,3-dione-5-norbornene was prepared as described in other literature [147]. Compound **2** (4.356 g, 21.12 mmol, 1 equiv.), cesium carbonate (Cs_2CO_3, 15.15 g, 46.5 mmol, 2.2 equiv.), and magnesium sulfate ($MgSO_4$, 10.1 g, 84 mmol, 4 equiv.) was charged into a flame-dried Schlenk flask under argon and then dissolved in 210 mL of MeCN. A solution of 2,3-dione-5-norbornene (3.87 g, 31.7 mmol, 1.5 equiv.) prepared in a vial with 6 mL of MeCN and injected into the Schlenk flask over 10 min. A yellow precipitate formed quickly. The solution was stirred at room temperature overnight. The solids were filtered from the solution through a Celite ®plug, washed with a small portion of MeCN, then eluted with DCM. The DCM was removed in vacuo and the product was recrystallized in acetone to give compound **3** as a yellow solid (2.46 g, 39.8% yield). ^{1}H NMR (400 MHz, $CDCl_3$) δ 8.64 (s, 2H), 8.08 (dd, J = 6.4, 3.3 Hz, 2H), 7.63 (dd, J = 6.4, 3.2 Hz, 2H), 6.87 (t, J = 2.0 Hz, 2H), 4.41 (t, J = 1.9 Hz, 2H), 2.59 (dt, J = 8.6, 1.6 Hz, 1H), 2.40 (d, J = 8.6 Hz, 1H). ^{13}C NMR (101 MHz, $CDCl_3$) δ 155.49, 141.87, 132.83, 128.21, 127.55, 126.40, 125.12, 115.51, 106.34, 77.35, 77.03, 76.72, 63.94, 49.64.

Synthesis of CN-macromonomers (4)

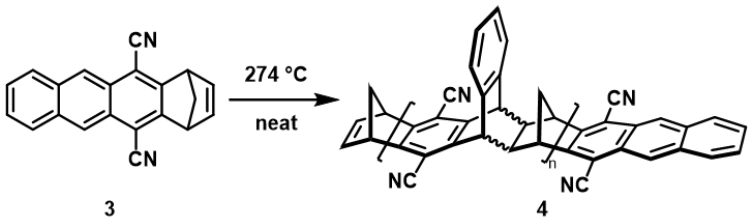

3 4

CN-ROMP monomer (2 g, 6.8 mmol, 1 equiv.) was charged into an oven-dried Schlenk tube. After three cycles of degas and backfill with Argon, the tube was heated to 274°C overnight. The reaction was cooled to room temperature and solids were dissolved in DCM then precipitated in 1:3 methanol/ethanol. Solids were collected via vacuum filtration and dried under vacuum to give polydisperse CN-macromonomers (**4**).

3.5.7 Synthesis of polymers

Synthesis of CN-ROMP

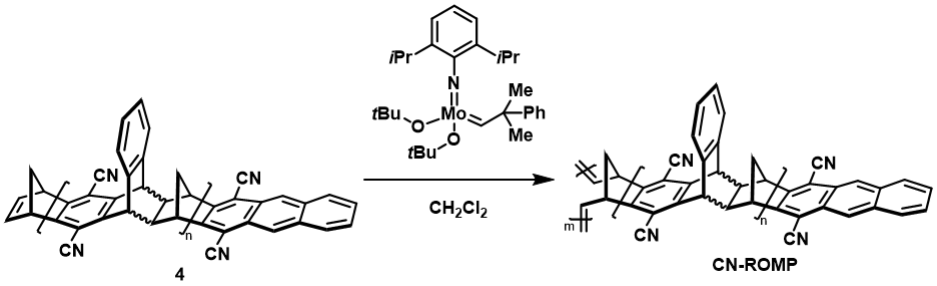

Dried CN-ROMP macromonomers (220 mg, 0.2 mmol, 1 equiv.) were added to an oven-dried vial with stir bar under nitrogen atmosphere in a glovebox. The macromonomers were dissolved in 1.9 mL of anhydrous DCM. Shrock's catalyst (1.1 mg, 0.002 mmol, 0.01 equiv.) was added to a vial in the glovebox and dissolved in 0.3 mL of anhydrous DCM. The catalyst solution was injected into the macromonomer solution and stirred overnight in the glovebox. The solution was quenched with 1 drop of benzaldehyde. CN-ROMP was purified using chloroform preparative GPC. Collected fractions were concentrated in vacuo and precipitated in methanol (100 mg yield).

Synthesis of statistical copolymers NN-3 and NN-13

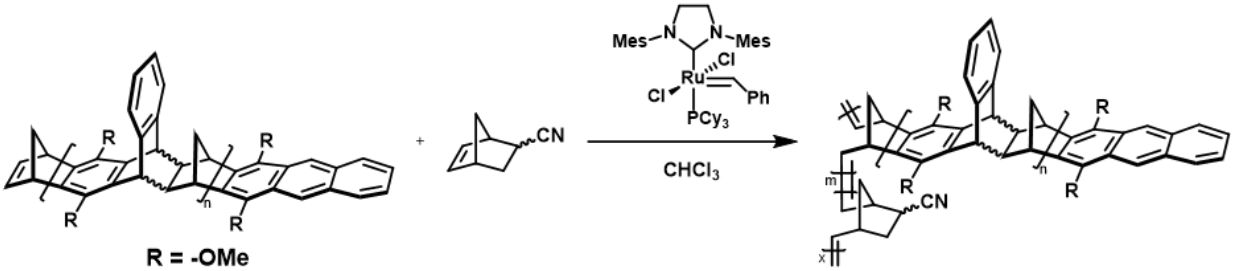

OMe-macromonomers were prepared following previously published procedures [83], [133]. NN-based statistical copolymers NN-3 and NN-13 were prepared using 27.5 wt% and 50 wt% of NN, respectively. An example of the copolymerization procedure follows. A Schlenk flask was charged with the macromonomers (500.7 mg, 0.3 mmol) and sealed. The flask was evacuated and backfilled three times with argon. Solids were dissolved in 15 mL of sparged chloroform. 5-norbornene-2-carbonitrile (0.5 mL, 4.2 mmol) was injected into the Schlenk flask followed by three freeze-pump-thaw cycles. A solution of Grubbs second-generation catalyst (2.547 mg, 0.003 mmol) in 2.5 mL of sparged chloroform was prepared and injected into the flask. The reaction was stirred at room temperature overnight. The reaction was quenched with ethyl vinyl ether and stirred for an additional 30 minutes before diluting with DCM and precipitating in methanol. The resulting NN copolymer was dried under vacuum

overnight (824.3 mg yield).

Synthesis of statistical copolymers N-3 and N-19

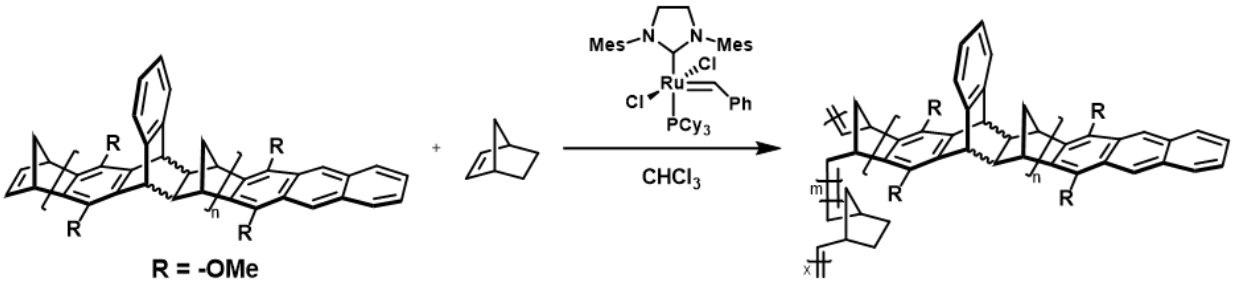

OMe-macromonomers were prepared following previously published procedures [83], [133]. N-based statistical copolymers N-3 and N-19 were prepared using 26.3 wt% and 50 wt% of N, respectively. An example of the copolymerization procedure follows. A Schlenk flask was charged with the macromonomers (494.7 mg, 0.3 mmol) and 2-norbornene (494.7 mg, 5.2 mmol) under argon atmosphere. The monomers were degassed and backfilled with argon three times before dissolving in 15 mL of sparged chloroform. A solution of Grubbs second-generation catalyst (2.687 mg, 0.003 mmol) in 2.5 mL of sparged chloroform was prepared and injected into the flask. The reaction was stirred at room temperature overnight. The reaction was quenched with ethyl vinyl ether and stirred for an additional 30 minutes before diluting with DCM and precipitating in methanol. The resulting N copolymer was dried under vacuum overnight (862.7 mg yield).

Synthesis of block copolymer NNb-24

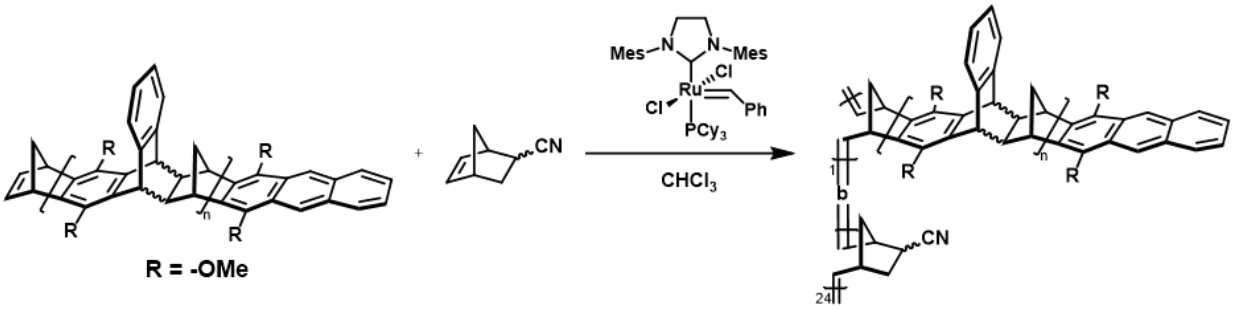

OMe-ROMP macromonomers were prepared following previously published procedures [83], [133]. A Schlenk flask charged with the macromonomers (614.1 mg, 0.49 mmol, 1.0 equiv.) was transferred into a glovebox under nitrogen atmosphere. The macromonomers were dissolved in 18 mL of dry THF before injecting a 2.8 mL THF solution containing Grubbs second generation catalyst (4.160 mg, 0.0049 mmol, 0.01 equiv.) into the flask. After ~15.5 hours, consumption of macromonomers was observed via TLC and 5-norbornene-2-carbonitrile (0.61 mL, 5.1 mmol, 10.41 equiv.) was injected into the flask. The solution

was removed from the glovebox and quenched with ethyl vinyl ether after 20 minutes. The quenched solution stirred for an additional 30 minutes before diluting with DCM and precipitating in methanol. The NN block copolymer was dried under vacuum overnight (818.7 mg yield).

Synthesis of poly(NN)

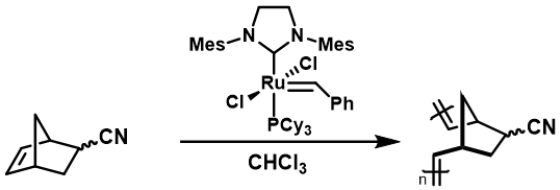

Sparged chloroform (6 mL) was injected into a flame-dried Schlenk flask holding 5-norbornene-2-carbonitrile (0.286 mL, 2.4 mmol). The mixture underwent three freeze-pump-thaw cycles. A solution of Grubbs second-generation catalyst (4.075 mg, 0.005 mmol) in 4 mL of sparged chloroform was injected and the reaction stirred overnight at room temperature. The reaction was quenched with ethyl vinyl ether and stirred for an additional 30 minutes before diluting with DCM and precipitating in methanol. The resulting poly(NN) was dried under vacuum overnight (271.8 mg yield).

Synthesis of poly(N)

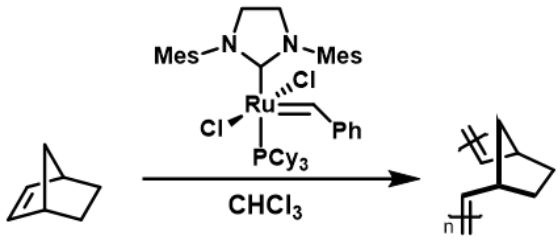

2-Norbornene (226.0 mg, 2.4 mmol) was dissolved in 6 mL of sparged chloroform injected into a flame-dried Schlenk flask under argon atmosphere. A solution of Grubbs second-generation catalyst (4.075 mg, 0.004 mmol) in 4 mL of sparged chloroform was injected and the reaction stirred overnight at room temperature. The reaction was quenched with ethyl vinyl ether and stirred for an additional 30 minutes before diluting with DCM and precipitating in methanol. The resulting N ROMP homopolymer was dried under vacuum overnight (158.6 mg yield).

3.5.8 Chemical, thermal, and physical characterization

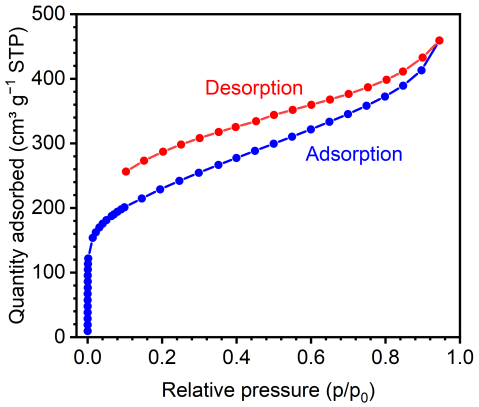

Figure 3.4: BET isotherm of N_2 at 77K for CN-ROMP.

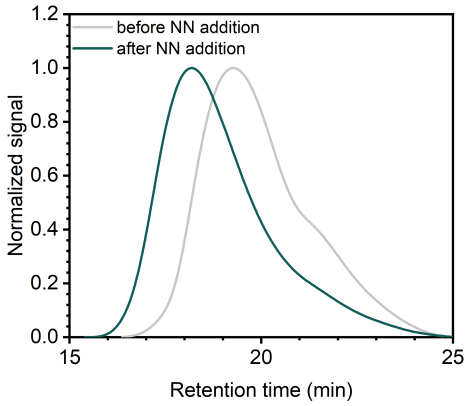

Figure 3.5: Molecular weight distributions of NNb-24 block copolymer.

Table 3.2: Molecular weight information determined by GPC for NN- and N-based copolymers studied. Densities were collected using a geometric method, as outlined in the experimental section.

Polymer	M_n	Đ	ρ (g cm^{-3})
CN-ROMP	77.0	1.2	1.10± 0.01
NN-3	118.0	2.5	/ ±
NN-13	197.1	1.8	1.15± 0.01
NNb-24	159.4	1.8	1.14± 0.06
Poly(NN)	63.2	1.8	/ ±
N-3	174.0	5.5	/ ±
N-19	210.8	1.6	1.04± 0.03
Poly(N)	203.3	1.3	/ ±

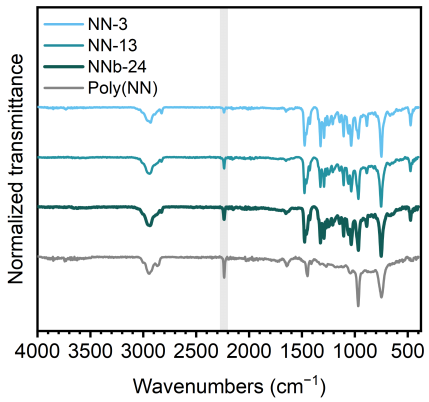

Figure 3.6: FTIR of NN-based statistical copolymers, NN block copolymer and NN homopolymer. The characteristic nitrile peak ~2260 cm^{-1} is highlighted with a reference band.

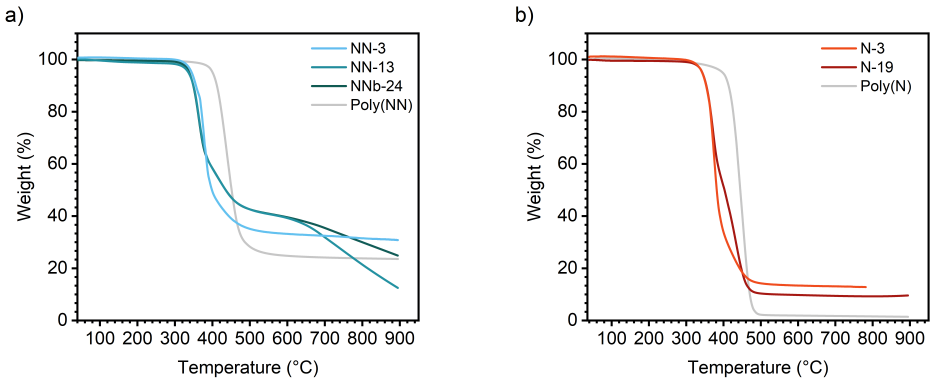

Figure 3.7: Heating curves of TGA for a) NN- and b) N-based copolymers.

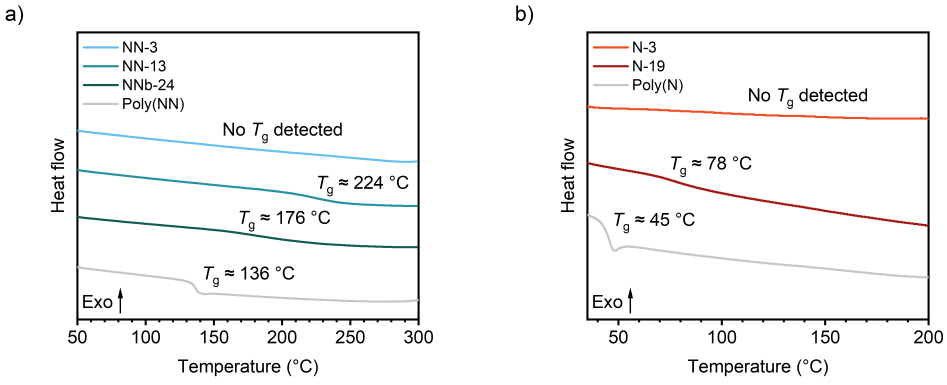

Figure 3.8: Last heating cycle of DSC for a) NN- and b) N-based copolymers.

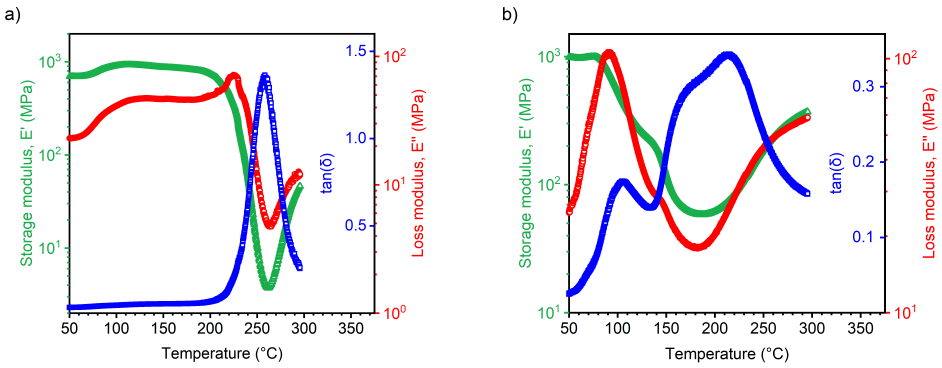

Figure 3.9: Heating curves from DMA of a) NN-13 and b) N-19 copolymers to confirm T_g.

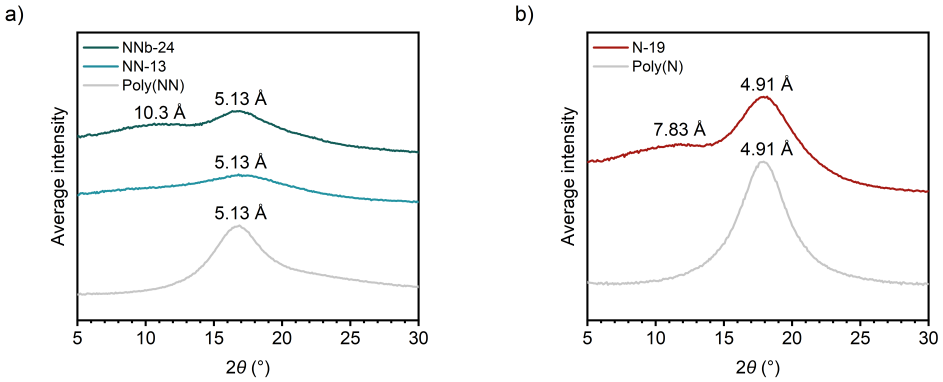

Figure 3.10: WAXS data of a) NN- and b) N-based copolymers. Observed d-spacing values are reported.

3.5.9 Sorption isotherms and dual-mode sorption parameters

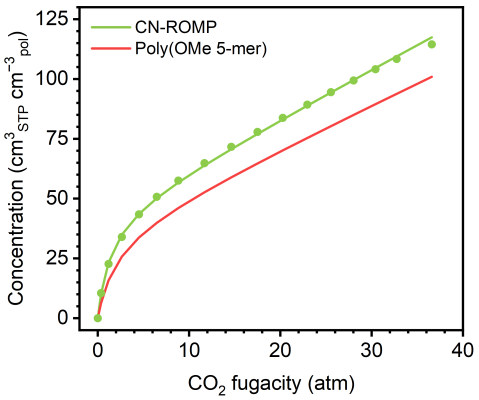

Figure 3.11: Sorption isotherms at 35°C from CO_2 DMS parameter fitting for CN-ROMP and poly(OMe 5-mer) [133]. Experimental data for CN-ROMP is included.

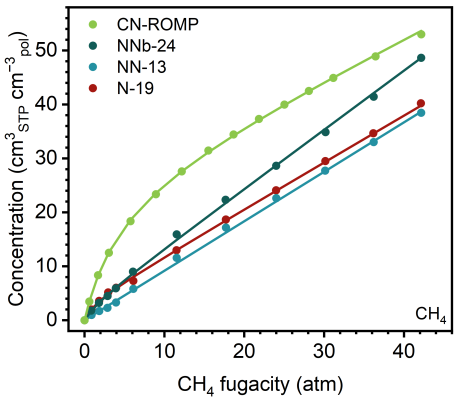

Figure 3.12: CH_4 sorption isotherms at 35°C for CN-ROMP, NNb-24, NN-13, and N-19.

Table 3.3: CO_2 Dual-mode sorption parameters for N-19, NN-13, NNb-24, and CN-ROMP. Data for poly(OMe 5-mer) [133] and PIM-1 [91] is included for comparison. Uncertainties do not account for co-dependencies in coupled parameters, such as b and $C_H^{'}$.

Polymer	b (atm^{-1})	k_D (cm^3_{STP} cm^{-3}_{pol} atm^{-1})	$C_H^{'}$ (cm^3_{STP} cm^{-3}_{pol})
N-19	0.9049±0.0002	1.7213± 0.0003	10.4 ± 0.3
NN-13	2.1939±0.0007	2.0650± 0.0005	7.76± 0.76
NNb-24	1.3306±0.0003	2.2075± 0.0004	12.7 ± 0.8
CN-ROMP	0.7410±0.0001	2.0293± 0.0004	44.75± 0.05
Poly(OMe 5-mer) [133]	0.500 ±/	1.8 ± /	37.0 ± /
PIM-1 [91]	0.518 ±/	3.5 ± /	86.0 ± /

3.5.10 Pure-gas Permeation Data

Table 3.4: Pure-gas permeabilities, diffusion coefficients and sorption coefficients at 1 atm of NN- and N-based copolymers tested. Permeabilities (P) are given in barrer (10^{-10} cm^3_{STP} cm cm^{-2} s^{-1} $cmHg^{-1}$), diffusion coefficients (D) are given in 10^{-8} cm^2 s^{-1}, and sorption coefficients (S) are given in cm^3_{STP} cm^{-3}_{pol} atm^{-1}. Additional significant figures are provided in certain cases to show data that was used in plotting figures. [a]Calculated from DMS parameters.

Permeability					
	NNb-24	NN-13	N-19	NN-3	N-3
P_{He}	51 ±11	37 ±11	45 ±5	152 ±10	109 ±10
P_{H_2}	73 ±24	49 ±14	64 ±6	246 ±14	191 ±17
P_{O_2}	11 ± 4	5 ± 2	11 ±1	38 ± 2	40 ± 4
P_{N_2}	2.7 ± 0.9	1.0 ± 0.3	2.9 ±0.3	9.7 ± 0.8	12 ± 1
P_{CH_4}	3.9 ± 1.4	1.4 ± 0.5	5.5 ±0.6	14 ± 1	22 ± 2
P_{CO_2}	61 ±26	30 ±11	58 ±6	252 ±16	257 ±30
Diffusion Coefficients					
	NNb-24	NN-13	N-19	NN-3	N-3
D_{O_2}	9.0 ± 1.7	5.2 ± 1.2	16 ±6	13 ± 1	25 ±10
D_{N_2}	2.9 ± 0.3	1.54± 0.04	4.0 ±0.4	3.8 ± 0.2	7.6 ± 2.5
D_{CH_4}	0.88± 0.21	0.44± 0.03	1.6 ±0.2	1.24± 0.05	3.2 ± 1.0
	[a]1.5 ± 0.6	[a]1.2 ± 0.4	[a]1.9 ±0.2		
D_{CO_2}	3.2 ± 0.2	1.60± 0.02	5.4 ±0.5	5.5 ± 0.4	13 ± 6
	[a]4.9 ± 2.1	[a]3.2 ± 1.2	[a]6.6 ±0.7		
Sorption Coefficients					
	NNb-24	NN-13	N-19	NN-3	N-3
S_{O_2}	0.94± 0.52	0.84± 0.40	0.58±0.20	2.3 ± 0.3	1.3 ± 0.4
S_{N_2}	0.71± 0.34	0.49± 0.15	0.55±0.06	2.0 ± 0.3	1.3 ± 0.3
S_{CH_4}	3.60± 2.03	2.5 ± 1.0	2.7 ±0.2	9.0 ± 1.0	5.4 ± 1.1
	[a]1.96± 0.32	[a]0.92± 0.01	[a]2.23±0.06		
S_{CO_2}	15.0 ± 7.6	14.6 ± 5.4	8.06±0.04	35.0 ± 5.0	15.6 ± 4.1
	[a]9.4 ± 0.5	[a]7.3 ± 0.5	[a]6.6 ±0.2		

[a]Calculated from DMS parameters.

Table 3.5: Diffusivity selectivity and sorption selectivity at 1 atm and 35°C for each gas tested. Additional significant figures are provided in certain cases to show data that was used in plotting figures. [a]Calculated from DMS parameters.

Polymer	Gas Pair	Diffusivity selectivity		Sorption selectivity	
NN-13	N_2/CH_4	3.5 ±	0.3	0.19±	0.10
	O_2/N_2	3.4 ±	0.8	1.7 ±	0.9
	CO_2/N_2	1.04±	0.03	29 ±	14
	CO_2/CH_4	3.7 ±	0.3	5.7 ±	3.1
		[a]2.7 ±	1.3	[a]8.0 ±	0.6
N-19	N_2/CH_4	2.6 ±	0.4	0.20±	0.03
	O_2/N_2	4.1 ±	1.5	1.1 ±	0.4
	CO_2/N_2	1.4 ±	0.2	15 ±	2
	CO_2/CH_4	3.5 ±	0.6	3.0 ±	0.3
		[a]3.5 ±	0.5	[a]3.0 ±	0.1
NN-3	N_2/CH_4	3.0 ±	0.2	0.22±	0.04
	O_2/N_2	3.3 ±	0.3	1.2 ±	0.2
	CO_2/N_2	1.5 ±	0.1	18 ±	3
	CO_2/CH_4	4.4 ±	0.3	3.9 ±	0.7
N-3	N_2/CH_4	2.4 ±	1.1	0.24±	0.07
	O_2/N_2	3.3 ±	1.7	1.0 ±	0.4
	CO_2/N_2	1.8 ±	0.9	12 ±	4
	CO_2/CH_4	4.2 ±	2.3	2.9 ±	0.9
NNb-24	N_2/CH_4	3.3 ±	0.9	0.20±	0.15
	O_2/N_2	3.1 ±	0.6	1.33±	0.97
	CO_2/N_2	1.1 ±	0.1	21 ±	15
	CO_2/CH_4	3.6 ±	0.9	4.2 ±	3.1
		[a]3.3 ±	1.9	[a]4.8 ±	0.8

[a]Calculated from DMS parameters.

3.5.11 CO_2 high pressure sweeps

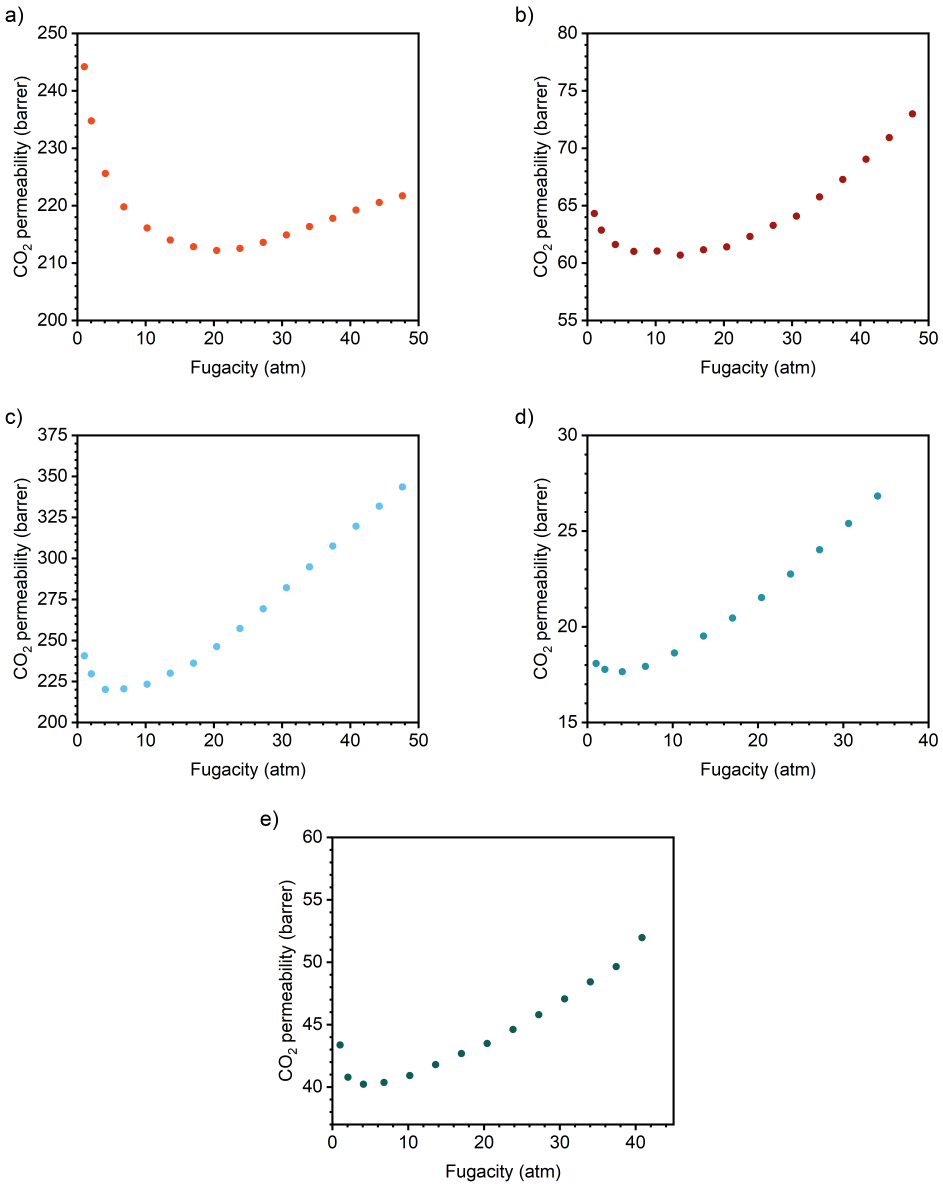

Figure 3.13: Pure-gas CO_2 plasticization of a) N-3, b) N-19, c) NN-3, d) NN-13, and e) NNb-24.

3.5.12 NMR spectra of monomers and polymers

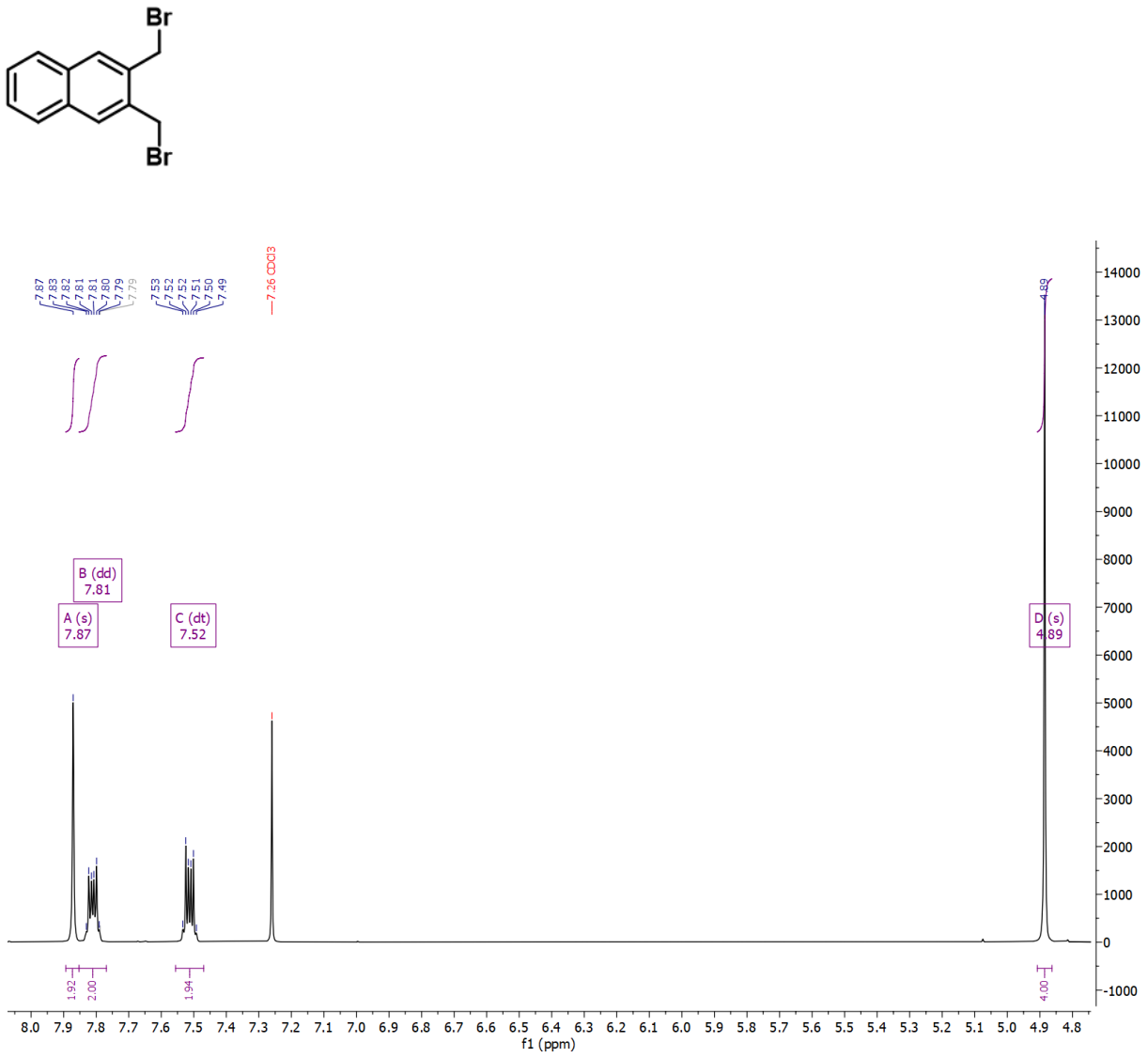

Figure 3.14: ^{1}H NMR spectrum of 2,3-bis(bromomethyl)naphthalene.

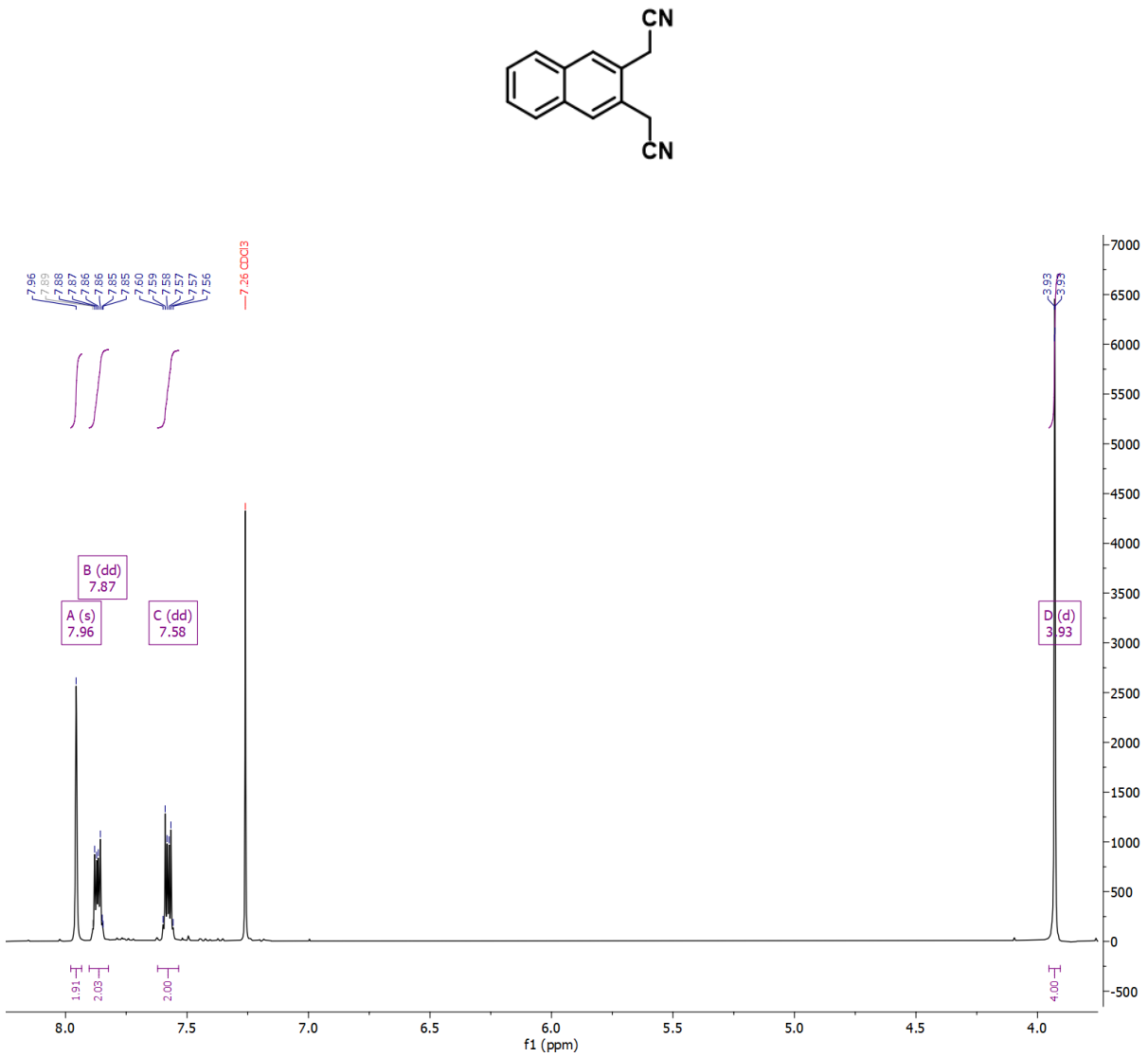

Figure 3.15: ^{1}H NMR spectrum of 2,3-bis(cyanomethyl)naphthalene.

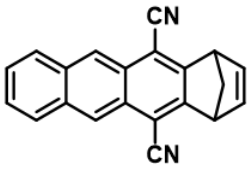
CN
CN

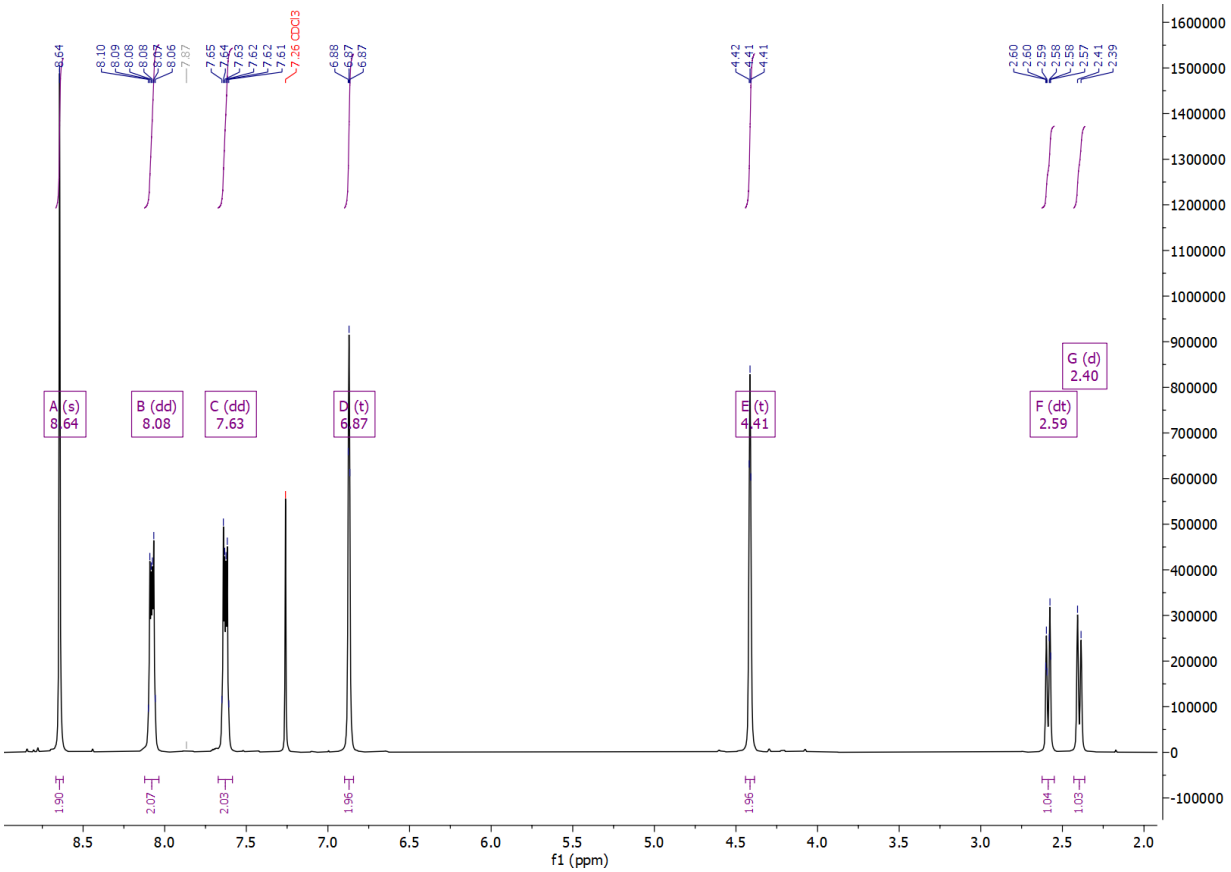

Figure 3.16: ^{1}H NMR spectrum of CN-ROMP monomer.

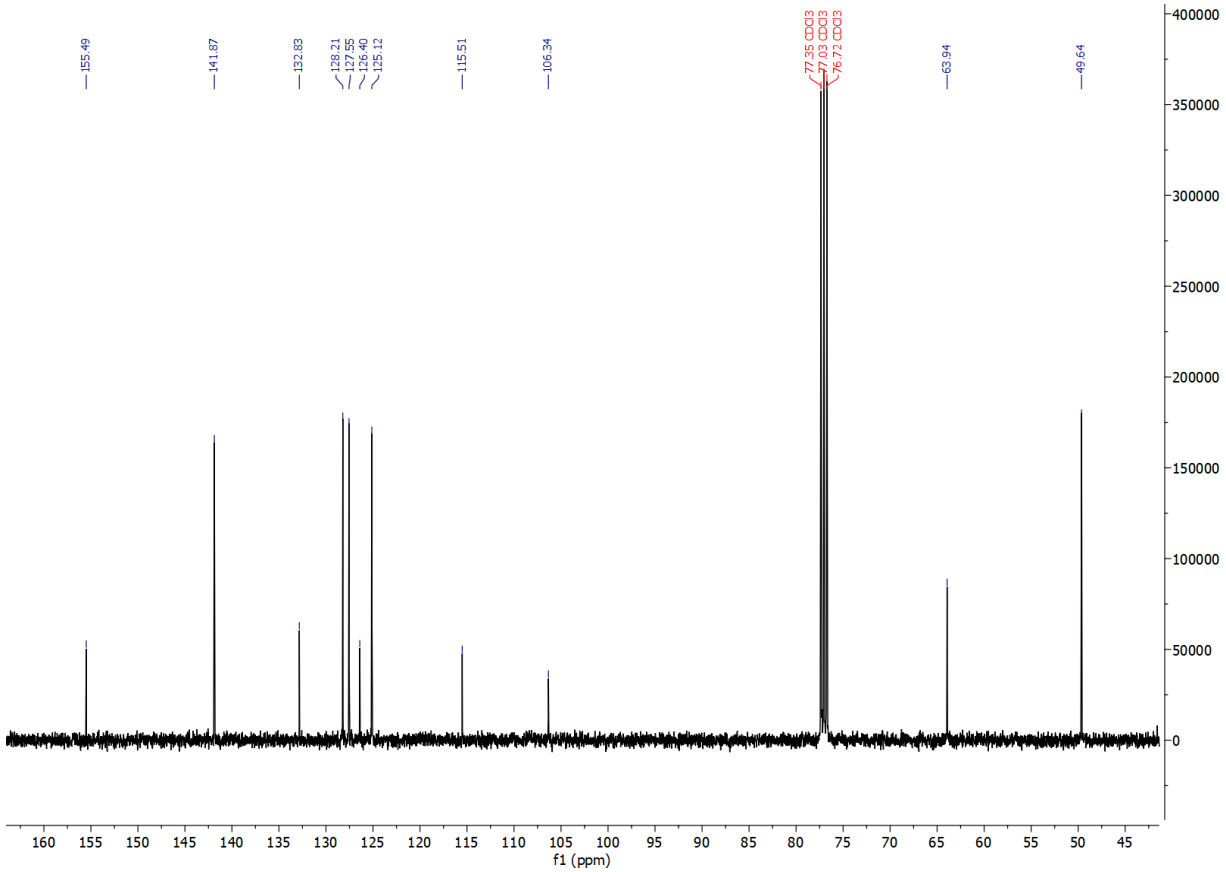

Figure 3.17: ^{13}C NMR spectrum of CN-ROMP monomer.

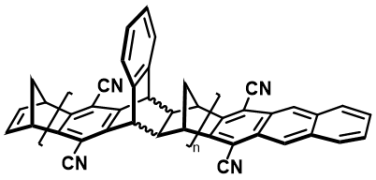
CN
CN
CN
CN
n

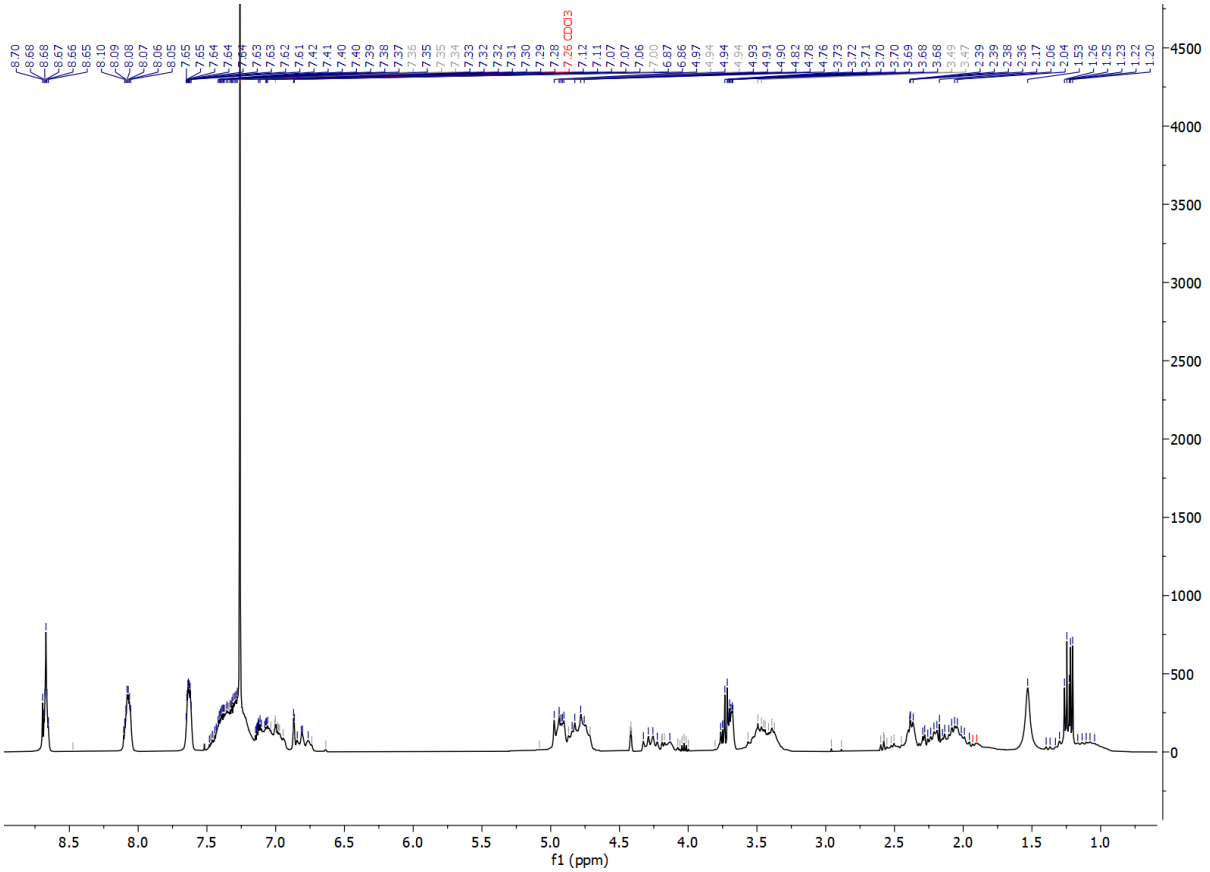

Figure 3.18: ^{1}H NMR spectrum of CN-macromonomers.

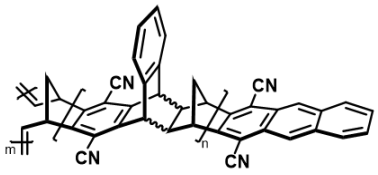
CN
CN
CN
CN
m
n

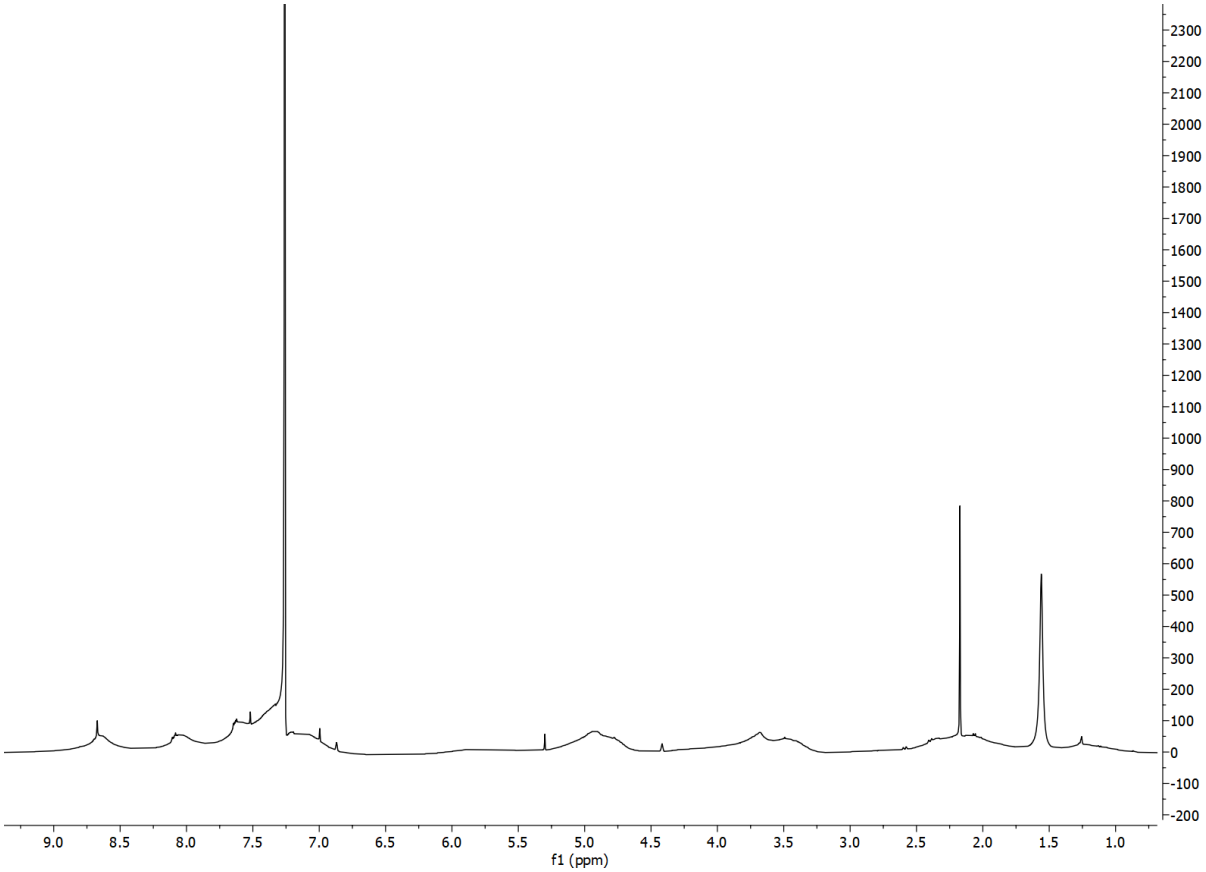

Figure 3.19: ^{1}H NMR spectrum of CN-ROMP.

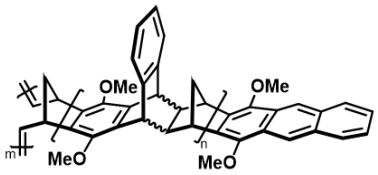
OMe
OMe
MeO
MeO
m
n

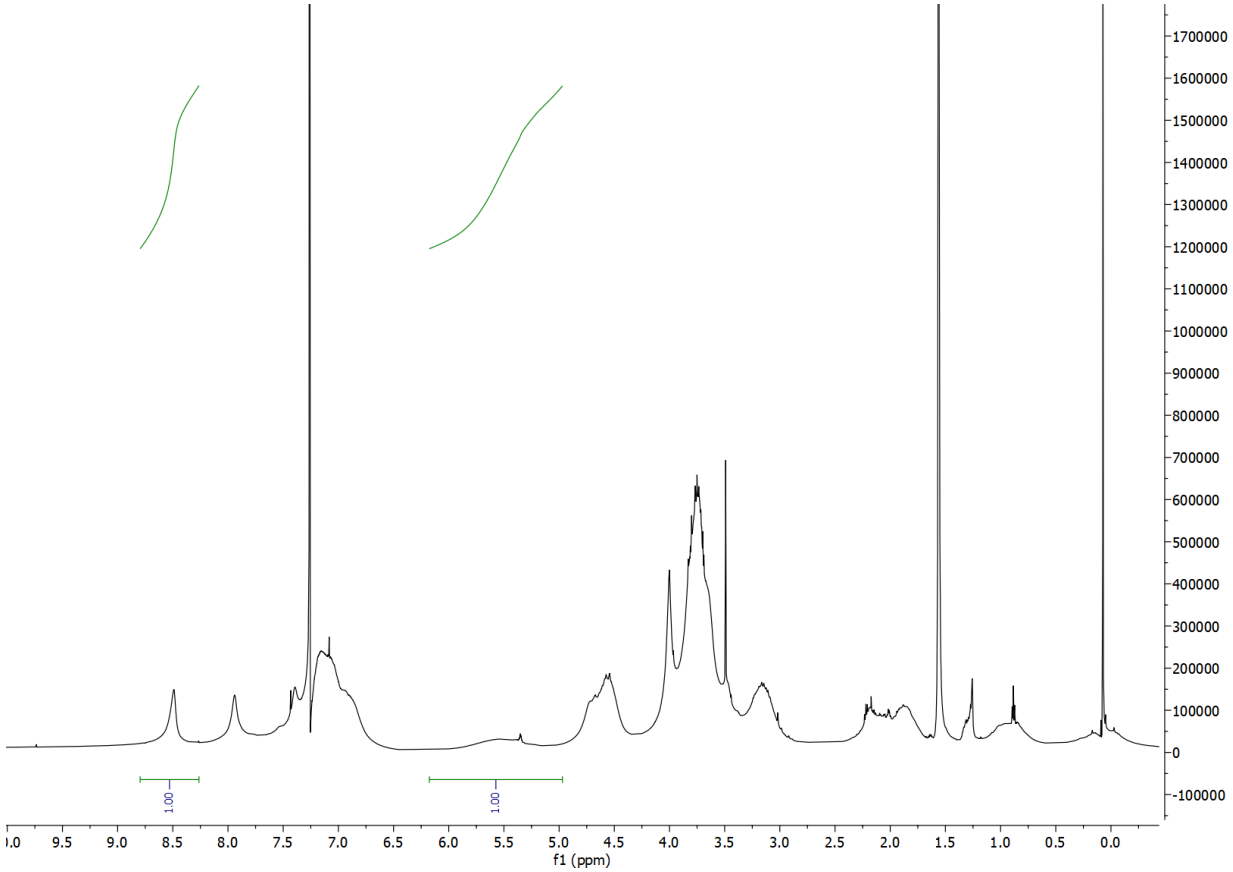

Figure 3.20: ^{1}H NMR spectrum of OMe-ROMP.

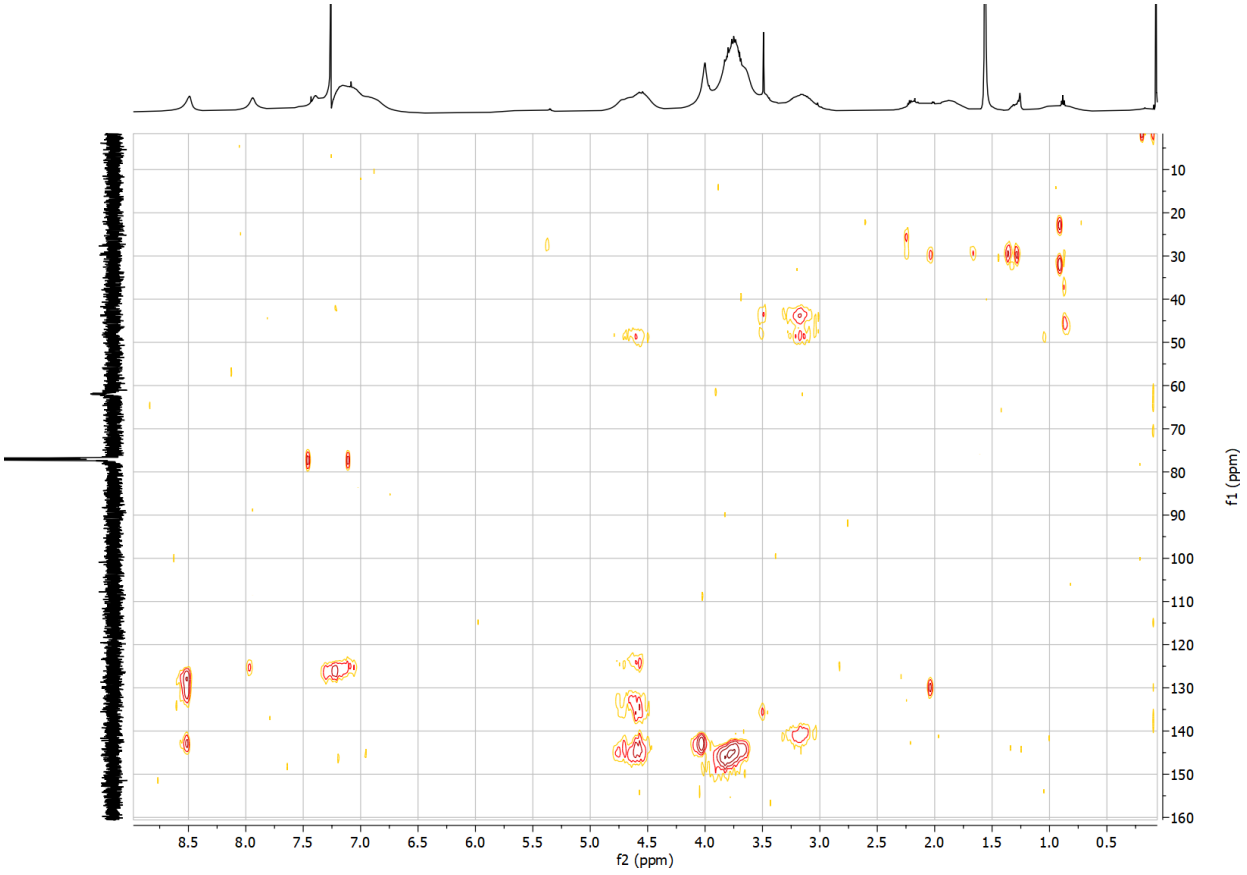

Figure 3.21: HMBC 2D NMR spectrum of OMe-ROMP.

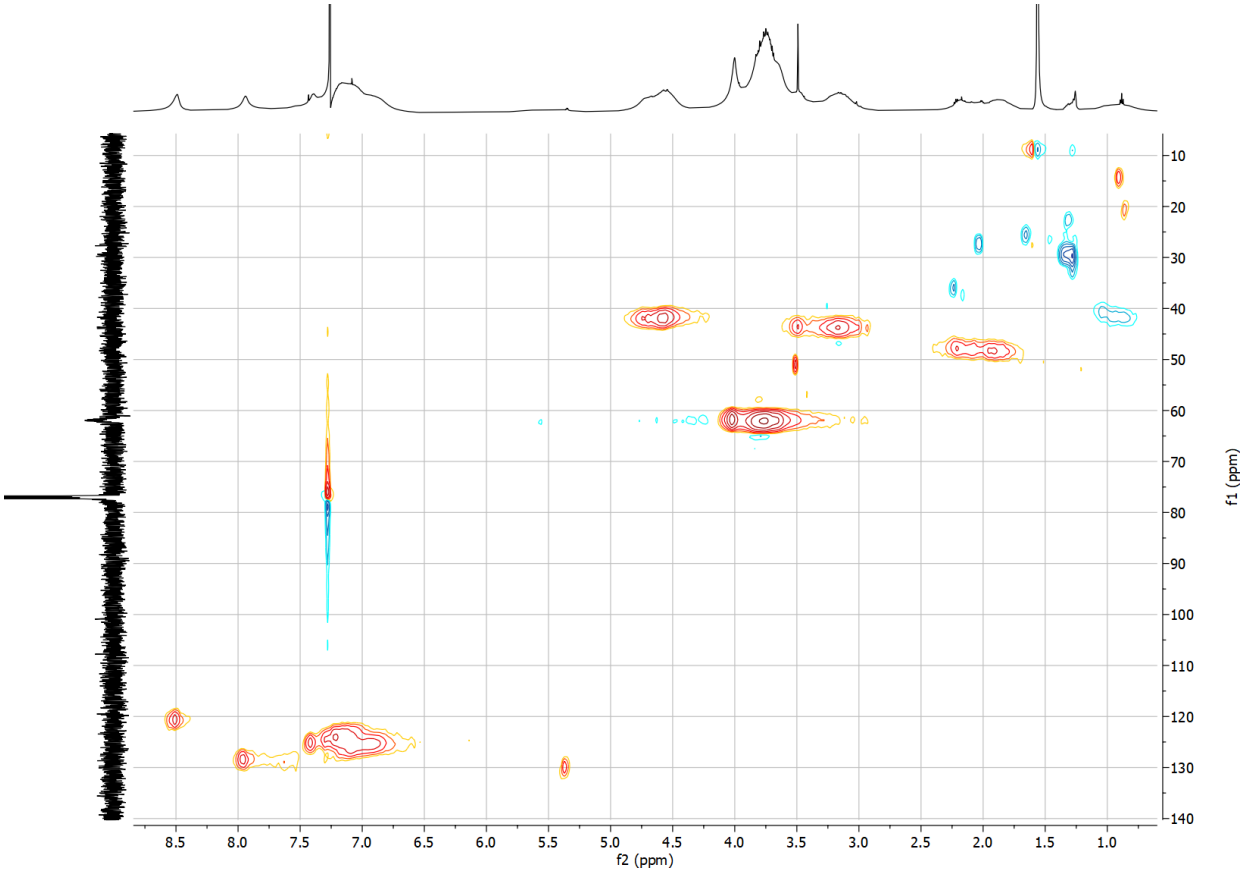

Figure 3.22: HSQC 2D NMR spectrum of OMe-ROMP.

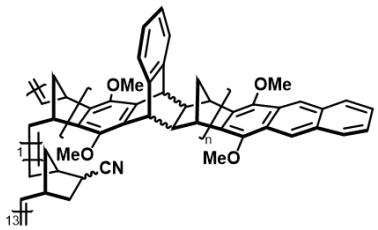
OMe
OMe
MeO
CN
MeO
n
1
13

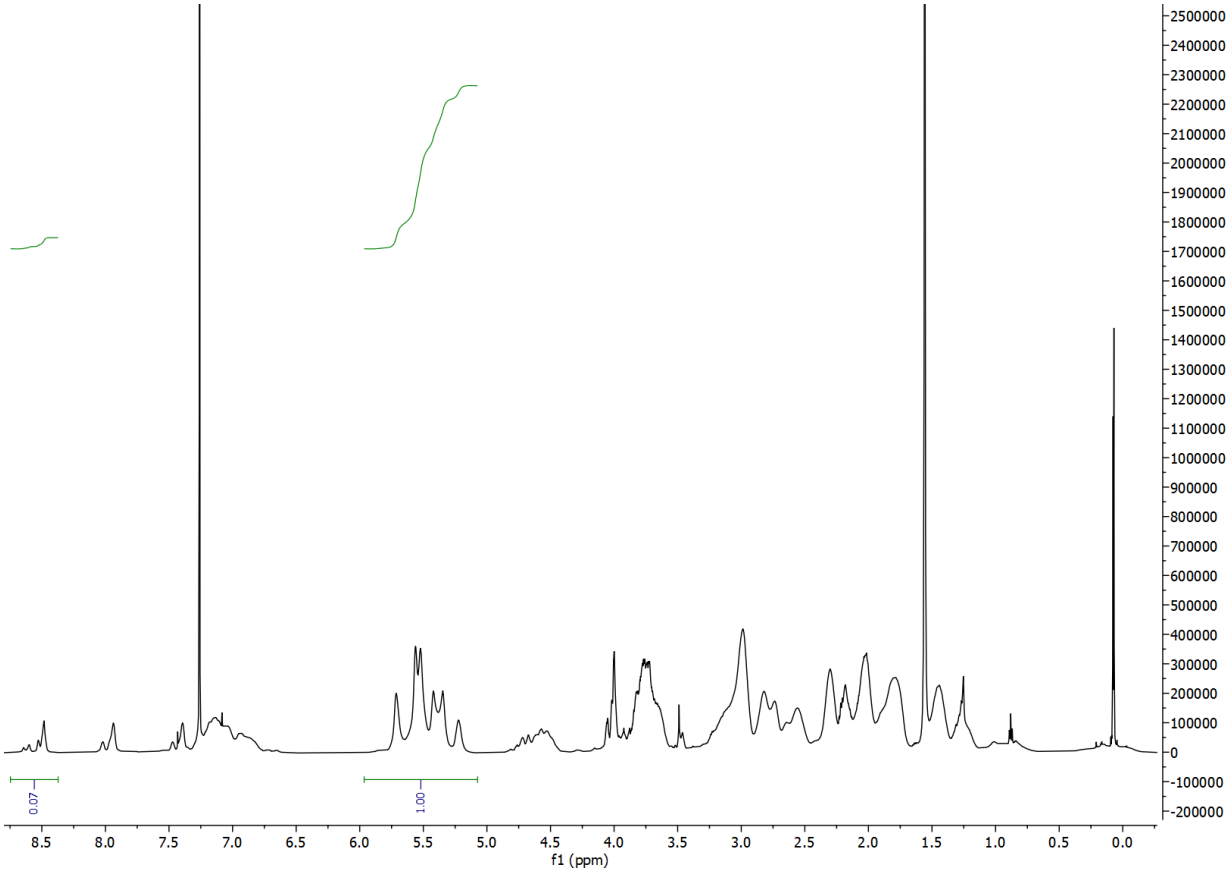

Figure 3.23: ^{1}H NMR spectrum of NN-13 copolymer.

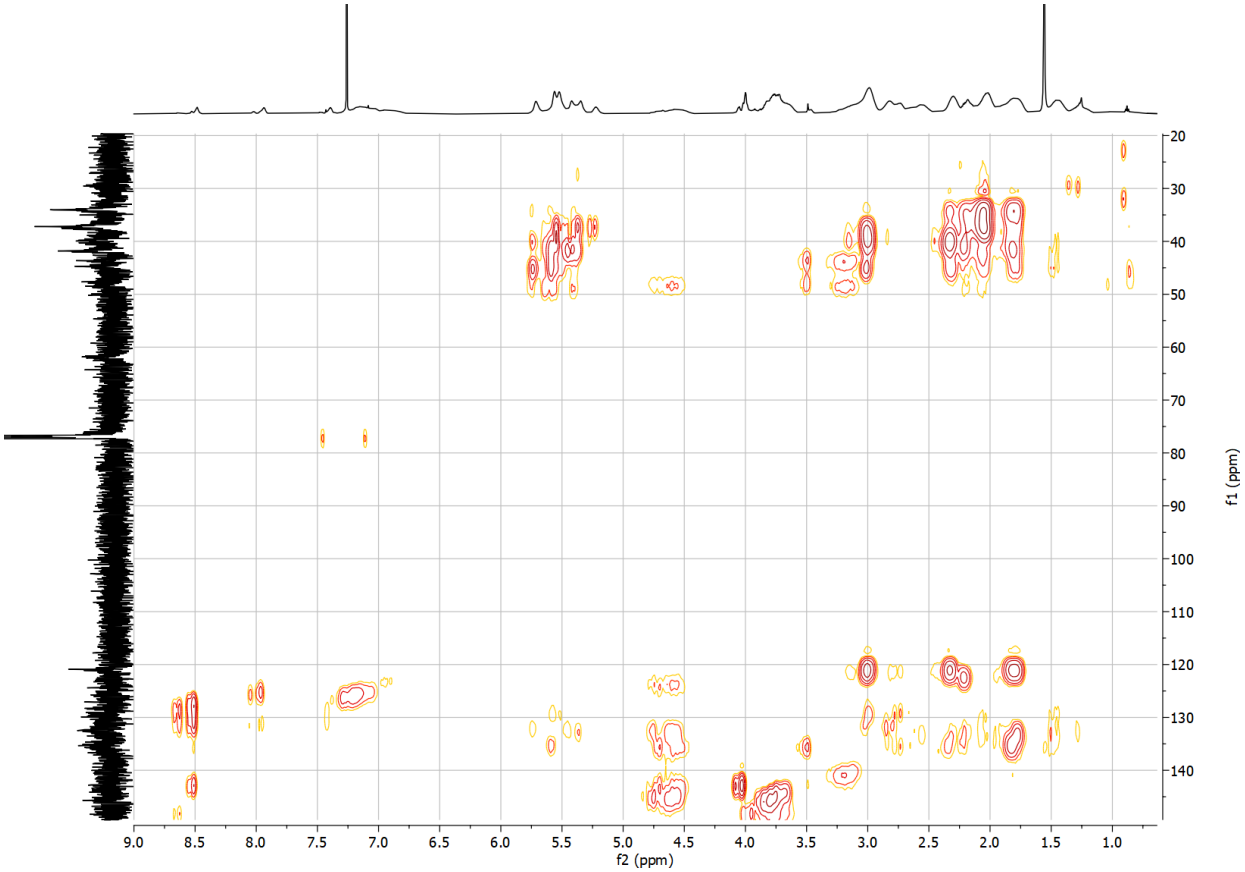

Figure 3.24: HMBC 2D NMR spectrum of NN-13 copolymer.

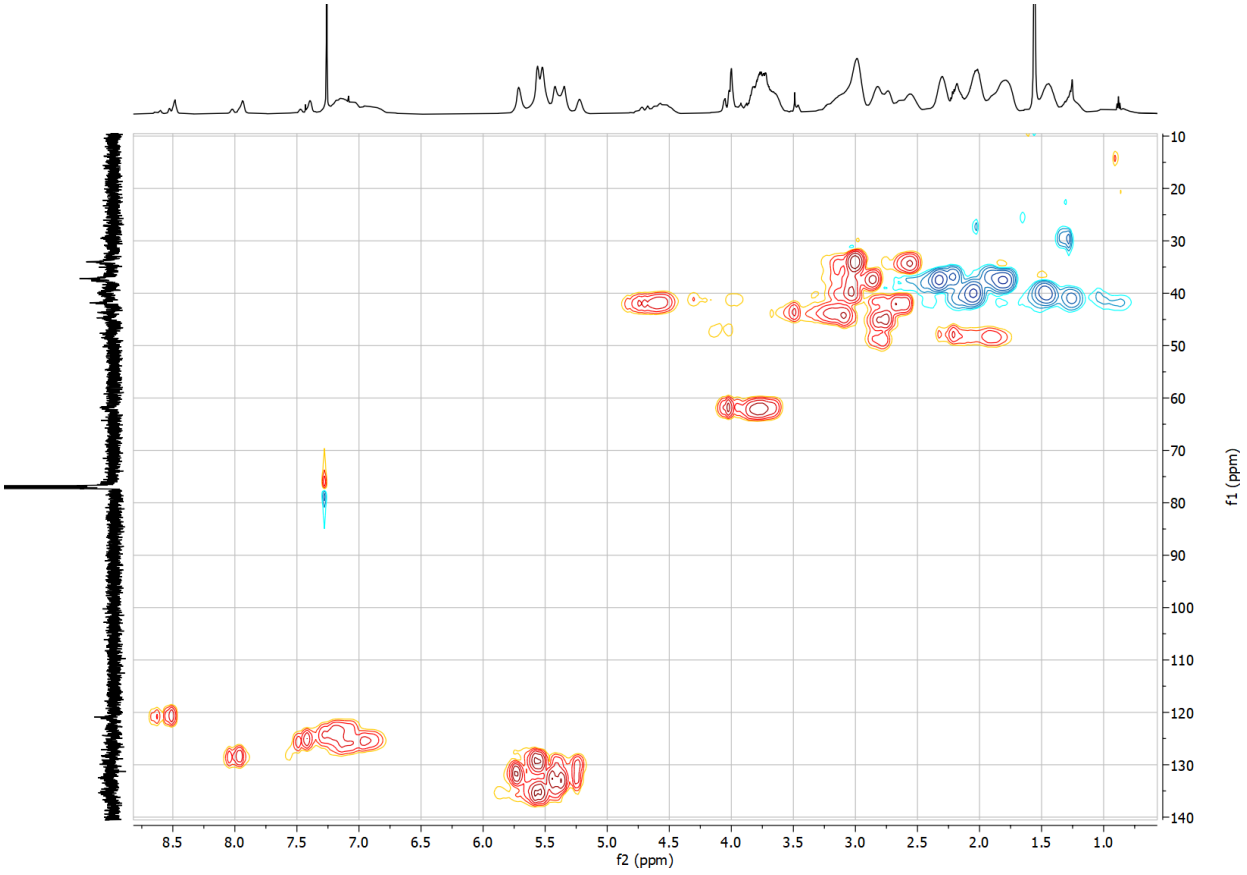

Figure 3.25: HSQC 2D NMR spectrum of NN-13 copolymer.

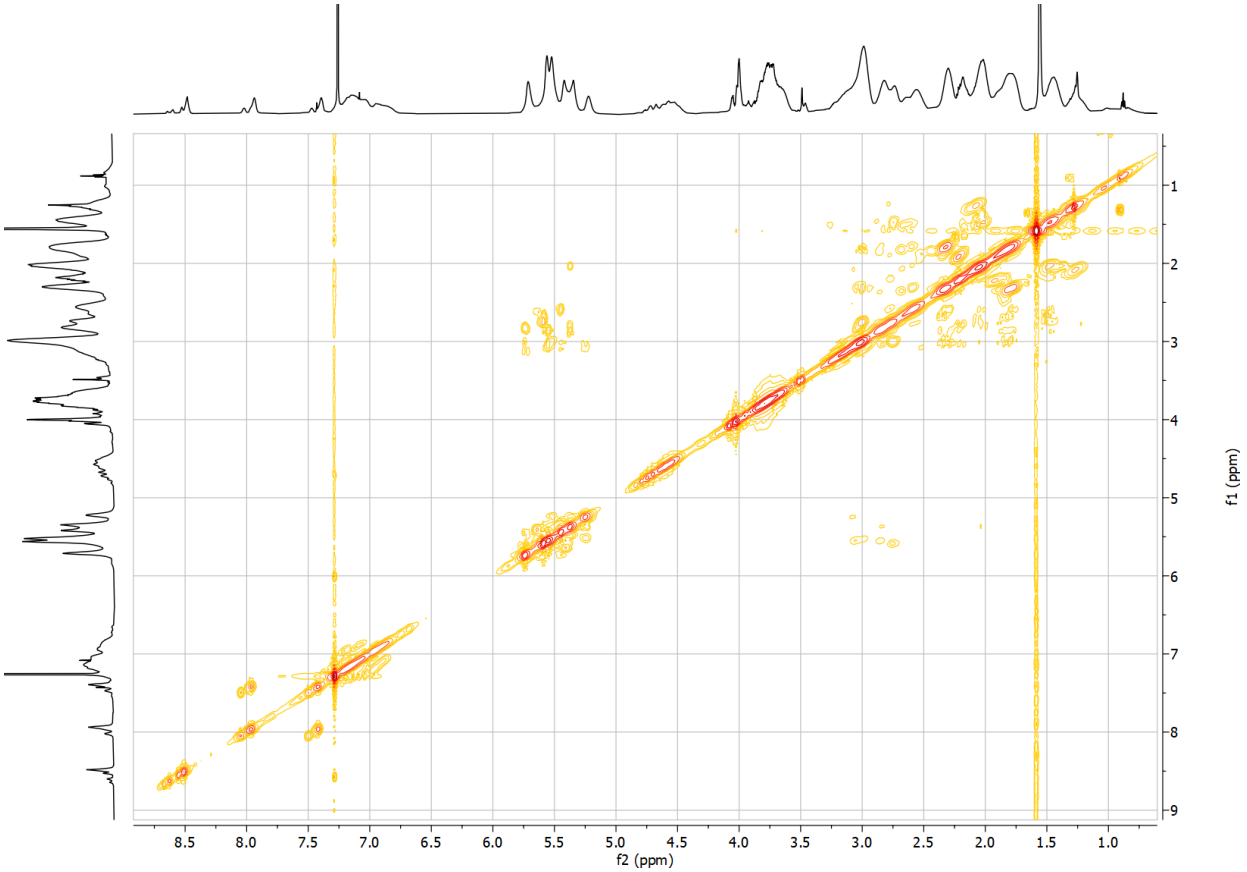

Figure 3.26: COSY 2D NMR spectrum of NN-13 copolymer.

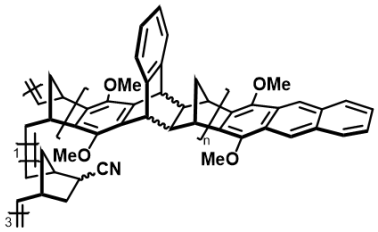
OMe
OMe
MeO
CN
MeO
n

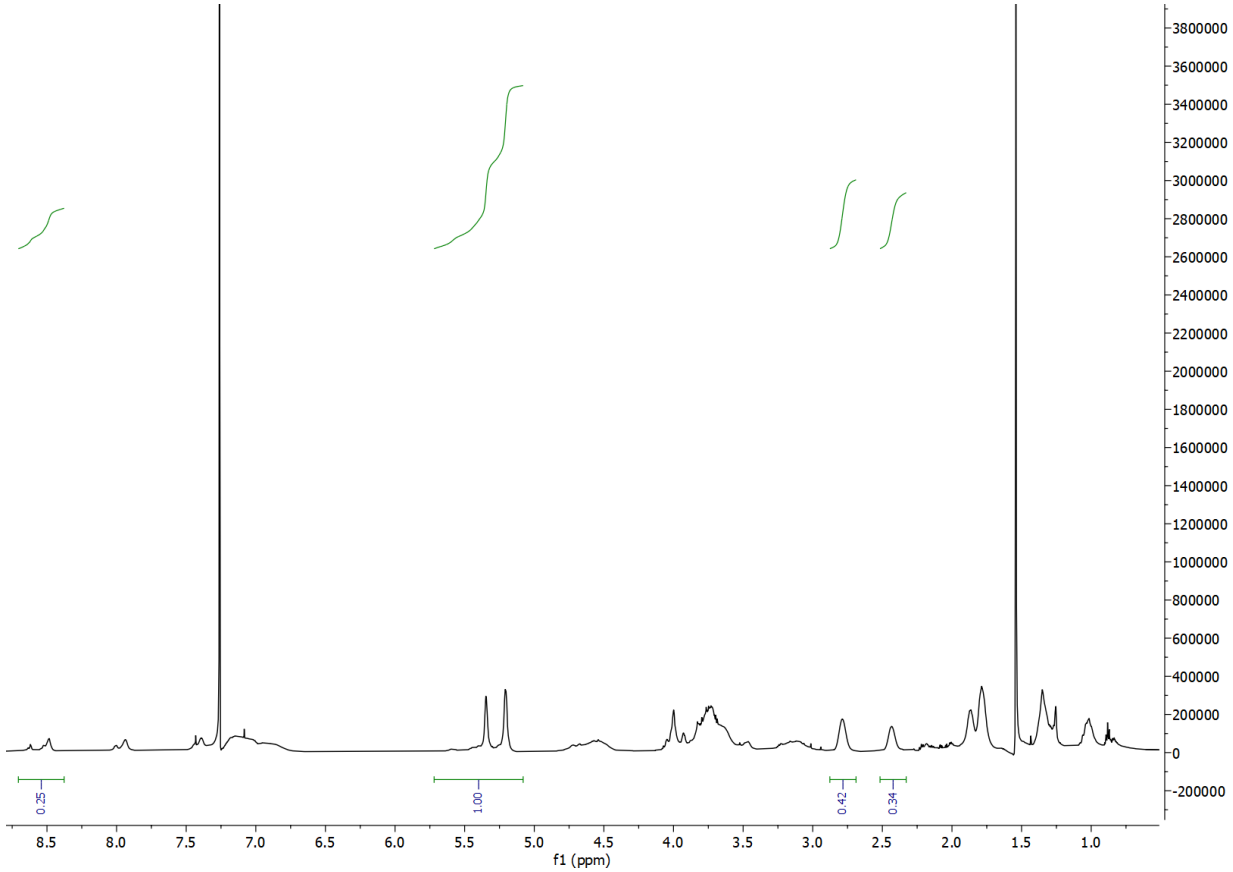

Figure 3.27: ^{1}H NMR spectrum of NN-3 copolymer.

Figure 3.28: HMBC 2D NMR spectrum of NN-3 copolymer.

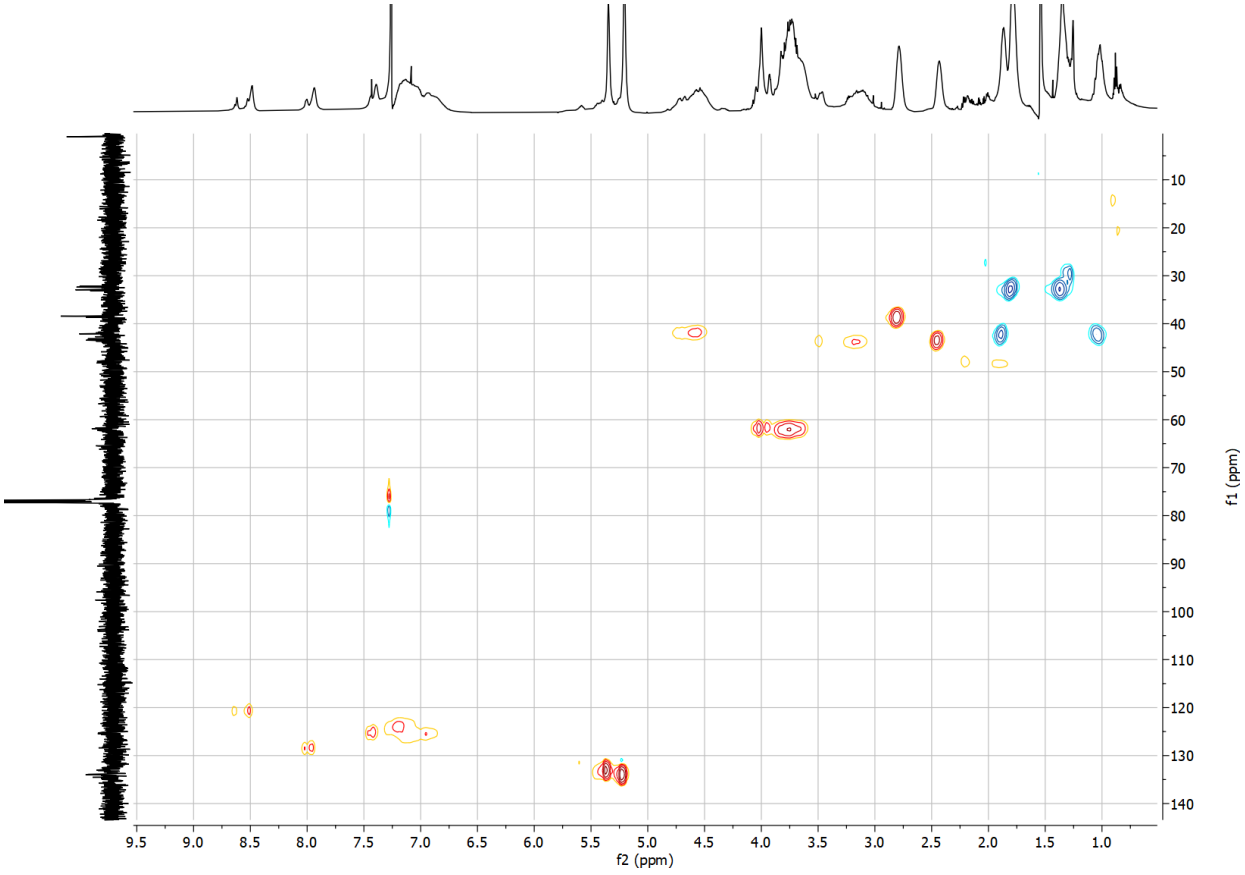

Figure 3.29: HSQC 2D NMR spectrum of NN-3 copolymer.

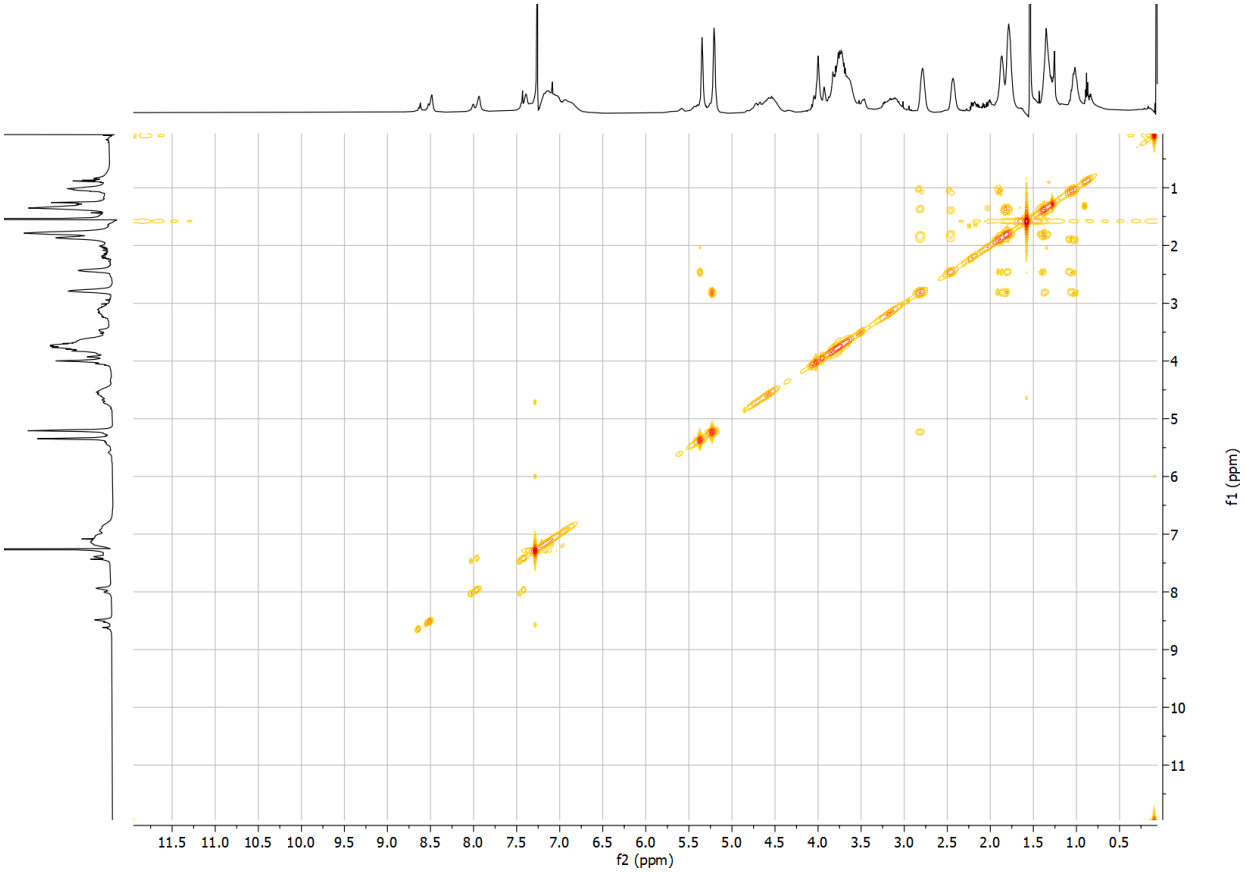

Figure 3.30: COSY 2D NMR spectrum of NN-3 copolymer.

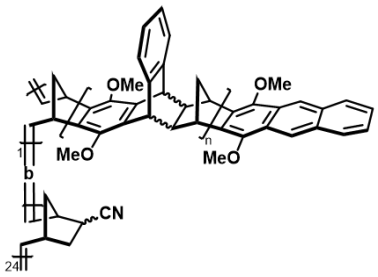
OMe
OMe
MeO
MeO
n
1
b
CN
24

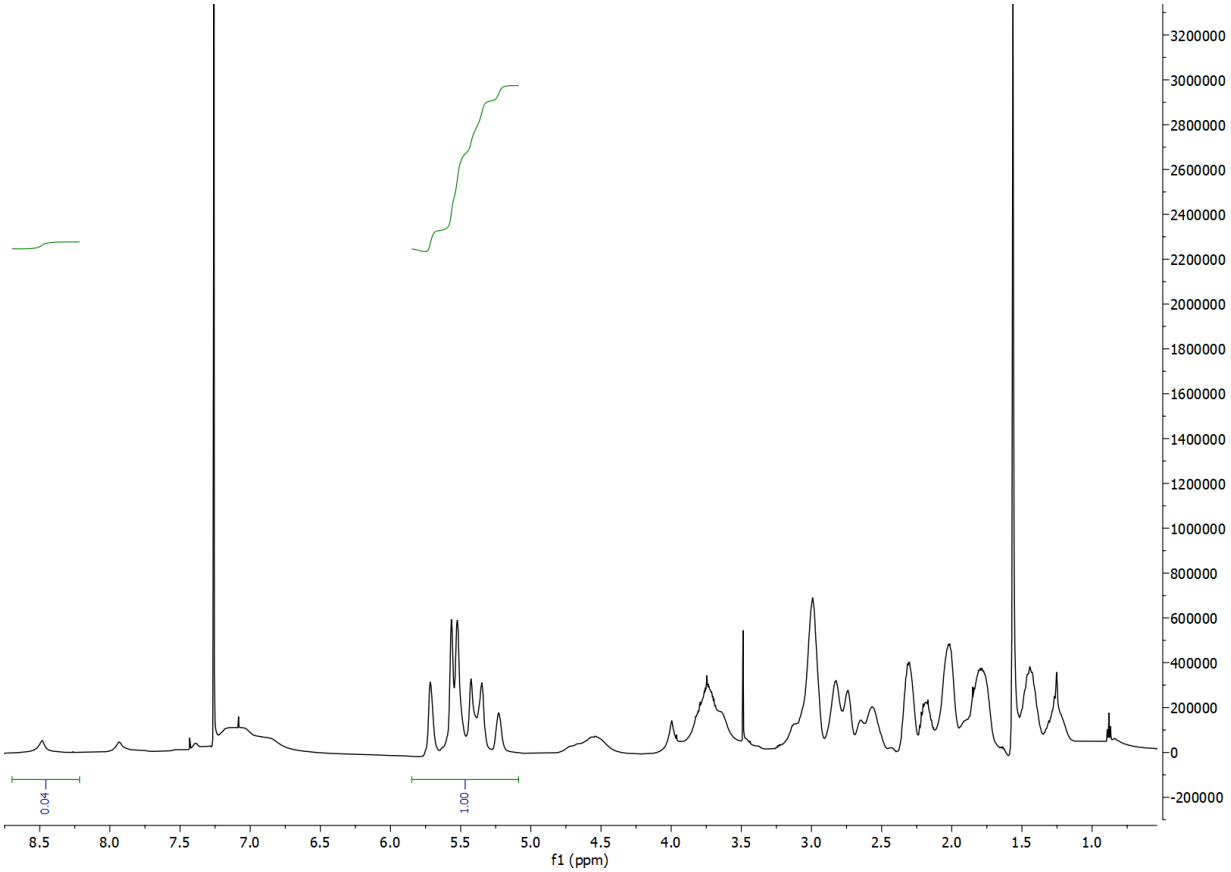

Figure 3.31: ^{1}H NMR spectrum of NNb-24 copolymer.

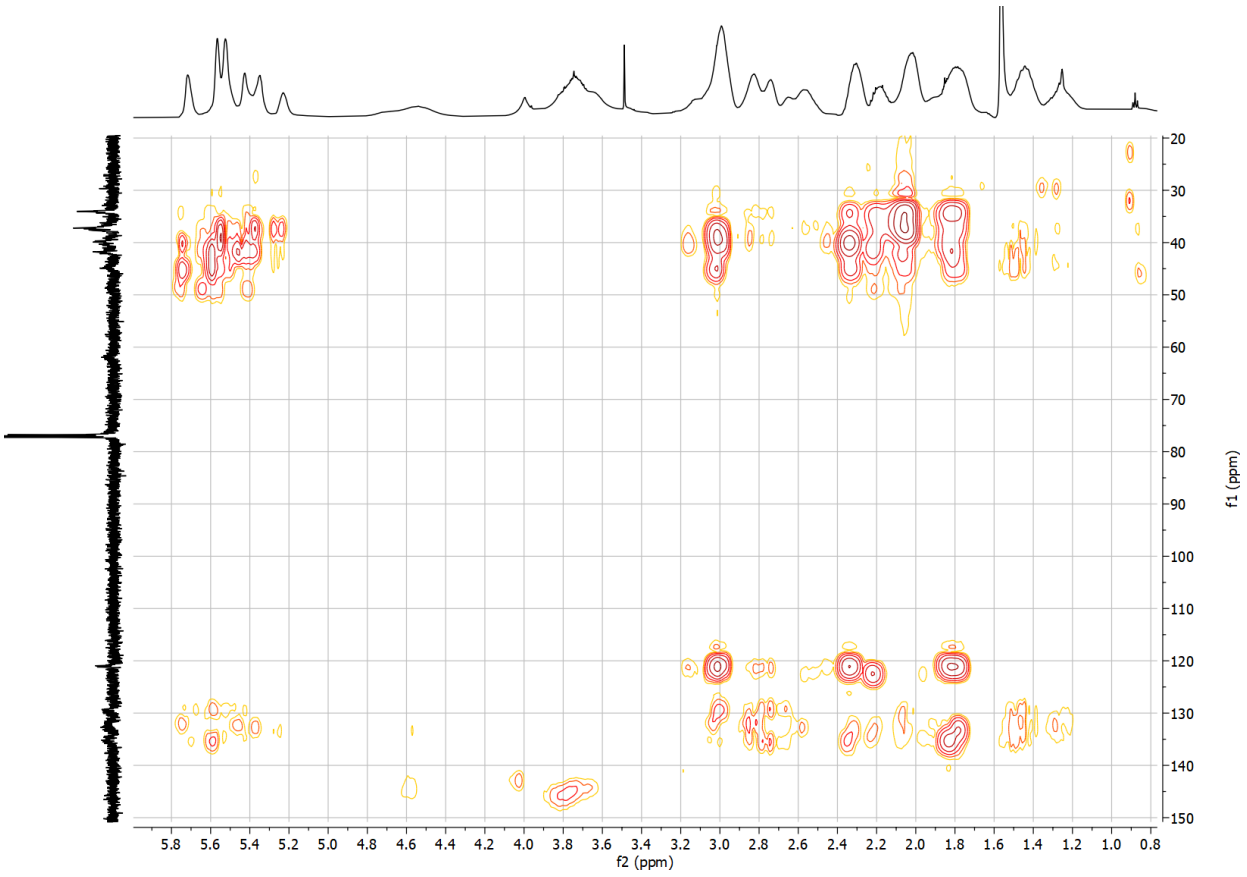

Figure 3.32: HMBC 2D NMR spectrum of NNb-24 copolymer.

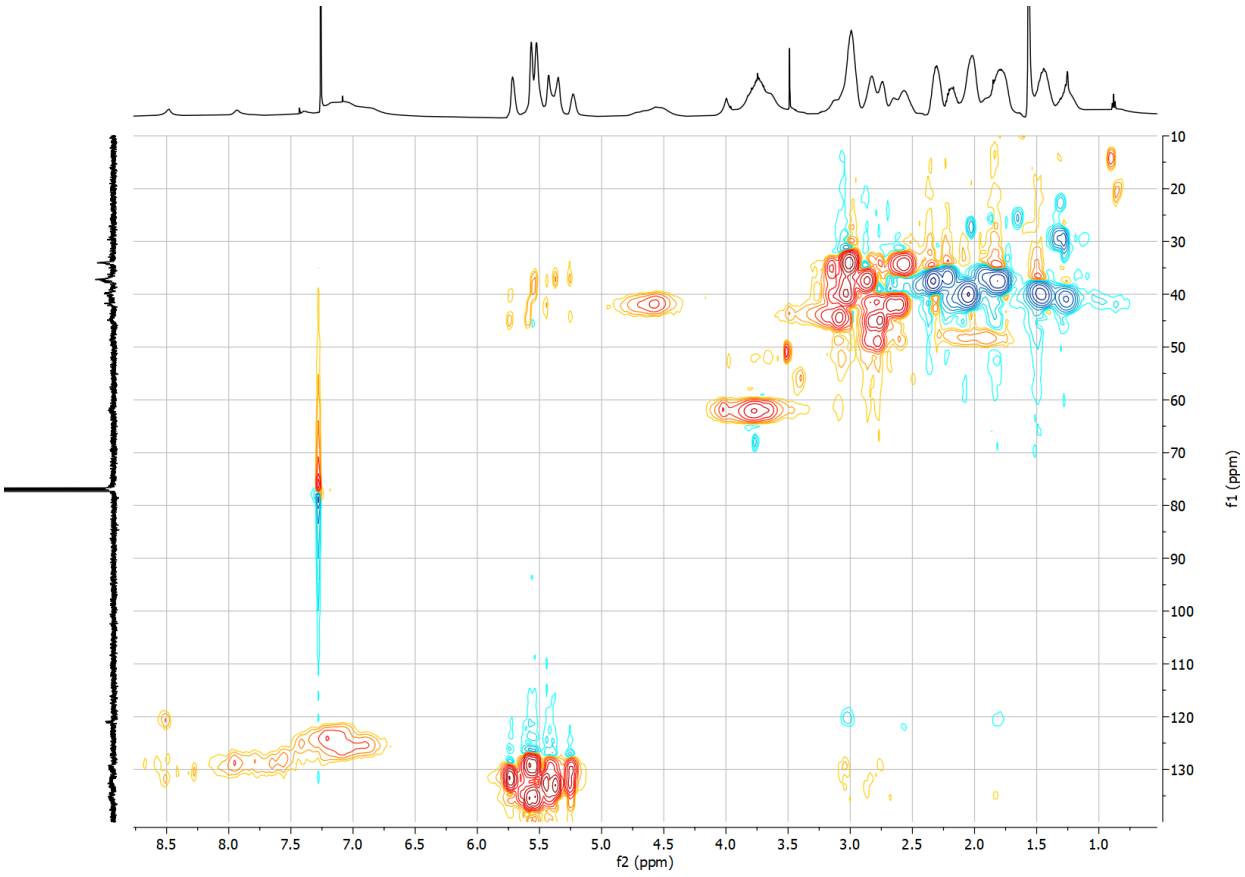

Figure 3.33: HSQC 2D NMR spectrum of NNb-24 copolymer.

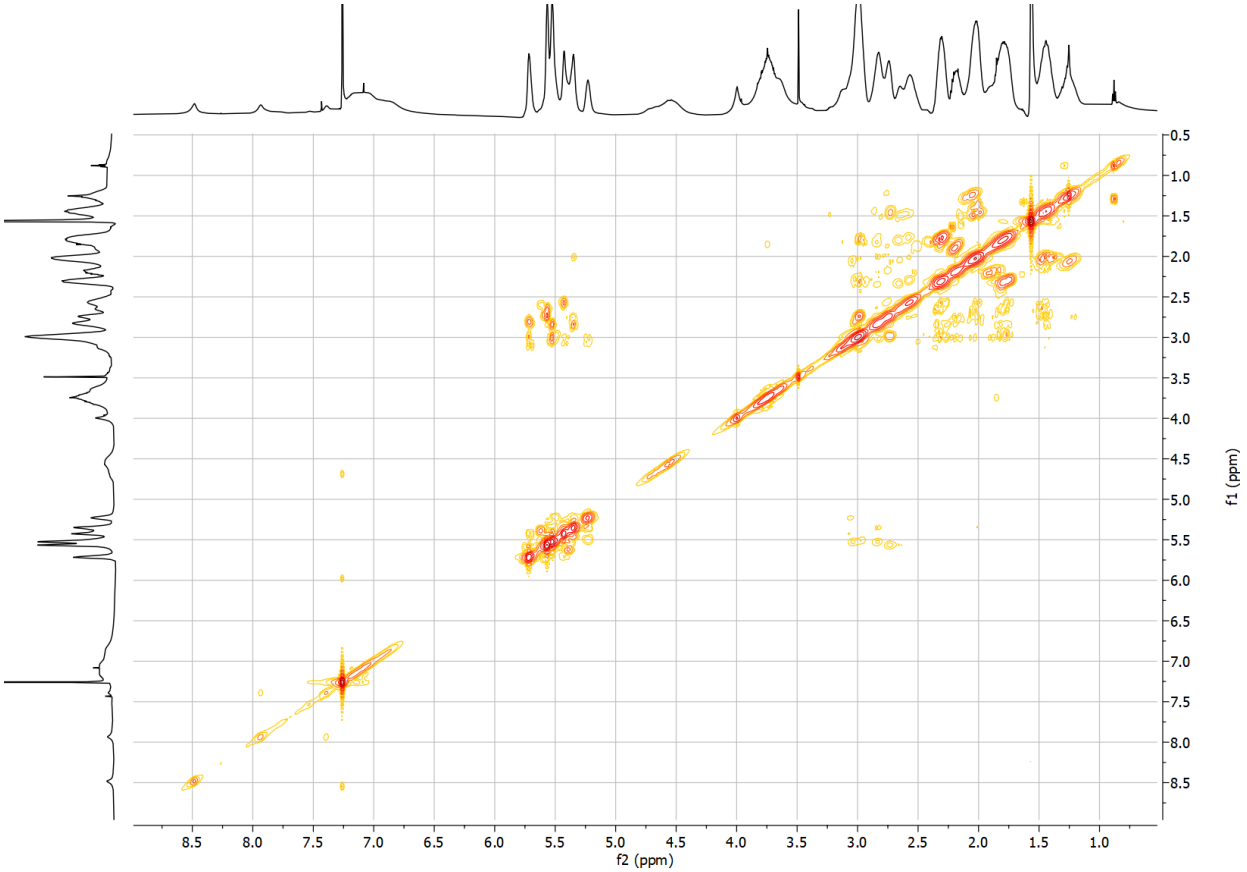

Figure 3.34: COSY 2D NMR spectrum of NNb-24 copolymer.

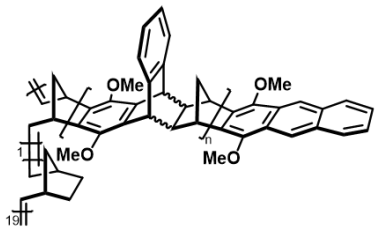
OMe
OMe
MeO
MeO
n
1
19

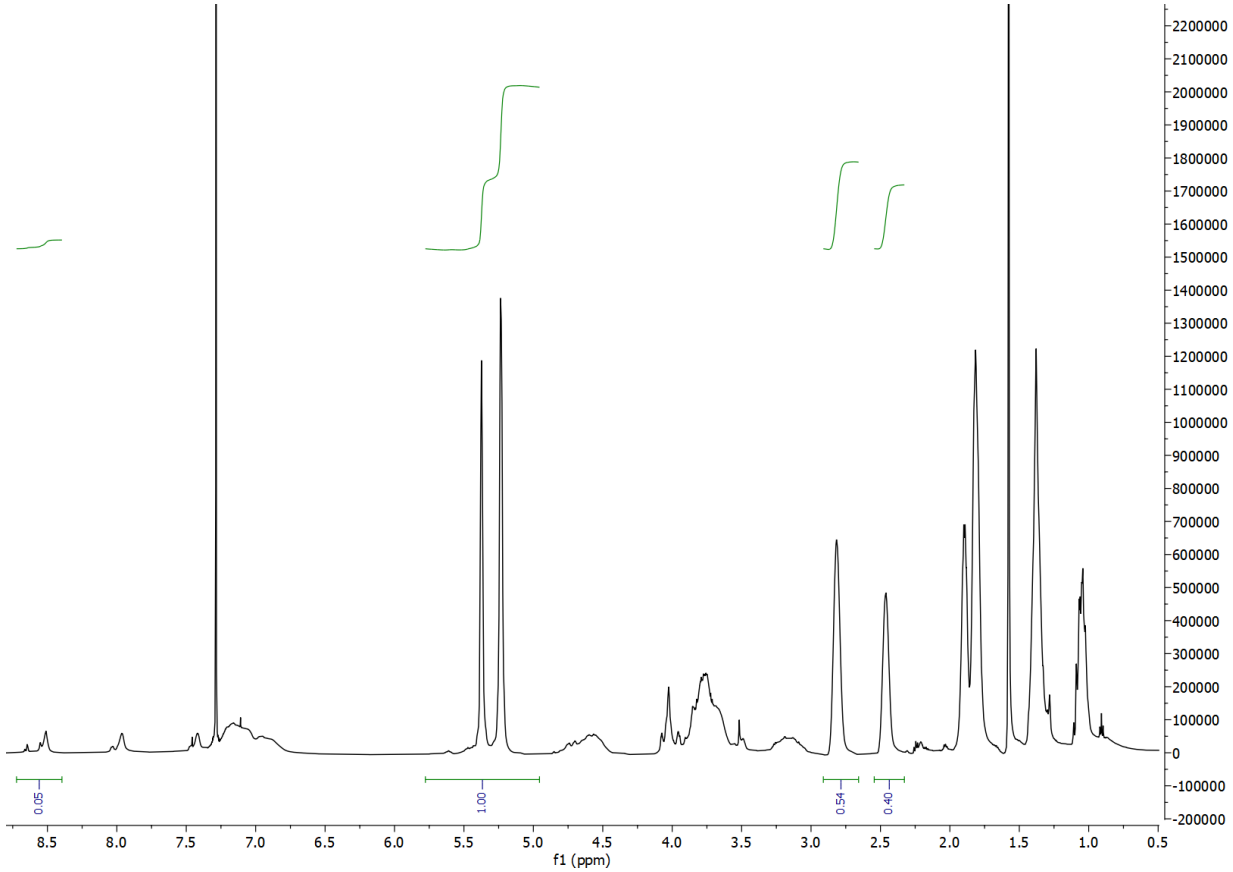

Figure 3.35: ^{1}H NMR spectrum of N-19 copolymer.

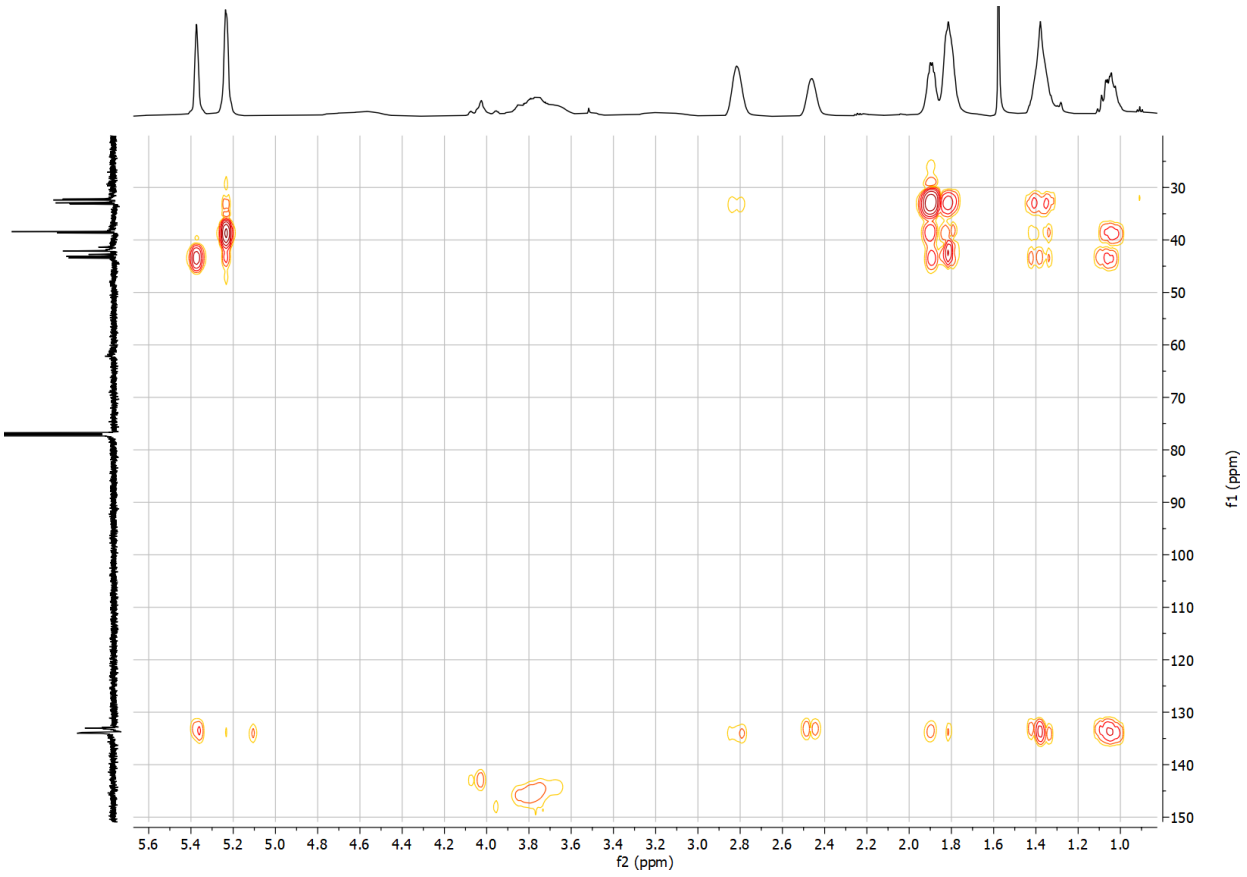

Figure 3.36: HMBC 2D NMR spectrum of N-19 copolymer.

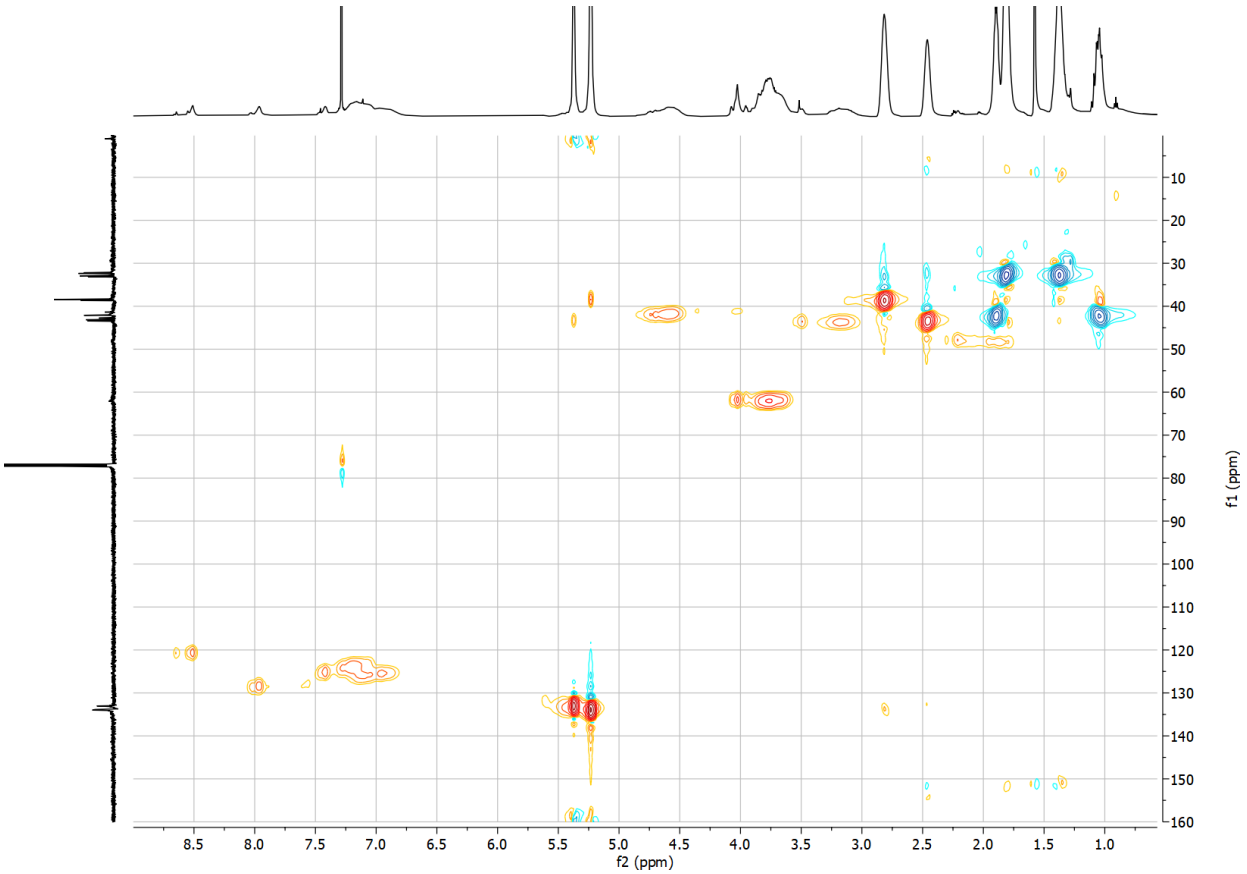

Figure 3.37: HSQC 2D NMR spectrum of N-19 copolymer.

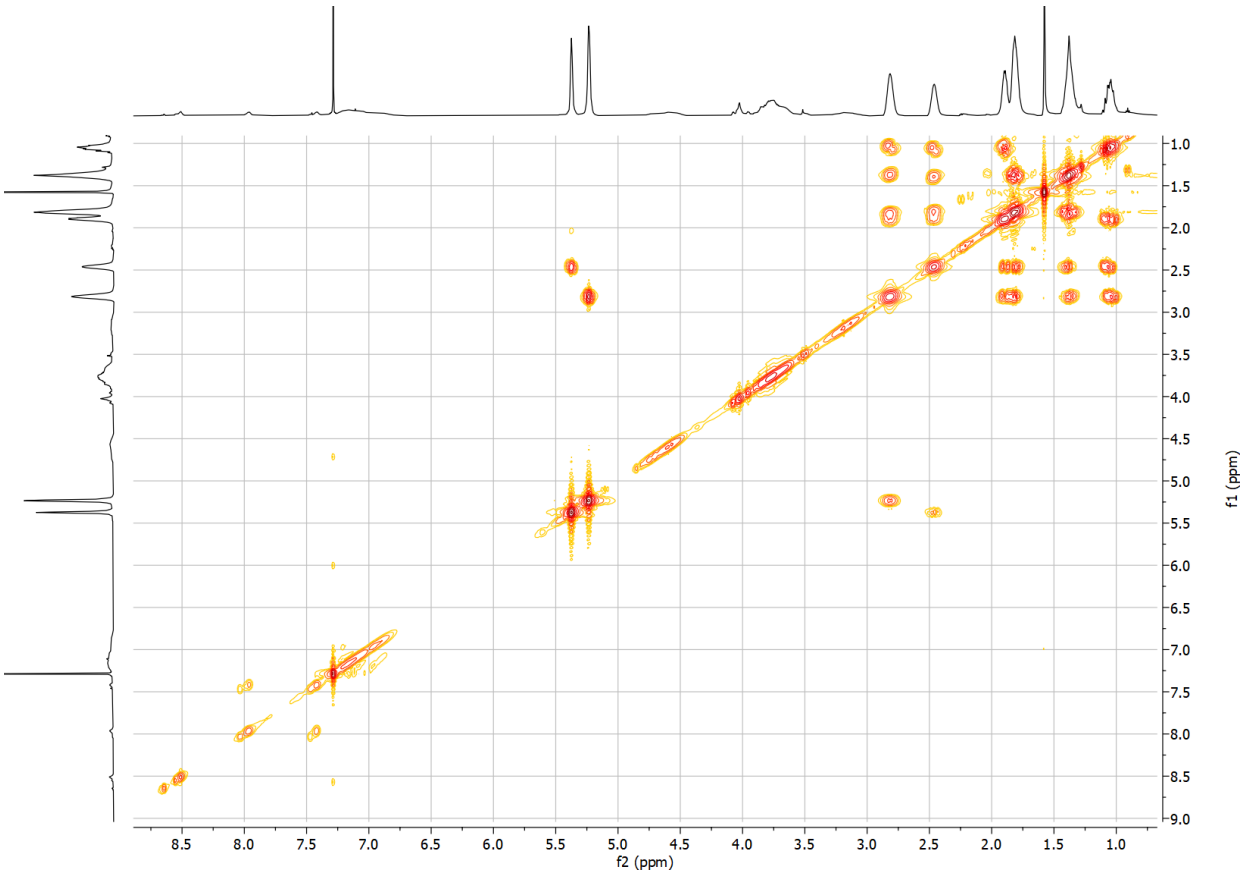

Figure 3.38: COSY 2D NMR spectrum of N-19 copolymer.

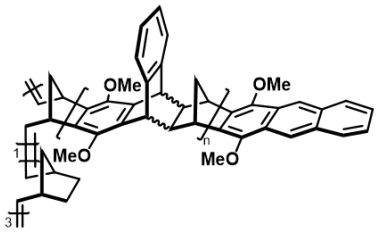
OMe
OMe
MeO
MeO
n

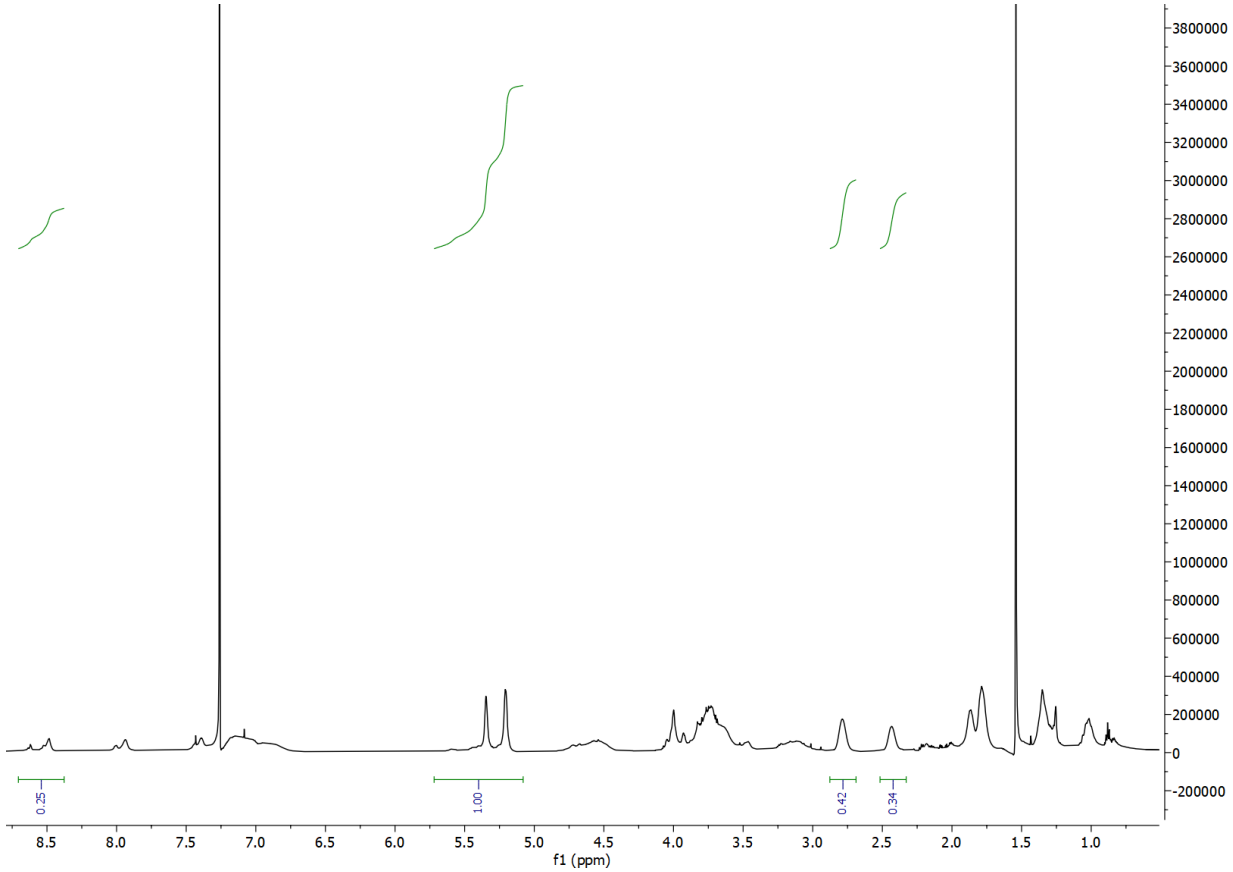

Figure 3.39: ^{1}H NMR spectrum of N-3 copolymer.

Figure 3.40: HMBC 2D NMR spectrum of N-3 copolymer.

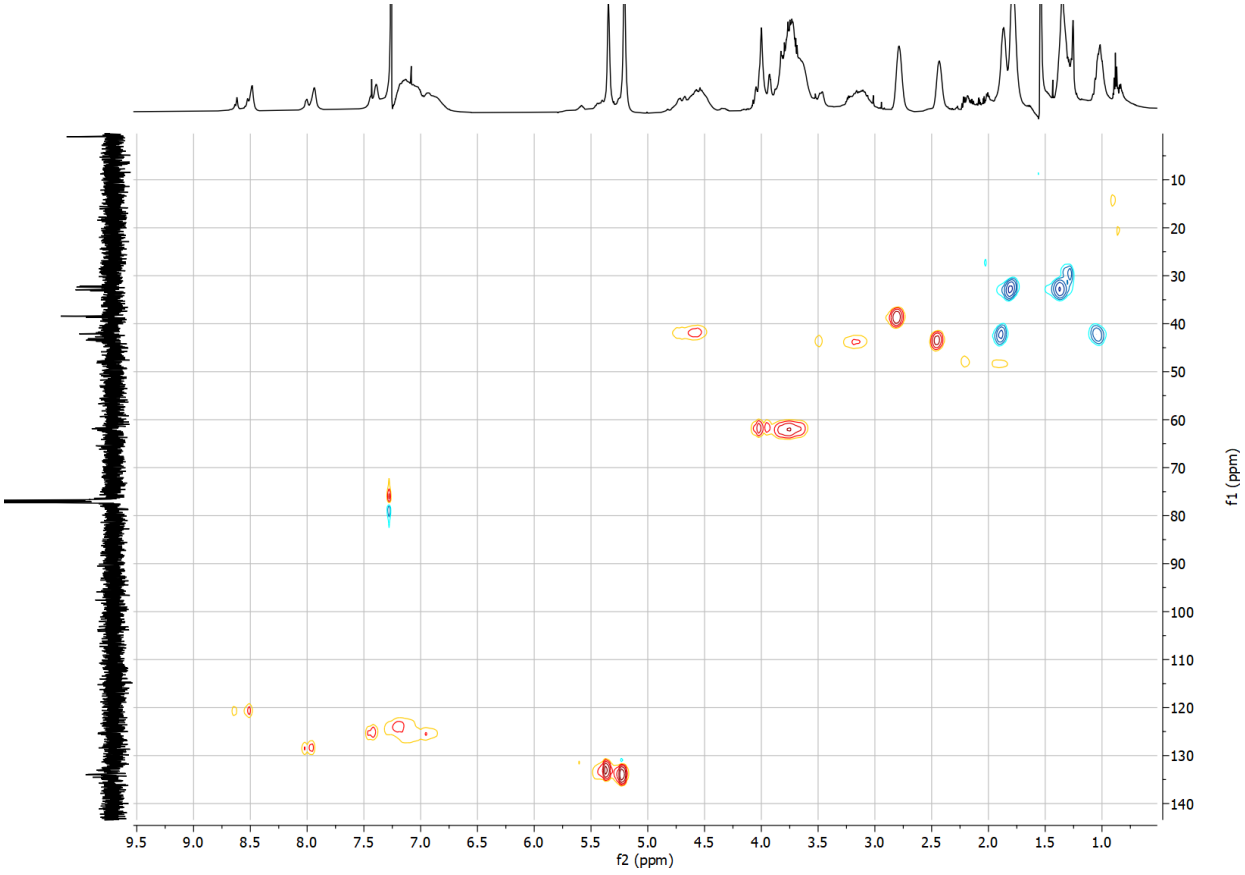

Figure 3.41: HSQC 2D NMR spectrum of N-3 copolymer.

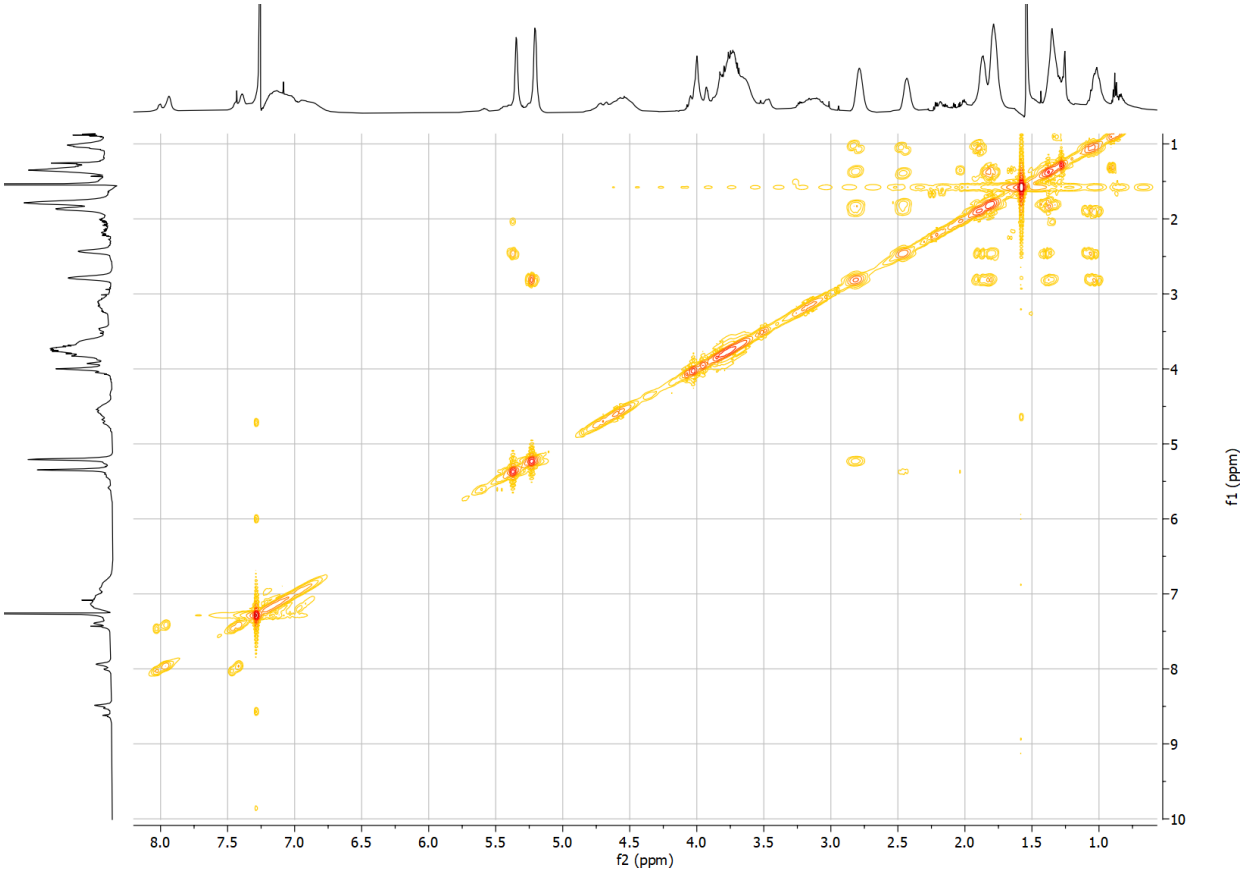

Figure 3.42: COSY 2D NMR spectrum of N-3 copolymer.

3.6 Acknowledgments

The synthetic design of materials to incorporate pore architecture was supported by the U.S. Department of Energy, Office of Science, Office of Basic Energy Sciences, Separation Science program through award number DE-SC0019087. The authors also gratefully acknowledge the Office of Naval Research under award number N00014-21-1-2666 for developing strategies related to site-specific CO_2 binding. K.R.S. acknowledges support from the National Science Foundation Graduate Research Fellowship under grant number 1745302. T.M.S. is grateful for funding from the National Science Foundation (DMR-2207299).

Chapter 4

Tuning porosity in triptycene-based poly(arylene ether)s

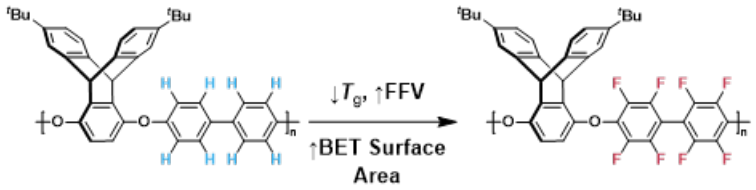

Kayla R. Storme, Zachary P. Smith, Timothy M. Swager

4.1 Abstract

We report the synthesis of high molecular weight poly(arylene ether)s (PAEs) using decafluorobiphenyl under S_NAr reaction conditions, the synthesis of a non-fluorinated biphenyl-based PAE using Pd-catalyzed polycondensation, and the characterization of these intrinsically porous polymers and their gas separation properties. The integration of free volume-promoting triptycene moieties as part of the mainchain gives rise to intrinsic porosity, which is modulated by incorporating biphenyl or perfluorobiphenyl comonomers. The fluorinated and non-fluorinated PAE exhibited BET surface areas of 454 $m^2\ g^{-1}$ and 270 $m^2\ g^{-1}$, respectively. WAXS revealed both polymers have greater disruption of chain packing compared to related polyimides, with the fluorinated PAE having the highest average interchain spacing. The fluorinated PAE also demonstrated high gas permeability as a result of its free volume and no plasticization pressure up to 31 bar of CO_2 pressure.

4.2 Introduction

Triptycenes and other related [2.2.2] and [2.2.1] bicyclic systems are configurationally rigid 3D structures that can promote high internal free volume in polymers when they are incorporated directly within the main chain of fused to it. These design principles have been leveraged to make intrinsically microporous polymers with targeted materials properties, including materials with low dielectric constants [9], [148], [149], high fluorescence quantum yields for efficient excitonic transport [150], superior ion transport [151], [152] and enhanced gas transport [131], [153]. Triptycene moieties have become a particularly desirable design motif for polymer gas separation membranes. When triptycene is introduced into a polyimide backbone, the fractional free volume and rigidity increases [148], resulting in enhanced gas permeability and anti-plasticization properties [74], [154]. A triptycene-based polysulfone also demonstrated improved permeability, selectivity, and resistance to physical aging [155]. Moreover, benzotriptycene-based polymers of microporosity (PIMs) recently redefined the CO_2/CH_4 and CO_2/N_2 upper bounds [131].

Similar to polyimides, poly(arylene ether)s (PAEs) are promising materials for gas separations because of their excellent thermal, mechanical, and chemical stability [156], [157]. Traditional PAE syntheses use S_NAr reactions that employ activated aryl fluoride monomers [9], [158]. Long et al. demonstrated that triptycene units disrupt chain packing in PAEs, thereby increasing the free volume of the polymer. In that study, one of the subject PAEs was first synthesized by the S_NAr reaction of decafluorobiphenyl and 6,11-di(tert-butyl)triptycene-1,4-hydroquinone (PAE-F, Scheme 4.1a) [9]. The free volume in this system was found to result in lower dielectric constants [9]. However, gas separations with PAE-F have yet to be investigated. Guo et al. recently developed a new Pd-catalyzed C–O polycondensation method that accommodates readily available unactivated aryl bromides, further diversifying the PAE structures available to researchers [159]. This new polycondensation methodology enabled us to synthesize PAE-H (Scheme 4.1b), the hydrocarbon analog to PAE-F.

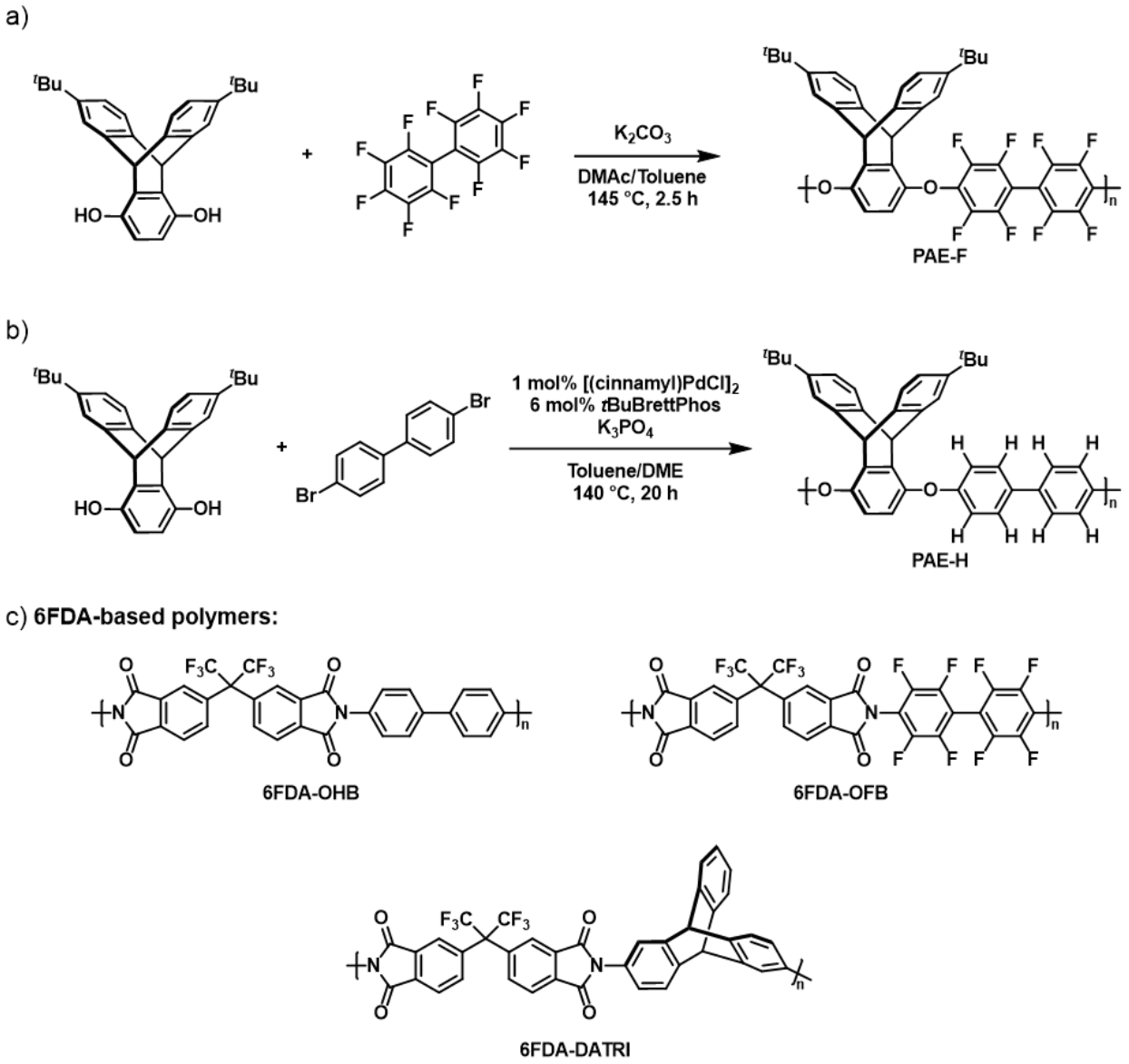

Scheme 4.1: Polymerization reaction schemes for a) PAE-F and b) PAE-H. Included are the c) structures of the 6FDA-based polymers referenced for comparisons [120], [160]–[162].

In this study, we report the optimized S_NAr synthesis of PAE-F to produce molecular weights considerably higher than that previously reported [9], and we report the synthesis of the analogous PAE-H that contains C–H functionality instead of C–F. The structure–property relationships of these PAE analogs were investigated through comparisons of thermal properties, BET surface area, and fractional free volume. PAE-H is found to be an intrinsically microporous polymer because the free volume-generating triptycene units inhibit dense packing of the biphenyl moieties. Perfluorobiphenyl groups boost the BET surface area and promote greater free volume in PAE-F. Thin films of PAE-F and PAE-H were fabricated, but the lower molecular weight of PAE-H resulted in brittle films that ruptured at ~1 bar of pressure. As a result, we were only able to characterize the pure-gas performance of PAE-F and compare our results to related structured reported in the literature.

4.3 Results and discussion

The synthesis of PAE-F and PAE-H using S_NAr and Pd-catalyzed C–O coupling conditions, respectively are shown in Scheme 4.1a and 4.1b. Toluene is added to the S_NAr reaction to form an azeotrope with water produced during the polymerization, which is removed from the reaction via distillation. Effective removal of the water is important to prevent potential hydroxide reactions with the perfluorobiphenyl monomer and maintain a 1:1 monomer equivalence for maximized molecular weight. Our optimized synthesis makes use of a stainless-steel dip tube to bubble argon *insitu* through the reaction mixture with 19.5 w/v% monomers and a short-path distillation apparatus to collect the distillate. During the polymerization, toluene and water are distilled from the reaction and into the receiving flask, the reaction was also concentrated by approximately 26% over the course of the polymerization. Under these conditions we obtained 74.2 kDa PAE-F. Other attempts starting with more concentrated solutions and/or without a dip tube yielded polymer at or below the ~32 kDa M_n, which is consistent with the previous reported polymerizations [9]. Since 4,4'-dibromobiphenyl is an unactivated aryl bromide and unsuitable for S_NAr reactions, we followed the previously reported Pd-catalyzed polycondensation [159] to polymerize 6,11-di(tert-butyl)triptycene-1,4-hydroquinone and 4,4'-dibromobiphenyl and yielded 15.6 kDa M_n PAE-H. Scheme 4.1c shows the structures of three 6FDA-based polymers with similar structural groups to the PAEs that we will use for comparison.

4.3.1 Thermal Properties of PAEs

Both synthesized polymers displayed high thermal stability characteristics of PAEs with degradation temperatures (T_d) above 450 °C (Figure 4.1a). The glass transition temperature (T_g) is higher in PAE-H than PAE-F (Figure 4.1b). This feature may be indicative of the tighter packing of polymer chains for PAE-H relative to PAE-F, and potentially from secondary interactions such as π-π stacking [163], [164]. The preferred solid-state conformation for biphenyl has been reported to be approximately coplanar [160], [163], [165], [166].

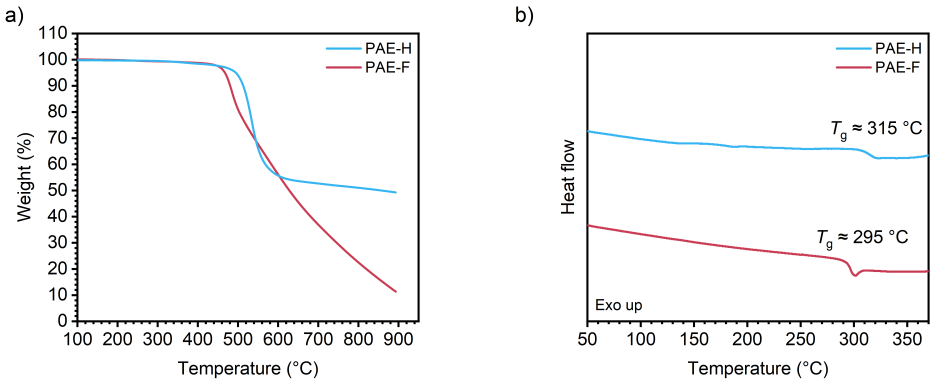

Figure 4.1: Heating curves for a) TGA and b) last heating cycle of DSC for PAE-F and PAE-H.

The coplanar conformation is stabilized by the delocalization of π-electrons [167] and/or by an attractive H—H bonding interaction between the 2-2'-Hs of the biphenyl [168]. A coplanar conformation will promote π-π stacking arrangements [164] in PAE-H. The 2,2'-F atoms in perfluorobiphenyl experience steric repulsion, which causes perfluorobiphenyl to adopt a conformation with a ~45 °dihedral angle between the phenyl groups [160].

4.3.2 Free Volume and Packing Structure Analysis

To evaluate the packing structure of PAE-F and PAE-H, we measured BET surface areas and calculated fractional free volume (FFV). BET is often used as an indirect, but highly correlated, indicator of the porosity of a material and surface areas typically scale with increasing free volume. FFV describes the "empty space" resulting from inefficient chain packing. Both PAE-F and PAE-H have characteristic Type I isotherms (Figure 4.2) with increasing pressure, indicating that these materials are high free volume. There is also pronounced hysteresis upon depressurization, suggesting a dilation effect at high N_2 activities or potentially some mesoporous characteristic in the packed polymer powder. The measured surface area of PAE-F was 454 m^2 g^{-1} and PAE-H was 270 m^2 g^{-1} (Table 4.1), indicating that PAE-F has a more open structure to accommodate small molecules relative to PAE-H. A similar interpretation was found by calculating FFV through group contribution methods [27], with PAE-F having a slightly higher FFV than that of PAE-H (Table 4.1). We anticipate that these findings relate to the non-planar conformation of perfluorobiphenyl inhibiting chain packing. Wu et al. investigated the impact of fluorine groups on morphology and transport and observed a 50% increase in FFV for 6FDA-OFB compared to the nonfluorinated 6FDA-OHB. The greater free volume was attributed to the non-planar conformation of perfluorobiphenyl [160]. Zhang et al. also noted an increase in FFV and d-spacing in a co-polyimide containing 2,2'-bis(trifluoromethyl) biphenyl compared to one containing unsubstituted biphenyl [169]. We noted the FFV for PAE-F and PAE-H is higher than 6FDA-OFB, 6FDA-OHB [160], and 6FDA-DATRI [162], affirming ^{t}Bu-triptycene as a residue that enhances free volume.

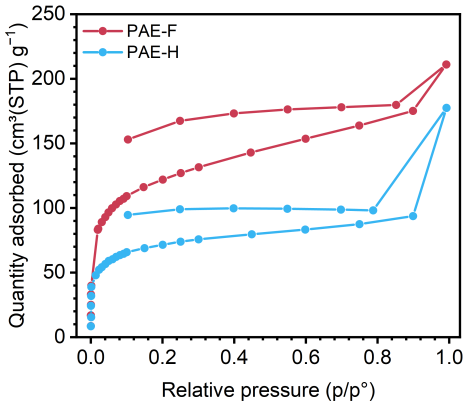

Figure 4.2: N_2 adsorption isotherms at 77 K for PAE-F and PAE-H.

To investigate the physical packing structure of the polymers, we collected WAXS spectra for each polymer. The polymers are amorphous and films are optically clear. In WAXS, diffuse scattering from voids between polymer chains are responsible for the peaks at lower q values, whereas scattering from intersegmental spacing produces peaks at higher q values (Figure 4.3) [170]. The peak centered at 14.5 Å in PAE-F shifts to 11.8 Å in PAE-H in accordance with the BET and free volume trends noted previously. Both of these amorphous halos are centered at d-spacing values that are larger than that observed in the 6FDA-based polymers considered (Scheme 4.1c) [160], [162]. Again, this finding indicates the unique free-volume generating feature of ^{t}Bu-triptycene residues. We attributed the secondary signal at 5.21 Å for PAE-H and 5.25 Å for PAE-F to interchain correlations as these distances are longer than would be expected for cofacial π-π stacking. This finding is also consistent with the triptycene moieties providing access to configurational free volume for molecular transport [13], [18], [171].

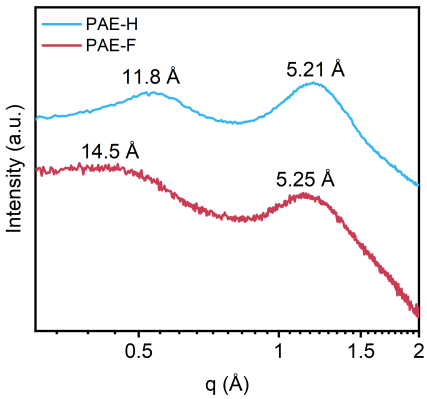

Figure 4.3: WAXS spectra results for PAE-H and PAE-F.

4.4 Pure-gas permeation analysis

Increases in permeability correlate with higher FFV, and as expected, PAE-F demonstrates higher permeability than 6FDA-OFB, 6FDA-OHB [160], and 6FDA-DATRI [162] (Figure 4.4). Correspondingly, selectivity was inversely correlated with FFV. We observed a decrease in N_2/CH_4, CO_2/CH_4, CO_2/N_2, and O_2/N_2 selectivity for PAE-F relative to the 6FDA-based polymers. We hypothesized that this feature was attributed to an increase in diffusivity for all gases, and we calculated the diffusion coefficients using the time-lag method (Table 4.3). Diffusion coefficients increase with decreasing effective permeability diameter, and the diffusivity order is CH_4 (3.81 Å) < N_2 (3.66 Å) < CO_2 (3.63 Å) < O_2 (3.44 Å) for the PAEs. We confirmed that PAE-F promotes greater diffusion of all gases compared to the 6FDA-based polymers and found CH_4 diffusion increased 8-fold compared to 6FDA-OFB and 6FDA-DATRI. Fluorinated polymers typically exhibit N_2/CH_4 selectivity higher than 1 [37], [172], [173], however PAE-F demonstrates a selectivity less than 1 for N_2/CH_4, indicating the CH_4/N_2 sorption selectivity from the non-equilibrium mode overwhelms N_2/CH_4 diffusivity selectivity. The N_2/CH_4 and CO_2/CH_4 diffusivity selectivity is approximately 2- to 3-fold lower in PAE-F compared to 6FDA-OFB and 6FDA-DATRI, respectively, indicating the greater free volume in PAE-F reduces its size-sieving capabilities and thus results in a switch in permselectivity for the N_2/CH_4 pair. CH_4 sorption is 52% higher in PAE-F than 6FDA-OFB, but both polymers exhibit the same CO_2 sorption. PAE-F exhibits CO_2/N_2 sorption selectivity that is 23% higher than that of 6FDA-DATRI and 24% lower than that of 6FDA-OFB. These findings suggest triptycene does not influence CO_2 interactions with the polymer. Sorption of all gases is increased in 6FDA-OFB compared to 6FDA-DATRI, indicating decafluorobiphenyl provides a greater boost in sorption than triptycene. The CO_2/CH_4 selectivity of PAE-F is similar to 6FDA-DATRI and 34% lower than 6FDA-OFB, suggesting decafluorobiphenyl and 6FDA moieties increase selectivity for CO_2 more than triptycene.

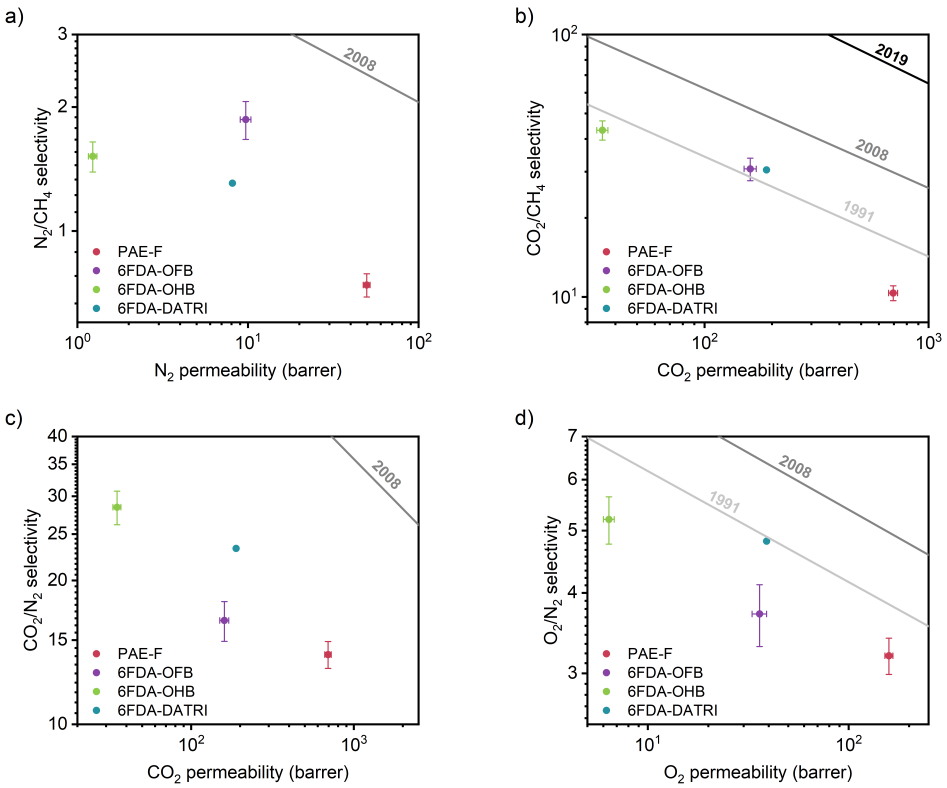

Figure 4.4: Pure-gas permeation of PAE-F compared to 6FDA-OHB, 6FDA-OFB [160], and 6FDA-DATRI [162] for a) N_2/CH_4, b) CO_2/CH_4, c) CO_2/N_2, and d) O_2/N_2.

The enhanced sorption selectivity may arise from interactions of CO_2 with the 6FDA moieties, which are known to produce some of the highest CO_2-sorptive polyimides [91]. In fact, 6FDA-based polyimides are easily plasticized by CO_2 due to strong gas–polymer affinity, which enhances the mobility of the polymer chains [161], [174]. This phenomenon results in a pure-gas CO_2 plasticization pressure of 8 bar for 6FDA-DATRI [161]. Subjecting PAE-F to high pressure sweeps of CO_2, reveals a plasticization pressure point of 31 bar (Figure 4.5), a nearly 4-fold improvement from 6FDA-DATRI, demonstrating that pairing perfluorobiphenyl with triptycene motifs can enhance resistance to CO_2-induced plasticization. Solid-state dynamics characterization will elevate our understanding of changes in packing structure that occur in the presence of CO_2 in addition to mixed-gas permeation and sorption experiments and will be the focus of future studies of PAE-F.

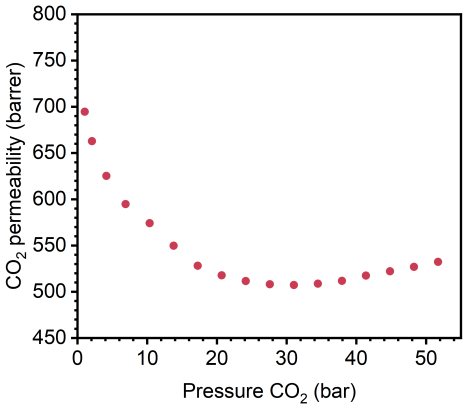

Figure 4.5: Pure-gas CO_2 permeabilities for high pressure sweep of PAE-F.

4.5 Conclusions

We report a synthetic method in this study to improve molecular weight of a previously reported PAE[9] in addition to the synthesis of the non-fluorinated analog using recently developed Pd-catalyzed polycondensation. Furthermore, we performed a comparative characterization study between a fluorinated and non-fluorinated PAE formed through the same synthetic mechanism to assess structure–property relationships. Triptycene moieties dependably enhanced free volume and porosity, as demonstrated from FFV and BET analysis. Our WAXS results also indicated that perfluorobiphenyl further disrupts chain packing compared to the non-fluorinated biphenyl analog. Both PAEs have higher FFVs compared to polyimide counterparts, resulting in increased permeability for PAE-F. No plasticization pressure effects were observed up to ~31 bar for PAE-F, demonstrating a resistance to plasticization for this class of materials.

4.6 Experimental methods

4.6.1 Materials

All materials were used as received unless otherwise noted. Potassium phosphate was purchased from Alfa Aesar. Decafluorobiphenyl was purchased from Alfa Aesar and recrystallized in hexanes before use. Palladium(π-cinnamyl) chloride dimer, N,N-dimethylacetamide (DMAc, 99.8%), ethyl acetate ($\geq$ 99.5%), and inhibitor free anhydrous 1,2-dimethoxyethane (99.5%) were purchased from Sigma Aldrich. ^{t}BuBrettPhos was purchased from Ambeed. Hexanes and methanol were purchased from Macron Fine Chemicals. Anhydrous toluene (99.85%) was purchased from Fisher Scientific. Hydrochloric acid (37%) solution in water was purchased from Sigma Aldrich and diluted with deionized water to make a 3 M solution. 4,4'-dibromobiphenyl was purchased from Sigma Aldrich and recrystallized from petroleum ether. 6,11-di(tert-butyl)triptycene-1,4-hydroquinone was purchased from Akita Innovations and purified via recrystallization with ethyl acetate and hexanes. All gases used for testing (He, H_2, CH_4, N_2, O_2, and CO_2) were ultra-high purity from Airgas.

4.6.2 Preparation of Polymer Films

A 2 wt% chloroform solution of PAE-F was prepared and cast into a 78 mm low profile PTFE evaporating dish set on a leveled platform inside a chemical fume hood. The dish was covered with aluminum foil containing punctured holes, and then a glass dish was placed on top of the foil overnight to allow slow solvent evaporation. Free-standing films were obtained and submerged in methanol for 24 hours and then dried for 24 hours inside a chemical fume hood.

4.6.3 Chemical Characterization

The chemical structure of the polymers was studied using ^{1}H, ^{13}C, and ^{19}F NMR spectra. NMR spectra were obtained using a three-channel Bruker Avance Neo spectrometer operating at 500.34 MHz. Samples were prepared in deuterated chloroform and referenced to the residual solvent signal. Molecular weight and dispersity of the polymers was obstained using an Agilent 1260 Infinity system equipped with an Agilent PLgel guard column (5 μm; 50 x 7.5 mm) and three Agilent PLgel analytical columns (5 µm; 300 x 7.5 mm; 10^5, 10^4, and 10^3 Å pore sizes). The instrument was calibrated with polystyrene standards between 1.7 and 3150 kg mol^{-1}. All samples were prepared in HPLC-grade tetrahydrofuran. Each run was performed at a 1.0 mL min^{-1} flow rate and 35 °C. Molecular weight values were calculated using ChemStation GPC data analysis software (Rev. B.01.01) based on the refractive index signal. The thermal stability of the polymers was evaluated using a TGA 550 from TA Instruments under nitrogen atmosphere (Airgas, ultra-high purity grade). Samples were conditioned with a 5-minute isotherm at 100 °C. Heating ramp speed was set to 10 °C min^{-1} and measurements are made up to 900 °C. Differential scanning calorimetry (DSC) measurements were performed on a DSC 250 from TA Instruments. Heating and cooling rates were set to 10 °C min^{-1} from 40–400 °C. Glass transition temperatures were determined using the last trace of the cyclic heating cycle.

Physical Characterization

The physical packing structure of the polymers was analyzed with wide angle X-ray scattering (WAXS), powder Brunauer–Emmett–Teller (BET) analysis, density measurements, and fractional free volume (FFV) calculations. WAXS measurements were performed using a SAXSLAB instrument equipped with a DECTRIS PILATUS3 R 300K detector and a Rigaku 002 microfocus X-ray source. Sample measurements were taken under 0.08 mbar vacuum for 300 s in the 3–70 Å range. Measurements were taken from the forward direction of radiation as a function of scattering angle, 2θ. The scattering profile was normalized to a wavelength independent scale through conversion to momentum transfer, q:

$$q = 4\pi \sin\theta/\lambda \tag{4.1}$$

Where θ is $\frac{1}{2}$ the scattering angle and λ is the wavelength in Ångstroms. The d-spacing, d, is then calculated from the relation shown in Equation 4.2.

$$q = 2\pi/d \tag{4.2}$$

BET surface areas of polymer samples were measured at 77 K using N_2 sorption using a Micromeritics 3Flex analyzer. All samples were degassed under high vacuum at 200 °C for at

least 24 hours prior to analysis. Circular films with 5 mm diameter were cut from the bulk film using a 5 mm hollow steel punch (General Tools MFG. Co. Inc.). The film thickness was measured using a micrometer. The volume of each film was calculated as the volume of a cylinder with the thickness as the height. Each film was weighed using a microbalance. Density was calculated by dividing the weight by the volume of each film.

The FFV was calculated for each polymer using Equation 4.3:

$$FFV = \frac{V - 1.3V_W}{V} \tag{4.3}$$

where V is the molar volume of the polymer ($cm^3\ mol^{-1}$) and V_W is the van der Waals volume of the polymer ($cm^3\ mol^{-1}$) determined using the group contribution method updated by Wu et al [27].

Pure-gas permeation

An automated constant-volume, variable-pressure permeation system from Maxwell Robotics was used to collect pure-gas permeation data. A 97 μm thick polymer film was cut and glued to the opening in the center of a brass disk using Devcon 5 min epoxy glue. After the glue dried, the polymer sample was loaded and sealed into a stainless-steel permeation cell. Before beginning the experiment, the sample was dosed with ~2 bar of helium gas to remove residual gas in the system and degassed for 8 h at 35 °C. The permeabilities of He, H_2, CH_4, N_2, O_2, and CO_2 were determined at ~1 bar in that order of testing. For plasticization studies, sample permeabilities were collected using an increasing pressure sweep of CO_2 pressures from 1–51 bar. Before switching to a new gas, samples were dosed with ~2 bar of helium then degassed for at least 1 h.

Pure-gas permeability (P) was calculated using the following equation:

$$P = \frac{V_d l}{p_2 ART}\left[\left(\frac{dp}{dt}\right)_{ss} - \left(\frac{dp}{dt}\right)_{leak}\right] \tag{4.4}$$

in which V_d is the volume downstream of the film, l is the film thickness, p_2 is the upstream pressure, A is the area of film exposed to the gas, R is the ideal gas constant, T is the absolute experimental temperature, $\left(\frac{dp}{dt}\right)_{ss}$ is the rate of pressure rise in the permeate at steady state, and $\left(\frac{dp}{dt}\right)_{leak}$ is the leak rate [48]. The ideal gas selectivity ($\alpha_{i,j}$) was taken to be the ratio of the pure-gas permeabilities (i.e., $\frac{P_i}{P_j}$). The time lag, θ, was determined and diffusion coefficients were calculated using the time-lag method for each gas [36].

$$D = \frac{l^2}{6\theta} \tag{4.5}$$

For He and H_2, the diffusion coefficients were sometimes outside of the acquisition time resolution of the permeation system (approximately 1–2 s), so the diffusion coefficients for these two gases are not reported. Sorption coefficients derived from the time lag were calculated using the sorption–diffusion model [35].

$$S = \frac{P}{D} \tag{4.6}$$

Diffusion and sorption selectivity were calculated from the ratio of diffusion coefficients (i.e., $\frac{D_i}{D_j}$) or sorption coefficients (i.e., $\frac{S_i}{S_j}$), respectively. All uncertainties were calculated from error propagation.

4.6.4 Synthesis of polymers

Synthesis of PAE-F

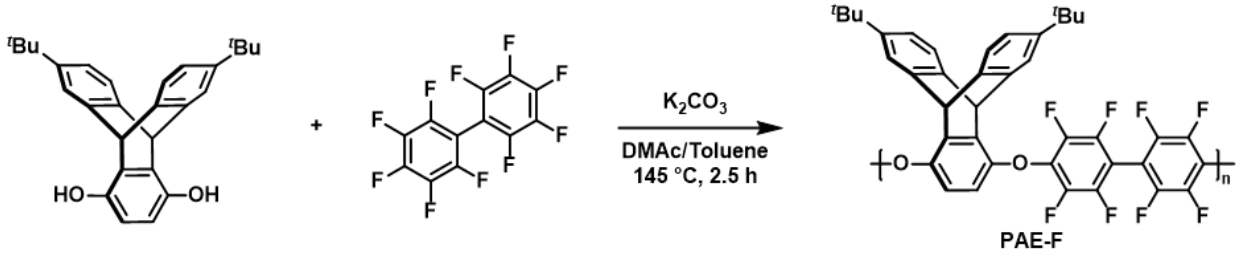

A 100 mL resin kettle fitted with a dip-tube, thermocouple, and short-path distillation apparatus was charged with 6,11-di(*tert*-butyl)triptycene-1,4-hydroquinone (7.1570 g, 18.0 mmol, 1.0 equiv.) and decafluorobiphenyl (6.0000 g, 18.0 mmol, 1.0 equiv.). Then, DMAc (60 mL) and toluene (7.4 mL) were poured into the resin kettle followed by K_2CO_3 (5.7080 g, 41.3 mmol, 2.3 equiv). The dip-tube was adjusted to a position below the solvent level so argon would sparge the solution. The receiving flask fixed to the distillation apparatus was placed into a dry ice/acetone bath. The solution was stirred with argon bubbling through the dip-tube to distill off the water-toluene azeotrope and concentrate the polymerization solution. The resin kettle was heated to 145 °C for 2.5 h. Once cooled to room temperature, the viscous solution was precipitated into boiling HCl water (pH ~2–3) to neutralize remaining carbonate and promote polymer aggregation. The polymer fibers were collected and dried using vacuum filtration before redissolving in THF. The THF solution was precipitated into DI water and polymer fibers were recovered via vacuum filtration. Residual DMAc remained in the fibers, so the fibers were dissolved in chloroform, precipitated into methanol, and collected via vacuum filtration. The fibers were dried in a vacuum oven at 200 °C for 48 h before characterizing (yield: 10.87 g). ^{1}H NMR (500 MHz, $CDCl_3$) δ 7.52 (d, J = 1.9 Hz, 1H), 7.40 (d, J = 7.7 Hz, 1H), 7.10 (dd, J = 7.7, 1.9 Hz, 1H), 6.52 (s, 1H), 6.02 (s, 1H), 1.30 (s, 9H), 1.29 (s, 1H). ^{13}C NMR (126 MHz, $CDCl_3$) δ 148.68, 148.30, 145.80, 144.34, 143.73, 142.67, 141.54, 140.77, 138.18, 136.55, 123.50, 122.11, 121.50, 113.68, 77.28, 77.03, 76.77, 47.70, 34.64, 31.49, 1.04. ^{19}F NMR (471 MHz, $CDCl_3$) δ -135.78 – -139.05 (m), -152.97 (dd, J = 24.2, 8.1 Hz).

Synthesis of PAE-H

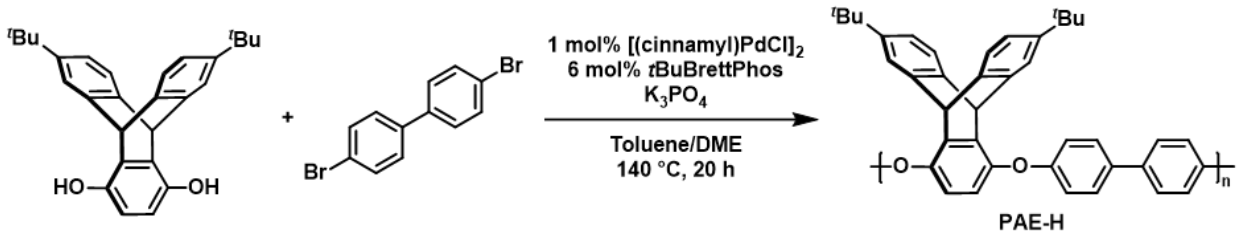

Synthesis of PAE-H followed previously reported procedures [159]. For the synthesis, 6,11-di(*tert*-butyl)triptycene-1,4-hydroquinone (200 mg, 0.502 mmol, 1.0 equiv.) and 4,4'-dibromobiphenyl (156.6 mg, 0.502 mmol, 1.0 equiv.) were used to yield 115 mg of pink powder. ^{1}H NMR (500 MHz, $CDCl_3$) δ 7.55 (dd, J = 8.7, 2.9 Hz, 2H), 7.29 (d, J = 2.1 Hz, 1H), 7.26 (d, J = 7.7 Hz, 1H), 7.03 (dd, J = 7.8, 1.9 Hz, 1H), 7.01 – 6.97 (m, 2H), 6.75 (s, 1H), 5.68 (d, J = 3.9 Hz, 1H), 1.26 (s, 8H). ^{13}C NMR (126 MHz, $CDCl_3$) δ 157.99, 148.26, 147.01, 146.98, 146.94, 146.91, 144.62, 141.88, 140.05, 140.02, 134.92, 134.83, 128.81, 128.40, 128.09, 128.03, 126.85, 123.45, 121.74, 121.49, 118.78, 118.71, 117.40, 117.33, 77.28, 77.03, 76.78, 48.09, 34.62, 31.55.

4.6.5 NMR spectra of polymers

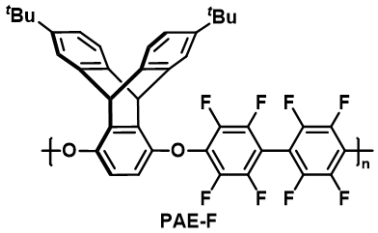

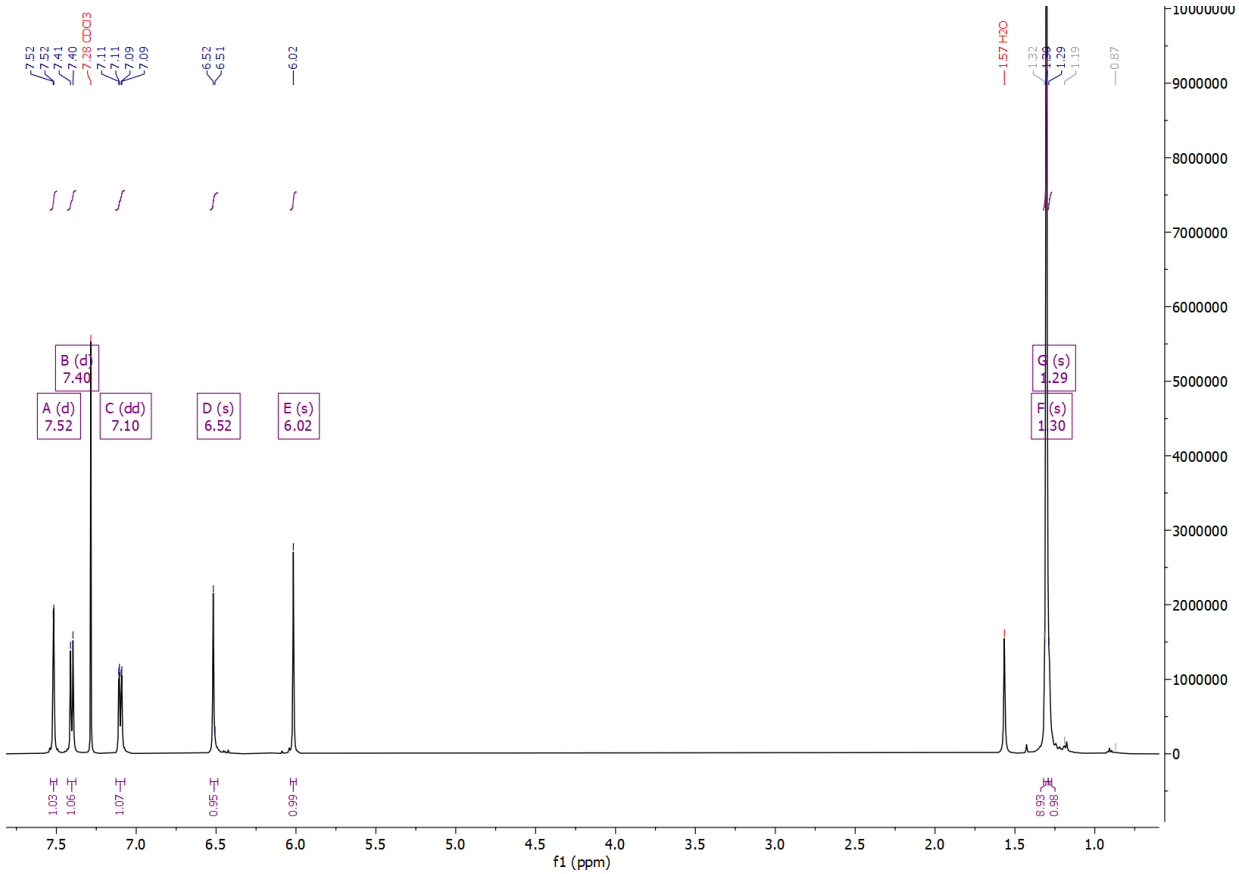

Figure 4.6: ^{1}H NMR of PAE-F.

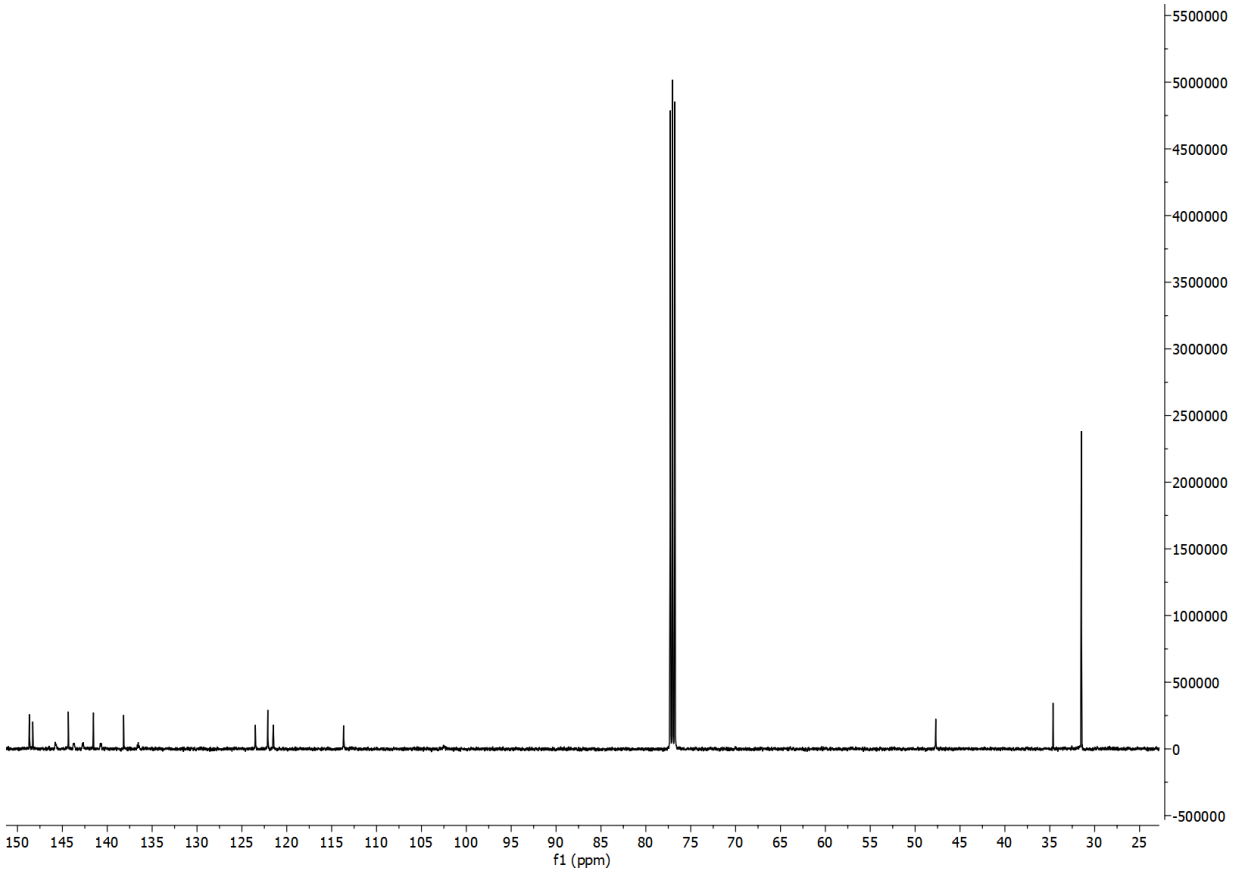

Figure 4.7: ^{13}C NMR of PAE-F.

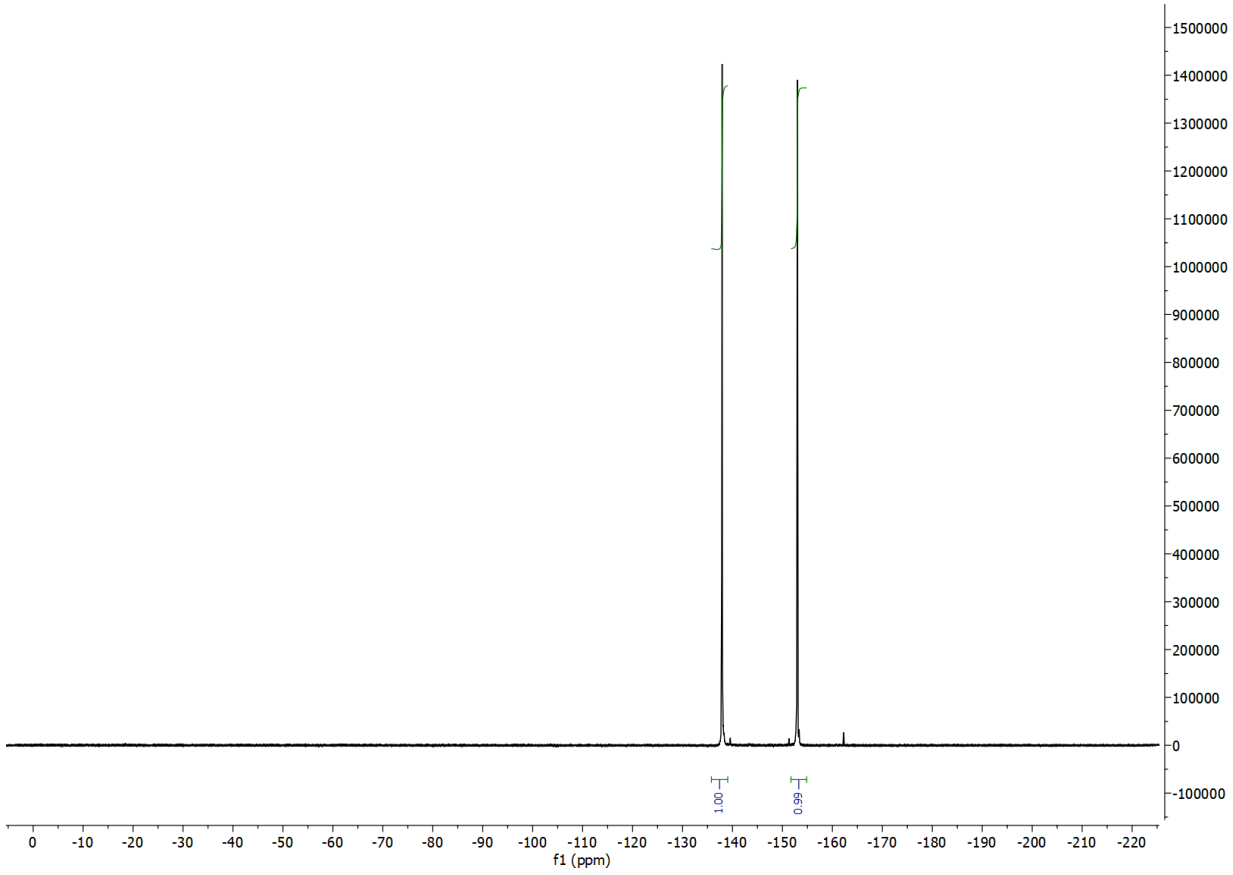

Figure 4.8: ^{19}F NMR of PAE-F.

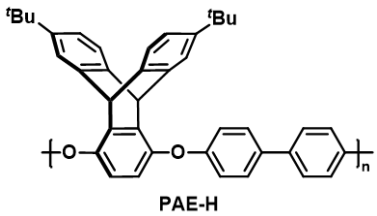

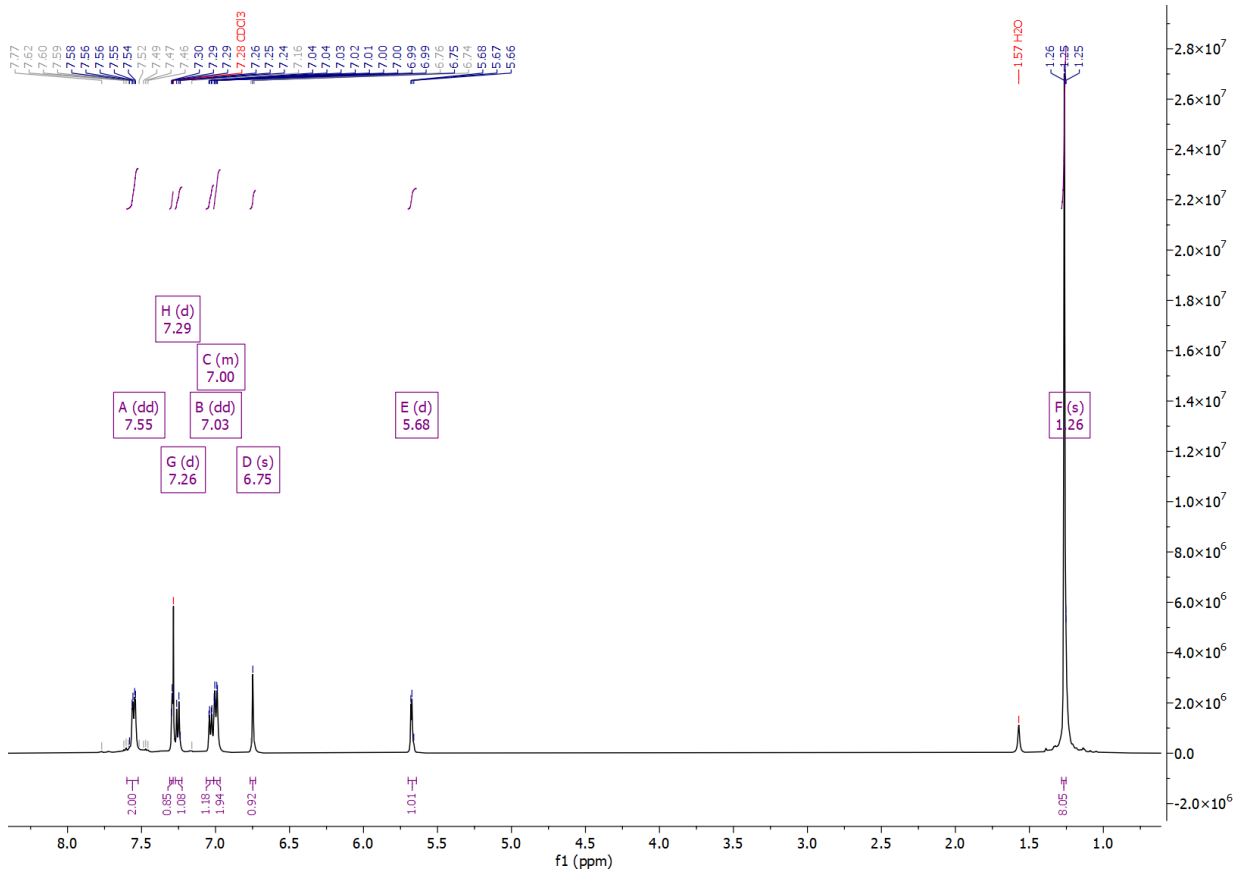

Figure 4.9: ^{1}H NMR of PAE-H.

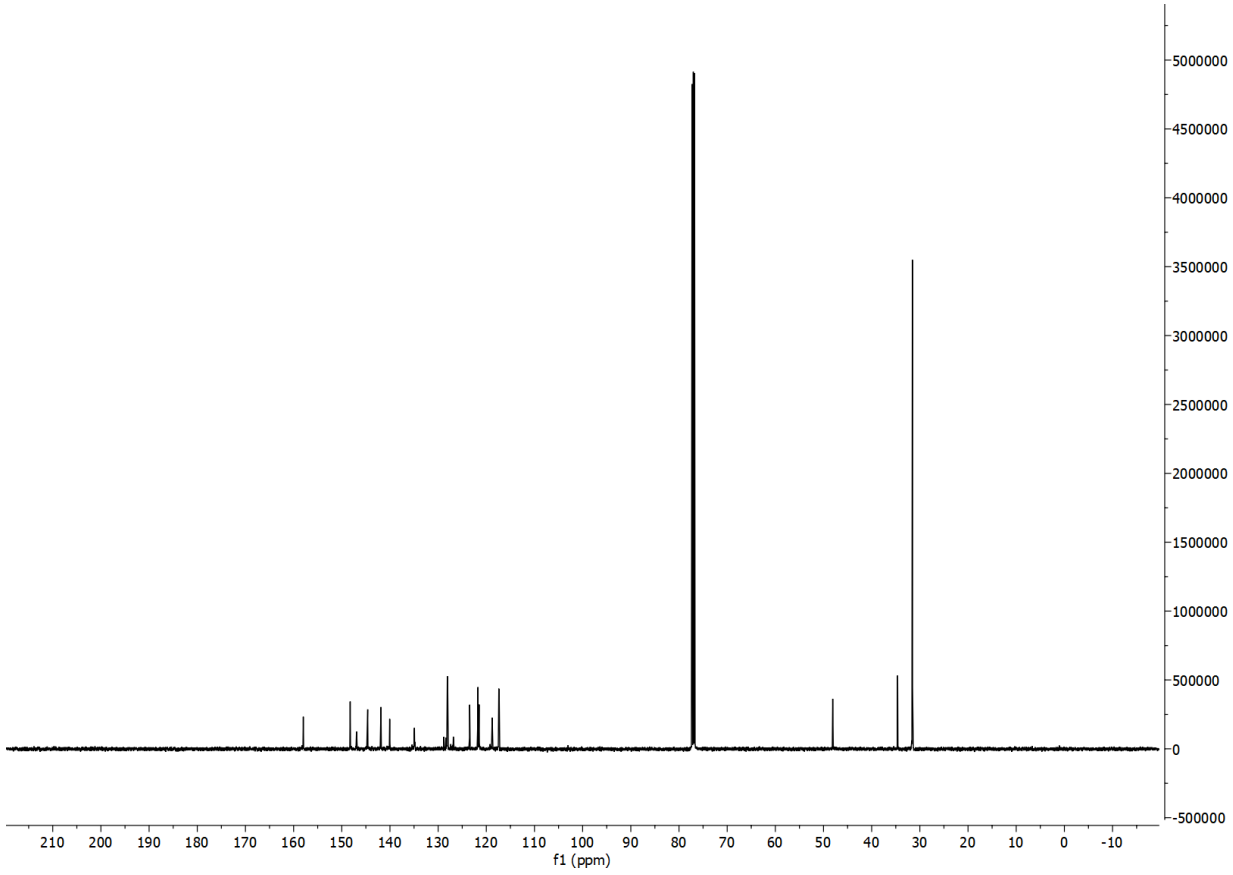

Figure 4.10: ^{13}C NMR of PAE-H.

4.6.6 Molecular weight, dispersity, thermal, and physical properties

Table 4.1: Molecular weight, thermal properties, and physical characterization (density, FFV, and BET surface area) of PAE-H and PAE-F. Information for 6FDA-OHB, 6FDA-OFB [160], and 6FDA-DATRI [162] is included for reference.

Polymer	M_n (kDa)	Đ	$T_{d,5}$ (°C)	T_g (°C)	ρ (g cm^{-3})	V_W (cm^3 mol^{-1})	FFV (%)	BET surface area m^2 g^{-1}
PAE-H	15.6	5.8	495	315	1.03 ±0.05	301.3 ± 0.8	26.6	270
PAE-F	74.2	4.4	467	295	1.12 ±0.04	334.5 ± 0.9	29.8	454
6FDA-OHB [160]	114	1.6	*N/A*	361	1.456±0.007	271.8 ± /	13.3	*N/A*
6FDA-OFB [160]	56	2.5	*N/A*	343	1.559±0.003	290 ± /	20.3	*N/A*
6FDA-DATRI [162]	21.1	5.2	540	352	1.297±0.02	413 ± /	22.6	*N/A*

4.6.7 Pure-gas permeation data

Table 4.2: Pure-gas permeability measured at 35 °C and ~1 bar. Permeability is reported in units of barrer. Information for 6FDA-OHB, 6FDA-OFB [160], and 6FDA-DATRI [162] is included for reference.

Gas	PAE-F	6FDA-OFB [160]	6FDA-OHB [160]	6FDA-DATRI [162]
He	395 ±18	220 ± 20	59 ± 3	198
H_2	593 ±27	220 ± 20	58 ± 3	257
O_2	159 ± 7	36 ± 3	6.4 ± 0.4	39
N_2	50 ± 2	10 ± 1	1.2 ± 0.1	8.1
CH_4	67 ± 3	5.2± 0.4	0.81± 0.05	6.2
CO_2	695 ±32	160 ± 10	35 ± 2	189

Table 4.3: Diffusion (D) and sorption (S) coefficients for PAE-F and diffusivity selectivity and sorption selectivity for O_2/N_2, N_2/CH_4, CO_2/CH_4, and CO_2/N_2. Values for 6FDA-OHB, 6FDA-OFB [160], and 6FDA-DATRI [162] is included for reference.

D (10^{-8} cm^2 s^{-1})								
Polymer	O_2		N_2		CH_4		CO_2	
PAE-F	81	±2	32.2	±0.5	13.4	±0.2	37.8	±0.6
6FDA-OFB [160]	25	±3	7.9	±0.7	1.6	±0.1	8.9	±0.8
6FDA-OHB [160]	7.4	±0.5	1.8	±0.1	0.24	±0.02	2.3	±0.1
6FDA-DATRI [162]	23	±/	5.5	±/	1.5	±/	13	±/
S (cm^3_{STP} cm^{-3}_{pol} atm^{-1})								
Polymer	O_2		N_2		CH_4		CO_2	
PAE-F	1.5	±0.1	1.17	±0.05	3.8	±0.2	14	±1
6FDA-OFB [160]	1.1	±0.1	0.9	±0.1	2.5	±0.3	14	±2
6FDA-OHB [160]	0.66	±0.06	0.52	±0.04	2.6	±0.2	11	±1
6FDA-DATRI [162]	0.017	±/	0.015	±/	0.041	±/	0.145	±/
Diffusivity selectivity								
Polymer	O_2/N_2		N_2/CH_4		CO_2/CH_4		CO_2/N_2	
PAE-F	2.5	±0.1	2.40	±0.05	2.8	±0.1	1.17	±0.03
6FDA-OFB [160]	3.2	±0.5	4.9	±0.5	5.6	±0.6	1.10	±0.05
6FDA-OHB [160]	4.1	±0.4	7.5	±0.7	9.6	±0.9	1.28	±0.09
6FDA-DATRI [162]	4.2	±/	3.7	±/	8.7	±/	2.4	±/
Sorption selectivity								
Polymer	O_2/N_2		N_2/CH_4		CO_2/CH_4		CO_2/N_2	
PAE-F	1.3	±0.1	0.31	±0.02	3.7	±0.2	11.9	±0.8
6FDA-OFB [160]	1.2	±0.2	0.36	±0.06	5.6	±1.0	15.6	±2.8
6FDA-OHB [160]	1.3	±0.1	0.20	±0.02	4.2	±0.5	21.1	±2.5
6FDA-DATRI [162]	1.1	±/	0.37	±/	3.5	±/	9.7	±/

4.7 Acknowledgments

The synthetic design of materials to incorporate pore architecture was supported by the U.S. Department of Energy, Office of Science, Office of Basic Energy Sciences, Separation Science program through award number DE-SC0019087. The authors also gratefully acknowledge the Office of Naval Research under award number N00014-21-1-2666 for developing strategies related to site-specific CO_2 binding. K.R.S. acknowledges support from the National Science Foundation Graduate Research Fellowship under grant number 1745302. T.M.S. is grateful for funding from the National Science Foundation (DMR-2207299).

References

[1] M. Galizia, W. S. Chi, Z. P. Smith, T. C. Merkel, R. W. Baker, and B. D. Freeman, "50^{th} anniversary perspective: Polymers and mixed matrix membranes for gas and vapor separation: A review and prospective opportunities," *Macromolecules*, vol. 50, no. 20, pp. 7809–7843, 2017. DOI: 10.1021/acs.macromol.7b01718.

[2] W. J. Koros and C. Zhang, "Materials for next-generation molecularly selective synthetic membranes," *Nat. Mater.*, vol. 16, no. 3, pp. 289–297, 2017. DOI: 10.1038/nmat4805.

[3] D. F. Sanders, Z. P. Smith, R. Guo, L. M. Robeson, J. E. McGrath, D. R. Paul, and B. D. Freeman, "Energy-efficient polymeric gas separation membranes for a sustainable future: A review," *Polymer*, vol. 54, no. 18, pp. 4729–4761, 2013. DOI: 10.1016/j.polymer.2013.05.075.

[4] N. B. McKeown and P. M. Budd, "Polymers of intrinsic microporosity (pims): Organic materials for membrane separations, heterogeneous catalysis and hydrogen storage," *Chem. Soc. Rev.*, vol. 35, no. 8, pp. 675–683, 2006. DOI: 10.1039/b600349d.

[5] I. Rose, C. G. Bezzu, M. Carta, *et al.*, "Polymer ultrapermeability from the inefficient packing of 2d chains," *Nat. Mater.*, vol. 16, no. 9, pp. 932–937, 2017. DOI: 10.1038/nmat4939.

[6] P. M. Budd, S. M. Makhseed, B. S. Ghanem, K. J. Msayib, C. E. Tattershall, and N. B. McKeown, "Microporous polymeric materials," *Mater. Today*, vol. 7, no. 4, pp. 40–46, 2004. DOI: 10.1016/S1369-7021(04)00188-9.

[7] P. M. Budd, B. S. Ghanem, S. Makhseed, N. B. McKeown, K. J. Msayib, and C. E. Tattershall, "Polymers of intrinsic microporosity (pims): Robust, solution-processable, organic nanoporous materials," *Chem. Commun.*, vol. 4, no. 2, pp. 230–231, 2004. DOI: 10.1039/b311764b.

[8] P. Li, T.-S. Chung, and D. R. Paul, "Gas sorption and permeation in pim-1," *J. Membr. Sci.*, vol. 432, pp. 50–57, 2013. DOI: 10.1016/j.memsci.2013.01.009.

[9] T. M. Long and T. M. Swager, "Molecular design of free volume as a route to low-κ dielectric materials," *J. Am. Chem. Soc.*, vol. 125, no. 46, pp. 14 113–14 119, 2003. DOI: 10.1021/ja0360945.

[10] M. Carta, M. Croad, R. Malpass-Evans, J. C. Jansen, P. Bernardo, G. Clarizia, K. Friess, M. Lanć, and N. B. McKeown, "Triptycene induced enhancement of membrane gas selectivity for microporous tröger's base polymers," *Adv. Mater.*, vol. 26, no. 21, pp. 3526–3531, 2014. DOI: 10.1002/adma.201305783.

[11] M. Carta, R. Malpass-Evans, M. Croad, Y. Rogan, J. C. Jansen, P. Bernardo, F. Bazzarelli, and N. B. McKeown, "An efficient polymer molecular sieve for membrane gas separations," *Science*, vol. 339, no. 6117, pp. 303–307, 2013. DOI: 10.1126/science.1228032.

[12] S. Luo, B. Zhang, J. R. Wiegand, B. D. Freeman, and R. Guo, "Pentiptycene-based polyimides with hierarchically controlled molecular cavity architecture for efficient membrane gas separation," *J. Membr. Sci.*, vol. 480, pp. 20–30, 2015. DOI: 10.1016/j.memsci.2015.01.043.

[13] T. Corrado and R. Guo, "Macromolecular design strategies toward tailoring free volume in glassy polymers for high performance gas separation membranes," *Mol. Syst. Des. Eng.*, vol. 5, no. 1, pp. 22–48, 2020. DOI: 10.1039/C9ME00099B.

[14] Y. Wang, B. S. Ghanem, Y. Han, and I. Pinnau, "Facile synthesis and gas transport properties of hünlich's base-derived intrinsically microporous polyimides," *Polymer*, vol. 201, p. 122 619, 2020. DOI: 10.1016/j.polymer.2020.122619.

[15] Z. P. Smith, G. Hernández, K. L. Gleason, *et al.*, "Effect of polymer structure on gas transport properties of selected aromatic polyimides, polyamides and tr polymers," *J. Membr. Sci.*, vol. 493, pp. 766–781, 2015. DOI: 10.1016/j.memsci.2015.06.032.

[16] H. B. Park, C. H. Jung, Y. M. Lee, A. J. hill, S. J. P. ad Stephen T. Mudie, E. V. Wagner, B. D. Freeman, and D. J. Cookson, "Polymers with cavities tuned for fast selective transport of small molecules and ions," *Science*, vol. 318, no. 5848, pp. 254–258, 2007. DOI: 10.1126/science.1146744.

[17] H. W. H. Lai, F. M. Benedetti, J. M. Ahn, A. M. Robinson, Y. Wang, I. Pinnau, Z. P. Smith, and Y. Xia, "Hydrocarbon ladder polymers with ultrahigh permselectivity for membrane gas separations," *Science*, vol. 375, pp. 1390–1392, 2022. DOI: 10.1126/science.abl7163.

[18] J. R. Wiegan, Z. P. Smith, Q. Liu, C. T. Patterson, B. D. Freeman, and R. Guo, "Synthesis and characterization of triptycene-based polyimides with tunable high fractional free volume for gas separation membranes," *J. Mater. Chem. A*, vol. 2, no. 33, pp. 13 309–13 320, 2014. DOI: 10.1039/C4TA02303J.

[19] Y. Zhao, Y. He, and T. M. Swager, "Porous organic polymers via ring opening metathesis polymerization," *ACS Macro Lett.*, vol. 7, no. 3, pp. 300–304, 2018. DOI: 10.1021/acsmacrolett.8b00041.

[20] Y. He, F. M. Benedetti, S. Lin, C. Liu, Y. Zhao, H.-Z. Ye, T. V. Voorhis, M. G. D. Angelis, T. M. Swager, and Z. P. Smith, "Polymers with side chain porosity for ultrapermeable and plasticization resistant materials for gas separations," *Adv. Mater.*, vol. 31, p. 1 807 871, 2019. DOI: 10.1002/adma.201807871.

[21] L. M. Robeson, "The upper bound revisited," *J. Membr. Sci.*, vol. 320, no. 1, pp. 390–400, 2008. DOI: 10.1016/j.memsci.2008.04.030.

[22] L. M. Robeson, "Correlation of separation factor versus permeability for polymeric membranes," *J. Membr. Sci.*, vol. 62, no. 2, pp. 165–185, 1991. DOI: 10.1016/0376-7388(91)80060-J.

[23] N. A. Seaton, J. P. R. B. Walton, and N. quirke, "A new analysis method for the determination of the pore size distribution of porous carbons from nitrogen adsorption measurements," *Carbon*, vol. 27, no. 6, pp. 853–861, 1989. DOI: 10.1016/0008-6223(89)90035-3.

[24] A. Bondi, "Van der waals volumes and radii," *J. Phys. Chem.*, vol. 68, no. 3, pp. 441–451, 1964. DOI: 10.1021/j100785a001.

[25] D. W. V. Krevelen and K. T. Nijenhuis, *Properties of polymers: their correlation with chemical structure; their numerical estimation and prediction from additive group contributions*. Elsevier, 2009.

[26] J. Y. Park and D. R. Paul, "Correlation and prediction of gas permeability in glassy polymer membrane materials via a modified free volume based group contribution method," *J. Membr. Sci.*, vol. 125, no. 1, pp. 23–29, 1997. DOI: 10.1016/S0376-7388(96)00061-0.

[27] A. X. Wu, S. Lin, K. M. Rodriguez, F. M. Benedetti, T. Joo, A. F. Grosz, K. R. Storme, N. Roy, D. Syar, and Z. P. Smith, "Revisiting group contribution theory for estimating fractional free volume of microporous polymer membranes," *J. Membr. Sci.*, vol. 636, p. 119 526, 2021. DOI: 10.1016/j.memsci.2021.119526.

[28] N. R. Horn, "A critical review of free volume and occupied volume calculation methods," *J. Membr. Sci.*, vol. 518, pp. 289–294, 2016. DOI: 10.1016/j.memsci.2016.07.014.

[29] T. Mitra, R. S. Bhavsar, D. J. Adams, P. M. Budd, and A. I. Cooper, "Pim-1 mixed matrix membranes for gas separations using cost-effective hypercrosslinked nanoparticle fillers," *Chem. Commun.*, vol. 52, no. 32, pp. 5581–5584, 2016. DOI: 10.1039/C6CC00261G.

[30] C. R. Mason, L. Maynard-Atem, N. M. Al-Harbi, P. M. Budd, P. Bernardo, F. Bazzarelli, G. Clarizia, and J. C. Jansen, "Polymer of intrinsic microporosity incorporating thioamide functionality: Preparation and gas transport properties," *Macromolecules*, vol. 44, no. 16, pp. 6471–6479, 2011. DOI: 10.1021/ma200918h.

[31] R. S. Bhavsar, T. Mitra, D. J. Adams, A. I. Cooper, and P. M. Budd, "Ultrahigh-permeance pim-1 based thin film nanocomposite membranes on pan supports for co_2 separation," *J. Membr. Sci.*, vol. 564, pp. 878–886, 2018. DOI: 10.1016/j.memsci.2018.07.089.

[32] A. F. Bushell, M. P. Attfield, C. R. Mason, *et al.*, "Gas permeation parameters of mixed matrix membranes based on the polymer of intrinsic microporosity pim-1 and the zeolitic imidazolate framework zif-8," *J. Membr. Sci.*, vol. 427, pp. 48–62, 2013. DOI: 10.1016/j.memsci.2012.09.035.

[33] L. E. Starannikova, A. Y. Alentiev, R. Y. Nikiforov, I. I. Ponomarev, I. V. Blagodatskikh, A. Y. Nikolaev, V. P. Shantarovich, and Y. P. Yampolskii, "Effects of different treatments of films of pim-1 on its gas permeation parameters and free volume," *Polymer*, vol. 212, p. 123 271, 2021. DOI: 10.1016/j.polymer.2020.123271.

[34] C. H. Lau, P. Li, F. Li, T.-S. Chung, and D. R. Paul, "Reverse-selective polymeric membranes for gas separations," *Prog. Polym. Sci.*, vol. 38, no. 5, pp. 740–766, 2013. DOI: 10.1016/j.progpolymsci.2012.09.006.

[35] J. G. Wijmans and R. W. Baker, "The solution-diffusion model: A review," *J. Membr. Sci.*, vol. 107, no. 1, pp. 1–21, 1995. DOI: 10.1016/0376-7388(95)00102-I.

[36] H. L. Frisch, "The time lag in diffusion," *J. Phys. Chem.*, vol. 61, no. 1, pp. 93–95, 1957. DOI: 10.1021/j150547a018.

[37] "Transport of gases and vapors in glassy and rubbery polymers," in *Materials Science of Membranes for Gas and Vapor Separation*, Y. Yampolskii, I. Pinnau, and B. Freeman, Eds. John Wiley & Sons, Ltd, 2006, pp. 1–47.

[38] A. Thran, G. Kroll, and F. Faupel, "Correlation between fractional free volume and diffusivity of gas molecules in glassy polymers," *J. Polym. Sci., Part B: Polym. Phys.*, vol. 37, no. 23, pp. 3344–3358, 1999. DOI: 10.1002/(SICI)1099-0488(19991201)37:23<3344::AID-POLB10>3.0.CO;2-A.

[39] M. H. Cohen and D. Turnbull, "Molecular transport in liquids and glasses," *J. Chem. Phys.*, vol. 31, no. 5, pp. 1164–1169, 1959. DOI: 10.1063/1.1730566.

[40] H. Lin and B. D. Freeman, "Gas permeation and diffusion in cross-linked poly(ethylene glycol diacrylate)," *Macromolecules*, vol. 39, no. 10, pp. 3568–3580, 2006. DOI: 10.1021/ma051686o.

[41] J. G. Seong, Y. Zhuang, S. Kim, Y. S. Do, W. H. Lee, M. D. Guiver, and Y. M. Lee, "Effect of methanol treatment on gas sorption and transport behavior of intrinsically microporous polyimide membranes incorporating tröger's base," *J. Membr. Sci.*, vol. 480, pp. 104–114, 2015. DOI: 10.1016/j.memsci.2015.01.022.

[42] P. M. Budd, N. B. McKeown, B. S. Ghanem, K. J. Msayib, D. ritsch, L. Starannikova, N. Belov, O. Sanfirova, Y. Yampolskii, and V. Shantarovich, "Gas permeation parameters and other physicochemical properties of a polymer of intrinsic microporosity: Polybenzodioxane pim-1," *J. Membr. Sci.*, vol. 325, no. 2, pp. 851–860, 2008. DOI: 10.1016/j.memsci.2008.09.010.

[43] Y. Rogan, L. Starannikova, V. Ryzhikh, Y. Yampolskii, P. Bernardo, F. Bazzarelli, J. C. Jansen, and N. B. McKeown, "Synthesis and gas permeation properties of novel spirobisindane-based polyimides of intrinsic microporosity," *Polym. Chem.*, vol. 4, pp. 3813–3820, 2013. DOI: 10.1039/c3py00451a.

[44] M. L. Jue, C. S. McKay, B. A. McCool, M. G. Finn, and R. P. Lively, "Effect of nonsolvent treatments on the microstructure of pim-1," *Macromolecules*, vol. 48, no. 16, pp. 5780–5790, 2015. DOI: 10.1021/acs.macromol.5b01507.

[45] A. Fuoco, B. Comesaña-Gándara, M. Long, E. Esposito, M. Monteleone, I. Rose, C. G. Bezzu, M. Carta, N. B. McKeown, and J. C. Jansen, "Temperature dependence of gas permeation and diffusion in triptycene-based ultrapermeable polymers of intrinsic microporosity," *ACS Appl. Mater. Interfaces*, vol. 10, no. 42, pp. 36 475–36 482, 2018. DOI: 10.1021/acsami.8b13634.

[46] M. Minelli, B. R. Pimentel, M. L. Jue, R. P. Lively, and G. C. Sarti, "Analysis and utilization of cryogenic sorption isotherms for high free volume glassy polymers," *Polymer*, vol. 170, pp. 157–167, 2019. DOI: 10.1016/j.polymer.2019.03.012.

[47] P. M. Budd, K. J. Msayib, C. E. Tattershall, B. S. Ghanem, K. J. Reynolds, N. B. McKeown, and D. Fritsch, "Gas separation membranes from polymers of intrinsic microporosity," *J. Membr. Sci.*, vol. 251, no. 1, pp. 263–269, 2005. DOI: 10.1016/j.memsci.2005.01.009.

[48] H. Lin and B. D. Freeman, "Permeation and diffusion," in *Springer-Handbook of Materials Measurement Methods*, H. Czichos, T. Saito, and L. Smith, Eds. Springer, 2006, pp. 371–387. DOI: 10.1007/978-3-540-30300-8.

[49] P. R. Bevington, D. K. Robinson, J. M. Blair, A. J. Mallinckrodt, and S. McKay, *Data Reduction and Error Analysis for the Physical Sciences*, 3rd ed. New York: McGraw-Hill, 2003.

[50] N. Alaslai, B. Ghanem, F. Alghunaimi, E. Litwiller, and I. Pinnau, "Pure- and mixed-gas permeation properties of highly selective and plasticization resistant hydroxyldiamine-based 6fda polyimides for co_2/ch_4 separation," *J. Membr. Sci.*, vol. 505, pp. 100–107, 2016. DOI: 10.1016/j.memsci.2015.12.053.

[51] R. W. Baker and K. Lokhandwala, "Natural gas processing with membranes: An overview," *Ind. Eng. Chem. Res.*, vol. 47, no. 7, pp. 2109–2121, 2008. DOI: 10.1021/ie071083w.

[52] C. Y. Chuah, K. Goh, Y. Yang, H. Gong, W. Li, H. E. Karahan, M. D. Guiver, R. Wang, and T.-H. Bae, "Harnessing filler materials for enhancing biogas separation membranes," *Chem. Rev.*, vol. 118, no. 18, pp. 8655–8769, 2018. DOI: 10.1021/acs.chemrev.8b00091.

[53] Q. Qian, P. A. Asinger, M. J. Lee, G. Han, K. M. Rodriguez, S. Lin, F. M. Benedetti, A. X. Wu, W. S. Chi, and Z. P. Smith, "Mof-based membranes for gas separations," *Chem. Rev.*, vol. 120, no. 16, pp. 8161–8266, 2020. DOI: 10.1021/acs.chemrev.0c00119.

[54] C. Bauer, K. Treyer, C. Antonini, *et al.*, "On the climate impacts of blue hydrogen production," *Sustain. Energy Fuels*, vol. 6, no. 1, pp. 66–75, 2022. DOI: 10.1039/d1se01508g.

[55] F. Ferella, A. Puca, G. Taglieri, L. Rossi, and K. Gallucci, "Separation of carbon dioxide for biogas upgrading to biomethane," *J. Clean. Prod.*, vol. 164, pp. 1205–1218, 2017. DOI: 10.1016/j.jclepro.2017.07.037..

[56] A. Bos, I. G. M. Pünt, M. Wessling, and H. Strathmann, "Co_2-induced plasticization phenomena in glassy polymers," *J. Membr. Sci.*, vol. 155, no. 1, pp. 67–78, 1999. DOI: 10.1016/S0376-7388(98)00299-3.

[57] M. Wessling, S. Schoeman, T. van der Boomgaard, and C. A. Smolders, "Plasticization of gas separation membranes," *Gas Sep. Purif.*, vol. 5, no. 4, pp. 222–228, 1991. DOI: 10.1016/0950-4214(91)80028-4.

[58] M. Wessling, I. Huisman, T. van der Boomgaard, and C. A. Smolders, "Time-dependent permeation of carbon dioxide through a polyimide membrane above the plasticization pressure," *J. Appl. Polym. Sci.*, vol. 58, no. 11, pp. 1959–1966, 1995. DOI: 10.1002/app.1995.070581105.

[59] W. Qiu, C.-C. Chen, L. Xu, L. Cui, D. R. Paul, and W. J. Koros, "Sub-t_g cross-linking of a polyimide membrane for enhanced co_2 plasticization resistance for natural gas separation," *Macromolecules*, vol. 44, no. 15, pp. 6046–6056, 2011. DOI: 10.1021/ma201033j.

[60] C. Staudt-Bickel and W. J. Koros, "Improvement of co_2/ch_4 separation characteristics of polyimides by chemical crosslinking," *J. Membr. Sci.*, vol. 155, no. 1, pp. 145–154, 1999. DOI: 10.1016/S0376-7388(98)00306-8.

[61] J. H. Kim, W. J. Koros, and D. R. Paul, "Effects of co_2 exposure and physical aging on the gas permeability of thin 6fda-based polyimide membranes: Part 2. with crosslinking," *J. Membr. Sci.*, vol. 282, no. 1, pp. 32–43, 2006. DOI: 10.1016/j.memsci.2006.05.003.

[62] Q. Song, S. Cao, R. H. Pritchard, B. Ghalei, S. A. Al-Muhtaseb, E. M. Terentjev, A. K. Cheetham, and E. Sivaniah, "Controlled thermal oxidative crosslinking of polymers of intrinsic microporosity towards tunable molecular sieve membranes," *Nat. Commun.*, vol. 5, no. 1, p. 4813, 2014. DOI: 10.1038/ncomms5813.

[63] A. Bos, I. G. M. Pünt, M. Wessling, and H. Strathmann, "Plasticization-resistant glassy polyimide membranes for co_2/co_4 separations," *Separ. Purif. Technol.*, vol. 14, no. 1, pp. 27–39, 1998. DOI: 10.1016/S1383-5866(98)00057-4.

[64] J. Vaughn and W. J. Koros, "Effect of the amide bond diamine structure on the co_2, h_2s, and ch_4 transport properties of a series of novel 6fda-based polyamide–imides for natural gas purification," *Macromolecules*, vol. 45, no. 17, pp. 7036–7049, 2012. DOI: 10.1021/ma301249x.

[65] J. T. Vaughn, W. J. Koros, J. R. Johnson, and O. Karvan, "Effect of thermal annealing on a novel polyamide-imide polymer membrane for aggressive acid gas separations," *J. Membr. Sci.*, vol. 401, pp. 163–174, 2012. DOI: 10.1016/j.memsci.2012.01.047.

[66] X. Duthie, S. Kentish, S. J. Pas, A. J. Hill, C. Powell, K. Nagai, G. Stevens, and G. Qiao, "Thermal treatment of dense polyimide membranes," *J. Polym. Sci., Part B: Polym. Phys.*, vol. 46, no. 18, pp. 1879–1890, 2008. DOI: 10.1002/polb.21521.

[67] R. Swaidan, B. Ghanem, E. Litwiller, and I. Pinnau, "Effects of hydroxylfunctionalization and sub-t_g thermal annealing on high pressure pure- and mixedgas co_2/ch_4 separation by polyimide membranes based on 6fda and triptycenecontaining dianhydrides," *J. Membr. Sci.*, vol. 475, pp. 571–581, 2015. DOI: 10.1016/j.memsci.2014.10.046.

[68] F. Alghunaimi, B. Ghanem, N. Alaslai, M. Mukaddam, and I. Pinnau, "Triptycene dimethyl-bridgehead dianhydride-based intrinsically microporous hydroxylfunctionalized polyimide for natural gas upgrading," *J. Membr. Sci.*, vol. 520, pp. 240–246, 2016. DOI: 10.1016/j.memsci.2016.07.058.

[69] N. Alaslai, B. Ghanem, F. Alghunaimi, and I. Pinnau, "High-performance intrinsically microporous dihydroxyl-functionalized triptycene-based polyimide for natural gas separation," *Polymer*, vol. 91, pp. 128–135, 2016. DOI: 10.1016/j.polymer.2016.03.063.

[70] W. Qiu, L. Xu, C.-C. Chen, D. R. Paul, and W. J. Koros, "Gas separation performance of 6fda-based polyimides with different chemical structures," *Polymer*, vol. 54, no. 22, pp. 6226–6235, 2013. DOI: 10.1016/j.polymer.2013.09.007.

[71] M. A. Abdulhamid, G. Genduso, Y. Wang, X. Ma, and I. Pinnau, "Plasticization-resistant carboxyl-functionalized 6fda-polyimide of intrinsic microporosity (pim-pi) for membrane-based gas separation," *Ind. Eng. Chem. Res.*, vol. 59, no. 12, pp. 5247–5256, 2020. DOI: 10.1021/acs.iecr.9b04994.

[72] N. Alaslai, X. Ma, B. Ghanem, Y. Wang, F. Alghunaimi, and I. Pinnau, "Synthesis and characterization of a novel microporous dihydroxyl-functionalized triptycenediamine-based polyimide for natural gas membrane separation," *Macromol. Rapid Commun.*, vol. 38, no. 18, pp. 1–5, 2017. DOI: 10.1002/marc.201700303.

[73] X. Ma, R. Swaidan, Y. Belmabkhout, Y. Zhu, E. Litwiller, M. Jouiad, I. Pinnau, and Y. Han, "Synthesis and gas transport properties of hydroxyl-functionalized polyimides with intrinsic microporosity," *Macromolecules*, vol. 45, no. 9, pp. 3841–3849, 2012. DOI: 10.1021/ma300549m.

[74] F. Li, C. Zhang, and Y. Weng, "Preparation and gas separation properties of triptycene-based microporous polyimide," *Macromol. Chem. Phys.*, vol. 220, no. 10, pp. 1–7, 2019. DOI: 10.1002/macp.201900047.

[75] S. Luo, J. R. Wiegard, B. Kazanowska, C. M. Doherty, K. Konstas, A. J. Hill, and R. Guo, "Finely tuning the free volume architecture in iptycene-containing polyimides for highly selective and fast hydrogen transport," *Macromolecules*, vol. 49, no. 9, pp. 3395–3405, 2016. DOI: 10.1021/acs.macromol.6b00485.

[76] S. Luo, Q. Zhang, T. K. Bear, T. E. Curtis, R. K. Roeder, C. M. Doherty, A. J. Hill, and R. Guo, "Triptycene-containing poly(benzoxazole-co-imide) membranes with enhanced mechanical strength for high-performance gas separation," *J. Membr. Sci.*, vol. 551, pp. 305–314, 2018. DOI: 10.1016/j.memsci.2018.01.052.

[77] R. Williams, L. A. Burt, E. Esposito, J. C. Jansen, E. Tocci, C. Rissuto, M. Lanć, M. Carta, and N. B. McKeown, "A highly rigid and gas selective methanopentacene-based polymer of intrinsic microporosity derived from tröger's base polymerization," *J. Mater. Chem.*, vol. 6, no. 14, pp. 5661–5667, 2018. DOI: 10.1039/C8TA00509E.

[78] E. Lasseuguette, R. Malpass-Evans, M. Carta, N. B. McKeown, and M.-C. Ferrari, "Temperature and pressure dependence of gas permeation in a microporous-tröger's base polymer," *Membranes*, vol. 8, no. 4, pp. 1–11, 2018. DOI: 10.3390/membranes8040132.

[79] X. Ma and I. Pinnau, "Effect of film thickness and physical aging on intrinsic gas permeation properties of microporous ethanoanthracene-based polyimides," *Macromolecules*, vol. 51, no. 3, pp. 1069–1076, 2018. DOI: 10.1021/acs.macromol.7b02556.

[80] P. M. Budd, E. S. Elabas, B. S. Ghanem, S. Makhseed, N. B. McKeown, K. J. Msayib, C. E. Tattershall, and D. Wang, "Solution-processed, organophilic membrane derived from a polymer of intrinsic microporosity," *Adv. Mater.*, vol. 16, no. 5, pp. 456–459, 2004. DOI: 10.1002/adma.200306053.

[81] R. Swaidan, B. Ghanem, E. Litwiller, and I. Pinnau, "Physical aging, plasticization and their effects on gas permeation in "rigid" polymers of intrinsic microporosity," *Macromolecules*, vol. 48, no. 18, pp. 6553–6561, 2015. DOI: 10.1021/acs.macromol.5b01581.

[82] R. Swaidan, B. Ghanem, M. Al-Saeedi, E. Litwiller, and I. Pinnau, "Role of intra-chain rigidity in the plasticization of intrinsically microporous triptycene-based polyimide membranes in mixed-gas co$_2$/ch$_4$ separations," *Macromolecules*, vol. 47, no. 21, pp. 7453–7462, 2014. DOI: 10.1021/ma501798v.

[83] F. M. Benedetti, Y.-C. M. Wu, S. Lin, Y. He, E. Flear, K. R. Storme, C. Liu, Y. Zhao, T. M. Swager, and Z. P. Smith, "Side-chain length and dispersity in romp polymers with pore-generating side chains for gas separations," *JACS Au*, vol. 2, no. 7, pp. 1610–1615, 2022. DOI: 10.1021/jacsau.2c00219.

[84] E. S. Sanders, "Penetrant-induced plasticization and gas permeation in glassy polymers," *J. Membr. Sci.*, vol. 37, no. 1, pp. 63–80, 1988. DOI: 10.1016/S0376-7388(00)85069-3.

[85] J. D. Wind, S. M. Sirard, D. R. Paul, P. F. Green, K. P. Johnston, and W. J. Koros, "Relaxation dynamics of co$_2$ diffusion, sorption, and polymer swelling for plasticized polyimide membranes," *Macromolecules*, vol. 36, no. 17, pp. 6442–6448, 2003. DOI: 10.1021/ma034359u.

[86] K. L. Gleason, Z. P. Smith, Q. Liu, D. R. Paul, and B. D. Freeman, "Pure- and mixed-gas permeation of co$_2$ and ch$_4$ in thermally rearranged polymers based on 3,3'-dihydroxy-4,4'-diamino-biphenyl (hab) and 2,2'-bis-(3,4-dicarboxyphenyl) hexafluoropropane dianhydride (6fda)," *J. Membr. Sci.*, vol. 475, pp. 204–214, 2015. DOI: 10.1016/j.memsci.2014.10.014.

[87] R. Swaidan, B. S. Ghanem, E. Litwiller, and I. Pinnau, "Pure- and mixed-gas co$_2$/ch$_4$ separation properties of pim-1 and an amidoxime-functionalized pim-1," *J. Membr. Sci.*, vol. 457, pp. 95–102, 2014. DOI: 10.1016/j.memsci.2014.01.055.

[88] R. Swaidan, X. Ma, E. Litwiller, and I. Pinnau, "High pressure pure- and mixed-gas separation of co$_2$/ch$_4$ by thermally-rearranged and carbon molecular sieve membranes derived from a polyimide of intrinsic microporosity," *J. Membr. Sci.*, vol. 447, pp. 387–394, 2013. DOI: 10.1016/j.memsci.2013.07.057.

[89] T. Visser and M. Wessling, "When do sorption-induced relaxations in glassy polymers set in?" *Macromolecules*, vol. 40, no. 14, pp. 4992–5000, 2007. DOI: 10.1021/ma070202g.

[90] K. M. Rodriguez, A. X. Wu, Q. Qian, G. Han, S. Lin, F. M. Benedetti, H. Lee, W. S. Chi, C. M. Doherty, and Z. P. Smith, "Facile and time-efficient carboxylic acid functionalization of pim-1: Effect on molecular packing and gas separation performance," *Macromolecules*, vol. 53, no. 15, pp. 6220–6234, 2020. DOI: 10.1021/acs.macromol.0c00933.

[91] K. M. Rodriguez, F. M. Benedetti, N. Roy, A. X. Wu, and Z. P. Smith, "Sorption-enhanced mixed-gas transport in amine functionalized polymers of intrinsic microporosity (pims)," *J. Mater. Chem. A*, vol. 9, no. 41, pp. 23 631–23 642, 2021. DOI: 10.1039/D1TA06530K.

[92] M. J. T. Raaijmakers, W. Ogieglo, M. Wiese, M. Wessling, A. Nijmeijer, and N. Benes, "Sorption behavior of compressed co_2 and ch_4 on ultrathin hybrid poly(poss-imide) layers," *ACS Appl. Mater. Interfaces*, vol. 7, no. 48, pp. 26 977–26 988, 2015. DOI: 10.1021/acsami.5b08286.

[93] K. Simons, K. Nijmeijer, J. G. Sala, H. van der Werf, N. E. Benes, T. J. Dingemans, and M. Wessling, "Co_2 sorption and transport behavior of odpa-based polyetherimide polymer films," *Polymer*, vol. 51, no. 17, pp. 3907–3917, 2010. DOI: 10.1016/j.polymer.2010.06.031.

[94] W. Ogieglo, B. Ghanem, X. Ma, M. Wessling, and I. Pinnau, "High-pressure co_2 sorption in polymers of intrinsic microporosity under ultrathin film confinement," *ACS Appl. Mater. Interfaces*, vol. 10, no. 13, pp. 11 369–11 376, 2018. DOI: 10.1021/acsami.8b01402.

[95] M. Wessling, I. Huisman, T. v. d. Boomgaard, and C. A. Smolders, "Dilation kinetics of glassy, aromatic polyimides induced by carbon dioxide sorption," *J. Polym. Sci., Part B: Polym. Phys.*, vol. 33, no. 9, pp. 1371–1384, 1995. DOI: 10.1002/polb.1995.090330907.

[96] R. R. Tiwari, Z. P. Smith, H. Lin, B. D. Freeman, and D. R. Paul, "Gas permeation in thin films of "high free-volume" glassy perfluoropolymers: Part ii. co_2 plasticization and sorption," *Polymer*, vol. 61, pp. 1–14, 2015. DOI: 10.1016/j.polymer.2014.12.008.

[97] M. Böhning and J. Springer, "Sorptive dilation and relaxational processes in glassy polymer/gas systems—i. poly(sulfone) and poly(ether sulfone)," *Polymer*, vol. 39, no. 21, pp. 5183–5195, 1998. DOI: 10.1016/S0032-3861(97)10114-8.

[98] P. D. Southon, D. J. Price, P. K. Nielsen, C. J. McKenzie, and C. J. Kepert, "Reversible and selective o2 chemisorption in a porous metal-organic host material," *J. Am. Chem. Soc.*, vol. 133, no. 28, pp. 10 885–10 891, 2011. DOI: 10.1021/ja202228v.

[99] R. Vaidhyanathan, S. S. Iremonger, G. K. H. Shimizu, P. G. Boyd, S. Alavi, and T. K. Woo, "Direct observation and quantification of co_2 binding within an amine-functionalized nanoporous solid," *Science*, vol. 330, no. 6004, pp. 650–653, 2010. DOI: 10.1126/science.1194237.

[100] P. I. Ravikovitch and A. V. Neimark, "Diffusion-controlled hysteresis," *Adsorption*, vol. 11, pp. 265–270, 2005. DOI: 10.1007/s10450-005-5935-2.

[101] S. A. Sapchenko, M. O. Barsukova, R. V. Belosludov, *et al.*, "Understanding hysteresis in carbon dioxide sorption in porous metal-organic frameworks," *Inorg. Chem.*, vol. 58, no. 10, pp. 6811–6820, 2019. DOI: 10.1021/acs.inorgchem.9b00016.

[102] J. Jeromenok and J. Weber, "Restricted access: On the nature of adsorption/desorption hysteresis in amorphous, microporous polymeric materials," *Langmuir*, vol. 29, no. 42, pp. 12 982–12 989, 2013. DOI: 10.1021/la402630s.

[103] L. Espinal, W. Wong-Ng, J. A. Kaduk, *et al.*, "Time-dependent co_2 sorption hysteresis in a one-dimensional microporous octahedral molecular sieve," *J. Am. Chem. Soc.*, vol. 134, no. 18, pp. 7944–7951, 2012. DOI: 10.1021/ja3014133.

[104] T. Hiratsuka, H. Tanaka, and M. T. Miyahara, "Mechanism of kinetically controlled capillary condensation in nanopores: A combined experimental and monte carlo approach," *ACS Nano*, vol. 11, no. 1, pp. 269–276, 2017. DOI: 10.1021/acsnano.6b05550.

[105] T. Horikawa, D. D. Do, and D. Nicholson, "Capillary condensation of adsorbates in porous materials," *Adv. Colloid Interface Sci.*, vol. 169, no. 1, pp. 40–58, 2011. DOI: 10.1016/j.cis.2011.08.003.

[106] S. Kanehashi and K. Nagai, "Analysis of dual-mode model parameters for gas sorption in glassy polymers," *J. Membr. Sci.*, vol. 253, no. 1, pp. 117–138, 2005. DOI: 10.1016/j.memsci.2005.01.003.

[107] R. J. Swaidan, B. Ghanem, R. Swaidan, E. Litwiller, and I. Pinnau, "Pure- and mixed-gas propylene/propane permeation properties of spiro- and triptycene-based microporous polyimides," *J. Membr. Sci.*, vol. 492, pp. 116–122, 2015. DOI: 10.1016/j.memsci.2015.05.044.

[108] C. R. Mason, L. Maynard-Atem, K. W. J. Heard, B. Satilmis, P. M. Budd, K. Friess, M. Lanc, P. Bernardo, G. Clarizia, and J. C. Jansen, "Enhancement of co_2 affinity in a polymer of intrinsic microporosity by amine modification," *Macromolecules*, vol. 47, no. 3, pp. 1021–1029, 2014. DOI: 10.1021/ma401869p.

[109] I. N. Haugan, M. J. Maher, A. B. Chang, T.-P. Lin, R. H. Grubbs, M. A. Hillmyer, and F. S. Bates, "Consequences of grafting density on the linear viscoelastic behavior of graft polymers," *ACS Macro Lett.*, vol. 7, no. 5, pp. 525–530, 2018. DOI: 10.1021/acsmacrolett.8b00116.

[110] B. Zhao, "Shape-changing bottlebrush polymers," *J. Phys. Chem. B*, vol. 125, no. 24, pp. 6373–6389, 2021. DOI: 10.1021/acs.jpcb.1c01819.

[111] J. X. Zheng, H. Xiong, W. Y. Chen, K. Lee, R. M. V. Horn, R. P. Quirk, B. Lotz, E. L. Thomas, A.-C. Shi, and S. Z. D. Cheng, "Onsets of tethered chain overcrowding and highly stretched brush regime via crystalline-amorphous diblock copolymers," *Macromolecules*, vol. 39, no. 2, pp. 641–650, 2006. DOI: 10.1021/ma052166w.

[112] N. Du, H. B. Park, G. P. Robertson, M. M. Dal-Cin, T. Visser, L. Scoles, and M. D. Guiver, "Polymer nanosieve membranes for co_2-capture applications," *Nat. Mater.*, vol. 10, no. 5, pp. 372–375, 2011. DOI: 10.1038/nmat2989.

[113] X. Ma, Z. Zhu, W. Shi, W. Ji, J. Li, Y. Wang, and I. Pinnau, "Unprecedented gas separation performance of adifluoro-functionalized triptycene-based ladder pim membrane at low temperature," *J. Mater. Chem. A*, vol. 9, no. 9, pp. 5404–5414, 2021. DOI: 10.1039/d0ta09703a.

[114] G. Genduso, Y. Wang, B. S. Ghanem, and I. Pinnau, "Permeation, sorption, and diffusion of co_2-ch_4 mixtures in polymers of intrinsic microporosity: The effect of intrachain rigidity on plasticization resistance," *J. Membr. Sci.*, vol. 584, pp. 100–109, 2019. DOI: 10.1016/j.memsci.2019.05.014.

[115] Y. Wang, X. Ma, B. S. Ghanem, F. Alghunaimi, I. Pinnau, and Y. Han, "Olymers of intrinsic microporosity for energy-intensive membrane-based gas separations," *Mater. Today Nano.*, vol. 3, pp. 69–95, 2018. DOI: 10.1016/j.mtnano.2018.11.003.

[116] J. H. Dymond, K. N. Marsh, R. C. Wilhoit, K. C. Wong, and M. D. Frenkel, *The Virial Coefficients of Pure Gases*. Berlin: Springer, 2002, vol. 21.

[117] P. R. Bevington, D. K. Robinson, J. M. Blair, A. J. Mallinckrodt, and S. McKay, "Data reduction and error analysis for the physical sciences," *Comput. Phys.*, vol. 7, no. 4, pp. 415–416, 1993. DOI: 10.1063/1.4823194.

[118] W. J. Box, M. T. Webb, and M. Galizia, "Evaluating the experimental uncertainty in gas and vapor sorption/adsorption measurements: Fundamental considerations and experimental design implications," *Ind. Eng. Chem. Res.*, vol. 61, no. 27, pp. 9856–9868, 2022. DOI: 10.1021/acs.iecr.2c01414.

[119] K. A. Stevens, Z. P. Smith, K. L. Gleason, M. Galizia, D. R. Paul, and B. D. Freeman, "Influence of temperature on gas solubility in thermally rearranged (tr) polymers," *J. Membr. Sci.*, vol. 533, pp. 75–83, 2017. DOI: 10.1016/j.memsci.2017.03.005.

[120] A. X. Wu, J. A. Drayton, K. M. Rodriguez, F. M. Benedetti, Q. Qian, S. Lin, and Z. P. Smith, "Elucidating the role of fluorine content on gas sorption properties of fluorinated polyimides," *Macromolecules*, vol. 54, no. 1, pp. 22–34, 2021. DOI: 10.1021/acs.macromol.0c01746.

[121] P. Stanovsky, M. Karaszova, Z. Petrusova, M. Monteleone, J. C. Jansen, B. Comesaña-Gándara, N. B. McKeown, and P. Izak, "Upgrading of raw biogas using membranes based on the ultrapermeable polymer of intrinsic microporosity pim-tmn-trip," *J. Membr. Sci.*, vol. 618, p. 118 694, 2021. DOI: 10.1016/j.memsci.2020.118694.

[122] H. Dong, Z. Zhu, K. Li, Q. Li, W. Ji, B. He, J. Li, and X. Ma, "Significantly improved gas separation properties of sulfonated pim-1 by direct sulfonation using so_3 solution," *J. Membr. Sci.*, vol. 635, p. 119 440, 2021. DOI: 10.1016/j.memsci.2021.119440.

[123] C. G. Bezzu, A. Fuoco, E. Esposito, M. Monteleone, M. Longo, J. C. Jansen, G. S. Nichol, and N. B. McKeown, "Ultrapermeable polymers of intrinsic microporosity containing spirocyclic units with fused triptycenes," *Adv. Funct. Mater.*, vol. 31, no. 37, pp. 2 104 474–, 2021. DOI: 10.1002/adfm.202104474.

[124] C. Zhang, L. Fu, Z. Tian, B. Cao, and P. Li, "Post-crosslinking of triptycene-based tröger's base polymers with enhanced natural gas separation performance," *J. Membr. Sci.*, vol. 556, pp. 277–284, 2018. DOI: 10.1016/j.memsci.2018.04.013.

[125] W. F. Yong, F. Y. Li, Y. C. Xiao, T. S. Chung, and Y. W. Tong, "High performance pim-1/matrimid hollow fiber membranes for co_2/ch_4, o_2/n_2 and co_2/n_2 separation," *J. Membr. Sci.*, vol. 443, pp. 156–169, 2013. DOI: 10.1016/j.memsci.2013.04.037.

[126] H. B. T. Jeazet, S. Sorribas, J. M. Román-Marin, B. Zornoza, C. T. J. Coronas, and C. Janiak, "Increased selectivity in co_2/ch_4 separation with mixed-matrix membranes of polysulfone and mixed-mofs mil-101(cr) and zif-8," *Eur. J. Inorg. Chem.*, vol. 2016, no. 27, pp. 4363–4367, 2016. DOI: 10.1002/ejic.201600190.

[127] D. S. Sholl and R. P. Lively, "Seven chemical separations change the world," *Nature*, vol. 532, pp. 435–437, 2016. DOI: 10.1038/532435a.

[128] DOE-EPSA. "Energy co_2 emissions impacts of clean energy technology innovation and policy." Accessed on November 6 2023. (2017), [Online]. Available: https://www.energy.gov/policy/articles/energy-co2-emissions-impacts-clean-energy-technology-innovation-and-policy.

[129] R. W. Baker, "Future directions of membrane gas separation technology," *Ind. Eng. Chem. Res.*, vol. 41, no. 6, pp. 1393–1411, 2002. DOI: 10.1021/ie0108088.

[130] M. Minelli and G. C. Sarti, "10^{th} anniversary: Gas and vapor sorption in glassy polymeric membranes-critical review of different physical and mathematical models," *Ind. Eng. Chem. Res.*, vol. 59, no. 1, pp. 341–365, 2019. DOI: 10.1021/acs.iecr.9b05453.

[131] B. Comesaña-Gándara, J. Chen, C. G. Bezzu, M. Carta, I. Rose, M.-C. Ferrari, E. Esposito, A. Fuoco, J. C. Jansen, and N. B. McKeown, "Redefining the robeson upper bounds for co_2/ch_4 and co_2/n_2 separations using a series of ultrapermeable benzotriptycene-based polymers of intrinsic microporosity," *Energy Environ. Sci.*, vol. 12, no. 9, pp. 2733–2740, 2019. DOI: 10.1039/c9ee01384a.

[132] H. W. H. Lai, F. M. Benedetti, Z. Jin, Y. C. Teo, A. X. Wu, M. G. D. Angelis, Z. P. Smith, and Y. Xia, "Tuning the molecular weights, chain packing, and gas-transport properties of canal ladder polymers by short alkyl substitutions," *Macromolecules*, vol. 52, no. 16, pp. 6294–6302, 2019. DOI: 10.1021/acs.macromol.9b01155.

[133] S. Lin, K. R. Storme, Y.-C. M. Wu, F. M. Benedetti, T. M. Swager, and Z. P. Smith, "Role of side-chain length on gas transport of co_2/ch_4 mixtures in polymers with side-chain porosity," *J. Membr. Sci.*, vol. 668, p. 121 194, 2023. DOI: 10.1016/J.MEMSCI.2022.121194.

[134] J. W. Jeon, D.-G. Kim, E.-h. Sohn, Y. Yoo, Y. S. Kim, B. G. Kim, and J.-C. Lee, "Highly carboxylate-functionalized polymers of intrinsic microporosity for co_2-selective polymer membranes," *Macromolecules*, vol. 50, no. 20, pp. 8019–8027, 2017. DOI: 10.1021/acs.macromol.7b01332.

[135] X. Weng, J. E. Baez, M. Khiterer, M. Y. Hoe, Z. Bao, and K. J. Shea, "Chiral polymers of intrinsic microporosity: Selective membrane permeation of enantiomers," *Angew. Chemie Int. Ed.*, vol. 54, no. 38, pp. 11 214–11 218, 2015. DOI: 10.1002/ange.201504934.

[136] K. M. Rodriguez, S. Lin, A. X. Wu, G. Han, J. J. Teesdale, C. M. Doherty, and Z. P. Smith, "Leveraging free volume manipulation to improve the membrane separation performance of amine-functionalized pim-1," *Angew. Chemie Int. Ed.*, vol. 60, no. 12, pp. 6593–6599, 2021. DOI: 10.1002/anie.202012441.

[137] Y. Kawakami, H. Toda, M. Higashino, and Y. Yamashita, "Polynorbornenes with oligodimethylsiloxanyl substituents for selectively oxygen permeable membrane material," *Polym. J.*, vol. 20, no. 4, pp. 285–292, 1988. DOI: 10.1295/polymj.20.285.

[138] H. Martinez, N. Ren, M. E. Matta, and M. A. Hillmyer, "Ring-opening metathesis polymerization of 8-membered cyclic olefins," *Polym. Chem.*, vol. 5, no. 11, pp. 3507–3532, 2014. DOI: 10.1039/C3PY01787G.

[139] B. Winkler, A. Rehab, M. Ungerank, and F. Stelzer, "A novel side-chain liquid crystal polymer of 5-substituted cis-cyclooctene via ring-opening metathesis polymerization," *Macromol. Chem. Phys.*, vol. 198, no. 5, pp. 1417–1425, 1997. DOI: 10.1002/MACP.1997.021980510.

[140] J. D. Hatjopoulos and R. A. Register, "Synthesis and properties of well-defined elastomeric poly(alkylnorbornene)s and their hydrogenated derivatives," *Macromolecules*, vol. 38, no. 24, pp. 10 320–10 322, 2005. DOI: 10.1021/MA0515331.

[141] A. G. McDermott, G. S. Larsen, P. M. Budd, C. M. Colina, and J. Runt, "Structural characterization of a polymer of intrinsic microporosity: X-ray scattering with interpretation enhanced by molecular dynamics simulations," *Macromolecules*, vol. 44, no. 1, pp. 14–16, 2011. DOI: 10.1021/MA1024945.

[142] W. J. Koros, "Model for sorption of mixed gases in glassy polymers," *J. Polym. Sci.: Polym. Phys. Ed.*, vol. 18, no. 5, pp. 981–992, 1980. DOI: 10.1002/pol.1980.180180506.

[143] T. C. Merkel, V. Bondar, K. Nagai, B. D. Freeman, and Y. P. Yampolskii, "Gas sorption, diffusion, and permeation in poly(2,2-bis(trifluoromethyl)-4,5-difluoro-1,3-dioxole-co-tetrafluoroethylene)," *Macromolecules*, vol. 32, no. 25, pp. 8427–8440, 1999. DOI: 10.1021/ma990685r.

[144] E. Ricci, M. Minelli, and M. G. D. Angelis, "Modelling sorption and transport of gases in polymeric membranes across different scales: A review," *Membranes*, vol. 12, no. 9, p. 857, 2022. DOI: 10.3390/MEMBRANES12090857.

[145] K. M. Rodriguez, W.-N. Wu, T. Alebrahim, *et al.*, "Multi-lab study on the pure-gas permeation of commercial polysulfone (psf) membranes: Measurement standards and best practices," *J. Membr. Sci.*, vol. 659, p. 120 746, 2022. DOI: 10.1016/J.MEMSCI.2022.120746.

[146] K. M. Rodriguez, S. Lin, A. X. Wu, K. R. Storme, T. Joo, A. F. Grosz, N. Roy, D. Syar, F. M. Benedetti, and Z. P. Smith, "Penetrant-induced plasticization in microporous polymer membranes," *Chem. Soc. Revi., accepted*, 2023.

[147] T. Kobayashi and S. Kobayashi, "Swern oxidation of bicyclo[2.2.1]hept-5-ene-2,3-diol and its pyrazine-fused derivatives: An improved synthesis of bicyclo[2.2.1]hept-5-ene-2,3-dione and an unexpected ring-opening reaction," *Molecules*, vol. 5, no. 9, pp. 1062–1067, 2000. DOI: 10.3390/50901062.

[148] S. A. Sydlik, Z. Chen, and T. M. Swager, "Triptycene polyimides: Soluble polymers with high thermal stability and low refractive indices," *Macromolecules*, vol. 44, no. 4, pp. 976–980, 2011. DOI: 10.1021/ma101333p.

[149] S.-H. Hsiao, H.-M. Wang, W.-J. Chen, T.-M. Lee, and C.-M. Leu, "Synthesis and properties of novel triptycene-based polyimides," *J. Polym. Sci., Part A: Polym. Chem.*, vol. 49, no. 14, pp. 3109–3120, 2011. DOI: 10.1002/pola.24748.

[150] J.-S. Yang and T. M. Swager, "Porous shape persistent fluorescent polymer films: An approach to tnt sensory materials," *J. Am. Chem. Soc.*, vol. 120, no. 21, pp. 5321–5322, 1998. DOI: 10.1021/ja982293q.

[151] L. C. H. Moh, J. B. Goods, Y. Kim, and T. M. Swager, "Free volume enhanced proton exchange membranes from sulfonated triptycene poly(ether ketone)," *J. Membr. Sci.*, vol. 549, pp. 236–243, 2018. DOI: 10.1016/J.MEMSCI.2017.11.041.

[152] Y. Kim, L. C. H. Moh, and T. M. Swager, "Anion exchange membranes: Enhancement by addition of unfunctionalized triptycene poly(ether sulfone)s," *ACS Appl. Mater. Interfaces*, vol. 9, pp. 42 409–42 414, 2017. DOI: 10.1021/acsami.7b13058.

[153] J. R. Weidman, S. Luo, J. M. Breier, P. Buckley, P. Gao, and R. Guo, "Triptycene-based copolyimides with tailored backbone rigidity for enhanced gas transport," *Polymer*, vol. 126, pp. 314–323, 2017. DOI: 10.1016/j.polymer.2017.04.016.

[154] Y. J. Cho and H. B. Park, "Gas separation properties of triptycene-based polyimide membranes," in *Modern Applications in Membrane Science and Technology*. American Chemical Society, 2011, ch. 8, pp. 107–128.

[155] T. Corrado, Z. Huang, J. Aboki, and R. Gup, "Microporous polysulfones with enhanced separation performance via integration of the triptycene moiety," *Ind. Eng. Chem. Res.*, vol. 59, no. 12, pp. 5351–5361, 2020. DOI: 10.1021/acs.iecr.9b04861.

[156] A. F. Yee and S. A. Smith, "Molecular structure effects on the dynamic mechanical spectra of polycarbonates," *Macromolecules*, vol. 14, no. 1, pp. 54–64, 1981. DOI: 10.1021/MA50002A009.

[157] R. F. Boyer, *Molecular Basis of Transitions and Relaxations*. CRC Press, 1978.

[158] J. W. Labadie and J. L. Hedrick, "New activating groups for poly(aryl ether) synthesis," *Makromol. Chemie. Macromol. Symp.*, vol. 54, no. 1, pp. 313–330, 1992. DOI: 10.1002/MASY.19920540124.

[159] S. Guo and T. M. Swager, "Versatile porous poly(arylene ether)s via pd-catalyzed c-o polycondensation," *J. Am. Chem. Soc.*, vol. 143, no. 30, pp. 11 828–11 835, 2021. DOI: 10.1021/JACS.1C05853.

[160] A. X. Wu, J. A. Drayton, K. M. Rodriguez, Q. Qian, S. Lin, and Z. P. Smith, "Influence of aliphatic and aromatic fluorine groups on gas permeability and morphology of fluorinated polyimide films," *Macromolecules*, vol. 53, no. 13, pp. 5085–5095, 2020. DOI: 10.1021/ACS.MACROMOL.0C01024.

[161] F. Alghunaimi, B. Ghanem, N. Alaslai, R. Swaidan, E. Litwiller, and I. Pinnau, "Gas permeation and physical aging properties of iptycene diamine-based microporous polyimides," *J. Membr. Sci.*, vol. 490, pp. 321–327, 2015. DOI: 10.1016/j.memsci.2015.05.010.

[162] Y. J. Cho and H. B. Park, "High performance polyimide with high internal free volume elements," *Macromol. Rapid Commun.*, vol. 32, no. 7, pp. 579–586, 2011. DOI: 10.1002/marc.201000690.

[163] G. L. Clark and L. W. Pickett, "Crystal structures of some derivatives of diphenyl," *Proc. Natl. Acad. Sci. U. S. A.*, vol. 16, no. 1, pp. 20–27, 1930. DOI: 10.1073/pnas.16.1.20.

[164] C. R. Martinez and B. L. Iverson, "Rethinking the term "pi-stacking."," *Chem. Sci.*, vol. 3, no. 7, pp. 2191–2201, 2012. DOI: 10.1039/C2SC20045G.

[165] A. T. Hargreaves and S. H. Rizvi, "The crystal and molecular structure of biphenyl," *Acta Crystallogr.*, vol. 15, no. 4, pp. 365–373, 1962. DOI: 10.1107/s0365110x62000894.

[166] J. Trotter, "The crystal and molecular structure of biphenyl," *Acta Crystallogr.*, vol. 14, no. 11, pp. 1135–1140, 1961. DOI: 10.1107/S0365110X6100334X.

[167] F. Grein, "Twist angles and rotational energy barriers of biphenyl and substituted biphenyls," *J. Phys. Chem. A*, vol. 106, no. 15, pp. 3823–3827, 2002. DOI: 10.1021/JP0122124.

[168] J. Hernández-Trujillo and C. F. Matta, "Hydrogen-hydrogen bonding in biphenyl revisited," *Struct. Chem.*, vol. 18, no. 6, pp. 849–857, 2007. DOI: 10.1007/S11224-007-9231-5.

[169] Z. Zhang, X. Ren, S. K. Guolong Huo, Z. Wang, and N. Li, "Tuning interchain cavity of fluorinated polyimide by daba for improved gas separation performance," *J. Membr. Sci.*, vol. 675, p. 121 485, 2023. DOI: 10.1016/j.memsci.2023.121485.

[170] Y.-H. Kim, H.-S. Kim, and S.-K. Kwon, "Synthesis and characterization of highly soluble and oxygen permeable new polyimides based on twisted biphenyl dianhydride and spirobifluorene diamine," *Macromolecules*, vol. 38, no. 19, pp. 7950–7956, 2005. DOI: 10.1021/MA047433X.

[171] W. Chen, K. Wu, Z. Qu, and M. Lu, "Intrinsic high thermal conductive co-polyester based on offset π-π stacking," *Eur. Polym. J.*, vol. 121, p. 109 275, 2019. DOI: 10.1016/j.eurpolymj.2019.109275.

[172] A. X. Wu, J. A. Drayton, and Z. P. Smith, "Perfluoropolymer upper bound," *AIChE J.*, vol. 65, no. 12, pp. 1–12, 2019. DOI: 10.1002/aic.16700.

[173] Y. Yampolskii, N. Belov, and A. Alentiev, "Perfluorinated polymers as materials of membranes for gas and vapor separation," *J. Membr. Sci.*, vol. 598, p. 117 779, 2020. DOI: 10.1016/j.memsci.2019.117779.

[174] J. D. Wind, D. R. Paul, and W. J. Koros, "Natural gas permeation in polyimide membranes," *J. Membr. Sci.*, vol. 228, no. 2, pp. 227–236, 2004. DOI: j.memsci.2003.10.011.